Behavior and Design of High-Performance Fiber-Reinforced Concrete Coupling Beams and Coupled-Wall Systems

by

Rémy D. Lequesne

A dissertation submitted in partial fulfillment
of the requirements for the degree of
Doctor of Philosophy
(Civil Engineering)
in The University of Michigan
2011

Doctoral Committee:

Professor James K. Wight, Co-Chair
Associate Professor Gustavo J. Parra-Montesinos, Co-Chair
Professor Carlos E. Cesnik
Professor Sherif El-Tawil

To My Parents and Brother
for their relentless love and support

ACKNOWLEDGEMENTS

The National Science Foundation is acknowledged for funding the research that supported this thesis through NEES grant #CMS 0530383. Bekaert is acknowledged for their donation of materials and funds to support construction of the specimens. Erico Corp. is also acknowledged for their donation of materials used in the construction of the specimens. Finally, the American Concrete Institute and the Charles Pankow Foundation are thanked for partially funding my studies through the 2007-2008 Charles Pankow Foundation ACI Student Fellowship. The ideas and conclusions expressed in this thesis are those of the writer and may not represent the views of the sponsors.

In addition to funding agencies, I would like to acknowledge those who offered their help, support, and friendship to me throughout my time in graduate school. Completion of this thesis itself is a testament to the impact they had on either my work or on my graduate school experience.

Numerous people helped by working with me in the laboratory to complete the large-scale experimental work reported herein. The specimens would not have been built and tested without the hard work and expertise of Bob Fischer, Jan Pantolin, and especially Bob Spence. In addition to countless hours helping to fabricate, construct, and test, they helped keep my time in the laboratory entertaining with colorful conversations. In addition, numerous students worked alongside me, and for this help I (and my back/hands) owe a great debt of gratitude. Namely, Terry McGovern, Peter Heeringa, Elizabeth Stek, Katie Farnum, Heather Munoz, Kristen Hinkle, Abdul Atassi, Andrew Schon, Beverly Smith, Alessandra Correa, and Jen Buisson all played some role in getting the specimens constructed and tested. I am fortunate to still count many of them as friends.

Furthermore, numerous fellow PhD students volunteered their time and insights to either help me in the laboratory or to help me adjust to the demands and expectations of graduate school. Included among these students are Min-Yuan Cheng, Matthew Fadden, Mike Stultz, Ekin Ekiz, Pascal Laumet, Monthian Setkit, Ray Foltz, Simon (Shi-Ho) Chao, Afsin Canbolat, Andy Zimmerman, Cole Olsen, Chung-Chan Hung, Wen-Cheng Liao, Alex DaCosta and Hai Dinh. I especially want to acknowledge Mantia Athanasopoulou, who was stuck in an office with me for 5 years. I could not have asked for a more respectful and helpful officemate and friend.

I want to thank my thesis committee for their time and input. In particular, I want to thank Prof. El-Tawil and Prof. Cesnik for the time they have spent meeting with me and reviewing my thesis, and appreciate the feedback I have received. I especially owe a great debt of gratitude to my advisers, Prof. Wight and Prof. Parra-Montesinos, for their immeasurable contributions to this thesis and to my own development as an engineer. In addition to acting as excellent advisers, they are tremendous engineers, teachers, and individuals. They both set the bar very high in regards to professionalism and integrity. As I venture out into the working world, I cannot imagine a greater professional honor than earning their continued respect.

Finally, I owe the greatest thanks to my family and to my girlfriend, Lydia. I especially want to thank my brother, Eric, for always being a lot of fun to be around. He has been a steady reminder not to take myself too seriously because there is so much life outside of school. I want to thank my parents for having been unreasonably supportive of my endeavors for as long as I can remember. They have been there to listen, advise, and offer their love and support throughout my studies. Their steadfast presence in my life is a major reason I have completed this thesis with some remaining shred of sanity. Finally, I want to thank Lydia for being such a wonderful addition to my life. Being with her has made the last year and a half of my PhD the most fun part of the process. Her patience with my sometimes demanding schedule and her relentless support and optimism have helped me relax and enjoy my life in ways I never had time to before.

TABLE OF CONTENTS

DEDICATION ii
ACKNOWLEDGEMENTS iii
LIST OF FIGURES x
LIST OF TABLES xix
ABSTRACT xx
Chapter 1: Introduction 1
1.1 Background and Motivation 1
1.2 Objectives 4
1.3 Organization of Thesis 5
Chapter 2: Literature Review 7
2.1 High-Performance Fiber Reinforced Concrete 7
2.1.1 Characterization of HPFRC 8
2.1.2 Impact of HPFRC on Shear Capacity 11
2.1.3 Impact of HPFRC on Flexural Response 13
2.1.4 Impact of HPFRC on Development Length 14
2.2 Coupling Beam Behavior and Design 15
2.2.1 Reinforced Concrete Coupling Beams 15
2.2.2 Steel/Hybrid Coupling Beams 22
2.2.3 HPFRC Coupling Beams 22
2.2.4 Code Requirements and Performance Criteria 23
2.3 Coupled Wall System Behavior 24
2.3.1 System Response 24
2.3.2 Modeling System Response 27
2.3.3 Wall Detailing Requirements and Fiber Reinforcement 29

Chapter 3: Experimental Program 31
3.1 Phase 1: Coupling Beam Component Tests 32
3.1.1 Test Setup 32
3.1.2 Coupling Beam Design and Detailing 35
3.1.2.1 Selection of Diagonal Reinforcement 35
3.1.2.2 Selection of Longitudinal Reinforcement 37
3.1.2.3 Selection of Transverse Reinforcement 38
3.1.2.4 Design of Beam-to-Wall Connection 39
3.1.3 Construction Of Specimens 42
3.1.4 Instrumentation 44
3.2 Phase 2: Coupled Wall Tests 50
3.2.1 Test Setup 51
3.2.2 Reinforcement Layout 54
3.2.2.1 Design of Coupling Beams 54
3.2.2.2 Design of Structural Walls 58
3.2.3 Construction 60
3.2.4 Instrumentation 64
3.3 Material Properties 74
3.3.1 High Performance Fiber Reinforced Concrete (HPFRC) 74
3.3.2 Conventional Concrete 78
3.3.3 Reinforcing Steel 79
3.3.3.1 Estimating Steel Stresses from Recorded Strains 80
3.3.3.2 Behavior of Mechanical Splices 80
Chapter 4: Coupling Beam Component Test Results 83
4.1 Cracking and General Discussion of Specimen Response 83
4.1.1 Specimen CB-1 Response 84
4.1.2 Specimen CB-2 Response 87
4.1.3 Specimen CB-3 Response 89
4.1.4 Elongation and Development of Axial Force in HPFRC Coupling Beams 91
4.1.5 Location of Inflection Point 98
4.2 Flexural Behavior of HPFRC Coupling Beams 100

4.2.1 Flexural Strength 100
4.2.2 Rotations 103
4.2.3 Longitudinal Strain Distribution 109
4.2.4 Plastic Hinge Length 112
4.3 Shear Behavior of HPFRC Coupling Beams 115
4.3.1 Shear Strength 115
4.3.1.1 Shear Stress at Onset of Cracking 116
4.3.1.2 Relative Contribution of Shear Resistance Mechanisms at Peak Force 116
4.3.2 Shear Stress/Shear Distortion Relationship 117
4.3.2.1 Sliding Shear Displacements 119
4.3.2.2 Initial Shear Stiffness 125
4.3.2.3 Shear Distortion 126
4.4 Drift Components 128
4.5 Energy Dissipation 130
4.6 Stiffness 134
4.6.1 Coupling Beam Flexural Stiffness 135
4.6.2 Coupling Beam Shear Stiffness 137
4.7 Reinforcing Steel Strains 139
4.8 Summary and Conclusions 143
Chapter 5: Coupled Wall System Test Results 146
5.1 Cracking and General Discussion of Specimen Response 148
5.1.1 Specimen CW-1 Response 148
5.1.2 Specimen CW-2 Response 153
5.2 Wall Deformations Within the First Story 161
5.2.1 Wall Curvature 161
5.2.2 Shear Deformation 164
5.2.2.1 Shear Failure in Specimen CW-2 169
5.2.2.2 Wall Twist 174
5.2.3 Axial Deformation 176
5.3 Coupling Beam Deformations 180
5.3.1 Coupling Beam Drift 180

5.3.2 Axial Deformation 183
5.3.3 Shear Deformation 185
5.3.4 Curvature 190
5.3.5 Coupling Beam Drift Components 191
5.4 System Strength 193
5.5 Reinforcing Steel Strains 198
5.5.1 Progression of Yielding 198
5.5.2 Cutoff Longitudinal Bar Strains 204
5.5.3 Coupling Beam Shear Stresses 204
5.6 Summary and Conclusions 210
5.6.1 Walls 211
5.6.2 Coupling Beams 213
5.6.3 Coupled Wall System 214
Chapter 6: Design Considerations for Coupled Walls 216
6.1 Flexure-Based Coupling Beam Design 216
6.1.1 Simplified Flexure-Based Design Method for HPFRC Coupling Beams 217
6.1.2 Comparison of Flexure- and ACI Code-Based Capacity Prediction 222
6.2 Axial Load Effects in Coupled Wall Systems 230
6.2.1 Axial Forces in Coupling Beams 230
6.2.1.1 Causes of Axial Forces in Coupling Beams 230
6.2.1.2 Axial Forces and Coupling Beam Strength 232
6.2.2 Effect of Wall Axial Forces Resulting from Coupling 233
6.2.2.1 Axial Force and the Distribution of Base Shear Force Between Walls .. 234
6.2.2.2 Effect of Axial Force on Walls 235
6.2.2.3 The Need to Limit Coupling Ratio 240
6.2.2.4 Effect of Underestimating the Axial Force Acting on Walls 241
6.3 Estimation of "Backbone" Curve for HPFRC Coupling Beams 242
6.3.1 Flexural Mechanisms 244
6.3.2 Shear Deformations 247
6.3.3 Sliding Shear Deformations 250
6.3.4 Comparison of Model and Test Results 251

Chapter 7: Summary and Conclusions 255
7.1 Background and Motivation 255
7.2 Research Goals 256
7.3 Summary of Tests 257
7.4 Conclusions 258
7.4.1 Conclusions From Coupling Beam Tests 259
7.4.2 Conclusions From Coupled Wall Tests 260
7.4.2.1 Walls 260
7.4.2.2 Coupling Beams 261
7.4.2.3 Coupled Wall System 262
7.5 Future Work 263
References 265

LIST OF FIGURES

Figure 1.1 – Coupling of shear walls 1
Figure 2.1 – Idealized HPFRC tensile constitutive relationship (Naaman, 1998) 9
Figure 2.2 – Compressive behavior for FRC with various fiber volume fractions (Fanella and Naaman, 1985) 10
Figure 2.3 – Deformed shape of a coupled wall system under to earthquake loading (Subedi, 1991) 15
Figure 2.4 – Alternative coupling beam reinforcement schemes (Lequesne et al., 2009) 17
Figure 2.5 – Proposed coupling beam reinforcement (Park and Paulay, 1975) 18
Figure 2.6 – On-site photo of diagonally reinforced coupling beam 21
Figure 3.1 – Coupling-beam component test setup 33
Figure 3.2 – Target drift history for component tests 33
Figure 3.3 – Coupling-beam specimen reinforcement details 34
Figure 3.4 – Precast coupling beam embedment. Coupling beam reinforcement (highlighted) is developed parallel to the transverse reinforcement in the wall 40
Figure 3.5 – Coupling beam reinforcement prior to casting HPFRC 42
Figure 3.6 – Precast coupling beam prior to end block casting 43
Figure 3.7 – Completed specimen and test setup 43
Figure 3.8 – Specimen CB-1 strain gauge layout (gauges A1, L4, L8, L9 and S10 were damaged during casting) 45
Figure 3.9 – Specimen CB-2 strain gauge layout (gauges D1, L4 and L5 were damaged during casting) 46
Figure 3.10 – Specimen CB-3 strain gauge layout (gauges D4 and L2 were damaged during casting) 47
Figure 3.11 – Optical system marker positions 48

Figure 3.12 – Optical system marker labels..... 48
Figure 3.13 – Location and labeling of traditional data acquisition system inputs 49
Figure 3.14 – Coupling beam instrumentation, (a) Optical system, (b) Traditional instrumentation system 49
Figure 3.15 – Photo of coupled wall test setup and specimen 52
Figure 3.16 – Target fourth story drift history for coupled wall tests..... 53
Figure 3.17 – Coupling beam reinforcement (as shown on left, longitudinal reinforcement was cutoff near the wall face in Specimen CW-1. All longitudinal bars were fully developed in Specimen CW-2) 55
Figure 3.18 – Specimen CW-1 reinforcement layout (shaded region is HPFRC)..... 61
Figure 3.19 – Specimen CW-2 reinforcement layout (shaded region is HPFRC)..... 62
Figure 3.20 – Slab reinforcement details 63
Figure 3.21 – Typical reinforcement for wall foundations (transverse wall reinforcement not shown for clarity)..... 63
Figure 3.22 – Mechanical anchorage for #5 (D16) longitudinal reinforcement in walls . 65
Figure 3.23 – Mechanical splice for #5 (D16) longitudinal reinforcement in walls..... 65
Figure 3.24 – Wall foundations prior to placement of concrete 66
Figure 3.25 – Precast coupling beam placement, supported by formwork prior to casting 67
Figure 3.26 – Precast coupling beam embedment detail 67
Figure 3.27 – Coupled wall strain gauge locations (wall diagram) 69
Figure 3.28 – Coupled wall strain gauge locations (coupling beam diagram) 70
Figure 3.29 – Optical system “marker” locations..... 71
Figure 3.30 – Optical system “marker” labels..... 71
Figure 3.31 – Layout of traditional instrumentation..... 72
Figure 3.32 – Photo of optical system “marker” layout prior to testing..... 72
Figure 3.33 – Photo of specimen, fully instrumented, prior to testing 73
Figure 3.34 – Compressive constitutive model..... 77
Figure 3.35 – Tensile constitutive model..... 77
Figure 3.36 – (top figure) Recorded strain from gauge L1 of Specimen CB-1; (bottom figure) Calculated stress versus recorded strain for strain gauge L1 of Specimen CB-1 . 81

Figure 3.37 – Mechanically spliced bar coupon ready for testing 82
Figure 3.38 – Effective stress versus apparent average strain relationship for straight and mechanically spliced coupons of #6 (D19) reinforcing bars 82
Figure 4.1 – Calculation of drift (chord rotation) from specimen deformation 83
Figure 4.2 – Specimen CB-1 shear stress versus drift response 84
Figure 4.3 – Ultimate damage state of Specimen CB-1: insufficient confinement and sliding are evident 86
Figure 4.4 – Specimen CB-2 shear stress versus drift response 87
Figure 4.5 – Damage of Specimen CB-2 at 3.5% and 5.5% drift, left and right, respectively 88
Figure 4.6 – Specimen CB-3 shear stress versus drift response 90
Figure 4.7 – Damage of Specimen CB-3 at 3% and 6% drift, left and right, respectively 91
Figure 4.8 – Average axial strain in coupling beam specimens at the peak drift of each loading cycle (positive strain is elongation) 92
Figure 4.9 – Axial force developed in coupling beam specimens at the peak drift of each loading cycle, normalized by the axial force capacity 93
Figure 4.10 – Relationship between the maximum previously imposed drift due to flexural rotations and average axial strain (positive is elongation) 94
Figure 4.11 – Relationship between the maximum previously imposed drift and average axial strain (positive is elongation) 95
Figure 4.12 – Average axial strain of coupling beam specimens at the peak drift of each loading cycle plotted against the loading cycle number in the positive and negative loading directions 96
Figure 4.13 – Axial force in coupling beams normalized by the applied shear force 97
Figure 4.14 – Location of inflection point, calculated at the peak drift imposed in each loading cycle, measured from the face of the wall 99
Figure 4.15 – Moment-curvature analysis used for design of specimens. Circled points indicate likely locations for ultimate failure planes to develop (example is for Specimen CB-2) 101

Figure 4.16 – Shear force versus drift response for Specimens CB-1, CB-2 and CB-3, with capacity bounds predicted by simplified sectional analysis 104
Figure 4.17 – Beam "strips" defined by adjacent rows of markers 105
Figure 4.18 – Moment-curvature relationship for strip 4 of Specimen CB-2 (typical of middle strips) 106
Figure 4.19 – Moment-curvature relationships for strip 2 of Specimen CB-2 (typical of end strips)..... 107
Figure 4.20 – Moment-"apparent curvature" relationships for strip 9 of Specimen CB-2 (typical of strips 1 and 9) 108
Figure 4.21 – Moment-curvature relationships for strip 9 of Specimen CB-2 adjusted for effective strip thickness (typical of strips 1 and 9) 109
Figure 4.22 – Longitudinal strain distribution at 0.5% drift in Specimens CB-1, CB-2 and CB-3 (top to bottom, respectively), at initiation of flexural yielding. Tension is positive. 110
Figure 4.23 – Longitudinal strain distribution at 1.5% drift in Specimens CB-1, CB-2 and CB-3 (top to bottom, respectively). Tension is positive. 111
Figure 4.24 – Curvature distribution for strips 2-8 of all three coupling beam specimens in the negative and positive loading direction (left and right plot, respectively) 114
Figure 4.25 – Typical region of the marker grid with quantities for determining shear distortion 118
Figure 4.26 – Envelope shear stress versus shear distortion for strip 4 of Specimen CB-2 119
Figure 4.27 – Identification of initiation of sliding shear displacements in strip 8 of Specimen CB-1 120
Figure 4.28 – Sliding shear displacement distribution for strips 1-9 of all three coupling beam specimens in the negative and positive loading direction (left and right plot, respectively)..... 122
Figure 4.29 – Observed initial shear stiffness for individual strips, normalized by the theoretical shear modulus 126

Figure 4.30 – Shear distortion distribution for strips 1-9 of all three coupling beam specimens in the negative and positive loading direction (left and right plot, respectively) 127
Figure 4.31 – Relative percentage contributions to specimen drift at the peak drift of each loading cycle (Specimens CB-1, CB-2 and CB-3, top to bottom, respectively) 129
Figure 4.32 – Energy dissipated per loading cycle plotted against the average peak drift achieved in the positive and negative loading directions..... 131
Figure 4.33 – Close-up of energy dissipated per loading cycle plotted against the average peak drift achieved in the positive and negative loading directions 132
Figure 4.34 – Energy dissipated per loading cycle normalized by an equivalent elasto-plastic hysteresis loop and plotted against the average peak drift achieved in the positive and negative loading directions 133
Figure 4.35 – Elasto-plastic hysteresis loop used for normalization of the energy dissipated per cycle, drawn to the peak force and displacement of each loading cycle (example taken from a late loading cycle from the test of Specimen CB-2)..... 133
Figure 4.36 – Experimentally obtained secant flexural stiffness reduction factors..... 136
Figure 4.37 – Experimentally obtained secant shear stiffness, normalized by G..... 138
Figure 4.38 – Experimentally obtained secant shear stiffness, normalized by E 138
Figure 4.39 – Yield progression for Specimen CB-1. Rectangles mark the location of a strain gauge prior to yielding, black dots indicate a location where yielding had occurred. 140
Figure 4.40 – Yield progression for Specimen CB-2. Rectangles mark the location of a strain gauge prior to yielding, black dots indicate a location where yielding had occurred. 140
Figure 4.41 – Yield progression for Specimen CB-3. Rectangles mark the location of a strain gauge prior to yielding, black dots indicate a location where yielding had occurred. 141
Figure 5.1 – Definition of terms used to calculate wall drift..... 147
Figure 5.2 – Overturning moment versus wall lateral drift response for Specimen CW-1 149

Figure 5.3 – Damage typical of coupling beams in Specimen CW-1 at a system drift of 0.75%. Cracking near the termination of the longitudinal beam reinforcement is evident in the wall. 150
Figure 5.4 – Damage localizing along termination of longitudinal coupling beam reinforcement at 1% system drift (Specimen CW-1). 151
Figure 5.5 – Final damage state at the base of Specimen CW-1 (left and right are east and west walls, respectively). Diagonal cracks occurred when each wall was in compression; flexural cracks predominantly occurred while each wall was in tension. 151
Figure 5.6 – Damage state of coupling beams in Specimen CW-1 after testing. Coupling beams from story level four down to one are shown from top to bottom, respectively. 152
Figure 5.7 – Overturning moment versus wall lateral drift response for Specimen CW-2 154
Figure 5.8 – Photo of the base of the wall showing flexural cracking that localized at the termination of the dowel bars extending from the foundation. 155
Figure 5.9 – Damage state of coupling beams at a system drift of 0.75%. HPFRC and reinforced concrete coupling beams are shown top and bottom, respectively. 156
Figure 5.10 – Final damage state of the first story walls of Specimen CW-2 (left and right are east and west walls, respectively). Diagonal cracks occurred when each wall was in compression, flexural cracks predominantly occurred while wall was in tension. 158
Figure 5.11 – Damage of coupling beam CB-4 in Specimen CW-2. Buckling may have begun by 6.0% drift. 159
Figure 5.12 – Damage state of coupling beams in Specimen CW-2 after testing. Coupling beams from story level four down to one are shown from top to bottom, respectively. 160
Figure 5.13 – Location of wall strips used in calculation of wall deformations. 162
Figure 5.14 – Average wall curvature for strips 1-3, 4-6, and 7-9 in the first story of the walls, with peak curvature ductility labeled 164
Figure 5.15 – Average shear distortion per strip in the first story of the walls 167
Figure 5.16 – Typical example of average principal strain distribution and orientation within the first story of the walls. Outward and inward pointing arrows indicate tensile and compressive strains, respectively. Arrow length is proportional to the magnitude of the principal strain. 168

Figure 5.17 – Photographs of the failure plane in Specimen CW-2 from both faces of the wall specimen..... 171
Figure 5.18 – Location of dominant cracks (left), and average shear strain in each instrumentation grid unit (in radians), calculated at various points within the final positive loading half-cycle..... 173
Figure 5.19 – The twist of individual walls about a vertical axis caused markers in row A (on the foundation) to move laterally relative to the markers in rows B through E (on the wall) due to their proximity to the stationary cameras 175
Figure 5.20 – Example of positive (or negative) twist in the tension wall forcing negative (or positive) twist to occur in the compression wall in order for out-of-plane compatibility to be maintained..... 176
Figure 5.21 – Wall twist in Specimen CW-2 (typical of wall specimens) 177
Figure 5.22 – Average wall axial deformation for strips in the first story of the walls (positive indicates tensile strains) 179
Figure 5.23 – Inputs for coupling beam drift calculation 181
Figure 5.24 – Coupling beam drift versus interstory wall drift 182
Figure 5.25 – Axial strain in coupling beams plotted versus coupling beam drift for Specimens CW-1 and CW-2 (top and bottom plot, respectively) 184
Figure 5.26 – "Strips" of the coupling beam at the first wall story used for calculating the distribution of deformation over the length of the coupling beam 186
Figure 5.27 – Average shear distortion (rad), per strip, in the coupling beam at the first story for Specimens CW-1 and CW-2 (top and bottom, respectively). Left and right plot represent negative and positive drift, respectively..... 187
Figure 5.28 – Sliding displacements (in.), per strip, in the coupling beam at the first story for Specimens CW-1 and CW-2 (top and bottom, respectively). Left and right plot represent negative and positive drift, respectively..... 188
Figure 5.29 – Sliding displacement in strip 7 of CB-1 in Specimen CW-2 versus coupling beam drift. 189
Figure 5.30 – Peak-to-peak sliding displacements (in.), per strip, in the coupling beam at the first story for Specimens CW-1 and CW-2 (left and right, respectively). 189

Figure 5.31 – Coupling beam curvature (rad/in.), per strip, in the first story coupling beam for Specimens CW-1 and CW-2 (top and bottom, respectively). Left and right plot represent negative and positive drift, respectively..... 191
Figure 5.32 – Relative contribution to the total drift of the first story coupling beam in Specimens CW-1 and CW-2 (top and bottom, respectively)..... 192
Figure 5.33 – Coupling of shear walls..... 194
Figure 5.34 – Experimental result and predicted capacity..... 196
Figure 5.35 – Wall Strength Index (WSI) for coupled wall specimens versus coupling ratio and theoretical moment capacity of individual walls versus coupling ratio..... 197
Figure 5.36 – Progression of yielding at strain gauge locations (Specimen CW-1, walls) 200
Figure 5.37 – Progression of yielding at strain gauge locations (Specimen CW-1, beams) 201
Figure 5.38 – Progression of yielding at strain gauge locations (Specimen CW-2, walls) 202
Figure 5.39 – Progression of yielding at strain gauge locations (Specimen CW-2, beams) 203
Figure 5.40 – Calculated bar stresses corresponding to the strains measured by strain gauge CB3-5 in Specimens CW-1 and CW-2 (top and bottom, respectively), plotted versus coupling beam drift..... 205
Figure 5.41 – Estimated shear force contributed by midspan hoops in the coupling beams of Specimens CW-1 and CW-2 (top and bottom, respectively) 207
Figure 5.42 – Estimated shear force contributed by diagonal reinforcement in the coupling beams of Specimens CW-1 and CW-2 (top and bottom, respectively)..... 208
Figure 5.43 – Estimated total shear force contributed by diagonal and hoop reinforcement in the coupling beams of Specimens CW-1 and CW-2 (top and bottom, respectively) . 209
Figure 6.1 – Schematic of reinforcement (diagonal reinforcement is black) 218
Figure 6.2 – Schematic of reinforcement (longitudinal reinforcement is black)..... 219
Figure 6.3 – Assumed strain profile and corresponding force resultants for determining A_s (A_d is the horizontal component of the force in the diagonal reinforcement)..... 219

Figure 6.4 – Schematic of reinforcement (intermediate depth longitudinal reinforcement is black) 220
Figure 6.5 – Schematic of reinforcement (dowel reinforcement is black) 221
Figure 6.6 – Forces in steel reinforcement near the bent-diagonal detail 222
Figure 6.7 – Ratio of experimental and calculated coupling beam capacity versus coupling beam aspect ratio, where $V_{predicted} = 2A_{diag}f_y \sin\theta$. Hollow markers indicate a ductile flexural failure mode. 227
Figure 6.8 – Ratio of experimental and calculated coupling beam capacity versus coupling beam aspect ratio, where $V_{predicted} = 2M_n/\ell_n$. Hollow markers indicate a ductile flexural failure mode. 227
Figure 6.9 – Typical P-M and P-ϕ interaction diagrams (Pfrang, Siess and Sozen, 1964) 236
Figure 6.10 – Theoretical wall flexural capacity versus coupling ratio for a hypothetical coupled system with rectangular walls 238
Figure 6.11 – Theoretical relationship between Wall Strength Index (WSI) and coupling ratio for a hypothetical coupled wall system with rectangular walls for various levels of axial loads from gravity 239
Figure 6.12 – Schematic of spring model for coupling beam 243
Figure 6.13 – Schematic of coupling beam backbone curve 243
Figure 6.14 – Assumed distribution of curvature at first instance of flexural yielding 245
Figure 6.15 – Assumed distribution of curvature at peak shear demand 246
Figure 6.16 – Comparison between calculated tri-linear backbone curve and test results for Specimens CB-1, CB-2 and CB-3 (top to bottom, respectively) 254

LIST OF TABLES

Table 3.1 – High-strength hooked steel fiber properties (specified by manufacturer) 75
Table 3.2 – HPFRC mixture proportions by weight 75
Table 3.3 – HPFRC properties 28 days after casting and on the day of specimen testing (specified $f_c' = 6$ ksi; 41 MPa) 76
Table 3.4 – Regular concrete properties 28 days after casting and on the day of specimen testing 78
Table 3.5 – Results from coupon tests of steel reinforcement 79
Table 4.1 – Upper-bound capacity predicted by sectional flexural analyses performed at the dowel cutoff point with $P = 0.4 \cdot V_{pr}$ 102
Table 4.2 – Lower-bound capacity predicted by sectional flexural analyses performed at the dowel cutoff point, with $P = 0$ kip 103
Table 4.3 – Contributions to shear resistance at peak shear force, normalized by f_c' 116
Table 4.4 – Drift at which sliding was first identified 121
Table 4.5 – Predicted versus experimentally obtained peak sliding shear capacity 124
Table 4.6 – Energy dissipated per loading cycle normalized by the energy corresponding to an elasto-plastic hysteresis loop for comparable reinforced concrete coupling beams 134
Table 6.1 – Database of diagonally reinforced coupling beam specimens 224

ABSTRACT

A series of tests has been conducted to investigate the use of strain-hardening, high-performance fiber-reinforced concrete (HPFRC) in the critical regions of coupled-wall systems. A component test phase, consisting of tests of three large-scale precast coupling beam specimens with span-to-depth ratios (ℓ_n/h) of 1.75 subjected to reversed cyclic loading, was conducted to evaluate various reinforcement details for HPFRC coupling beams. A new design approach for HPFRC coupling beams, developed from these tests, has been shown to result in a ductile flexurally-dominated failure mode. The results from these tests confirmed that HPFRC can provide adequate confinement to the diagonal reinforcement, and that $5\sqrt{f_c'}$ [psi] $\left(0.42\sqrt{f_c'}\text{ [MPa]}\right)$ is an appropriate estimate of the shear stress contribution from HPFRC in coupling beams. The viability of precasting the coupling beam and connecting it to adjacent structural walls without interfering with wall boundary reinforcement was demonstrated.

Subsequently, two large-scale, four-story coupled-wall specimens, which were designed based on the results from the component test phase, were tested under lateral displacement reversals. Each coupled wall consisted of four precast coupling beams linking two T-shaped reinforced concrete structural walls. The reinforcement details of the precast beams were varied slightly, allowing a comparison of the response of different detailing schemes when integrated into a coupled wall system. The second coupled-wall specimen also incorporated fiber reinforcement in the plastic hinge regions of the walls, which allowed for a reduction in confinement reinforcement and a higher contribution from the concrete to wall shear capacity. The response of both coupled-wall specimens showed good strength and stiffness retention, and substantial energy dissipation up to system drifts of approximately 3.0%. It is recommended that

$4\sqrt{f_c'}$ [psi] $\left(0.33\sqrt{f_c'}\text{ [MPa]}\right)$ is appropriate for the shear stress contribution from HPFRC in coupled walls. Relaxing the maximum spacing of wall boundary confinement reinforcement to $t_w/2$ was shown to be permissible in HPFRC coupled walls.

CHAPTER 1:
INTRODUCTION

1.1 BACKGROUND AND MOTIVATION

Concrete structural walls are commonly used as the primary lateral force resisting system for both medium- and high-rise buildings. Due to their stiffness and strength, structural walls attract considerable lateral force when the building is subjected to an earthquake. Architects generally place these walls near the center of the building's floor plan, and often require that the walls have openings for either doors or windows. When these openings occur at every story level, the result is a reduced lateral stiffness as the structural wall acts more similar to independent walls than a single system. This is shown in Figure 1.1 in the left-most and center images. The stiffness and strength of the system

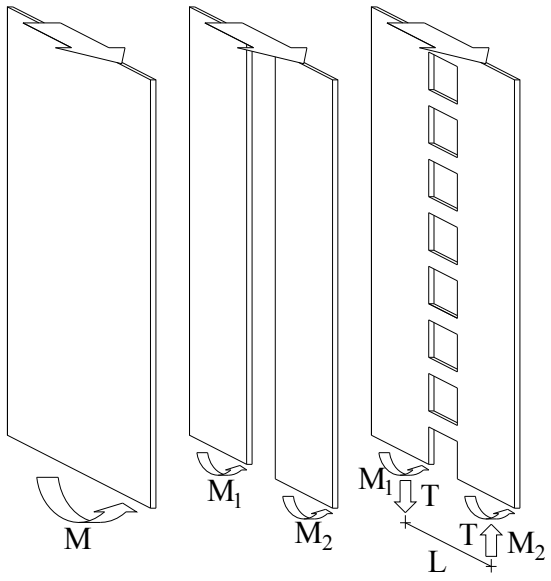

Figure 1.1 – Coupling of shear walls

can be largely regained by coupling two or more consecutive walls together through the use of short coupling beams, as shown in the right-most image in Figure 1.1. This coupling action reduces the need for flexural stiffness and strength from the individual walls by taking advantage of the couple that develops from the transfer of shear between the coupling beams and the walls, which provides additional resistance to overturning moment.

For the coupled system to behave as intended during a seismic event, the coupling beams are required to sustain high shear forces while undergoing large displacements. If the coupling beams are damaged and lose their ability to resist shear forces, the individual walls will no longer be coupled and structural drifts may increase substantially due to the reduced system stiffness. To prevent this, it has been shown (Paulay and Binney, 1974) that diagonal reinforcement combined with closely spaced transverse reinforcement is required in moderate to highly stressed beams with span-to-depth ratios of less than two. This diagonal reinforcement prevents development of a sliding shear failure and increases the coupling beam ductility and energy dissipation capacity. Unfortunately, the reinforcement detailing required by the ACI Building Code (ACI 318-08) to ensure stable behavior, which is based on the work by Paulay and Binney (1974), is difficult to construct and often fails to maintain the integrity of the full concrete section through large displacement reversals. The use of transverse reinforcement confining the entire coupling beam, as opposed to only the diagonal reinforcement cages, has recently been allowed in the ACI Building Code as a means to simplify the construction of coupling beams. This detail has been shown to be effective by Naish et al. (2009). Although this detail is simpler, it is still cumbersome to construct.

Other coupling beam design alternatives have been proposed and investigated (Harries, Gong and Shahrooz, 2000), including various reinforced concrete, steel, and hybrid steel-concrete coupling beam designs. Of these potential solutions, steel and hybrid steel-concrete coupling beams exhibit the most favorable response to reversed cyclic loading and have begun to find their way into design practice. However, despite the improved hysteretic behavior exhibited by steel coupling beams, providing proper anchorage of the steel section without disrupting reinforcement in the wall remains a significant challenge to engineers and contractors.

Recent coupling beam component tests on short coupling beams with span-to-depth ratios (ℓ_n/h) of 1.0 have demonstrated that precasting coupling beams with strain-hardening high-performance fiber reinforced concrete (HPFRC) provides improved ductility over more traditional concrete coupling beams and significantly simplifies detailing requirements (Canbolat, Parra-Montesinos and Wight, 2005). However, without further study, these findings are generally limited to coupling beams with aspect ratios near 1.0. There is a need for tests of more slender HPFRC coupling beams that are more heavily influenced by flexural behavior. These medium to slender coupling beams are commonly found in practice and their design requires experimental evidence for validation purposes. There is also a need to simplify the detailing of the precast beam-wall connection.

Desirable performance of a coupled wall system is also dependent on the base of each wall developing a ductile flexural hinge. These lower stories must accommodate appreciable flexural rotations without exhibiting significant shear distress, buckling of reinforcement, or crushing of concrete. To achieve the required ductility, concrete walls are typically reinforced with both horizontal shear reinforcement and tightly spaced boundary element confinement reinforcement that can be labor intensive to construct and interferes with the development of coupling beam reinforcement. In addition to relaxing the reinforcement requirements for coupling beams, it is probable that HPFRC can be used to simplify the reinforcement detailing requirements in the plastic hinge region of structural walls. Little experimental work has been done on slender HPFRC structural walls, and none on coupled HPFRC structural walls, where wall coupling affects the distribution of shear stresses between walls and the ductility demands placed on the wall compression zone. Therefore, there is a need to evaluate whether HPFRC can reduce the need for shear and confinement reinforcement in coupled walls, thus simplifying construction without sacrificing performance.

Finally, the behavior of a whole coupled wall system incorporating precast HPFRC coupling beams has not previously been studied. There is a need to consider the impact of incorporating HPFRC coupling beams on the overall behavior of the whole system. There is also interest in the deformation demands placed on each system component at various system drift levels. Furthermore, whether the proposed precast

coupling beam is a viable alternative to current construction methods needs to be demonstrated.

1.2 OBJECTIVES

The first phase of the experimental work described herein was undertaken to investigate the extent to which the conclusions drawn from tests of short coupling beams with span-to-depth ratios (ℓ_n/h) of 1.0 apply more slender beams with span-to-depth ratios of 1.75, and to develop an improved embedment detail. On the basis of these tests, a summary of the reinforcement detailing required to ensure a ductile response is presented and a design methodology that properly accounts for the use of HPFRC is proposed. In particular, it was the aim of the first phase of the study to:

- Confirm that HPFRC can be relied on to confine diagonal reinforcement,
- Quantify the shear strength that can safely be attributed to the HPFRC in design,
- Determine whether the response of coupling beams with an aspect ratio of 1.75 can be controlled by flexure, thereby improving ductility,
- Evaluate the stiffness, energy dissipation and drift capacity of HPFRC coupling beam specimens, and,
- Compare alternatives for embedding the precast HPFRC section into the adjoining structural walls without interfering with the boundary element reinforcement.

To accomplish this, three large-scale, diagonally reinforced HPFRC coupling beams with an aspect ratio of 1.75 were precast and tested.

The second phase of the experimental work described herein was undertaken to study the interaction between precast HPFRC coupling beams and structural walls, and to develop reinforcement detailing recommendations for HPFRC coupled walls that ensure adequate shear resistance and boundary element confinement. Specifically, it was the aim of the second phase of the study to:

- Demonstrate the ease with which precast coupling beams can be embedded in cast-in-place structural wall systems, thereby improving the constructability of such systems relative to current practice,

- Provide a comparison of the performance of HPFRC and reinforced concrete coupling beams subjected to similar shear stress and deformation demands,
- Develop detailing recommendations for shear and confinement reinforcement in HPFRC coupled walls,
- Consider whether wide wall flanges along the exterior of coupled wall systems markedly impact the shift of shear stresses to the wall subjected to compression as a result of coupling action,
- Study the distribution of deformation demands throughout the walls, coupling beams, and slabs, and,
- Develop a better understanding of the impact that walls and slabs have on the restraint of axial deformations in the coupling beams.

To accomplish this, two 1/3-scale, four-story coupled structural wall systems were built and subjected to reversed cyclic lateral displacements.

In addition to presenting an analysis of the test results, this report contains a discussion of:

- A simple design methodology for HPFRC coupling beams, and,
- Modeling guidance to the design professional seeking a reasonable estimate of the coupled HPFRC system response to inelastic displacement demands, including discussion of a method for estimating an envelope of the shear stress versus drift response for HPFRC coupling beams.

1.3 ORGANIZATION OF THESIS

This thesis is organized into seven chapters. The topic and motivation for the study are described in the first chapter. The specific objectives of each phase of the project are outlined. A review of relevant literature that provides a basis for the project is presented in the second chapter. Both phases of the experimental program are described in the third chapter, including a detailed record of the design, construction and testing of the specimens. Characteristics of the materials used for construction, obtained from coupon tests, are also reported in the third chapter. In-depth analysis of the data recorded

from the coupling beam component and coupled wall system test phases are reported in the fourth and fifth chapters, respectively. Conclusions drawn on the basis of each test series are summarized at the end of these chapters. Further discussion of the design and analysis of coupling beams and coupled walls is presented in chapter six. This discussion includes a proposed design procedure for HPFRC coupling beams, an analytical method for predicting the shear stress versus drift response of HPFRC coupling beams, and a discussion of the effects of axial forces on coupling beams and walls. Finally, the work conducted and the primary conclusions drawn are summarized in the seventh chapter, and then some relevant follow-up work is proposed.

CHAPTER 2:
LITERATURE REVIEW

2.1 HIGH-PERFORMANCE FIBER REINFORCED CONCRETE

The idea of improving the behavior of concrete in tension by controlling the propagation and opening of cracks with randomly distributed discrete fibers throughout the matrix can be traced to patents dating as early as 1918 (Naaman, 1985). Although some exploratory research was done in the decades that followed, it was not until the 1960s that significant attention was paid to understanding the behavior of the composite at a material (Romualdi and Mandel, 1964; Monfore, 1968; Shah and Rangan, 1971) and structural level (Snyder and Lankard, 1972; Batson, Jenkins, and Spatney, 1972; ACI SP-44, 1974). These advances led to standardization of testing and design methodologies (ACI Committee 544, 1988a; 1988b), and an industry-wide acceptance of fiber reinforcement as a means to improve the resistance to crack growth, and thus the durability, toughness, and ductility of concrete elements. However, as recently as 1991, this acceptance was primarily centered on slabs, floors, decks, and pavements, where shrinkage is the primary cause of cracking (Vondran, 1991).

Although the potential for fiber reinforcement to provide improved ductility and toughness to concrete structures subjected to earthquake induced deformations was forecast as early as 1973 (ACI Committee 544, 1973), only recently has a significant body of experimental work grown to support this assertion. In particular, a special class of fiber reinforced composites referred to as high-performance fiber reinforced concrete (HPFRC), which is unique for its ability to exhibit a strain-hardening response in tension (Naaman and Reinhardt, 1996), has been shown to markedly improve ductility and

toughness of structural members subjected to earthquake-type reversed cyclic displacements (Parra-Montesinos, 2005).

2.1.1 CHARACTERIZATION OF HPFRC

A significant amount of research has been directed towards characterizing the response of HPFRC to tensile, flexural, compressive and, more recently, to bi-axial and dynamic loading, due to the observation that fibers influence the mechanical properties of concrete and mortar in essentially all failure modes, especially those that induce fatigue and tensile stress (Gopalaratnam and Shah, 1987). A brief review of tensile, flexural, and compressive behavior is presented here, as it relates to this research project.

The response of a fiber reinforced cement composite to uniaxial tensile deformations has drawn considerable attention, and proposed test methods for obtaining a reliable tensile response are nearly as numerous as the researchers who have addressed the issue (e.g. Wang, Li, and Backer, 1990; Naaman, Otter, and Najm, 1991; Li et al., 1998; Barragan, Gettu, and Zerbino, 2002). Regardless, the volume of research focused on measuring the response of HPFRC in tension has led to a general acceptance of the idealized response shown in Figure 2.1. Initially, the uncracked composite responds elastically, with approximately the same modulus as an unreinforced matrix. Once cracking initiates, the HPFRC will exhibit a quasi-strain hardening behavior as the opening of cracks is controlled by fibers bridging the interface. These fibers transfer an increasing amount of tension across cracks and force the development of multiple fine cracks. This multiple cracking is what distinguishes HPFRC from other FRC materials (Naaman, 1996), and results in an appreciably tougher and more ductile composite. Eventually, the tensile stress capacity at one of the cracks is reached and all further deformation of the composite results from opening of that critical crack. This crack opening is a gradual process controlled by the pullout of fibers, and results in the softening portion of the curve shown in Figure 2.1.

Unlike tensile testing, there is general agreement on appropriate flexural test methodology for fiber reinforced cement composites (ASTM C1609/C1609M – 05, RILEM TC 162-TDF, 2000). The flexural response of FRC composites can be described

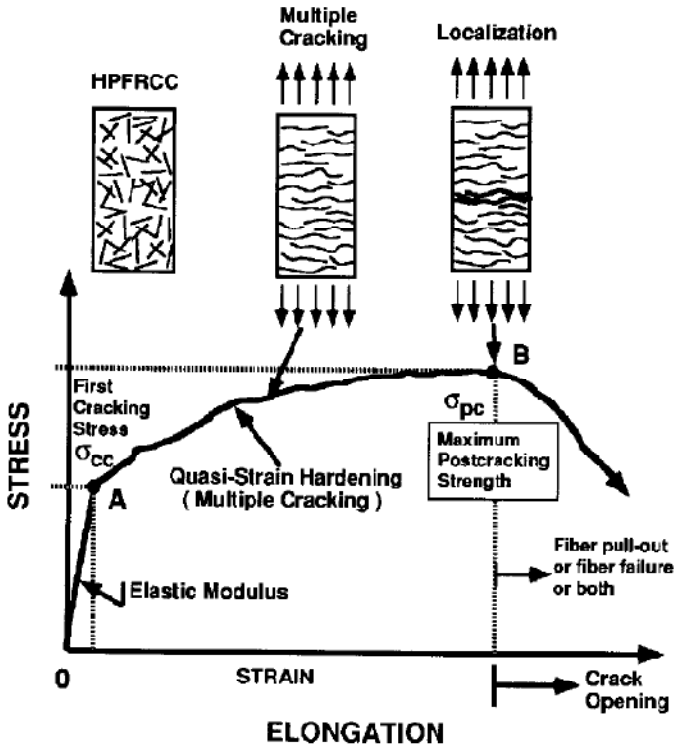

Figure 2.1 – Idealized HPFRC tensile constitutive relationship (Naaman, 1998)

as initially linear-elastic, followed by either a hardening or softening response. Deflection hardening can be achieved with FRC composites that do not exhibit strain-hardening in tension (Naaman, 2003), so the flexural test is not sufficient for classifying a composite as HPFRC. However, this standardized flexural test is useful for providing comparisons of the behavior of FRC composites and for characterizing the flexural response of FRC. Recent research has also indicated that the flexural toughness exhibited in this test correlates well with the shear toughness of the composite, thus providing a simpler test for gauging the response to shear (Higashiyama and Banthia, 2008). Given the reliability of this flexural test relative to current tensile testing methods, researchers have attempted to develop methods for deriving uniaxial tensile constitutive relationships from results obtained through flexural tests, but more work is needed on the subject (Soranakom and Mobasher, 2007; ACI Committee 544, 2007; Soranakom and Mobasher, 2008).

Early work on the compressive response of FRC indicated that the inclusion of fiber reinforcement has minimal impact on the peak compressive strength of the composite (Chen and Carson, 1971). Subsequent studies have confirmed this, but have

also indicated that FRC exhibits considerable improvements in post peak ductility, as shown in Figure 2.2. Furthermore, it has been noted that FRC exhibits modest increases in secant modulus and increased strains at peak stress, when compared to tests of the matrix alone (ACI Committee 544, 1988b; Ezeldine and Balaguru, 1992). Also of interest to this study is work done on the interaction between conventional steel confinement and FRC. Tests of FRC specimens with and without longitudinal and transverse reinforcement (Campione and Mindess, 1999; Massicotte et al., 1999) have indicated the following:

- Fiber reinforcement increases compressive ductility substantially, in some cases more than traditional stirrups,
- Traditional stirrups are more effective than FRC at increasing the compressive strength of concrete,
- Inclusion of fibers greatly improves the energy dissipation and damage tolerance of the specimen,
- Loss of cover is delayed and the overall integrity of the concrete section is improved with fiber reinforcement, and
- The longitudinal concrete strains required to induce fracture of stirrups is increased when fibers are included.

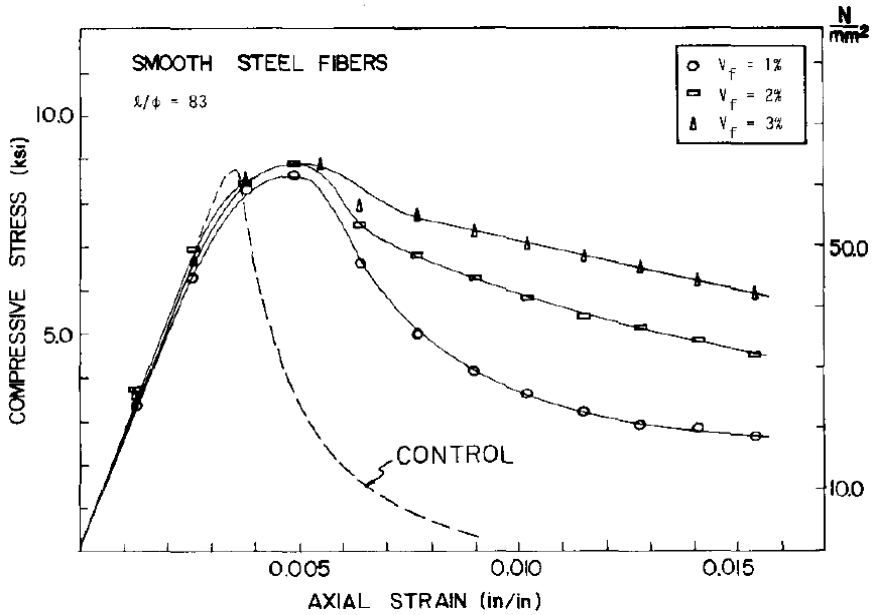

Figure 2.2 – Compressive behavior for FRC with various fiber volume fractions (Fanella and Naaman, 1985)

2.1.2 IMPACT OF HPFRC ON SHEAR CAPACITY

The effectiveness of FRC of resisting shear has been recognized and investigated since Batson, Jenkins, and Spatney (1972) first experimentally demonstrated that FRC may be a viable alternative to vertical or inclined stirrups. The inclusion of fibers will result in a reduction in crack widths and spacing, and an overall increase in the post-cracking stiffness of shear dominated beams (Narayanan and Darwish, 1987). These narrower cracks lead to increased aggregate interlock (Paulay and Loeber, 1974) relative to beams reinforced with stirrups. Furthermore, fiber reinforcement has been shown to act compositely with stirrups. Shearing stresses are resisted by the fiber reinforced concrete and stirrups, thereby reducing shear deformations and deflections when compared to beams reinforced with only one or the other (Swamy and Bahia, 1985; Oh et al., 1998; Oh et al., 1999). Also, because fibers act to arrest the growth of cracks, a stiffer and stronger contribution from dowel action has been shown to result (Swamy and Bahia, 1979). Relatively simple models developed on the basis of extensive reviews of these and other experimental programs have shown to be in good agreement with the reported results, indicating that the mechanisms resisting shear are relatively well understood (Tan, Murugappan, and Paramasivam, 1993; Khuntia, Stojadinovic, and Goel, 1999; Choi, Park, and Wight, 2007). A database of more than 200 FRC and companion reinforced concrete beams failing in shear was compiled as part of a recent effort by ACI Committee 318-F. The database was used to evaluate a new provision that allows fiber reinforcement to be used to satisfy minimum shear reinforcement requirements in beams (Parra-Montesinos, 2006). This provision was adopted in the most recent code cycle (ACI 318-08), marking the first inclusion of fiber reinforcement as shear reinforcement in a building code.

The problem of shear in reinforced concrete is further complicated when the direction of loading is reversed and the member is forced to undergo multiple load cycles in the post-yield range (Brown and Jirsa, 1971; Bertero and Popov, 1975; Wight and Sozen, 1975; Scribner and Wight, 1980). As a concrete member is subjected to post-yield deformations, the cracking of the concrete and plastic deformation in the reinforcement affect the ability of the member to resist shear, particularly when the direction of loading is reversed and again carried past yield. This degradation of shear capacity is of great

concern in earthquake-resistant design, where cyclic loading can potentially lead members to fail in shear, even after the full flexural capacity of the section has been reached. The substantial reduction in shear capacity due to multiple post-yield cycles can be ascribed to the breakdown of multiple mechanisms, as summarized by Biskinis, Roupakias, and Fardis (2004):

- The accumulation of plastic deformations in reinforcing steel result in wider cracks, resulting in diminished aggregate interlock and deeper crack penetration into the compression zone,
- The capacity of the compression zone to resist shear is compromised by tensile cracking from opposing load cycles, and,
- The transfer of shear stresses across cracks through aggregate interlock is diminished due to the grinding of aggregates along crack faces.

Simply discounting the contribution of concrete to the shear capacity of members subjected to load reversals is not adequate for ensuring safe design, because the role of the concrete is critical to developing the capacity of the stirrups (Wight and Sozen, 1975). Therefore, providing confinement to maintain the integrity of the concrete core is of critical importance.

Fiber reinforced concrete, particularly HPFRC, has been shown to markedly improve the stability of a concrete member subjected to high shear. Early work (Henager, 1977) demonstrated that steel fiber reinforcement may lead to high shear strength and improved damage tolerance, allowing for the use of a lower transverse reinforcement ratio through the critical plastic hinge region. Further work on beam-column connections (Jiuru et al., 1992; Filiatrault, Ladicani, and Massicotte, 1994; Parra-Montesinos and Wight, 2000; Bayasi and Gebman, 2002) has shown that fiber reinforcement increases the joint shear strength and provides confinement to the concrete within the joint, thus delaying the breakdown of shear resisting mechanisms with cycling and improving the overall damage tolerance and energy dissipation capacity of the joint. This increased shear capacity and confinement, resulting in higher toughness and energy dissipation, has been demonstrated in other shear critical members including shear walls (Kim and Parra-Montesinos, 2003; Dazio, Buzzini, and Trub, 2008), slabs (Theodorakopoulos and Swamy, 1999; Naaman, Likhitruangsilp, and Parra-Montesinos, 2007; Lee et al., 2008;

Cheng, Parra-Montesinos, and Shield, 2008), and coupling beams (Canbolat, Parra-Montesinos, and Wight, 2005; Zhang, Zhang, and Huang, 2007; Yun et al., 2008; Lequesne et al., 2009; Parra-Montesinos, Wight, and Setkit, 2010; Lequesne et al., 2011), even as the amount and complexity of reinforcement detailing is reduced.

2.1.3 Impact of HPFRC on Flexural Response

Early studies of the flexural response of fiber reinforced beams focused on the material response, and often did not include steel reinforcement. The results of these studies showed that the inclusion of fibers increased the ultimate flexural strength as fiber volume fraction and resistance to pullout were increased (Snyder and Lankard, 1972). However, the improvement in flexural toughness was significantly more noticeable. In one study, the toughness increased by a factor of 20, whereas strength increased by only a factor of 2 (Shah and Rangan, 1971). Quickly researchers focused on the improved toughness because it was recognized that flexural strength increases did not capture the full impact of fiber inclusion (Halvorsen and Kesler, 1979; Balaguru, Narahari, and Patel, 1992).

Flexural testing of fiber reinforced beams with longitudinal reinforcement has shown that the ultimate flexural capacity is increased, but that this increase is less significant than the change in cracking pattern and load-deformation response attained (Swamy, Al-Ta'an, and Ali, 1979; Swamy and Al-Ta'an, 1981; Oh, 1992; Ashour and Wafa, 1993). These tests indicate that the inclusion of fibers noticeably increases the flexural crack density, reduces crack widths, and delays crack penetration into the flexural compression zone. These studies also showed that fiber reinforcement results in a stiffer moment-curvature response in the cracked elastic range, resulting in reduced deflections at service loads.

The impact of fiber reinforcement on the flexural toughness and damage tolerance of concrete members subjected to displacement reversals may be greater than for monotonic loading conditions. Studies of polymer fiber reinforced cement composite flexural members subjected to displacement-reversals have confirmed that fibers provide confinement to the reinforcing steel and concrete core, effectively preventing splitting or spalling of the concrete (Fischer and Li, 2002; Fischer and Li, 2003). As previously

established, providing sufficient confinement to the concrete section is critical for developing the full member capacity and ensuring a stable hysteretic response of a plastic hinge (Wight and Sozen, 1975). The confinement provided by fibers to beam-column connections (Filiatrault, Ladicani, and Massicotte, 1994; Parra-Montesinos and Wight, 2000; Bayasi and Gebman, 2002; Parra-Montesinos, Peterfreund, and Chao, 2005) has been shown to be effective in flexural hinges as well (Parra-Montesinos, Peterfreund, and Chao, 2005; Parra-Montesinos and Chompreda, 2007), resulting in superior damage tolerance, resistance to longitudinal bar buckling, and an overall increase in energy dissipation of the member.

2.1.4 Impact of HPFRC on Development Length

The behavior of the bond between HPFRC and reinforcing steel has also drawn attention from researchers seeking to quantify the beneficial effect of fibers to this interaction. Ezeldine and Balaguru (1989) showed that fibers arresting the propagation of splitting cracks initiating at the steel-concrete interface leads to appreciable improvements in the post-peak ductility of the bond stress-slip relationship. Further work has shown that FRC improves the pullout strength and ductility, which allows for shorter bar development lengths (Krstulovic-Opara, Watson and LaFave, 1994). Results from tests of HPFRC beam-column joints indicated that HPFRC reduces the development length and significantly reduces slip for bars subjected to large reversed cyclic inelastic strain demands (Parra-Montesinos, Peterfreund and Chao, 2005).

FRC has also been shown to have a marked impact on tension stiffening and the cracking behavior of FRC reinforced with steel bars (Noghabai, 1999). While these effects are more pronounced for deformed steel reinforcement, where the pullout behavior is generally governed by splitting of the surrounding concrete, there is also a discernable improvement in the pullout response of bars controlled by crushing/shear (Krstulovic-Opara, Watson and LaFave, 1994), and friction-type bond (Chao, 2005), due to the confinement provided by the HPFRC to the development region.

2.2 COUPLING BEAM BEHAVIOR AND DESIGN

Nearly every theoretical and experimental study that has addressed the behavior of coupled wall systems has emphasized the need for coupling beams to exhibit significant inelastic deformation capacities. The deformed shape of a coupled wall subjected to earthquake loading, with the resulting deformed shape of a coupling beam highlighted, is shown in Figure 2.3. A coupling beam can easily be subjected to chord rotation demands, referred to herein as "drift," which are several times greater than the story drifts in the walls themselves. This drift is calculated as the differential movement shown in Figure 2.3, divided by the length of the coupling beam.

To aggravate this design scenario, coupling beams must also possess and maintain high stiffness and strength for the system to develop a meaningful degree of coupling. Unfortunately, the low span-to-depth ratios of coupling beams, which are typically less than 4 ($\ell_n/h < 4$), make the achievement of a stable hysteretic behavior under shear reversals challenging.

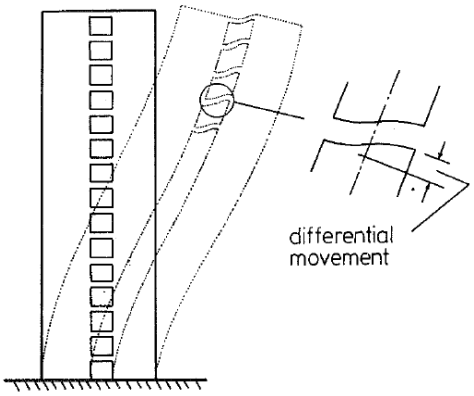

Figure 2.3 – Deformed shape of a coupled wall system under earthquake loading (Subedi, 1991)

2.2.1 REINFORCED CONCRETE COUPLING BEAMS

The design of coupling beams that possess sufficient strength, stiffness, and ductility to ensure a reliable coupling mechanism for resisting earthquake motions has drawn the attention of researchers since the late 1960s. Paulay's work (Paulay, 1969) was the first to provide experimental evidence highlighting the inadequacy of "moment-type"

reinforcement (Figure 2.4(a)) schemes for coupling beams. Paulay conducted three series of coupling beam tests with aspect ratios (ℓ_n/h) of 1.0, 1.3, and 2.0. Each of the specimens, subjected to either monotonic or cyclic loading regimens, failed in a brittle manner characterized as either diagonal tension or a combined crushing/sliding shear failure mode near the coupling beam-to-wall interface. Whether diagonal tension or sliding shear controlled the failure depended on whether sufficient transverse reinforcement was provided to prevent a diagonal tension failure. Attempts to provide additional confinement to the compression zone were insufficient to provide a ductile response under cyclic loading.

Furthermore, Paulay's specimens failed to reach the theoretically predicted ultimate capacity, which he concluded was an indication that traditional reinforced concrete beam principles were not appropriate for short coupling beams. The observation that tensile strains develop in the flexural reinforcement along the full length of the beam, which is in contrast to the expected strain profile based on the imposed sectional moments, was used to bolster this assertion. Ultimately, the fundamental conclusion to be drawn from these tests – that traditional "moment-type" reinforcement is not adequate for short coupling beams subjected to large nominal shear stresses – highlighted the need for new approaches to the design of coupling beams and spurred several research projects aimed at developing alternative designs.

In a follow-up study (Binney, 1972), it was demonstrated that providing the primary steel reinforcement for short coupling beams in the form of two intersecting diagonal groups, as shown in Figure 2.4(d), significantly improves their ductility and energy dissipation capacity. The concept of using bent-up or diagonal reinforcement to resist shear was not new; the idea was outlined by Morsch (Morsch, 1909) in his discussion of a truss analogy for shear in beams, and has been studied extensively since (ACI Committee Report, 1920; Godfrey, 1920; Morsch, 1927; Sorensen, 1974). The adoption of diagonal reinforcement in coupling beams for shear walls was already being explored, with some success (Luisoni, Somenson, and Ungaro, 1971). However, Paulay and Binney's series of tests was the first to demonstrate the effectiveness of diagonal reinforcement for large-scale coupling beam specimens subjected to reversed cyclic displacements. Specifically, these tests demonstrated that diagonal reinforcement can

prevent diagonal tension and sliding shear failures, and instead force the yielding of diagonal steel to govern beam capacity and ensure ductile behavior. To account for this beam behavior, Eq. 2.1 was proposed for predicting the capacity of diagonally reinforced coupling beams with aspect ratios (ℓ_n/h) less than 2 (Park and Paulay, 1975). This equation discounts the contribution of concrete or transverse reinforcement to the shear capacity, and has been shown to be in reasonably good agreement with test results.

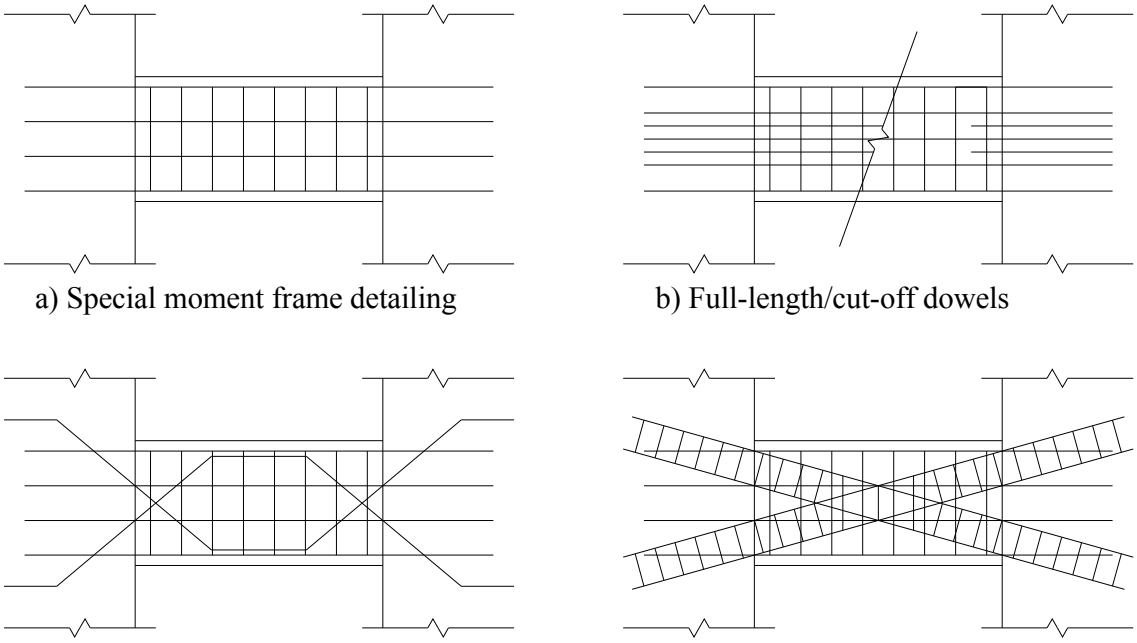

a) Special moment frame detailing

b) Full-length/cut-off dowels

c) Rhombic reinforcement layout

d) Diagonal reinforcement

Figure 2.4 – Alternative coupling beam reinforcement schemes (Lequesne et al., 2009)

$$V_n = 2A_s f_y sin\alpha \tag{2.1}$$

It was noted by Paulay and Binney (Binney, 1972; Paulay and Binney, 1974) that ensuring the stability of the diagonal bars with some confinement would lead to further improvements in performance, because the failure of the test specimens was initiated by buckling of the diagonal bars subjected to compression near the wall faces. Such confinement was explicitly shown by Park and Paulay (Park and Paulay, 1975) in their discussion of recommended coupling beam reinforcement layouts (See Figure 2.5).

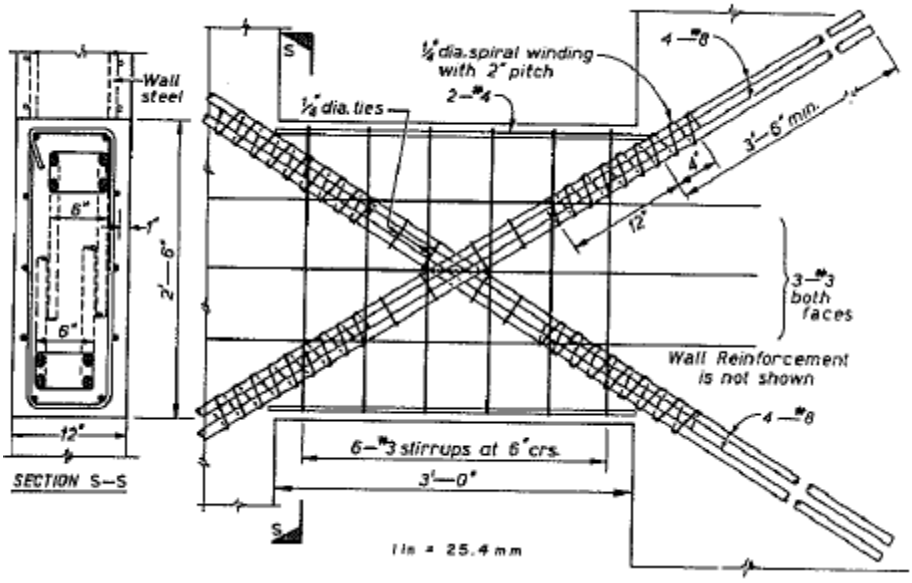

Figure 2.5 – Proposed coupling beam reinforcement (Park and Paulay, 1975)

Binney's tests also indicated that the termination of "secondary" longitudinal reinforcement near the beam-to-wall interface led to the initiation of damage localization in two of the three specimens tested. It would therefore seem that termination of reinforcement at the interface is undesirable, although the proposed reinforcement layout shown in Figure 2.5 does not account for this.

Subsequently, small-scale experimental work (Irwin and Ord, 1976; Mirza, 1980) was conducted to expand on the experimental observations reported by Paulay and Binney. These studies reported that diagonally reinforced coupling beams exhibit less severe cracking and crushing than comparable "moment type" coupling beams. Although these tests are perhaps useful for comparative or parametric-type studies of system behavior, they are of limited value for examining proposed reinforcement details due to their scale (beam depths less than 0.5 in. (12.5 mm)).

A pilot study at the Portland Cement Association tested coupling beam specimens with aspect ratios (ℓ_n/h) of 2.5 and 5.0. The goal of this study was to identify the most desirable coupling beam reinforcement layout to be adopted in a subsequent study of coupled walls (Barney et al., 1976; Shiu et al., 1978). The specimens had either moment-type, rhombic, or diagonal reinforcement, shown in Figure 2.4(a), (c), and (d), respectively. All of the beams tested were subjected to shear stresses ranging from

7 to $11\sqrt{f_c'}$ [psi] $\left(0.58 \text{ to } 0.91\sqrt{f_c'} \text{ [MPa]}\right)$. In addition, this study was the first to provide resistance to the longitudinal expansion of the specimens, which represents a more realistic set of boundary conditions than previous experimental work. The significant findings of this study can be summarized as:

- Moment-type reinforcement is limited by sliding-shear failure modes in beams with smaller aspect ratios, with specimens failing near 3.5% drift,
- Diagonal reinforcement in the hinge region ("rhombic reinforcement") eliminates sliding shear failures, but fails to improve the hysteretic response – specimens failed around 2.5% drift,
- Full-length diagonal reinforcement dramatically improved the ductility and toughness of the shorter coupling beam, which failed at approximately 6% drift,
- The improvements due to full-length diagonal reinforcement do not seem to manifest in longer coupling beams with aspect ratios of 5, and,
- Only the coupling beams with full-length diagonal reinforcement were able to reach their predicted shear capacity – most of the other beams were more than 10% below their predicted strength.

Although relatively small scale, these tests confirm the superior performance achievable with diagonal reinforcement for shorter span coupling beams. These tests were cited, along with Paulay and Binney's work, as justification when ACI Committee 318 adopted provisions for diagonally reinforced concrete beams in the Building Code (ACI 318-99).

A decade after the tests at the Portland Cement Association, two independent research programs studied the use of full length diagonal reinforcement for improving the hysteretic response of short columns subjected to high shear stresses. The first study (Kuramoto, Minami and Wakabayashi, 1988) tested fifteen specimens with aspect ratios (ℓ_n/h) of 2.0, twelve of which were diagonally reinforced. The primary conclusion was that for columns under low levels of axial load (very similar to coupling beams) diagonal reinforcement improves the strength and ductility of the element if adequately confined to prevent buckling. The need for confinement for the diagonal reinforcement increases as the axial load increases. In a similar study (Tegos and Penelis, 1988), 24 column and coupling beam specimens with aspect ratios (ℓ_n/h) of 2.0, 3.0, and 4.0 were tested. Eighteen of the 24 specimens evaluated the rhombic reinforcement detail shown in Figure

2.4(c), which was conceived as a simplified alternative to the relatively complicated reinforcement detailing required to ensure stability of diagonal reinforcement in coupling beams. Both the diagonal and rhombic reinforcement layouts were shown to dramatically increase the deformation capacity (by a factor of greater than 2) relative to the "moment-type" beams.

Two relatively recent studies (Tassios, Moretti, and Bezas, 1996; Galano and Vignoli, 2000), sought to compare the relative strength, ductility, and damage tolerance of several proposed alternatives to diagonally reinforced concrete coupling beams. The alternatives considered, shown in Figure 2.4, included a) special moment-frame detailing, b) full-length and cut-off dowel bars crossing the coupling beam-to-wall interface to prevent sliding shear failures, c) "rhombic" type reinforcement, which provides unconfined diagonal reinforcement through the plastic hinge, and, d) confined and unconfined diagonally reinforced coupling beams. These tests were performed on short coupling beams with aspect ratios of 1.0, 1.5, and 1.66. The results of these studies illustrate the following key points:

- Special moment-frame detailing was again shown to be inappropriate for short coupling beams subjected to high shear stresses,
- Dowel bars crossing the coupling beam-to-wall interface were shown to help prevent sliding shear failures, but could not prevent stiffness degradation and severe pinching in the hysteretic response,
- A rhombic layout of diagonal reinforcement required less complicated detailing than diagonally reinforced coupling beams, and exhibited less stiffness degradation than coupling beams detailed as special moment frames. However, pinching of the hysteretic loops was still present, and,
- Of the reinforced concrete options considered, confined diagonal reinforcement appeared to provide the most stable behavior and highest energy dissipation. It was noted that providing sufficient confinement to ensure stability of the diagonal bars is "indispensable", despite the significant field placement difficulties.

After the adoption of provisions for diagonal reinforcement in coupling beams by ACI Committee 318 in 1999, it became clear that placing the extensive transverse

reinforcement required by the code was causing difficulties for contractors and engineers alike. A beam detailed to satisfy the 1999 ACI Building Code (ACI 318-99) is shown in Figure 2.6. In this photo, possible construction difficulties become clear. ACI Committee 318 has adopted simplified alternative detailing provisions for coupling beams in the most recent code cycle (ACI 318-08) that permit confinement of the entire section, rather than only the diagonal reinforcement, in an effort to simplify both design and construction. Two research projects have been undertaken in conjunction with these efforts by ACI to evaluate simplified reinforced concrete coupling beam details. The first study included the testing of reinforced concrete coupling beams with relaxed confinement details to evaluate whether special confinement was necessary over the middle third of the span to ensure stability of the diagonal reinforcement (Fortney, Rassati and Shahrooz, 2008). The conclusions were not as hoped for; the final recommendation was to increase the minimum volume ratio of confinement above the current code requirements. In the second study, a comparison of the 2005 and 2008 ACI code requirements was performed. Test results indicated that the 2008 provision that allows the use of full section confinement leads to comparable, if not improved, behavior compared with the confinement around diagonal bars previously required (Naish et al., 2009).

Figure 2.6 – On-site photo of diagonally reinforced coupling beam

2.2.2 STEEL/HYBRID COUPLING BEAMS

As a consequence of the difficulties associated with designing and constructing concrete coupling beams, alternatives have been investigated. The first to be studied, and perhaps the most widely used alternative to reinforced concrete coupling beams, consists of a steel member embedded into concrete shear walls. When properly embedded, these steel coupling beams have been shown to develop significant strength while requiring relatively shallow depths compared to concrete beams. Perhaps most importantly, steel coupling beams exhibit an excellent hysteresis response characterized by high levels of ductility and energy dissipation (Shahrooz, Remmetter and Qin, 1993; Harries, Gong and Shahrooz, 2000; Park et al., 2005). A variation on the steel coupling beam scheme consists of encasing the steel section within a minimally reinforced concrete beam. Encasing a wide flange section or plate in concrete can be a desirable alternative to plain steel coupling beams as a means to provide additional capacity and, more importantly, prevent undesirable web-buckling at higher deformation levels (Shahrooz and Gong, 1998; Gong and Shahrooz, 2001a; Gong and Shahrooz, 2001b; Lam, Su and Pam, 2005). Despite the advantages, these steel and hybrid coupling beam alternatives present construction issues, as their embedment into the walls inevitably interferes with the placement of longitudinal and transverse reinforcement in the wall boundary elements.

2.2.3 HPFRC COUPLING BEAMS

Another alternative to reinforced concrete is the adoption of HPFRC in the design of coupling beams. Canbolat, Parra-Montesinos and Wight tested four short coupling beams with aspect ratios (ℓ_n/h) of 1.0. This series of tests included a reinforced concrete specimen detailed to satisfy the ACI Building Code (ACI 318-02) requirements, an HPFRC specimen with no diagonal reinforcement, and two precast, diagonally reinforced, HPFRC coupling beams (Canbolat, Parra-Montesinos and Wight, 2005). This series of tests demonstrated that HPFRC can:

- provide confinement to the diagonal reinforcement, eliminating the need for transverse reinforcement to prevent buckling,
- improve the toughness of the member, allowing the concrete to contribute to shear resistance at much higher drift levels,

- increase the shear capacity of the section by actively resisting diagonal tension stresses,
- increase the energy dissipated by the coupling beam, and,
- improve the damage tolerance of the member by distributing damage over multiple finer cracks, likely requiring reduced repair costs for similar drift levels.

Subsequent studies verified these results, offering greater confidence in the applicability of HPFRC to the design of shear dominated coupling beams (Yun et al., 2007; Zhang, Zhang and Huang, 2007).

2.2.4 Code Requirements and Performance Criteria

Most current code provisions or design guidelines for reinforced concrete coupling beams are of the prescriptive type. Of most relevance in the United States is the ACI Building Code (ACI 318-08), which requires diagonal reinforcement for coupling beams with aspect ratios (ℓ_n/h) of less than two and nominal shear stresses over $4\sqrt{f_c'}$ [psi] $\left(0.33\sqrt{f_c'}\text{ [MPa]}\right)$. For coupling beams with aspect ratios between two and four, the engineer is given the option of using diagonal or special moment frame detailing, per ACI Code Section 21.5. All other coupling beams are required to be detailed per ACI Code Section 21.5. The detailing requirements are made clear within the code document for each of these reinforcement layouts, and are intended to ensure a ductile performance of the element. Design guides born of the same prescriptive philosophy are available in IBC (International Code Council, 2000) and draft versions of documents developed by ACI Committee 374 (2006).

A shift of attention from prescriptive to performance-based design approaches has spurred the creation of documents establishing acceptable performance levels for coupling beams (ATC, 2009). A document in which performance-based design methods for hybrid coupled wall systems are proposed was recently published by ASCE (El-Tawil et al., 2010). However, most of these documents only provide a frame-work methodology, and avoid quantifying performance requirements for specific building components. Individual researchers have gone further, indicating that coupling beams require displacement ductilities on the order of 8 to 12, based primarily on simulations (Harries, 2001; Paulay, 2002).

2.3 COUPLED WALL SYSTEM BEHAVIOR

Understanding and predicting the response of coupled walls has been the focus of considerable research since the 1940s due to the complexity and high degree of redundancy inherent in the system. Initial attempts to model coupled systems (Chitty, 1947; Beck, 1962; Coull and Choudhury, 1967) showed that replacing the discrete coupling beams with a continuous laminar medium, and subjecting the structure to either uniform or triangular lateral force distributions, allowed for the derivation of a closed-form solution for the internal force distributions and roof level drifts. However, coupled systems are seldom simple enough to be accurately approximated in this way, so considerable experimental and analytical work has since been conducted in order to better understand the response of coupled systems.

2.3.1 SYSTEM RESPONSE

To the writer's knowledge, the first experimental work done on coupled systems involved the testing of a 1/20th scale model of a 20 story coupled core wall system (Hisatoku and Matano, 1972). A quasi-static test was conducted to evaluate assumptions regarding the deformed shape of the system, the influence of coupling on wall axial loads, and the general failure mechanism controlling the capacity of a coupled system. Unfortunately, due to the lack of an English translation for the publications describing these tests, this research has not received much attention from subsequent researchers.

Following the Managua earthquake in 1972, an analytical study involving elastic and inelastic analyses of a representative coupled wall structure was undertaken to identify critical design parameters affecting system behavior (Mahin and Bertero, 1976). Among other design issues, it was emphasized that high levels of ductility are required from coupling beams for the system to exhibit a meaningful level of ductility and damage tolerance. Results from this study also indicated that to ensure stable hinging behavior at the base of the structural walls, average base shear stresses below $5\sqrt{f_c'}$ [psi] $\left(0.42\sqrt{f_c'}\text{ [MPa]}\right)$ and low axial loads resulting from coupling are desirable.

Results from quasi-static testing of two 1/4 scale, 7-story coupled-wall specimens by Paulay and Santhakumar (1976) emphasized the critical role that highly ductile and

damage tolerant coupling beams play in improving the ductility, stiffness retention, and energy dissipation capacity of a coupled system. These tests allowed a comparison of the behavior of moment-frame-type and diagonally reinforced coupling beams, and indicated that the improved ductility exhibited by diagonally reinforced coupling beams leads to improved overall system response. In particular, the importance of energy dissipation being dispersed over the full height of the system rather than localized at the base of the walls was identified.

Around that same time, two parallel studies involving dynamic tests of small scale coupled-wall systems were conducted at the University of Illinois. The first study involved dynamic tests of 10-story coupled systems, and addressed a multitude of coupled wall system performance characteristics that had not yet been identified (Aristizabal-Ochoa and Sozen, 1976). In particular, this study showed that dynamic structural behavior can be approximated by a linear substitute structure if the effective member stiffnesses are appropriately reduced to account for cumulative damage. This linear analysis was shown to predict story shears, moments, and system deflections with reasonable accuracy. In addition, the following observations regarding the dynamic response of coupled systems were made:

- Cracking in the coupling beams and walls very quickly reduced the natural frequencies of the first and second modes by 50% and 40% respectively,
- First mode deformations dominated the response of the system, with secondary modes contributing less than 7% of the top story drift,
- P-delta effects were shown to be unimportant to the response of the system,
- The centroid of lateral action occurs at roughly 0.7H, where H is the height of the structure, indicating that a triangular distribution of lateral force may be most appropriate for testing and modeling purposes.

The second related study involved dynamic testing of 12-story coupled systems (Lybas and Sozen, 1977). This series of tests indicated that analytical modeling of system modes, and resulting drift amplitudes, can be achieved with relative accuracy when equivalent viscous dampers are defined for each element of the system based on component tests. Models that incorporated 10% damping using equivalent viscous dampers showed good

agreement with both first and second mode responses. Finally, the importance of member hysteresis responses on the overall hysteresis response of the system was emphasized.

Shiu et al. (1981) tested two 6-story coupled systems at 1/3 scale to investigate the effects of coupling beam strength and stiffness on system response. The first specimen was very lightly coupled, with a coupling ratio of 10%. Coupling ratio is defined as the percentage of the total overturning moment resulting from the coupling action of the beams. The result of this light coupling was that the beams yielded early in the test, and their contribution to the capacity of the system degraded quickly. This resulted in the coupled system behaving like two individual walls. When such a low level of coupling is present, it was concluded that enormous deformation capacities are required of the coupling beams. The second specimen was moderately coupled, with a coupling ratio of 30%. The test indicated that large axial stresses resulted from this degree of coupling which led to web crushing in the base of the structural walls. Measurements of deformations indicated that roughly 80% of the base shear was transferred through the coupling beams to the compression side of the system. In addition, it was noted that for heavily coupled systems, wall axial loads (both tension and compression) should be accounted for in design. Although the increased compression would perhaps increase wall flexural and shear capacities, it is detrimental to the ductility of the section.

Subsequent testing of 1/3 scale 4-story specimens by Aktan and Bertero (1984) confirmed the effects of high coupling ratios on the system described by Shiu et al., and went further to indicate that a coupling ratio of 60% should be an upper bound for concrete wall systems. This study also highlighted the importance of bar slip to predictions of beam rotations, recommended that axial compression of coupling beams resulting from the transfer of base shear to the compression side of the system should be considered in design of coupling beams, and emphasized the need for accurately estimating the axial-flexural stiffness of coupling beams for developing meaningful predictions for system deflections.

In 1996, a 1/3-scale quasi-static test of a 12-story coupled system with flanged walls was conducted at the Building Research Institute in Japan (Teshigwara et al., 1998a). The specimen was subjected to cyclic lateral displacements with moderate peak

base shear stresses, on the order of $3.5\sqrt{f_c'}$ [psi] $\left(0.29\sqrt{f_c'}\text{ [MPa]}\right)$, occurring at approximately 1.5% drift. Following this peak, the coupling beams degraded and the wall behavior was increasingly similar to uncoupled walls. Near 3.3% drift, buckling of some diagonal reinforcement in the coupling beams and fracture of some wall reinforcement was observed. The test was subsequently terminated at around 4.0% drift. Load cells placed at mid-span of all twelve coupling beams measured the transfer of base shear to the compression wall, and indicated that approximately 90% of the peak base shear force was resisted by the compression side of the system (Teshigwara et al., 1998b). This test also showed that the transfer of shear forces to the compression wall was most pronounced in the first two stories of the system, and that the distribution of lateral shear force was far more equitable between the two walls at higher stories. A series of subsequent analytical research projects was undertaken to expand on this test result. Of these studies, the most notable were a study by Kato, Sugaya and Nagatsuka (1996), in which it was recommended that coupling ratios between 40% and 60% were most preferable for concrete coupled systems, and a study by Kabeyasawa and Nakamura (1998), where a displacement-based design approach for coupled wall systems was outlined.

2.3.2 Modeling System Response

Given the complexity and redundancy inherent in coupled wall systems, the ability to accurately model coupled wall systems has progressed in step with advancements in technology, which have permitted the analysis of increasingly complex models. Prior to computer modeling, models of coupled wall systems (Chitty, 1947; Beck, 1962; Coull and Choudhury, 1967) generally relied on replacing discrete coupling beams with a continuous laminar medium and subjecting the structure to either uniform or triangular lateral force distributions. This technique allowed for the derivation of a closed-form solution for the internal force distributions and roof level drifts. Efforts were made to develop design charts to estimate ductility demands for system components based on these closed form solutions (Pekau and Gocevski, 1978).

As technology improved, computer analysis quickly replaced these approximate methods. In the late 1970s and 1980s, researchers explored how the rapidly expanding

capabilities of computer simulations could be used to improve the simulation of coupled walls. A study by Takayanagi and Schnobrich (1979) showed that reasonably accurate results from static and dynamic analyses can be obtained by replacing the walls and coupling beams with flexural elements with specified (elastic) shear and axial stiffnesses. Although this was an improvement over previous analytical work, the simple model was limited by the availability of computational power. Saatcioglu, Derecho and Corley (1983) sought to identify the most critical parameters controlling the accuracy of coupled wall models so that efficient use could be made of the limited computer resources available. They showed that the impact of axial force-moment interaction effects due to coupling should be included in models of coupled walls, and that strength degradation of coupling beams leads to large coupling beam ductility demands. This study indicated that variations in model parameters simulating shear yielding, pinching of hysteresis loops, and post-yield and unloading slopes had relatively small impacts on the accuracy of the model. In numerous other studies, models of coupled walls were developed based on equivalent frames, with each beam and wall segment represented by a single line element (Smith, Girgis, and Abate, 1981; Elsied, Ragab, and Emam, 1990). By the end of the 1980s, such models had been refined sufficiently to be useful for evaluating the design of specific building systems by predicting strength and ductility demands for components and identifying the likely wall failure mode (Bolander, 1989).

The last 20 years have seen the development of a variety of approaches to finite element (FE) modeling of coupling beams and coupled wall systems. The form of these models has ranged from a variety of "layered" line elements to represent individual system components (with each layer simulating a particular deformation mechanism, i.e. flexure, shear, axial, etc.) to more intricate 2-D mesh models that seek to capture more specific information about reinforcement and concrete stresses (Harries et al., 1998; El-Tawil and Kuenzli, 2002a; El-Tawil and Kuenzli, 2002b; Doran, 2003; Hossain, 2003; Hassan and El-Tawil, 2004; Lu and Chen, 2005; Wallace, 2007; Hung, 2010). These FE models have supported studies of system behavior that are very useful for understanding the influence of various parameters that are difficult to determine experimentally, and for providing comparative analyses of various structural systems. Examples of useful applications of FE models include the study of the influence of coupling ratio on system

performance, the distribution of base shear stress between walls, and the effective slab width active in coupling. FE models have also been useful for comparing reinforced concrete and hybrid steel/concrete coupled wall systems. A combination of improved modeling techniques, further improvements in computational power, and detailed research into the fundamental mechanics driving reinforced concrete structural behavior is required to further improve FE modeling.

2.3.3 Wall Detailing Requirements and Fiber Reinforcement

Considerable work has been done developing seismic detailing requirements for structural walls of various aspect ratios (Cardenas et al., 1973; Aktan and Bertero, 1985; Wallace and Moehle, 1992; Wallace, 1995; Wallace and Thomsen, 1995). However, limited attention has been paid to investigating either the impact of incorporating fiber reinforcement on these requirements, or on the need for special requirements for coupled-walls to accommodate the axial loads imposed by coupling. To the knowledge of the writer, no experimental work has been conducted to evaluate the use of FRC to confine the boundary elements of structural walls in coupled systems.

Tests of three fiber reinforced cantilever walls with no transverse reinforcement provided for shear or confinement showed that high volume fractions of steel fibers (between 3.5% and 6%) could potentially replace the reinforcement required to resist shear forces and provide boundary element confinement in slender reinforced concrete structural walls (Dazio, Buzzini and Trub, 2008). However, the specimens were subjected to relatively low nominal shear stresses, on the order of $2\sqrt{f_c'}$ [psi] $\left(0.17\sqrt{f_c'}\text{ [MPa]}\right)$, which are not representative of the levels of base shear stress commonly developed in walls during strong ground motions. However, these results do indicate that FRC could potentially simplify detailing requirements for lightly stressed walls subjected to displacement reversals.

Subsequent tests of slender (Parra-Montesinos, Canbolat and Jeyaraman, 2006) and squat (Kim and Parra-Montesinos, 2003; Athanasopoulou, 2010) HPFRC structural walls subjected to higher shear stresses have demonstrated that HPFRC can be relied on to increase the damage tolerance and toughness of shear walls subjected to higher deformations and stress demands. These studies also confirmed that HPFRC can provide

confinement to the boundary element reinforcement. Slender walls with aspect ratios of 3.7 and boundary transverse reinforcement provided at a spacing of $1.5t_w$, where t_w is the thickness of the wall, were subjected to shear stresses of approximately $4\sqrt{f_c'}$ [psi] $\left(0.33\sqrt{f_c'}\text{ [MPa]}\right)$ and showed no evidence of instability in the boundary region. This indicated that the HPFRC was effective in providing lateral support to the wall flexural reinforcement. Tests of shorter walls with aspect ratios of 1.2 and 1.5 demonstrated that adequate confinement of the boundary region could be achieved with no transverse reinforcement when shear stresses of approximately $5\sqrt{f_c'}$ [psi] $\left(0.42\sqrt{f_c'}\text{ [MPa]}\right)$ are applied, and with transverse reinforcement spaced at t_w for higher shear stresses of up to $9\sqrt{f_c'}$ [psi] $\left(0.75\sqrt{f_c'}\text{ [MPa]}\right)$.

The viability of fiber reinforcement as a replacement for transverse reinforcement in the base of coupled-wall systems, however, has not been demonstrated. The coupling of structural walls will tend to transfer considerable shear stresses to the compression side of the system (Shiu et al., 1981; Teshigwara et al., 1998b), demanding a greater shear resistance than is required of uncoupled walls. In addition, the axial loads resulting from wall coupling may result in a deeper compression zone and a possible underestimation of the need for boundary region confinement (Fortney and Shahrooz, 2009). Given the impact of coupling on the shear stress and compressive strain demands placed on coupled walls, there exists a need to experimentally validate the adoption of fiber reinforcement as a replacement for transverse reinforcement in these systems.

CHAPTER 3:
EXPERIMENTAL PROGRAM

The experimental work for this project comprised two distinct phases. The first phase consisted of three coupling beam component tests designed to evaluate the use of high-performance fiber reinforced concrete (HPFRC) in coupling beams with relatively short aspect ratios. An aspect ratio (ℓ_n/h) of 1.75, where ℓ_n and h are the clear span and height of the coupling beam, respectively, was selected for these tests to represent coupling beams where flexural deformations contribute more significantly to drift capacity than in previous HPFRC coupling beam tests (Canbolat, Parra-Montesinos and Wight, 2005). The specimens were precast with HPFRC and then embedded into stiff reinforced concrete blocks that simulated the interface with adjoining structural walls. Each specimen was subjected to increasing lateral displacement cycles to simulate earthquake-type displacement demands. Specifically, this phase of the experimental work was conducted to: 1) confirm that HPFRC can be relied on to confine diagonal reinforcement, 2) quantify the shear stress capacity that can be safely attributed to HPFRC in design, 3) determine whether the response of coupling beams with $\ell_n/h = 1.75$ can be controlled by flexure, thereby improving ductility, 4) evaluate the degree of stiffness degradation at various drift levels, and 5) validate a method for embedding the precast HPFRC section into structural walls without interfering with the boundary element reinforcement.

In the second experimental phase the lessons learned from the component tests were implemented in the design of two approximately 1/3-scale coupled walls. The general intent of these tests was to study the impact that the ductility exhibited by HPFRC components has on system performance. A four-story coupled wall that consisted of T-shaped walls, coupling beams and slabs, was assumed to provide a relevant

experimental example of the interaction between these structural components. Each of the two coupled wall specimens included a reinforced concrete (RC) coupling beam along with three HPFRC coupling beams to allow a comparison of their behavior. Additionally, fiber reinforcement was included in the first two stories of the second coupled wall specimen to compare the behavior of plastic hinges in the base of reinforced concrete and HPFRC coupled walls. In particular, there was interest in evaluating whether reduced confinement and shear reinforcement details would result in adequate ductility for the HPFRC system. This experimental phase was conducted to: 1) evaluate the interaction between HPFRC coupling beams, slabs and structural walls, 2) compare the behavior of coupling beams with various details under similar deformation demands, 3) evaluate the possibility of reducing confinement and shear reinforcement details in plastic hinge regions of HPFRC coupled walls, and 4) demonstrate the ease with which precast coupling beams can be embedded in cast-in-place structural wall systems.

3.1 PHASE 1: COUPLING BEAM COMPONENT TESTS

3.1.1 TEST SETUP

A diagram of the component test setup is shown in Figure 3.1. The coupling beam was precast with HPFRC as a way of limiting the use of HPFRC to the most critical regions of the system, thereby reducing material cost and construction difficulties on-site. Once precast, the coupling beam was embedded into the adjacent blocks, simulating the interface with the structural wall boundary element. A shallow embedment of the precast section into the adjoining wall sections was accomplished with a new detail described in the following section.

For testing, one of the simulated wall boundary elements was bolted to the laboratory strong floor, using eight unbonded 1.25 in. (31 mm) diameter threaded rods, to approximate a fixed boundary condition. Lateral displacement reversals were applied to the other simulated wall boundary element (or “block”) by direct bearing of the actuator in the positive loading direction, and through four unbonded 1.5 in. (38 mm) diameter threaded rods that passed through the top “block” to bear on its opposite face when the

actuator was pulling away from the specimen. This top "block" was restrained from rotating by steel links, which had a stiffness of approximately 250 kip/in. (43.8 kN/mm), to impose a state of double curvature on the coupling beam. These steel links also provided passive, partial restraint to elongation of the coupling beam resulting from damage caused by cyclic displacements. This passive resistance is similar to the restraint provided by stiff structural walls (Teshigawara et al., 1998a). The imposed lateral displacement reversals were intended to follow the history plotted in Figure 3.2. Any deviation from this history was recorded and accounted for in the results reported in Chapter 4. The "true" drift imposed was calculated using Eq. 4.1, as shown in Figure 4.1.

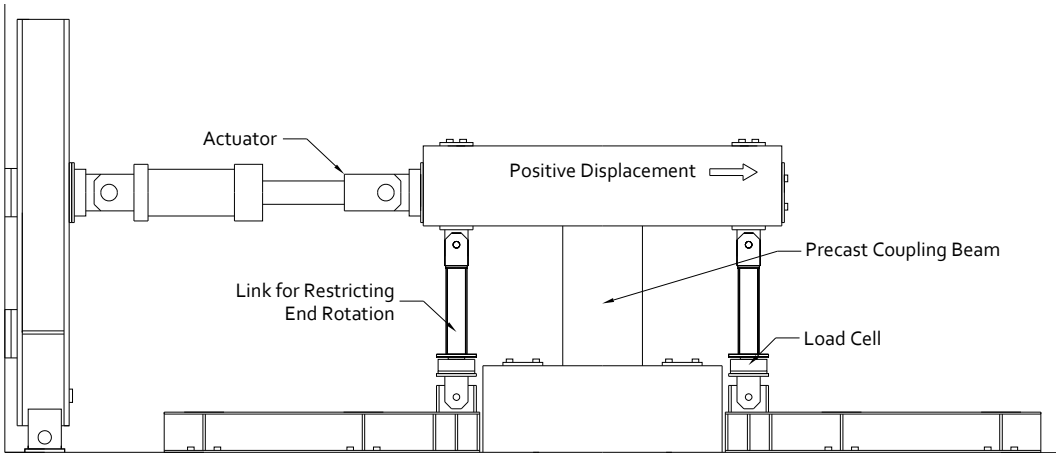

Figure 3.1 – Coupling-beam component test setup

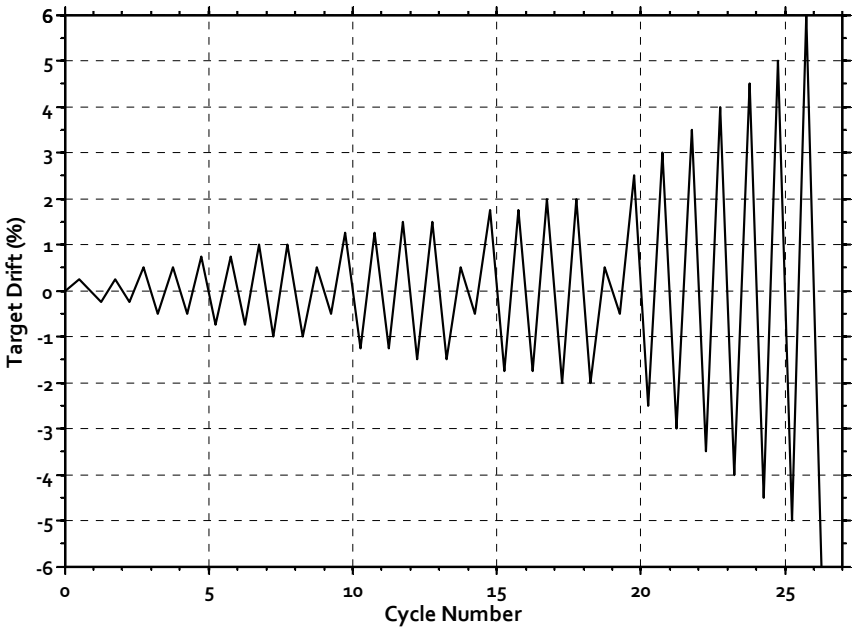

Figure 3.2 – Target drift history for component tests

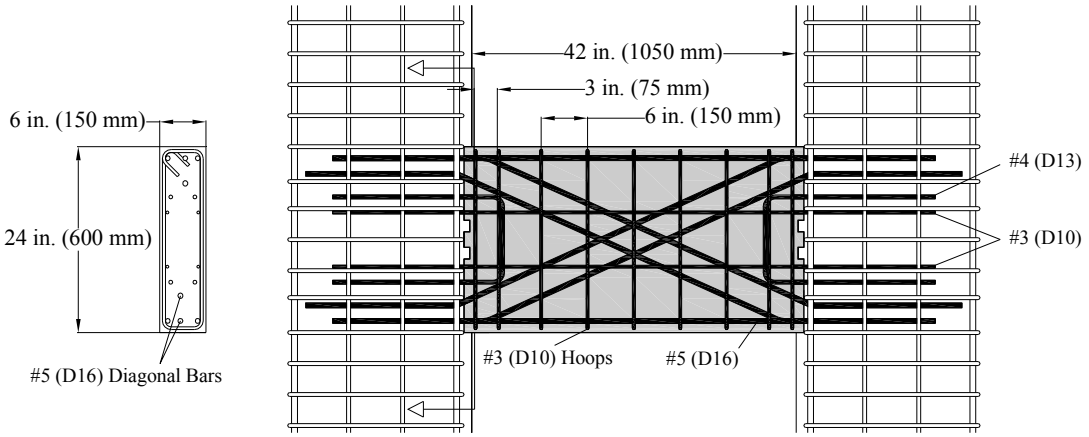

(a) Specimen CB-1

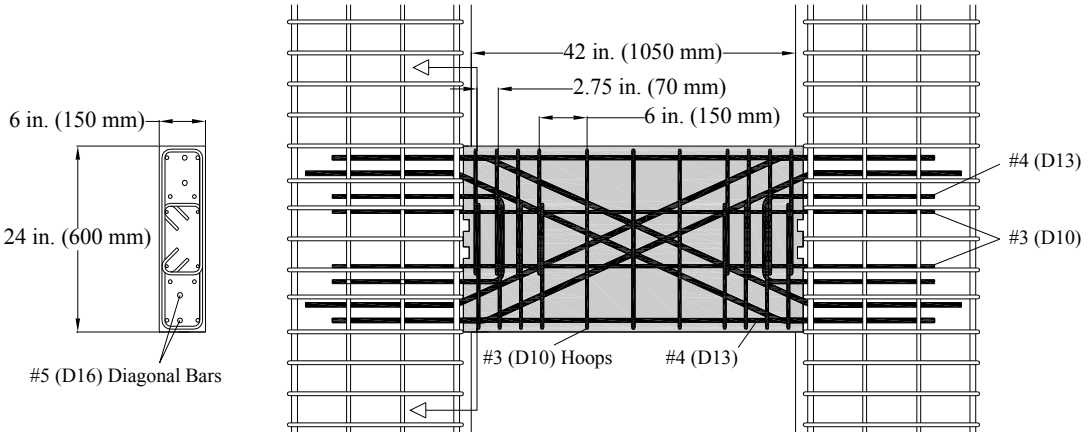

(b) Specimen CB-2

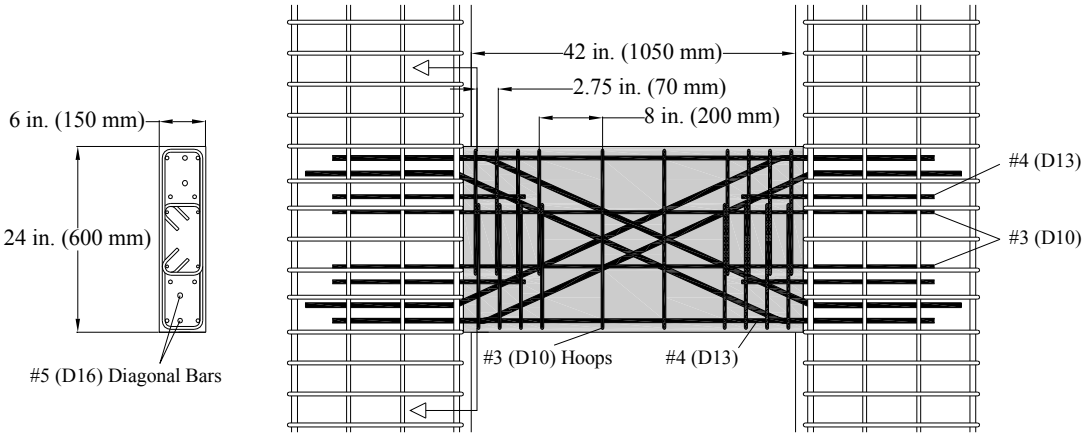

(c) Specimen CB-3

Figure 3.3 – Coupling-beam specimen reinforcement details

3.1.2 COUPLING BEAM DESIGN AND DETAILING

The design of the coupling beam reinforcement, which is shown in Figure 3.3, represented a change from the state-of-the-art. Rather than assuming the capacity of the coupling beam would be uniquely controlled by two intersecting diagonal reinforcement cages, the full HPFRC coupling beam section was assumed to remain sufficiently sound to actively resist shear and moment up to large component drift levels. Basing the design approach on this assumption accounted for the improved damage tolerance previously exhibited by HPFRC and reduced the reliance on diagonal steel reinforcement. In these tests, the assumed diagonal steel contribution to shear capacity was reduced from the total V_n, as prescribed by the ACI Building Code (ACI 318-08), to approximately $1/3 \cdot V_n$, where V_n is the nominal shear capacity of the coupling beam. The remaining shear is assumed to be resisted by transverse reinforcement and the HPFRC.

With the combination of diagonal reinforcement, HPFRC and stirrups resisting shear, it was assumed that a more reliable and ductile flexural hinge would develop at each end of the beam and control the response. Flexural reinforcement at the coupling beam-to-wall interface was selected such that a moment strength associated with the targeted level of shear demand would be imposed.

3.1.2.1 Selection of Diagonal Reinforcement

The design of the coupling beam specimens began with selection of the diagonal bar area and orientation. The diagonal reinforcement was designed to resist 30-40% of the expected shear demand (V_u). In other words, the required area of each diagonal steel cage was approximated with Eq. 3.1, where A_{vd} is the area of steel in each group of diagonal bars, f_y is the yield stress of the steel and α is the angle between the diagonal reinforcement and the longitudinal axis of the beam. A design shear force demand, V_u, of $10\sqrt{f_c'}A_{cw}, [psi]\left(0.83\sqrt{f_c'}A_{cw}, [MPa]\right)$, where A_{cw} is the gross cross-sectional area of the coupling beam and f_c' is the specified compressive strength of the concrete, was selected for these specimens because it is the upper limit for shear capacity permitted by the ACI Building Code (318-08) for coupling beams. This upper limit is considered appropriate for HPFRC coupling beams.

The diagonal bars were bent within the clear span of the beam such that they exit the precast portion of the coupling beam parallel to the other beam longitudinal reinforcement. This bent diagonal detail makes it easier to thread the coupling beam reinforcement through the reinforcement in the adjacent walls, facilitates removal of the formwork after precasting the coupling beam, and makes it possible to cast the wall concrete up to the bottom of the coupling beam prior to its installation. Bending the diagonal bars within the clear span also permitted a slight increase of the angle of inclination of the diagonal reinforcement, α, from 22 to 24 degrees. This small change increases the contribution of the diagonal reinforcement to shear by nearly 9%.

$$A_{vd} \approx \frac{(0.3\ to\ 0.4) * V_u}{2 f_y \sin(\alpha)} \tag{3.1}$$

The motivation for the significant reduction of diagonal reinforcement area relative to an ACI Building Code (ACI 318-08) design warrants further discussion. This reduction is justifiable at longer aspect ratios and advantageous for construction, where placement of large amounts of diagonal reinforcement through adjacent wall boundary reinforcement can be challenging. For very short coupling beams with aspect ratios near 1.0, shear deformations play a dominant role in the drift of the specimen. It is therefore reasonable to assume, as Paulay and Binney (1974) did, that the diagonal reinforcement crisscrossing the coupling beam and oriented at nearly 45 degrees provides the dominant shear resisting mechanism. However, as the coupling beam aspect ratio increases, the inclination of the diagonal reinforcement quickly decreases. For the beams tested herein, with an aspect ratio of 1.75, the angle of inclination was 24°. At this shallow angle, the vertical force component in the diagonal steel is only 40% of the total force in the diagonal steel. The efficiency of diagonal reinforcement for resisting shear force decreases further as coupling beams become more slender, resulting in unreasonably large areas of diagonal reinforcement that make the constructability of slender coupling beams with high shear stresses problematic (Harries et al., 2005). Furthermore, the use of shallow diagonal struts in coupling beams appears contradictory to the strut-and-tie provisions of the ACI Building Code (ACI 318-08), which require strut inclination angles

to be larger than 25° with respect to ties. This limit, which would seem to preclude the use of diagonal struts in coupling beams with aspect ratios larger than 1.75, was adopted by ACI Committee 318 in recognition that shallower struts are theoretically problematical, and that in reality more complex internal stress fields develop that cannot be represented by a single strut (Muttoni, Schwartz and Thurlimann, 1997).

Aside from the shallow angle issue, the assumption that diagonal reinforcement is the primary shear resisting mechanism in coupling beams is based on the following two premises that do not hold up well for the design of slender HPFRC coupling beams. First, the premise that the degradation of concrete due to large displacement reversals under high shear stresses is severe enough to render mechanisms relying on the integrity of the concrete unreliable is too conservative for HPFRC members. This was discussed in Chapter 2 of this document. Secondly, the premise that shear distortion is a primary contributor to the deformation of coupling beams is questionable for coupling beams where flexural rotations become important. Therefore, a design methodology that also considers the flexural behavior of coupling beams would seem more appropriate.

For these reasons, the specimens tested herein had diagonal reinforcement proportioned to resist approximately one third of the expected shear demand to explore whether such a severe reduction in reinforcement was feasible in HPFRC beams with an aspect ratio of 1.75. Complete elimination of the diagonal reinforcement did not seem appropriate at this aspect ratio due to the benefits it provides beyond resistance to diagonal tension stresses. These benefits include considerably improved resistance to sliding shear and improved rotational ductility resulting from a lengthening of the plastic hinge region (Bertero and Popov, 1975; Paulay and Spurr, 1977; Buchnan, 1979).

3.1.2.2 Selection of Longitudinal Reinforcement

The behavior of the HPFRC coupling beam specimens was expected to be dominated by flexural hinge formation at both ends. Therefore, the capacity of the coupling beam could be controlled by selecting longitudinal reinforcement at the precast beam-to-wall interface to supplement the previously selected bent-diagonal reinforcement such that the flexural capacity of the beam correlated with the target shear demand. To achieve this, moment-curvature analyses were performed at the coupling beam-to-wall

interface, and at various points along the span of the beam, for various reinforcement scenarios. The final selection of longitudinal reinforcement corresponded to a probable moment capacity (M_{pr}) that resulted in a probable shear ($V_{pr} = 2M_{pr}/\ell_n$) of approximately $10\sqrt{f_c'}A_{cw}, [psi]\left(0.83\sqrt{f_c'}A_{cw}, [MPa]\right)$.

Unlike current coupling beam design practice, all longitudinal reinforcement was fully developed into the wall to allow this reinforcement to yield at the precast beam-to-wall interface. An ideal arrangement of longitudinal and diagonal reinforcement would provide the largest coupling beam moment capacity at the beam-to-wall interface and would reduce this flexural capacity further into the span, thereby encouraging a longer plastic hinge length. The effect of terminating the longitudinal reinforcement in the wall, near the beam-to-wall interface, as recommended by the ACI Building Code (ACI 318-08) for diagonally reinforced coupling beams, counters this effort. This would result in a lower moment capacity near the interface than elsewhere, and likely force an undesirable localization of plastic rotations for precast coupling beams at the beam-to-wall interface.

3.1.2.3 Selection of Transverse Reinforcement

The primary functions of transverse reinforcement, to transfer tension stresses and thus resist the opening of diagonal cracks, and to provide confinement to the concrete core and longitudinal and diagonal reinforcement, are aided by the inclusion of fibers in the concrete matrix. It has been shown (Canbolat, Parra-Montesinos and Wight, 2005) that special transverse reinforcement along each of the diagonal reinforcement cages is not necessary when the beam is cast with HPFRC, so none was provided in these tests. Rather, closed stirrups (hoops) were provided along the length of the span to resist shear and to confine the entire section. For placement of hoops, the beam span was treated as two distinct regions: midspan and the plastic hinge regions.

Hoops in the midspan region were included to work with the HPFRC to control the growth of diagonal cracks. For Specimens CB-1 and CB-2, the midspan hoops were sized to carry roughly 40% of the shear associated with the probable moment (M_{pr}), leaving the HPFRC to resist the remaining 30-40% of the shear (i.e. the component of shear not assumed to be resisted by hoops and diagonal reinforcement). No. 3 (D10) hoops spaced at $h/4$ (6 in.) were selected, which resulted in a transverse reinforcement

ratio of 0.6% (and a volumetric ratio of 0.89%). After no significant opening of diagonal cracks was observed in the first two tests, a wider spacing of hoops was selected for Specimen CB-3. The same #3 (D10) hoops were placed at a spacing of $h/3$ (8 in.), resulting in a transverse reinforcement ratio of 0.45% (and a volumetric ratio of 0.67%). These hoops accounted for only approximately 30% of the shear strength, leaving the HPFRC to carry 40-50% of the expected shear force.

The plastic hinge regions required additional transverse reinforcement, similar to special column detailing, to provide confinement and to stabilize the diagonal reinforcement near the point where it was bent to enter the wall. The plastic hinge region was defined as the portion of the coupling beam within $h/2$ from the face of the wall. The design of Specimen CB-1 had transverse reinforcement in these regions corresponding to a relatively high volumetric reinforcement ratio of 1.8%, calculated as the volume of a hoop layer divided by the volume of core it confines. However, due to the tall, narrow nature of the selected coupling beam cross-section, the #3 (D10) hoops spaced at 3 in. (75 mm) fell far short of satisfying the ACI Building Code (ACI 318-08) cross-sectional area requirements for rectangular hoop reinforcement in special columns in the transverse direction. HPFRC was expected to provide confinement to the section as well; however, as discussed in Chapter 4, the hoops and HPFRC proved to provide inadequate confinement. The result was an undesirable transverse expansion of the beam, which led to a premature failure.

The response of Specimen CB-1 motivated a change for the design of Specimens CB-2 and CB-3. For these specimens, the plastic hinge regions were confined by a pair of #3 hoops placed every 2.75 in. (70 mm), which provided four legs resisting transverse expansion of the beam. This resulted in a high volumetric reinforcement ratio of 2.9%. This reinforcement layout was much closer to satisfying the ACI Building Code (ACI 318-08) requirements for special column confinement and, in combination with the HPFRC, provided satisfactory confinement to the ends of the coupling beam.

3.1.2.4 Design of Beam-to-Wall Connection

It has been proposed (Canbolat, Parra-Montesinos and Wight, 2005) that precasting the HPFRC coupling beam and embedding it into the adjacent structural walls

could allow for HPFRC to be utilized where it is most beneficial, without negatively impacting the cost of the entire structure. Precasting has the added benefit of providing a more controlled environment for manufacturing, thereby helping to ensure a high quality of construction for the coupling beams. Furthermore, if a connection detail that does not interfere with reinforcement in the wall boundary element can be shown effective, placement of these precast beams could prove to be much less disruptive to the construction sequence than comparable steel and hybrid beams.

Figure 3.4 – Precast coupling beam embedment. Coupling beam reinforcement (highlighted) is developed parallel to the transverse reinforcement in the wall

Two connection details were tested in this series. Both details assumed that the precast concrete is only embedded as deep as the wall concrete cover, as shown in Figure 3.4, which for the scale considered was only 1 in. (25 mm). Coupling beam reinforcement was extended beyond the precast section and into the walls to transfer shear and moment across this interface. As will be discussed in Chapter 4, this embedment detail allowed for full transfer of moment and shear between the precast section and the adjacent structural walls without significantly interfering with wall boundary reinforcement.

The two details shown in Figure 3.3, consisting of either U-shaped or straight dowel bars, were considered for forcing plastic rotations to occur within the precast element rather than at the precast beam-to-wall interface. This is desirable because the fiber reinforcement and column-type confinement within the precast section should ensure the development of a more stable flexural hinge than would be possible at the interface.

The first detail was used in Specimens CB-1 and CB-2. Two U-shaped reinforcing bars that extended 6 in. (150 mm) into the coupling beam before being bent for anchorage were used to increase the moment capacity at the precast beam-to-wall interface. The result of this detail was that the ratio of moment capacity to moment demand in the coupling beam, at the termination of the U-shaped bar, was similar to this same ratio at the face of the wall. The second detail, used in Specimen CB-3, consisted of straight dowel bars placed across the cold joint and terminated 8 in. (200 mm) into the coupling beam. It was assumed that the stress in the dowel bars varied linearly from zero at the point where it was terminated to near yield at the cold joint, thus resulting in a gradually diminishing contribution from the dowel bars to moment capacity at cross sections away from the interface. As a result, the moment capacity and demand should follow a similarly sloped decline throughout the plastic hinging zone, thus encouraging a more desirable spreading of flexural yielding. It was therefore believed that the use of straight dowel bars would better distribute plastic rotations throughout the hinge than the abruptly bent U-shaped bar, while also simplifying the detail.

To prevent sliding at the precast beam-to-wall interface, the shear friction analogy adopted by the ACI Building Code (318-08) was used to calculate the area of dowel reinforcement required across the interface. In accordance with the ACI Building Code (318-08) commentary, the diagonal bar that is forced into compression by sliding (although bent at the interface) is neglected in this calculation. Two shear keys were included to prevent sliding of the precast section relative to the wall concrete in Specimens CB-1 and CB-2. These shear keys were considered to be an "intentionally roughened" interface, based on work by Bass, Carrasquillo and Jirsa (1989) that showed that shear keys are comparable to a roughened surface. This allowed the use of a friction coefficient (μ) of 1.0. Any potential axial load developed due to the axial restraint

provided by the test setup was neglected in this calculation. No significant sliding was observed at the interface in the test of either Specimen CB-1 or CB-2; thus, the shear keys were eliminated in the design of Specimen CB-3. The elimination of the shear keys proved to be successful, as discussed in Chapter 4.

3.1.3 Construction Of Specimens

Construction of the specimens began with precasting the coupling beam in the University of Michigan Structures Laboratory. Reinforcing steel was obtained from a local supplier and assembled by students in plywood formwork constructed by laboratory technicians. HPFRC was then mixed by technicians and students in a drum mixer and placed with care to ensure adequate consolidation. Specimen CB-2 is shown in Figure 3.5 prior to placement of the HPFRC.

Figure 3.5 – Coupling beam reinforcement prior to casting HPFRC

The formwork was removed from the HPFRC coupling beam within a day or two of casting, and the section was set aside while the specimen end blocks were constructed. The top and bottom end blocks were designed to simulate wall boundary elements to provide a reasonable approximation of performance of the precast coupling beam embedment into the adjacent structural walls. To achieve this, these blocks were reinforced with a relatively dense cage of longitudinal and transverse steel similar to wall

Figure 3.6 – Precast coupling beam prior to end block casting

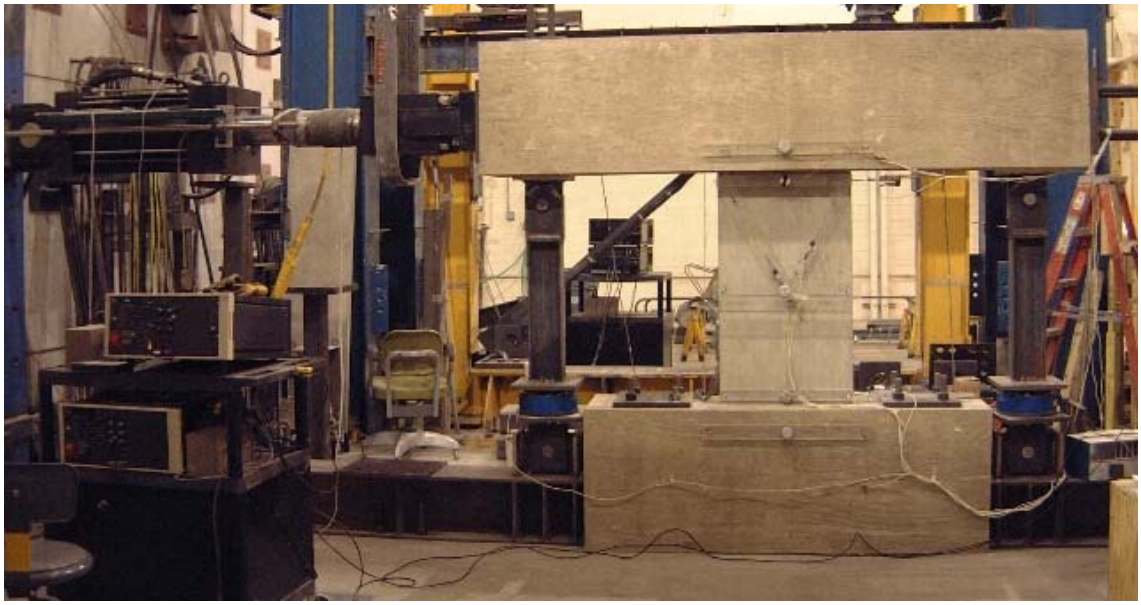

Figure 3.7 – Completed specimen and test setup

boundary element reinforcement. The precast coupling beam was then slid through an opening in the formwork and threaded through the end block reinforcement. The coupling beam shown in Figure 3.6 has been inserted into the end block forms and is ready for casting of the end blocks. A local concrete supplier was hired to supply concrete for the end blocks, which was placed through the use of a crane and bucket system by technicians and students. The formwork was removed within a few days of casting, and the specimen was cured in the laboratory environment until testing. The completed specimen, in position for testing, is shown in Figure 3.7.

3.1.4 INSTRUMENTATION

An array of instrumentation was selected for tracking the behavior of the coupling beam specimens for later analysis. In addition to a load cell and displacement transducer fixed to the hydraulic actuator, load cells were placed on each of the steel links to determine the force/moment imposed on the top end of the coupling beam. These load cells are visible in Figure 3.7 near the bottom of each link.

To record the strains developed in the reinforcing steel, strain gauges were fixed to the diagonal, longitudinal and transverse steel. The layout of the strain gauges for each of the specimens is shown in Figures 3.8-3.10. The gauges and adhesive selected were intended to remain intact through large inelastic deformations, thereby providing a measure of steel strains throughout the duration of the test.

To monitor the external deformations of the specimen throughout the test, an optical system was employed to track the position of 54 independent points fixed to the surface of the specimen. The system consists of infrared emitting “markers” that are fixed to the surface of the concrete and infrared cameras that autonomously triangulate the position of each point in real-time. The markers were attached to the concrete surface of the specimen in a 5.5 in. (137 mm) grid, as shown in Figure 3.11. The markers were labeled sequentially from top-left to bottom-right, as shown in Figure 3.12. This field of data can be mined for relative displacements, flexural rotations, shear distortions, etc.

The optical system was new to the laboratory when this series of tests was undertaken, so a redundant layout of five inclinometers and four linear potentiometers

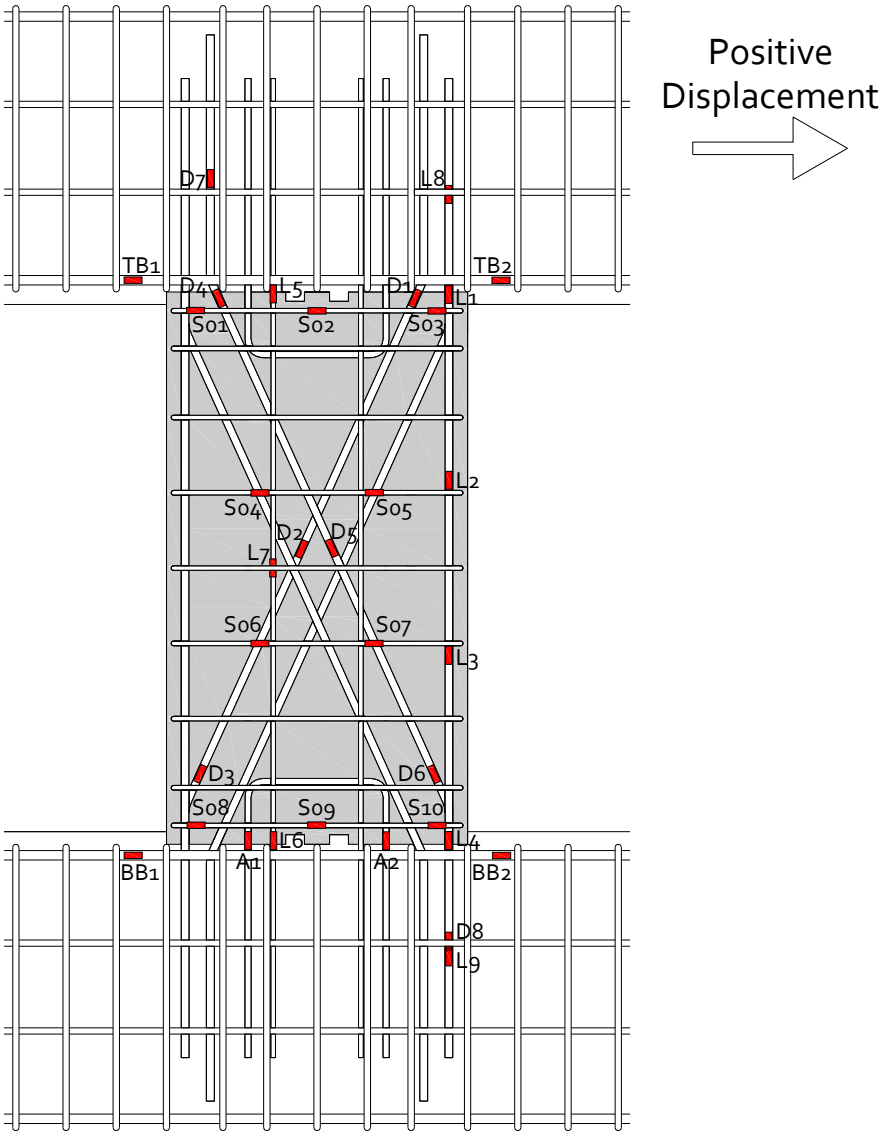

Figure 3.8 – Specimen CB-1 strain gauge layout (gauges A1, L4, L8, L9 and S10 were damaged during casting)

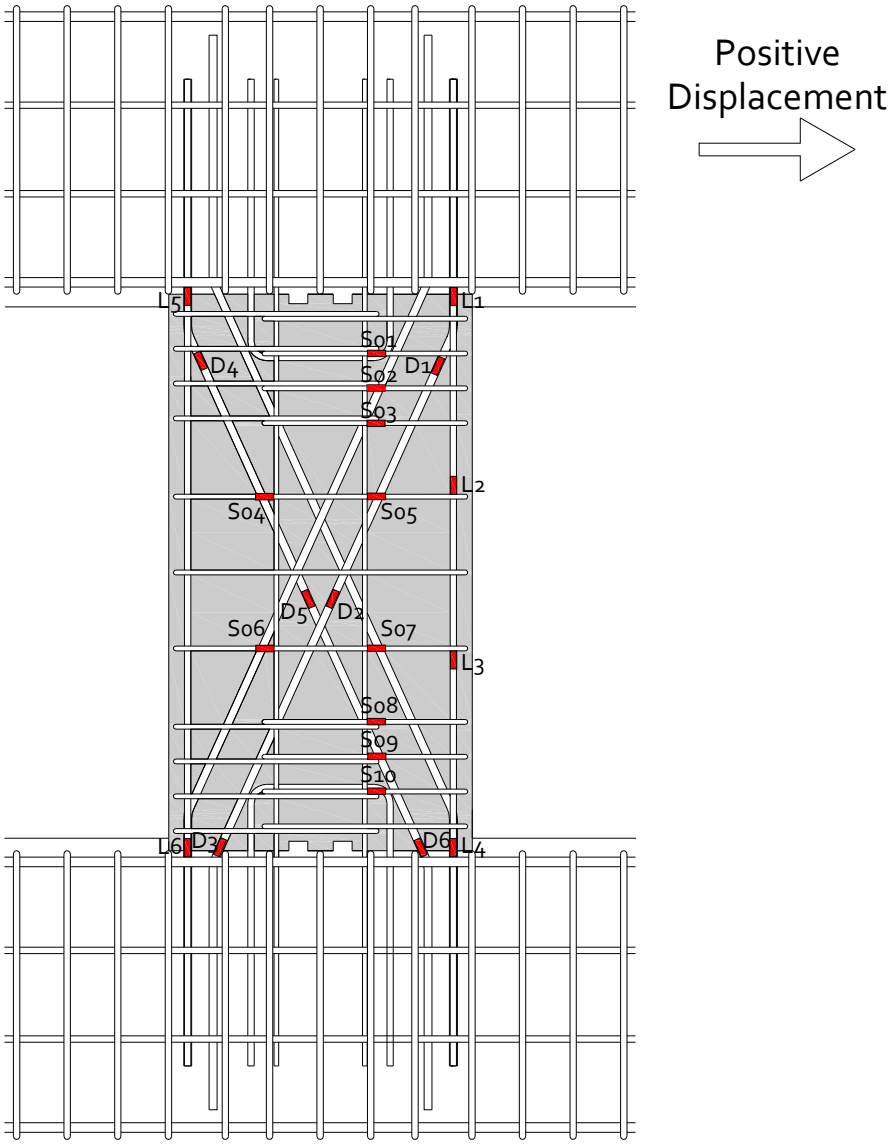

Figure 3.9 – Specimen CB-2 strain gauge layout (gauges D1, L4 and L5 were damaged during casting)

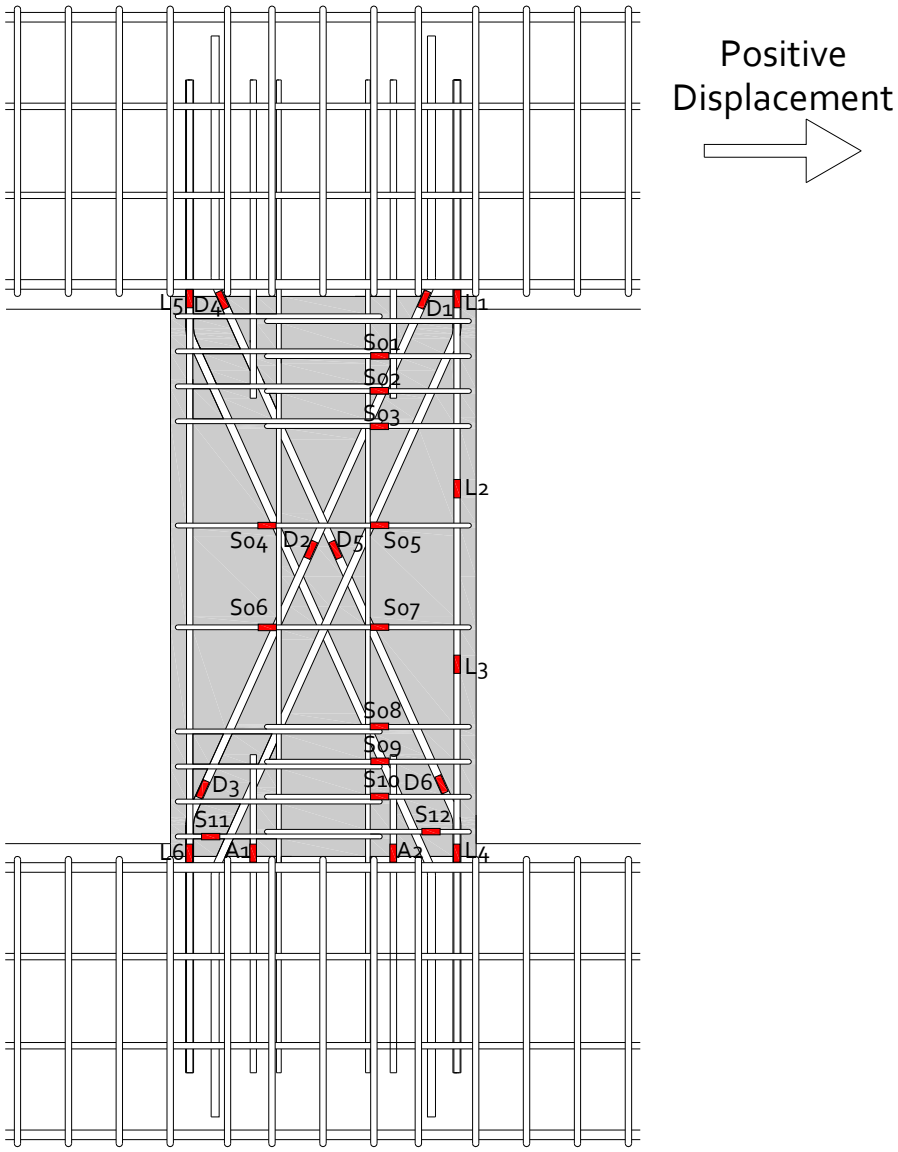

Figure 3.10 – Specimen CB-3 strain gauge layout (gauges D4 and L2 were damaged during casting)

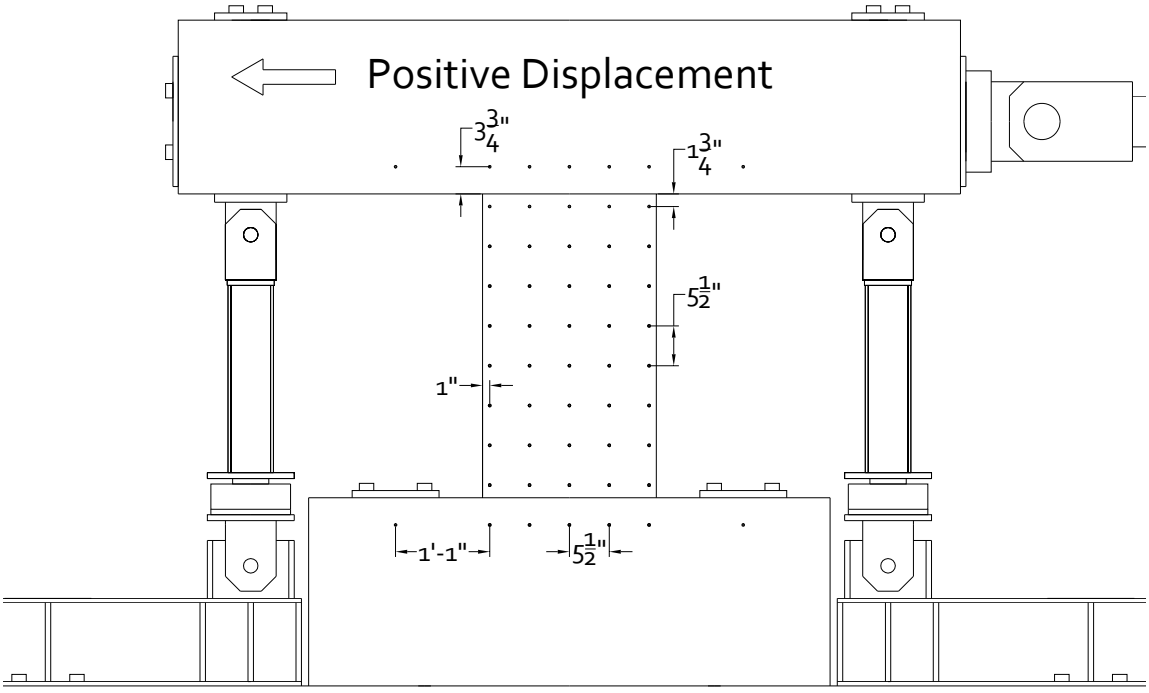

Figure 3.11 – Optical system marker positions

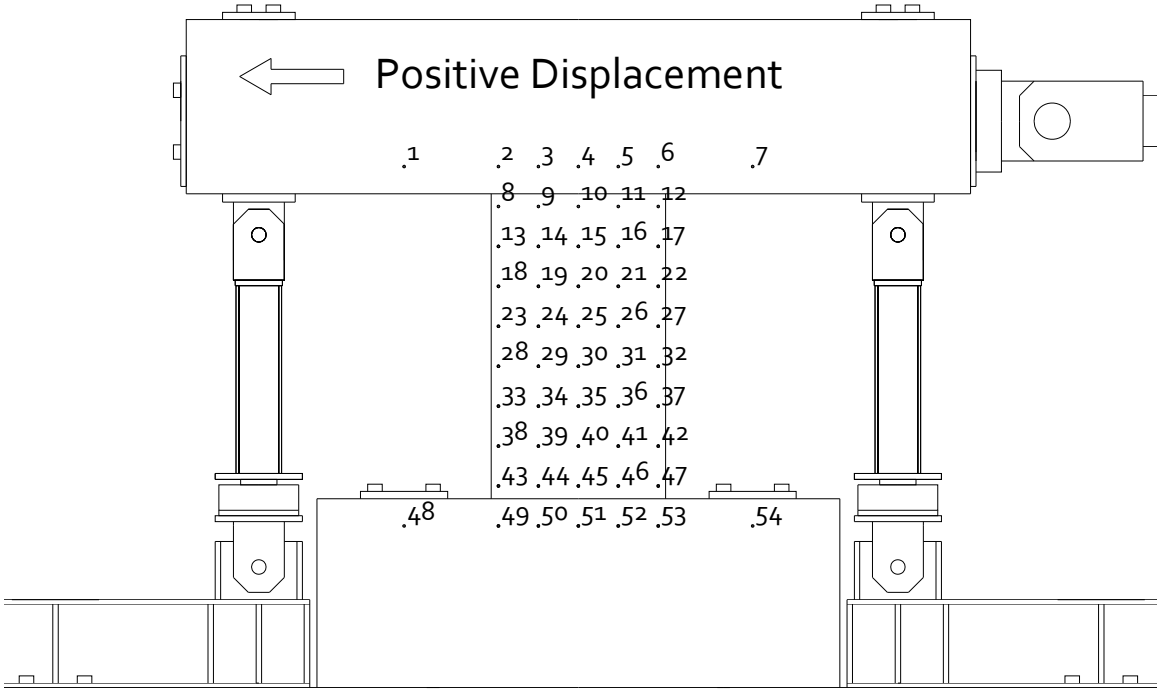

Figure 3.12 – Optical system marker labels

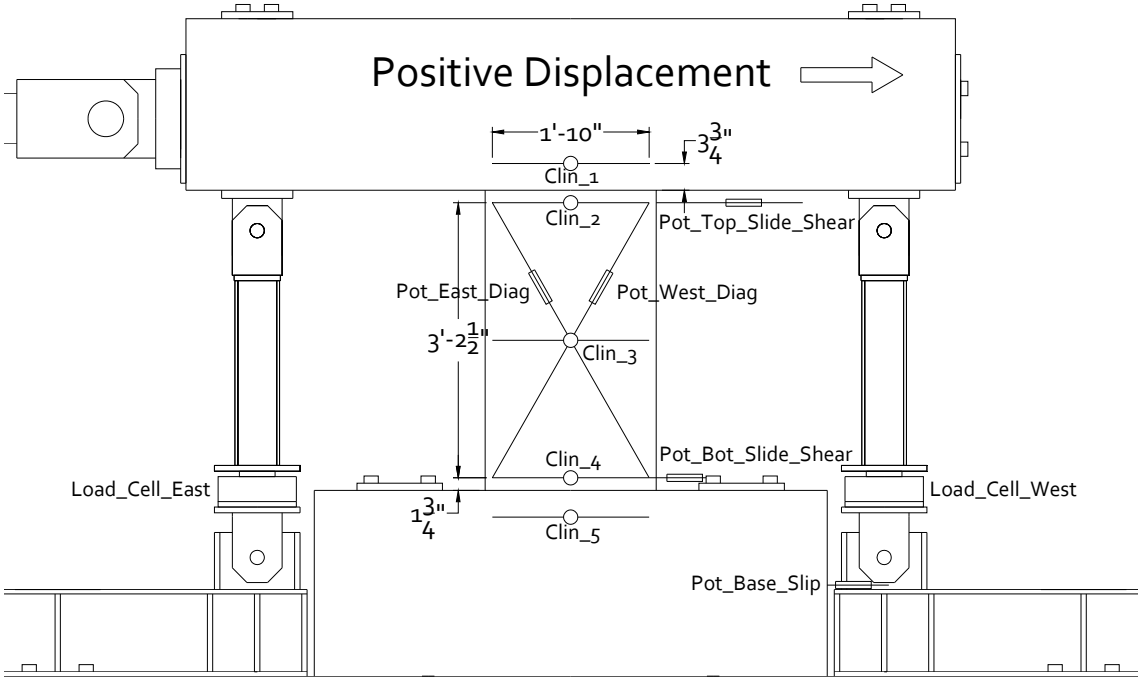

Figure 3.13 – Location and labeling of traditional data acquisition system inputs

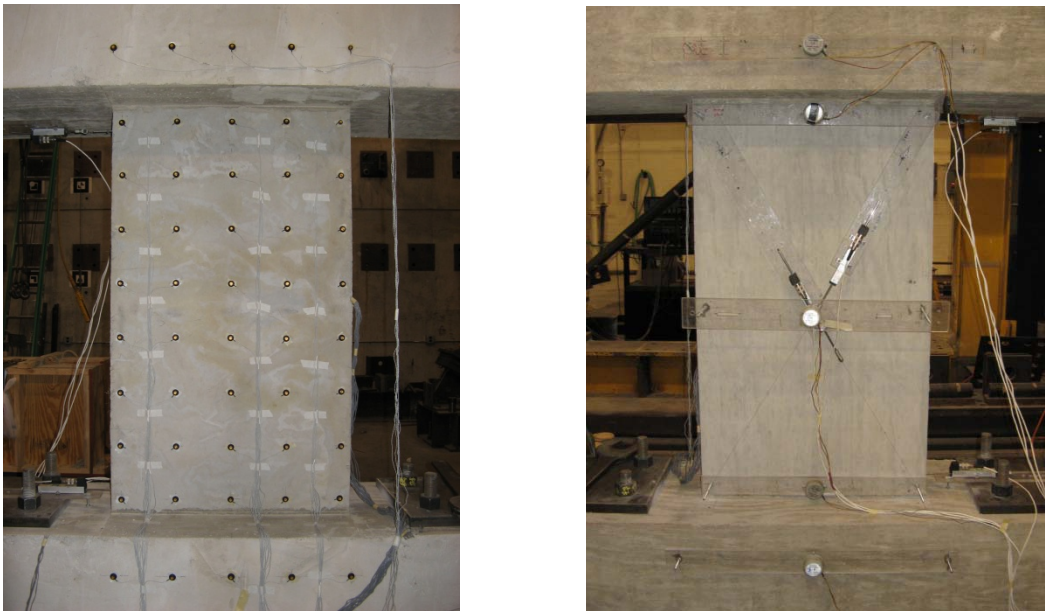

(a) (b)

Figure 3.14 – Coupling beam instrumentation, (a) Optical system, (b) Traditional instrumentation system

was fixed to Specimens CB-1 and CB-2 for validation of the optical system. These instruments, positioned as shown in Figure 3.13, allowed the measurement of rotations, average shear distortion and sliding between the precast beam and the end blocks. Good agreement was found between the two data gathering systems, confirming their interchangeability. The optical system delivered greater precision with lower signal noise content though, so the data presented herein will be based on the optical position sensors. For this same reason, it was decided to forgo use of the more traditional system for the testing of Specimen CB-3. Photos of the two data gathering systems prior to the beginning of a test are shown in Figure 3.14.

3.2 PHASE 2: COUPLED WALL TESTS

In the second experimental phase the conclusions drawn from the component test phase were implemented into the design of two approximately 1/3-scale coupled walls. The primary intent of these tests was to study the impact on system performance of using highly ductile HPFRC coupling beams and to confirm the ease of using precast coupling beams in a more complete structural system. The four-story coupled walls consisted of a pair of T-shaped walls, coupling beams and slabs. The design was intended to provide a relevant experimental example of the interaction between these structural components. Care was taken throughout the construction of the specimens to employ realistic construction methods in an effort to demonstrate the ease with which precast coupling beams can be embedded in cast-in-place structural walls. Each of the two specimens included a reinforced concrete (RC) coupling beam alongside three HPFRC coupling beams to provide a comparison of their inelastic behavior. The reinforced concrete and HPFRC coupling beams were designed to exhibit similar strength and stiffness, but had different reinforcement detailing to provide a comparison of their responses when subjected to similar deformation demands.

As an additional test variable, fiber reinforcement was included in the first two stories of the second coupled wall specimen (Specimen CW-2). This was done to compare the behavior of plastic hinges in reinforced concrete and HPFRC coupled walls,

and to evaluate whether the reduced confinement and shear reinforcement details associated with the use of HPFRC would result in adequate ductility for the HPFRC system.

The main objectives of this experimental phase were to: 1) compare different coupling beam reinforcement details subjected to similar deformation demands within the same system, 2) evaluate reduced confinement and alternate shear reinforcement details in HPFRC coupled wall plastic hinge regions, 3) evaluate the interaction between HPFRC coupling beams, slabs and structural walls, and 4) demonstrate the ease with which precast coupling beams can be embedded in cast-in-place structural walls.

3.2.1 TEST SETUP

Each coupled wall specimen consisted of two T-shaped structural walls, four coupling beams, and slabs at the second and fourth levels. The T-shaped structural walls were oriented with the wider flange section on the outer edges of the specimen, such that the narrower "stems" of the walls were joined by coupling beams, as shown in Figure 3.15. In practice, coupled walls are often located near the center of structures as part of a structural core, which is more often tubular than planar in nature. Therefore, a non-planar coupled wall cross-section was believed to be more representative of typical systems found in practice, yet these systems have less commonly been studied experimentally. The flanged wall sections permitted a larger area of longitudinal reinforcement to be located along the outside edges of the coupled wall, increasing the overturning moment capacity. There was also interest regarding the shift of base shear to the wall subjected to axial compression as a result of the coupling action from the coupling beams. It has been observed previously (Teshigwara et al., 1998b) that as much as 90% of the base shear is resisted by the compression side of a coupled wall.

For design, it was assumed that the base of each wall was fixed. This was approximated experimentally through the use of deep reinforced concrete foundation elements bolted directly to the laboratory strong floor. The foundation blocks were cast first, set into place, and subsequent wall construction progressed vertically.

At the second and fourth floor levels of the coupled wall, a small strip of slab was cast alongside the walls. The slabs served two important functions. First, lateral

displacements were pseudo-statically applied to the coupled walls through a yolk and four channel sections that were attached to the top and bottom of the outer edges of the slabs. This load transfer mechanism was believed to provide a realistic distribution of lateral forces to each of the structural walls. Secondly, the slabs provided an opportunity to observe the interaction between the precast coupling beams and the adjacent slabs. The decision to precast the coupling beams resulted in a question of how to detail the beam-to-slab interface that would, in current practice, be cast monolithically. It was decided that no reinforcement encouraging interaction between the precast beam and surrounding slab would be provided, thereby simplifying the precasting process. Therefore, slab

Figure 3.15 – Photo of coupled wall test setup and specimen

reinforcement perpendicular to the loading direction ran continuously through the structural walls, but not the precast coupling beams. During testing, special attention was paid to the development of damage at this interface to evaluate the need for design modifications intended to minimize unsightly damage at this connection.

At the second floor level, a vertical force was applied to both walls to simulate the axial stress present in coupled walls due to gravity loads. A vertical force equivalent to an axial stress of approximately 7% of the specified compression strength of the concrete (f_c'), based on the gross area of the walls, was applied by external prestressing tendons anchored at the bottom of the foundation elements. Steel tube sections embedded into each wall above the second floor slab transferred the force from the external tendons into the walls. Hydraulic jacks were used to apply this vertical force before any lateral displacement was applied, and it was held constant throughout the duration of the test. This level of gravity load is consistent with typical design axial forces for structural walls and was expected to offset the uplift force resulting from the coupling of the walls.

The actuator mounted on the fourth floor level applied a predetermined sequence of reversing lateral displacements (shown in Figure 3.16), while the actuator at the second level applied a force equivalent to 60% of the force applied by the top actuator.

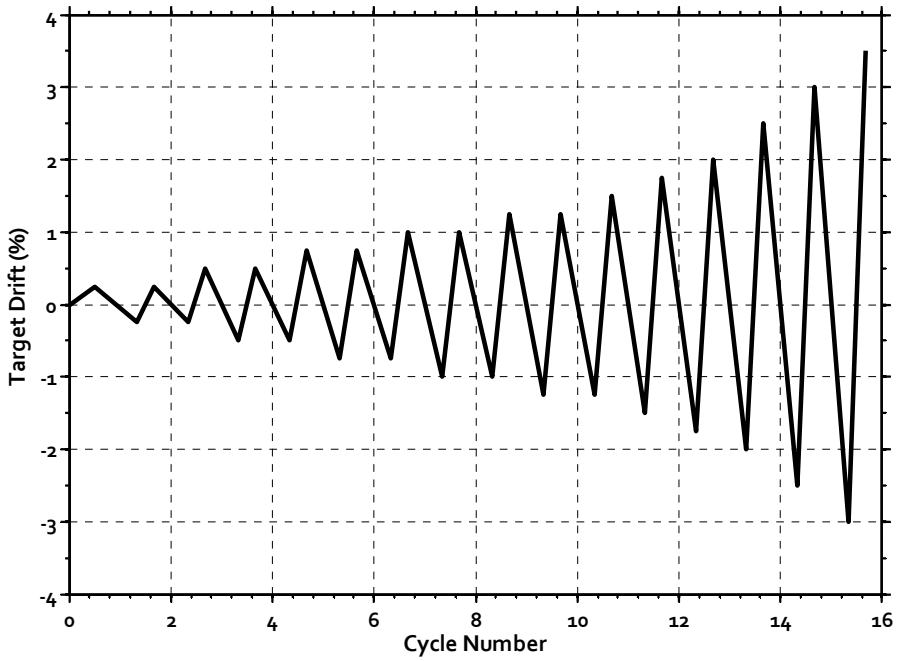

Figure 3.16 – Target fourth story drift history for coupled wall tests

3.2.2 REINFORCEMENT LAYOUT

The coupling beam dimensions and detailing were of special interest in this project, and thus, the design of the beams was the initial focus of the coupled wall design. Together with the coupling beams, the structural walls of each specimen were designed to provide the required overturning moment capacity, shear strength and ductility for the coupled wall system to behave realistically. To achieve this, the walls in the first specimen, Specimen CW-1, were designed in accordance with the seismic provisions of the ACI Building Code (ACI 318-08). In the second specimen, Specimen CW-2, the HPFRC in the first two stories of the system provided an increased shear resistance and allowed for a reduction in boundary element confinement reinforcement.

3.2.2.1 Design of Coupling Beams

Three different reinforcement details, shown in Figure 3.17, were selected for the coupling beams. All the coupling beams were designed to exhibit similar initial stiffnesses and ultimate flexural capacities. This was done to prevent any particular beam from attracting more shear than the others. In the coupling beams for Specimen CW-1, a decision was made to depart in one significant way from the design approach developed for the coupling beam component test phase: to be more consistent with current design practice, the longitudinal reinforcement was terminated in the wall only 3 in. (75 mm) from the precast beam-to-wall interface. The result was that the calculated ultimate flexural capacity of the beams corresponded to a probable peak shear stress of approximately $5\sqrt{f_c'}, [psi]\left(0.42\sqrt{f_c'}, [MPa]\right)$. For Specimen CW-2, all of the coupling beam flexural reinforcement was fully developed into the wall, resulting in higher flexural capacities that corresponded to a probable peak shear stress of approximately $9\sqrt{f_c'}, [psi]$ $\left(0.75\sqrt{f_c'}, [MPa]\right)$. Otherwise, the coupling beam designs were identical between the two coupled wall specimens.

The first coupling beam design, which was used as Beams 1 and 4 in the coupled wall specimens, is labeled “Bonded FRC” in Figure 3.17(a). This design is comparable to the component tests described previously, and can be summarized as follows:

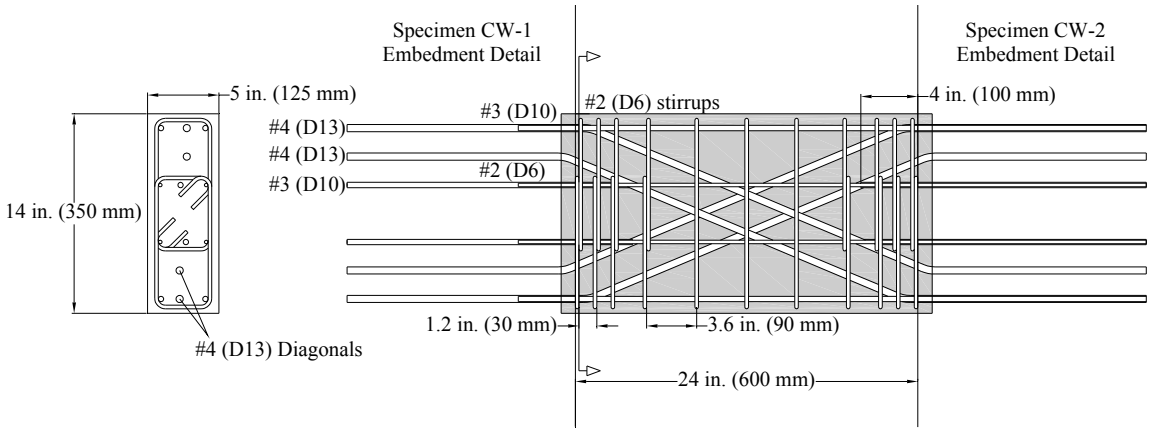

(a) Beam 1, 4: Bonded FRC

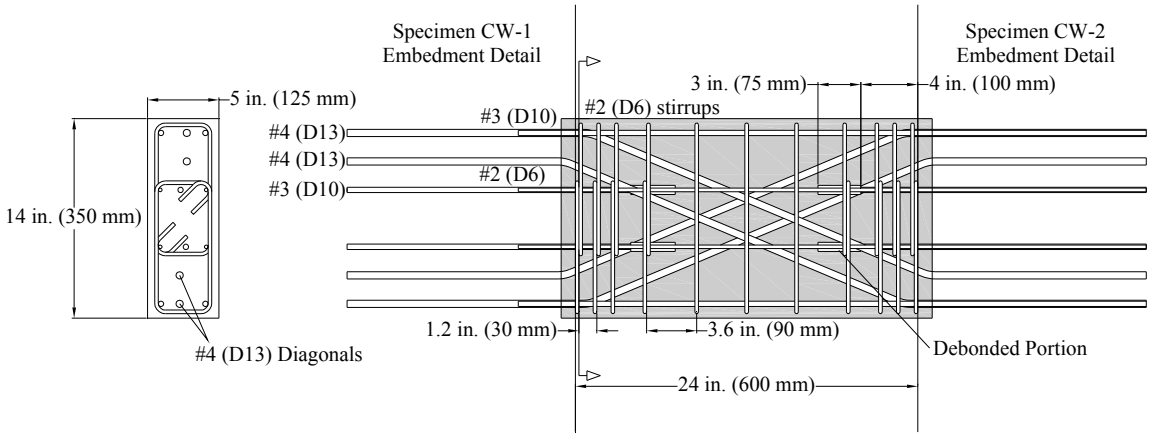

(b) Beam 3: Debonded FRC

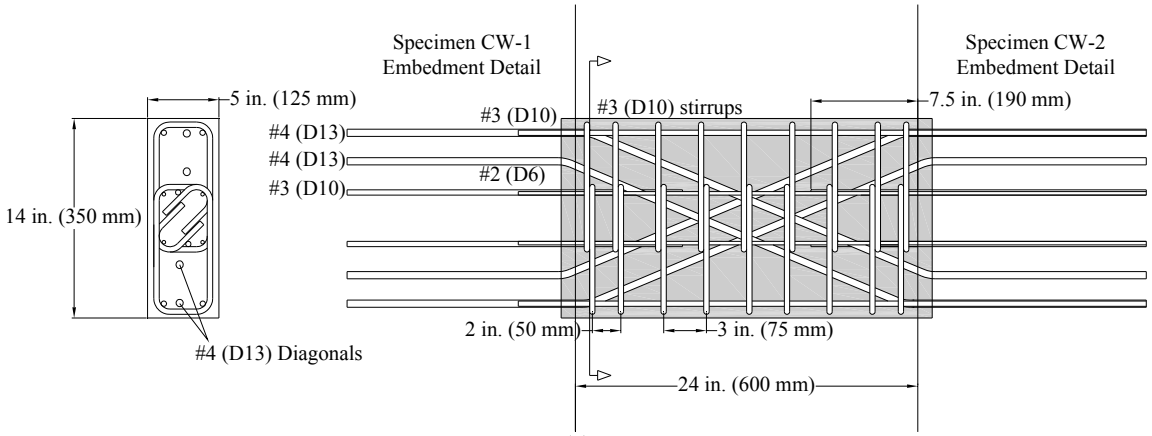

(c) Beam 2: RC

Figure 3.17 – Coupling beam reinforcement (as shown on left, longitudinal reinforcement was cutoff near the wall face in Specimen CW-1. All longitudinal bars were fully developed in Specimen CW-2)

- Two pairs of #4 (D13) diagonal bars were provided at an angle of approximately 28º with the horizontal axis of the beam. This accounts for approximately 90% of the expected shear capacity for the coupling beams in Specimen CW-1 and 50% of the expected shear capacity for the coupling beams in Specimen CW-2. No special transverse reinforcement was provided to prevent buckling of the diagonal bars because strain-hardening HPFRC composites have been shown to confine diagonal reinforcement and arrest the tendency of bars to buckle (Canbolat, Parra-Montesinos and Wight, 2005).
- No. 3 (D10) longitudinal reinforcement was provided at the top and bottom of the coupling beam, and #2 (D6) longitudinal reinforcing bars were placed closer to mid-depth. This reinforcement was embedded 3 in. (75 mm) into the walls for Specimen CW-1, which is commonly done to limit the contribution of the longitudinal reinforcement to the flexural capacity of the coupling beam. All reinforcement was fully developed for Specimen CW-2 to avoid localization of rotations at the beam-to-wall interface.
- To strengthen the interface between the precast fiber reinforced beam and the structural wall, and to encourage plastic hinging to develop inside the precast section, #3 (D10) dowel bars were provided across the beam-to-wall interface and terminated 5 in. (125 mm) into the beam from the end of the precast section. This resulted in an average bond stress demand of approximately 1100 psi (7.6 MPa) at first yield of the dowel reinforcement. The high bond stress developed between HPFRC and reinforcing bars was expected to make this very short development length sufficient to fully develop the dowel bars near the interface.
- Transverse reinforcement conforming to ACI Building Code (ACI 318-08) requirements for special column confinement was provided in the beam for the first $h/2$ away from the wall face to confine the beam plastic hinge regions and support the bent portion of the diagonal reinforcement. A wider spacing of hoops was provided throughout the midspan region to assist in resisting shear.

The second coupling beam design, which was used as Beam 3 in the coupled wall specimens, is labeled “Debonded FRC” in Figure 3.17(b). This design was identical to

the previous design, with one detailing change. Within the beam, the dowel bars were extended 3 in. (75 mm) beyond the 5 in. (125 mm) development length and debonded over that added length. The term "debonding" is used here to describe the use of mechanical means to prevent the fiber reinforced concrete from bonding with the reinforcing bar. This was accomplished by wrapping the bar with a few layers of plastic sheeting and sealing it with tape. The intent was to delay the development of a single failure plane by moving the disturbance resulting from the physical discontinuity of the terminated bar away from the point where the development length is terminated. The motivation for this detail came from the observation that the dowel bars in previous component tests successfully moved the ultimate failure plane away from the interface to the plane where the dowel bars were terminated, but led to more localization of damage at the point of dowel termination than was desirable. If possible, it would be advantageous to spread flexural yielding and the associated inelastic rotations out through a larger portion of the coupling beam, thus delaying the localization of damage.

The third coupling beam design, which was used as Beam 2 in the coupled wall specimens, is labeled "RC" in Figure 3.17(c). This reinforced concrete beam design is unique because it investigates the potential for precasting non-fiber reinforced concrete coupling beams, which could offer construction time savings if proven to be successful. To account for the precasting and embedment of this coupling beam, the ACI Building Code (318-08) requirements were modified and a detail more similar to the "Bonded FRC" design, discussed above, was selected. The following modifications to the "Bonded FRC" design were made to compensate for the lack of fiber reinforcement.

- The dowel bars were extended 8.5 in. (213 mm) past the end of the precast section, rather than the 5 in. (125 mm) provided in the HPFRC beams. This longer embedment is consistent with ACI Building Code (318-08) requirements, which require a development length of 7 and 8.75 in. (175 and 220 mm) to develop nominal stresses of 60 and 75 ksi (415 and 520 MPa) in a #3 (D10) bar, respectively. The longer development length was required to compensate for the lower bond stress capacity developed between conventional concrete and reinforcing steel compared to fiber reinforced concrete. The result is an average

bond stress demand of approximately 700 psi (4.7 MPa) at first yield of the dowel bars.

- The transverse reinforcement provided in the plastic hinge region (defined as a distance of $h/2$ from the wall face) was approximately doubled (larger diameter) to compensate for the loss of confinement from the fiber reinforcement. The hoops provided exceeded the area of transverse reinforcement required by the ACI Building Code (318-08) by approximately 90%, and satisfied the maximum spacing requirements.
- The transverse reinforcement in the remaining span was approximately doubled (larger diameter and reduced spacing) when compared to the HPFRC beams. This provided confinement to the concrete and the diagonal bars, and also compensated for the loss of the contribution of the fiber reinforcement to the shear capacity of the section. The hoops provided throughout the midspan region exceeded the area of transverse reinforcement required by the ACI Building Code (318-08) by approximately 25%, and satisfied the maximum spacing requirements.

3.2.2.2 Design of Structural Walls

With the design of the coupling beams completed, the structural walls were subsequently detailed. The final reinforcement layouts for the walls in Specimens CW-1 and CW-2 are shown in Figs. 3.18 and 3.19, respectively. Also, the reinforcement layout for the slabs and foundations are shown in Figs. 3.20 and 3.21, respectively. The specimen coupling ratio, which expresses the quotient of the overturning moment resistance provided by the axial forces generated in the walls by the "coupling action" of the coupling beams and the total overturning moment capacity of the coupled walls, was targeted to be roughly 0.40. This is consistent with design practice, where typical wall coupling ratios often fall in the range of 0.20 to 0.55. Coupling ratios below 0.2 provide very little benefit over uncoupled wall systems and ratios over 0.55 place undesirably high axial load demands on the individual walls. For the final reinforcement layouts, the design coupling ratio was approximately 0.37 for Specimen CW-1, and 0.44 for Specimen CW-2. The difference between the two specimens came from the choice to fully develop the flexural reinforcement in the coupling beams in Specimen CW-2. This

increased their ultimate capacities and, as a direct result, the contribution of the coupling beams to the overturning moment capacity of the specimen.

Within each coupled wall specimen, the ultimate flexural capacity of the individual walls was targeted to be approximately equivalent under positive (wall flange in compression) and negative bending once the axial compression and tension resulting from the coupling action of the beams was accounted for. When the wall section was in positive bending (wall flange in compression), the coupling action for the coupled wall increased the axial compression in the wall, thus compensating for the lower amount of longitudinal reinforcement in the web (stem portion) of the T-section. When the wall section was subjected to negative bending (wall flange in tension), the larger area of reinforcement accommodated by the flanges along the outside edges of the system compensated for the lower axial load acting on the section. Moment curvature analyses were conducted to predict the capacity of each wall.

For both coupled wall specimens, the shear design of the walls was based on the expected ultimate capacity of the system, assuming the development of a mechanism consisting of flexural hinging at the base of both walls and at both ends of the coupling beams. The average base shear stress for each specimen, considering only the cross-sectional area of the web of the wall, was predicted to be $5.7\sqrt{f_c'}, [psi]\left(0.48\sqrt{f_c'}, [MPa]\right)$ and $6.4\sqrt{f_c'}, [psi]\left(0.53\sqrt{f_c'}, [MPa]\right)$ for Specimens CW-1 and CW-2, respectively. A specified concrete strength (f_c') of 4 and 6 ksi (28 and 41 MPa) was used for Specimens CW-1 and CW-2, respectively. To resist the expected shear demand, the wall concrete was assumed to carry a shear stress (v_c) equivalent to $2\sqrt{f_c'}, [psi]\left(0.17\sqrt{f_c'}, [MPa]\right)$ for Specimen CW-1, and $4\sqrt{f_c'}, [psi]\left(0.33\sqrt{f_c'}, [MPa]\right)$ for Specimen CW-2. The larger shear stress attributed to the concrete in the design of Specimen CW-2 was intended to account for the contribution of fiber reinforcement to the shear capacity. This higher v_c value made it possible to keep the same transverse reinforcement ratio of 0.45% in both coupled wall specimens, even though the expected base shear stress demand in Specimen CW-2 was higher. This increased base shear stress demand was due to the increased overturning moment capacity of the system caused by the fully developed coupling beam

reinforcement. Two curtains of wall transverse reinforcement, anchored by alternating 90- and 135-degree hooks, were provided to resist the remaining shear.

The area of transverse reinforcement provided to confine the boundary elements of the structural walls was another important variation between Specimens CW-1 and CW-2. The transverse reinforcement provided in the boundary regions of Specimen CW-1 was detailed to satisfy minimum area and maximum spacing requirements of the ACI Building Code (ACI 318-08). The result was #2 (D6) ties spaced at $t_w/3$, where t_w is the minimum dimension of the wall. To account for the use of HPFRC in Specimen CW-2, the transverse reinforcement for the wall boundary elements was reduced. The east wall (shown to the right of Figure 3.19) had transverse reinforcement spaced at $t_w/2$, resulting in a volumetric reinforcement ratio of 0.9% and 1.0% for the flange and stem boundary elements, respectively. The west wall (shown to the left of Figure 3.19) had transverse reinforcement spaced at t_w, resulting in a volumetric reinforcement ratio of 0.6% and 0.5% for the flange and stem boundary elements, respectively. Volumetric reinforcement ratio is calculated by dividing the volume of stirrups by the product of the area of the core and the spacing of hoops. This relaxed spacing, if proven adequate for HPFRC walls, would appreciably simplify the construction of coupled wall systems.

There was one more detailing variation between the two coupled wall specimens. Two curtains of three #4 (D13) dowel bars supplemented the wall flexural reinforcement at the interface between the HPFRC wall and foundation in Specimen CW-2. This was done to prevent localization of flexural rotations and to move the critical failure plane away from the cold joint.

Longitudinal reinforcement was anchored in the foundation and at the top of the walls by ACI Building Code (ACI 318-08) compliant screw-on mechanical anchors, pictured in Figure 3.22. Similarly, mechanical splices, shown in Figure 3.23, were used near mid-height of the walls to reduce reinforcement congestion. These mechanical anchorages and splices were supplied by ERICO Corp. in Cleveland, Ohio.

3.2.3 CONSTRUCTION

Efforts were made throughout the construction of the coupled wall specimens to be as realistic as possible in terms of both construction methods and sequencing. It was

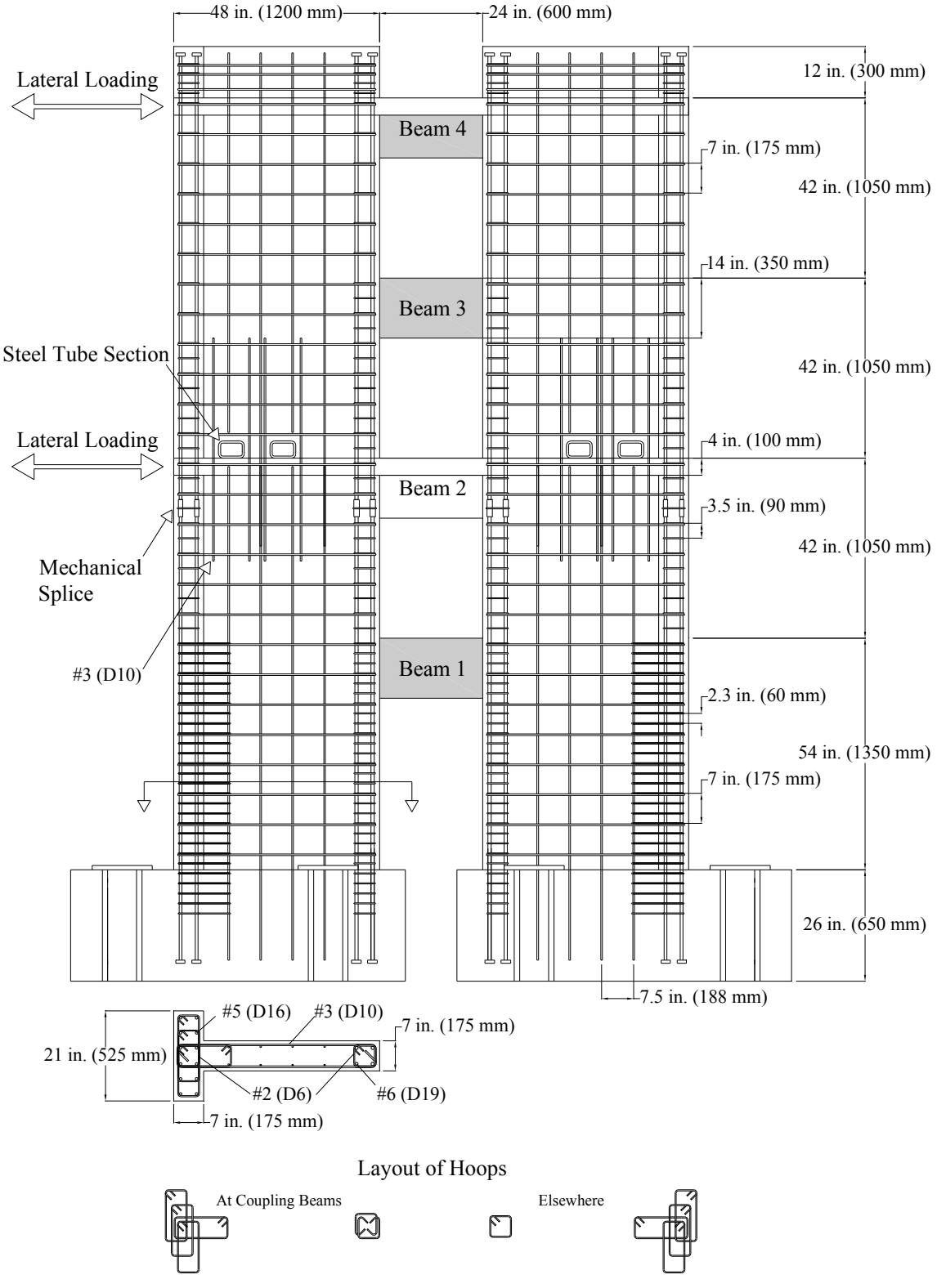

Figure 3.18 – Specimen CW-1 reinforcement layout (shaded region is HPFRC)

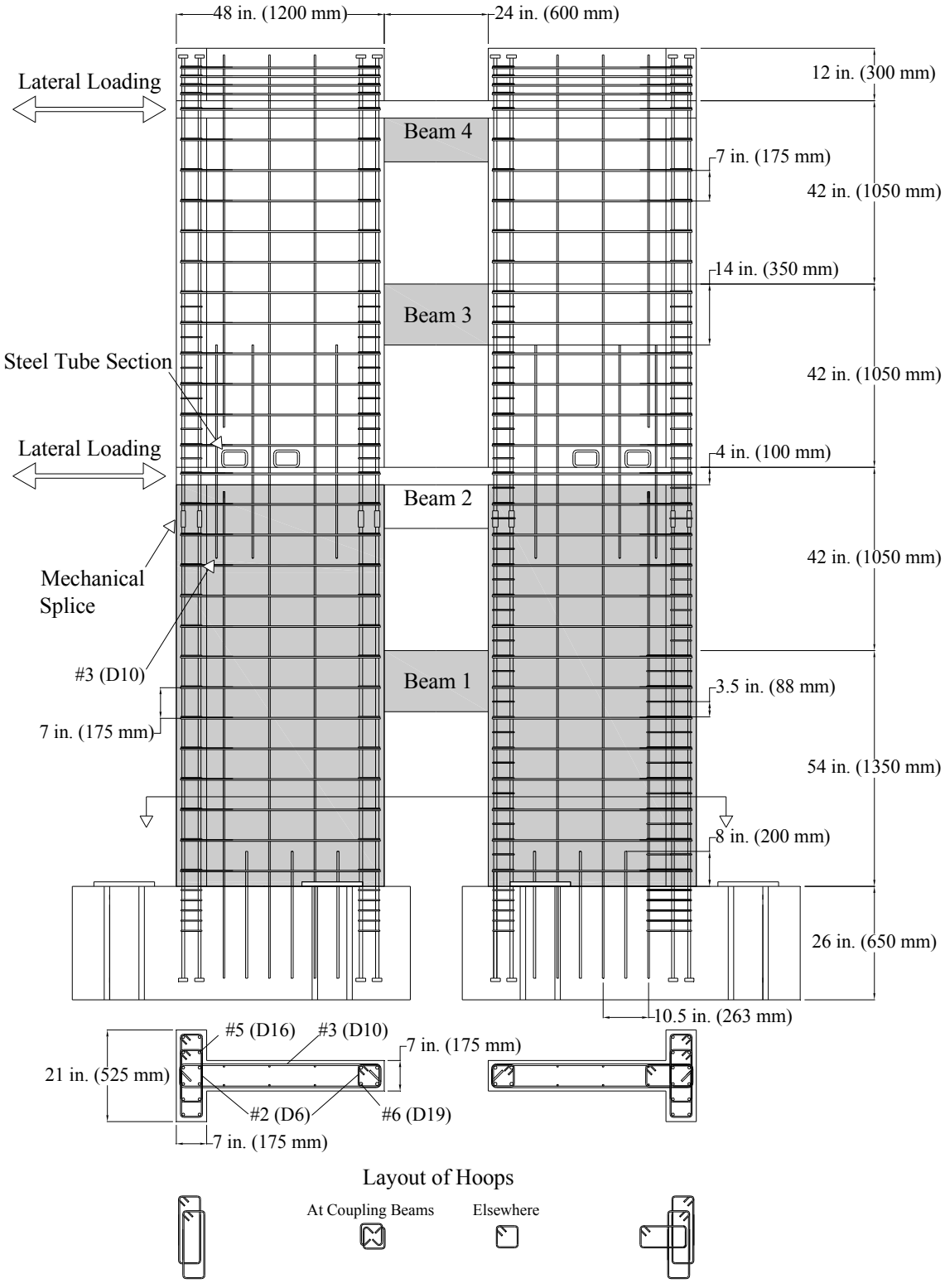

Figure 3.19 – Specimen CW-2 reinforcement layout (shaded region is HPFRC)

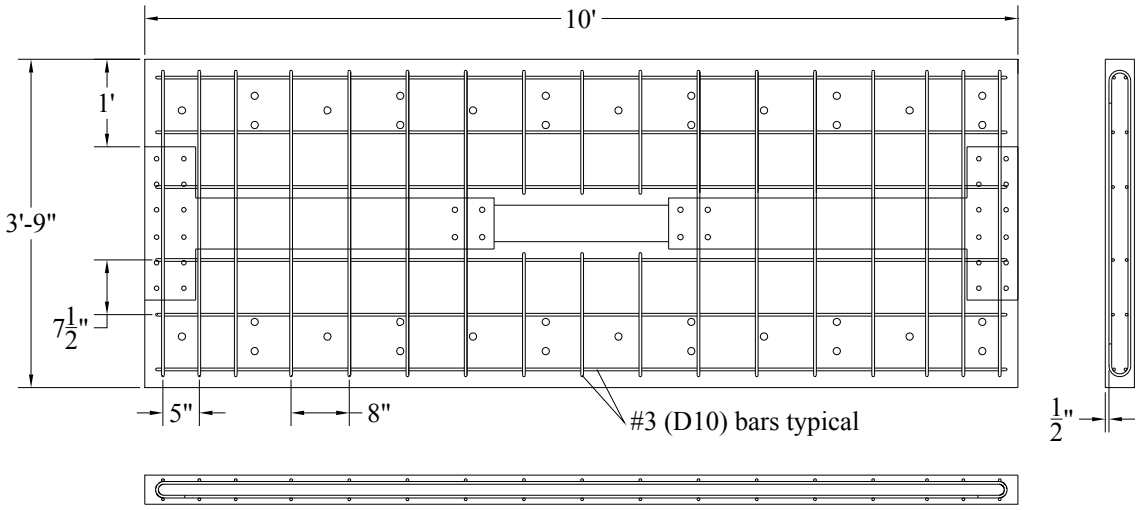

Figure 3.20 – Slab reinforcement details

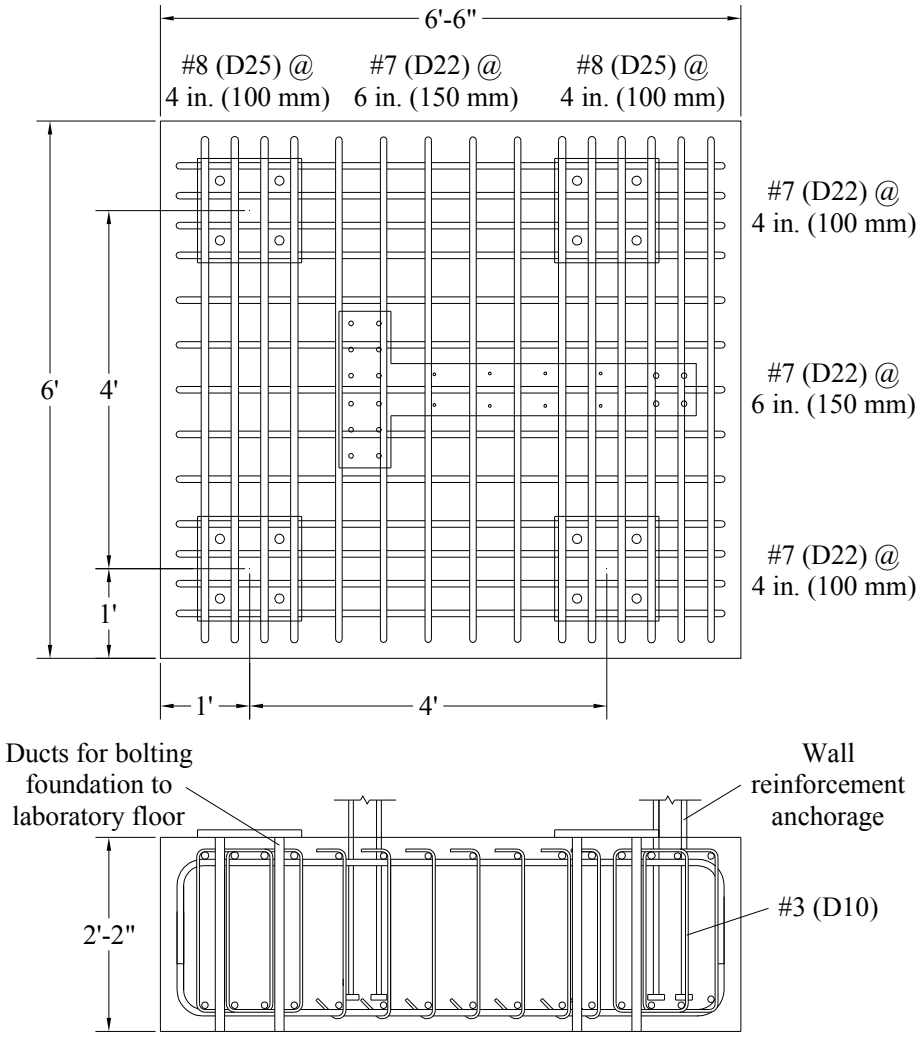

Figure 3.21 – Typical reinforcement for wall foundations (transverse wall reinforcement not shown for clarity)

felt that this approach was critical for qualitatively gauging the possible construction scheduling advantages gained by incorporating precast coupling beams.

The construction process began with precasting the coupling beams through the same procedure described in Section 3.1.3 and storing them until needed for placement in the coupled wall structure. The construction of the walls began with assembly of the plywood formwork and reinforcement cages for the foundation elements. All of the vertical wall reinforcement was set into place and embedded into the foundation when the concrete was delivered and poured, as shown in Figure 3.24. The foundation elements were then moved into position and bolted to the floor of the laboratory.

Each level of the wall was then constructed, in turn, according to the following general procedure. The wall reinforcement was assembled and then enough of the wall formwork to support the precast beam was assembled and put into place. The precast beam was then slid into position with an overhead crane and supported by the formwork (Figure 3.25) until the wall concrete was placed. The overlapping U-shaped stirrups that were used to provide confinement to the wall boundary element in the region where the coupling beam reinforcement intersected the longitudinal reinforcement in the adjacent wall are shown in Figure 3.26. Ensuring adequate anchorage for the special transverse reinforcement is critical, yet the preferred detail is dependent on the layout of the wall boundary element. The detail selected for this specimen consisted of anchoring the overlapping U-shaped stirrups with 135-degree bends around the longitudinal reinforcement (Figures 3.18-19). Finally, the wall formwork assembly was completed and the concrete was placed. Formwork was then moved up the wall and the sequence was repeated. The process proved to be efficient.

3.2.4 INSTRUMENTATION

A large number of instruments were placed on each of the coupled wall specimens to document their behavior for later analysis. Each of the actuators on the second and fourth levels had a load cell and displacement transducer to monitor the force and displacement applied to the specimen. However, the displacements of the actuators were not exactly representative of the motion of the specimen. The system of yolk and

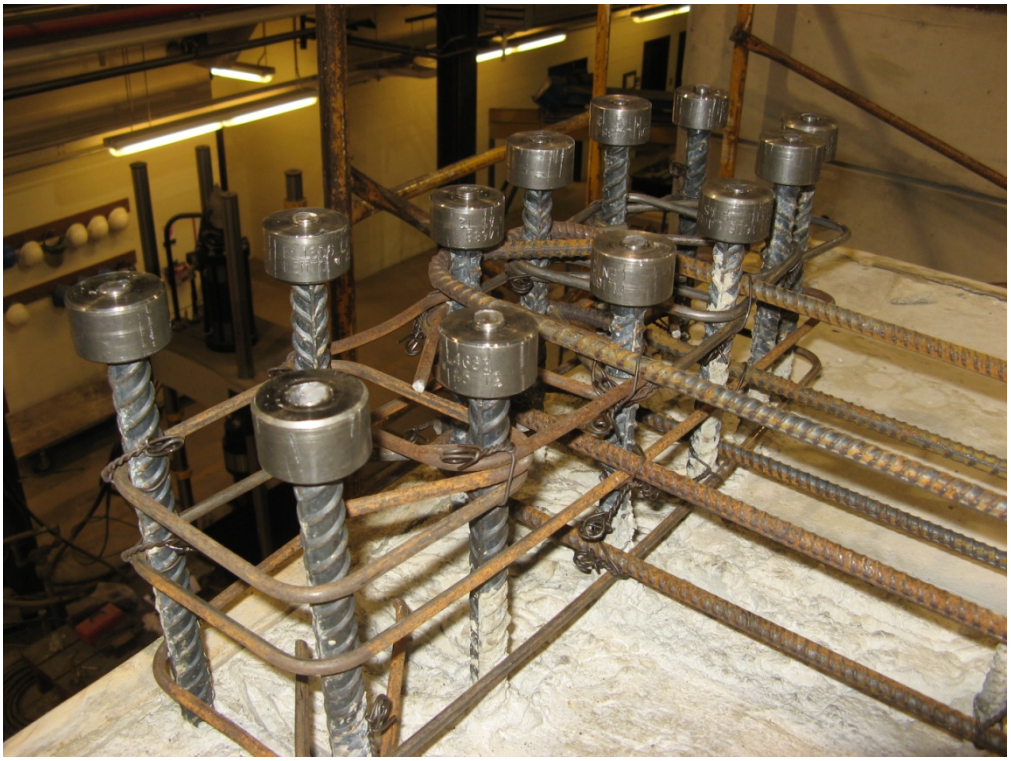

Figure 3.22 – Mechanical anchorage for #5 (D16) longitudinal reinforcement in walls

Figure 3.23 – Mechanical splice for #5 (D16) longitudinal reinforcement in walls

Figure 3.24 – Wall foundations prior to placement of concrete

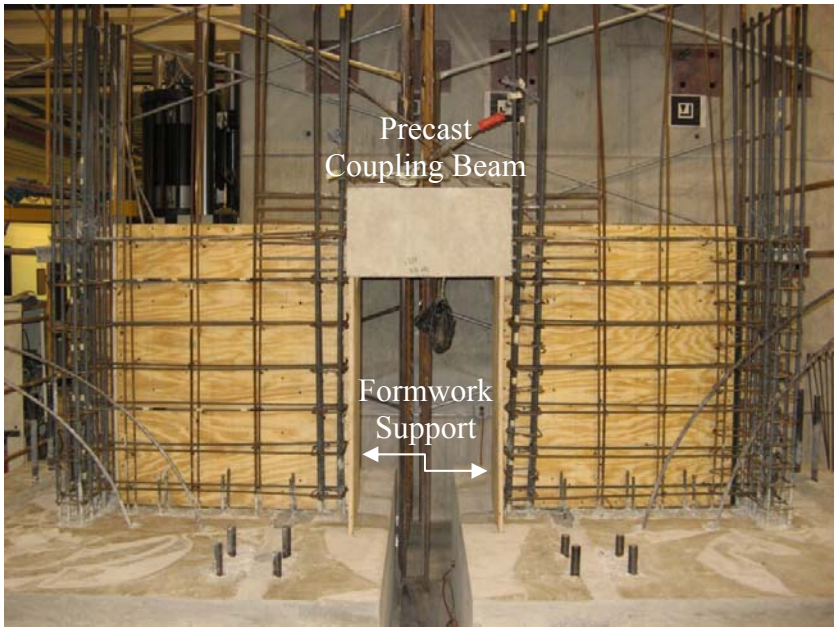

Figure 3.25 – Precast coupling beam placement, supported by formwork prior to casting

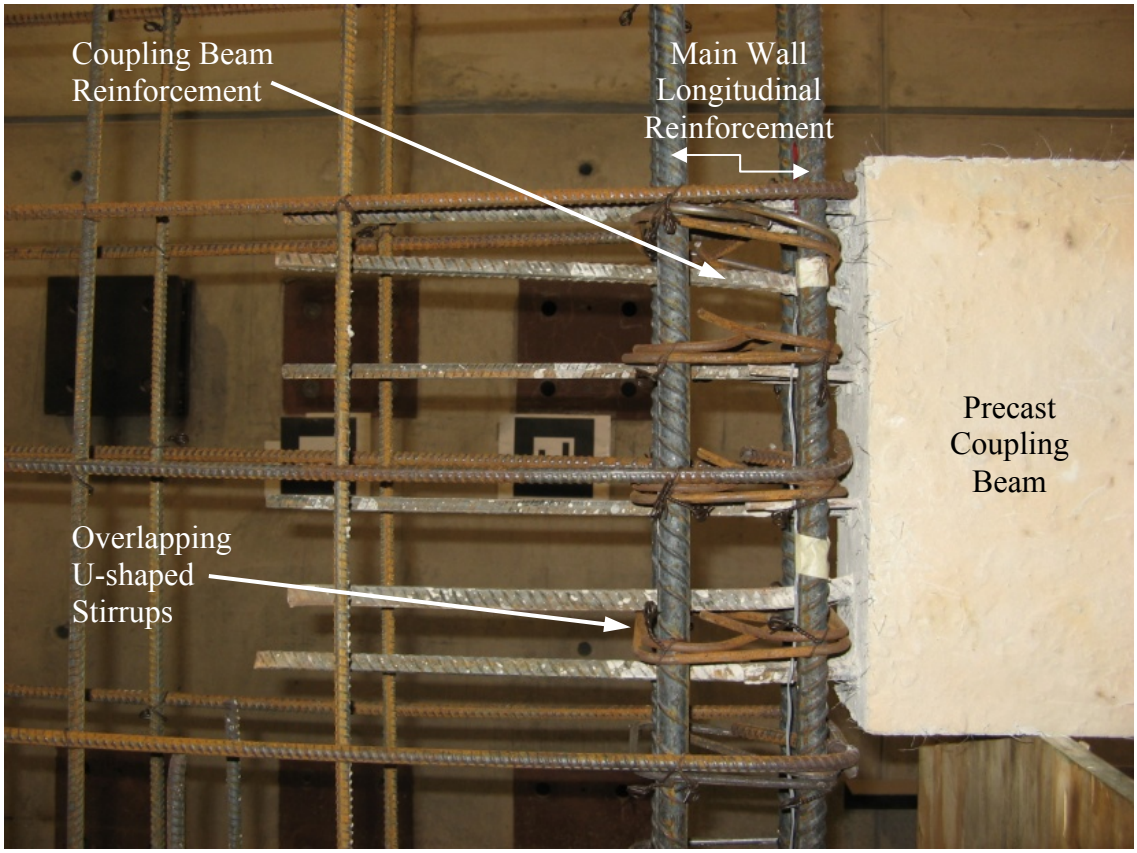

Figure 3.26 – Precast coupling beam embedment detail

channel sections transferring force from the actuator to the specimen would likely experience some elastic deformation and slippage, so two linear potentiometers were fixed directly to the specimen at the second and fourth levels to more accurately measure the lateral displacement of the specimen.

To record the strains developed in the reinforcing steel, strain gauges were fixed to reinforcement in the coupling beams and on both transverse and longitudinal reinforcement in the walls. The layout of strain gauges is shown in Figs. 3.27 and 3.28. The gauges and adhesive selected were intended to remain intact through large inelastic deformations, thereby providing a measure of steel strains for the duration of the test.

To document the external deformations of the specimen, the same optical system employed in the first phase of testing was applied to the first story level of each coupled wall specimen. One hundred forty-four independent points were fixed to the surface of the specimen in a grid pattern, shown in Figure 3.29, to track the deformation of the plastic hinge regions in the walls and the deformation of the first story coupling beam. The individual markers were labeled as shown in Figure 3.30. This field of data can be mined for relative displacements, flexural rotations, shear distortions, etc.

Unfortunately, the specimens were too large to be captured within the field of view of the optical system. Therefore, a layout of six inclinometers and twenty linear potentiometers was fixed to the specimen to record the deformations above the first story level. This instrumentation, positioned as shown in Figure 3.31, was placed to measure flexural rotations, shear distortions, coupling beam elongations, and wall displacements.

A photo of the optical marker layout is shown in Figure 3.32 prior to testing of the specimen. The full instrumented specimen, prior to testing, is shown in Figure 3.33. Both data gathering systems are visible on the specimen, as well as the positioning of the cameras for the optical system.

The eight hydraulic jacks used to apply the vertical “gravity” load, visible in Figure 3.33, shared a hydraulic line pressurized by a single pump. This arrangement ensured that each jack applied the same force to the system. The pressure in the line was set prior to lateral loading of the specimen and monitored throughout the test with a dial gauge.

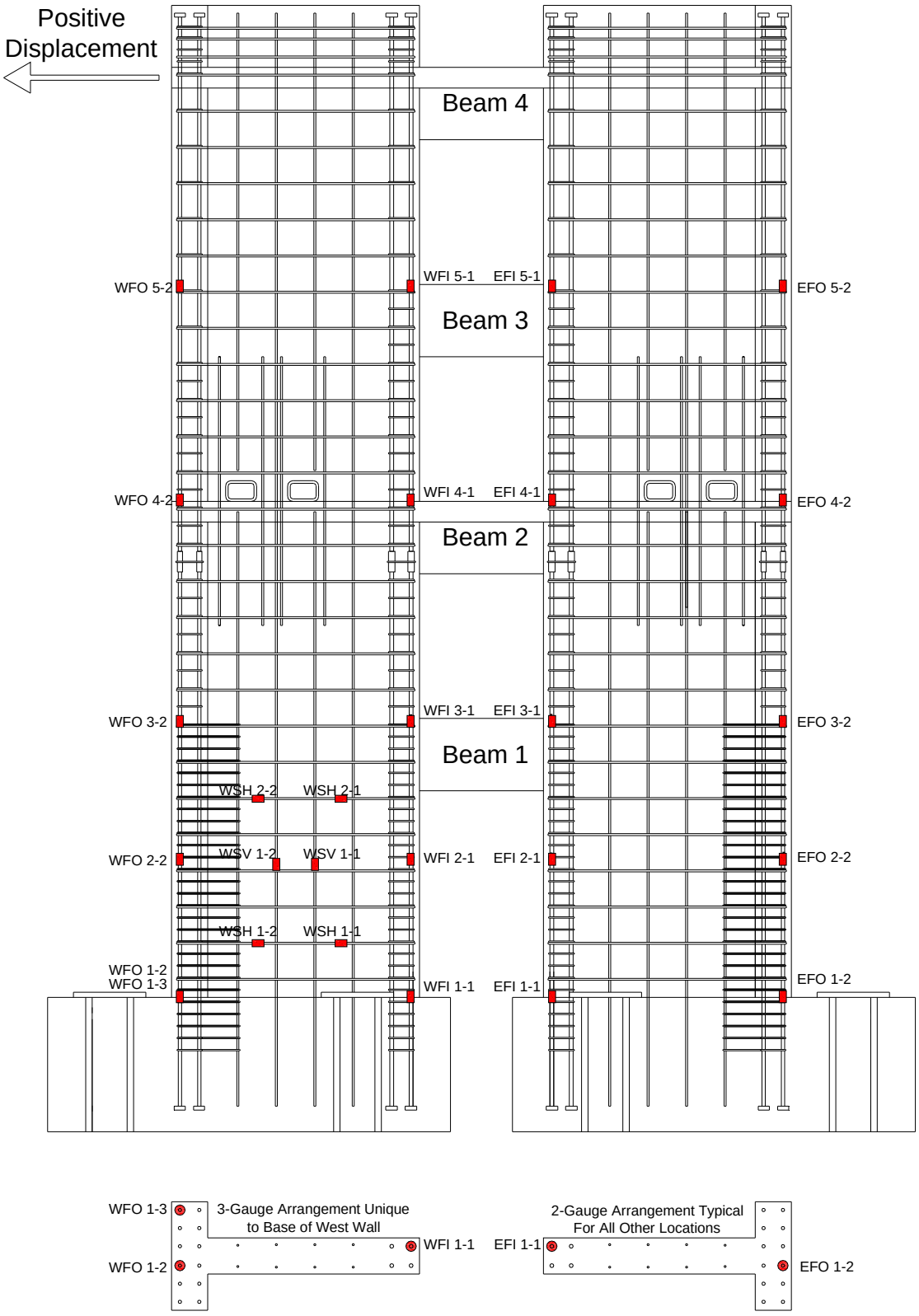

Figure 3.27 – Coupled wall strain gauge locations (wall diagram)

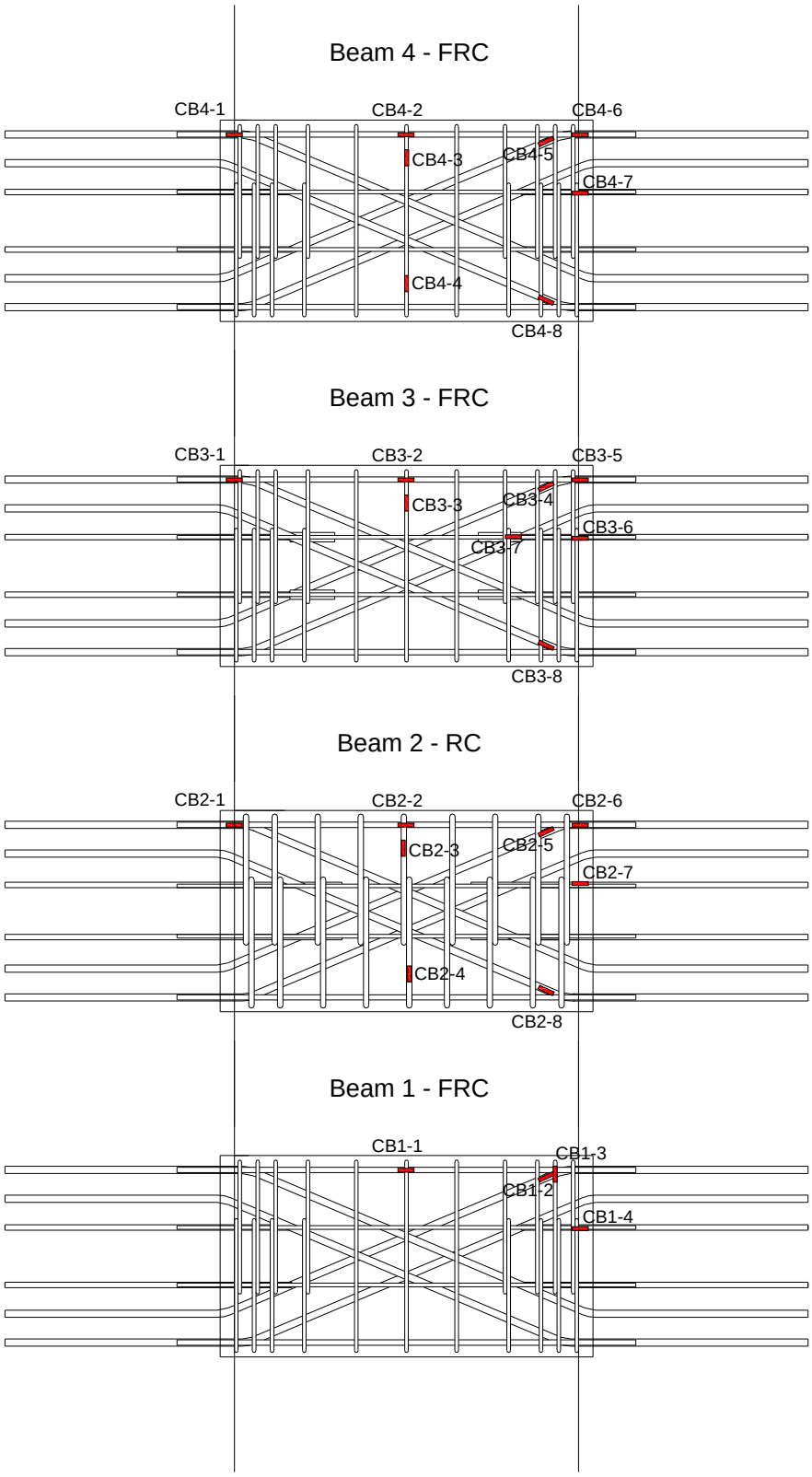

Figure 3.28 – Coupled wall strain gauge locations (coupling beam diagram)

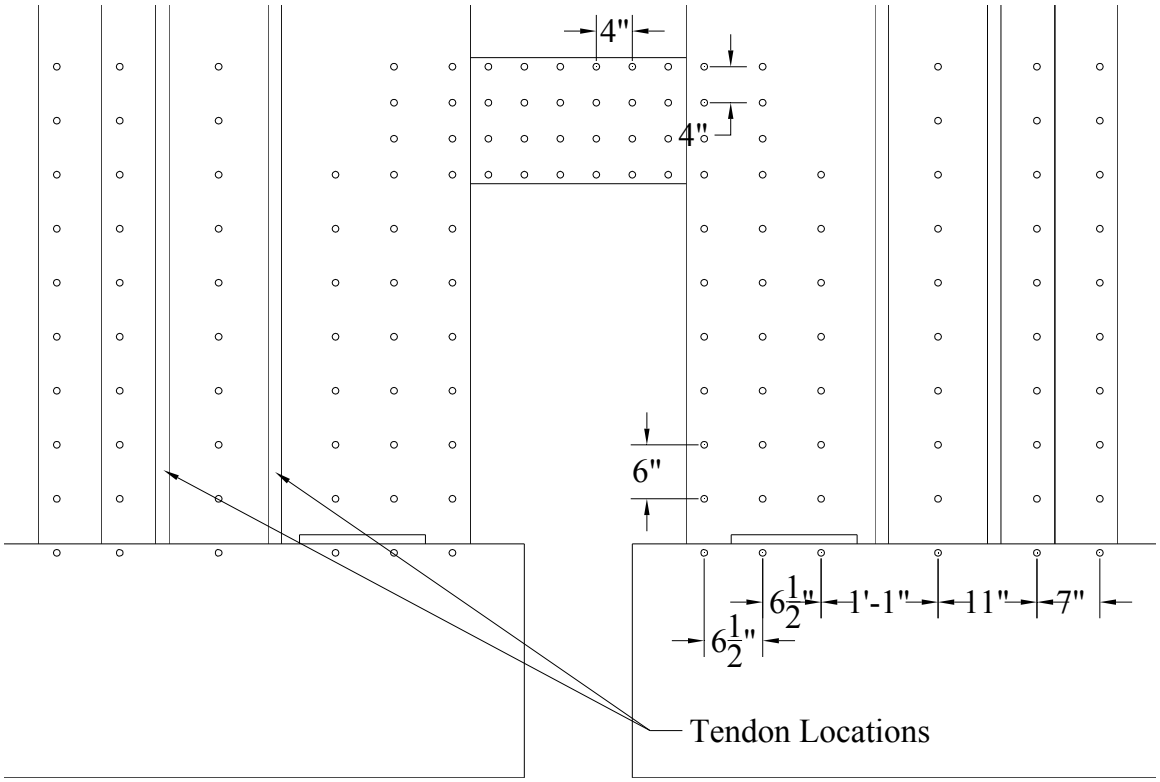

Figure 3.29 – Optical system “marker” locations

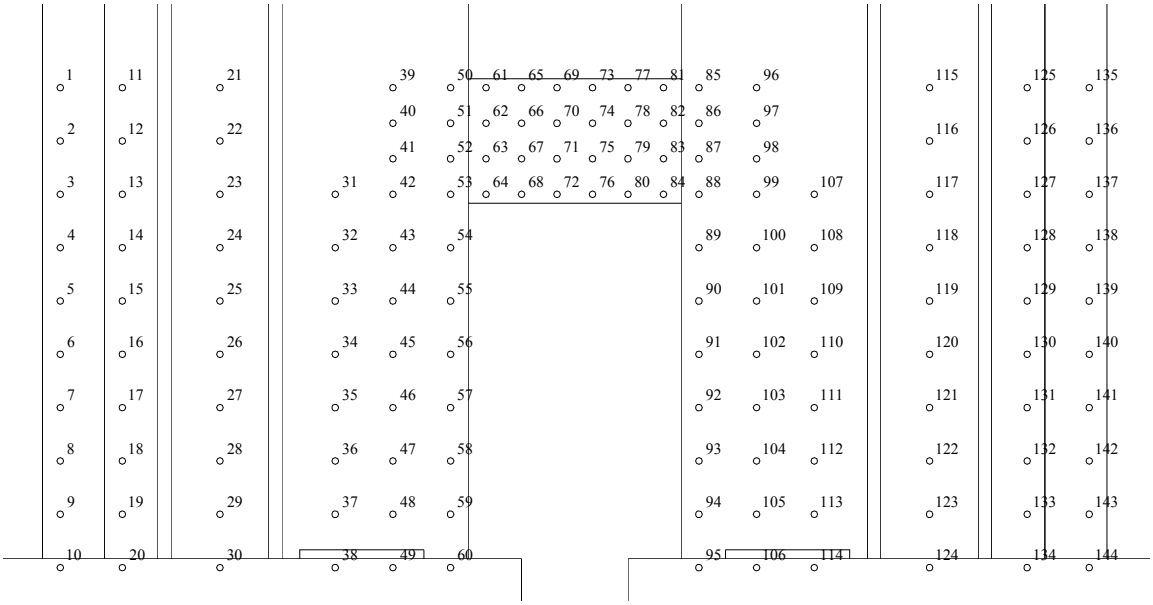

Figure 3.30 – Optical system “marker” labels

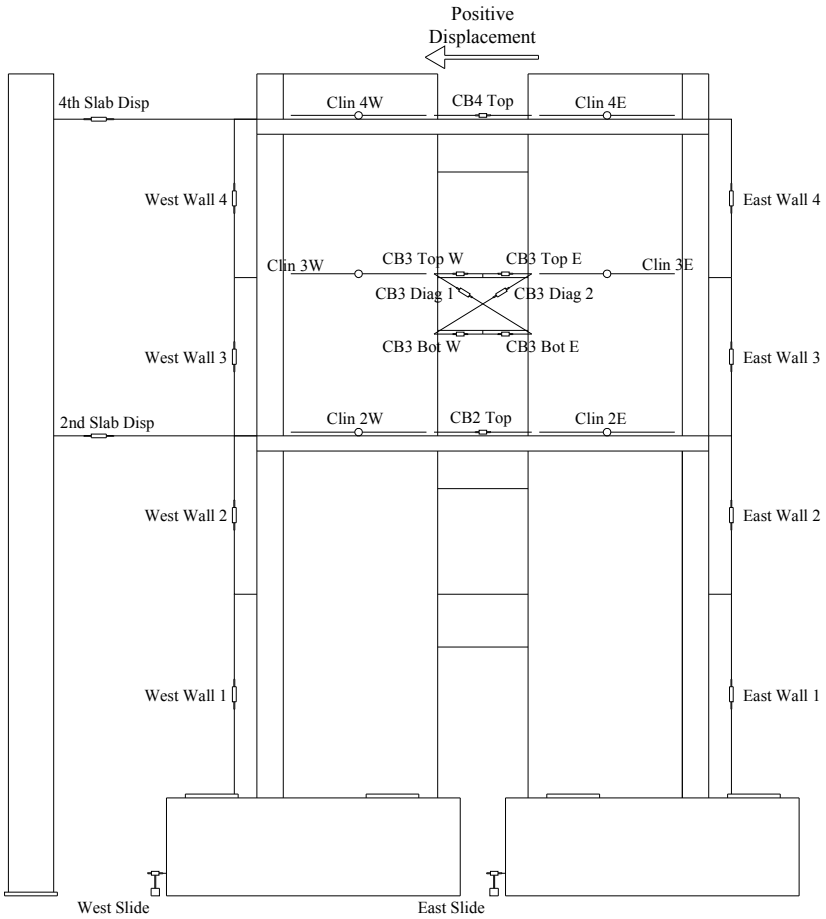

Figure 3.31 – Layout of traditional instrumentation

Figure 3.32 – Photo of optical system "marker" layout prior to testing

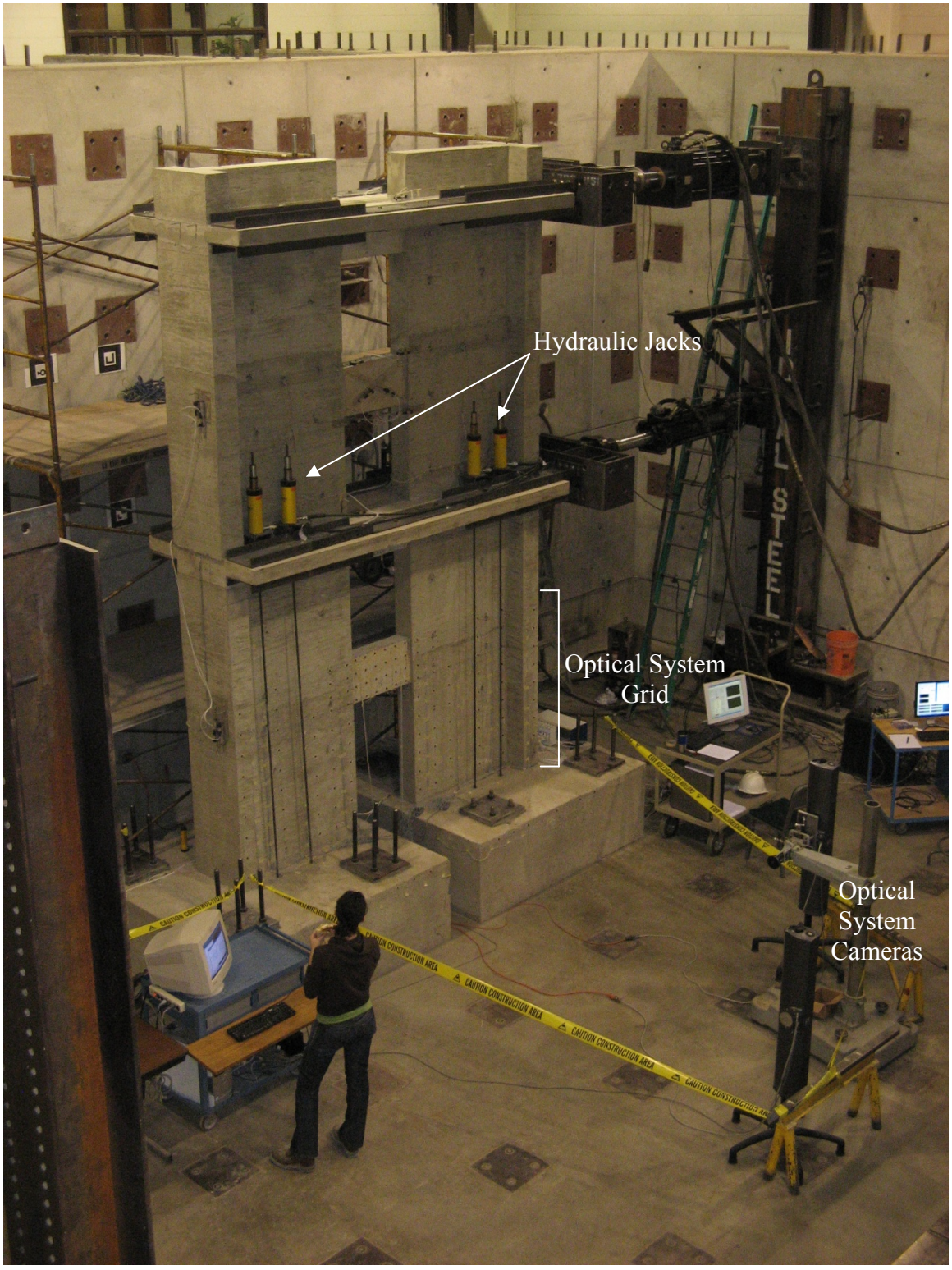

Figure 3.33 – Photo of specimen, fully instrumented, prior to testing

3.3 MATERIAL PROPERTIES

Each of the coupling beam and coupled wall specimens described previously was constructed with Grade 60 mild-steel reinforcement obtained from local suppliers. The concrete was either obtained from local suppliers and delivered to the University of Michigan Structures Laboratory or mixed directly in the laboratory facility. The following sections present the mixture proportions used for the HPFRC, as well as data from companion material tests for the HPFRC, conventional concrete and reinforcing steel.

3.3.1 HIGH PERFORMANCE FIBER REINFORCED CONCRETE (HPFRC)

Two different mixture designs were used for the HPFRC in this study. The first mixture was developed at the University of Michigan (Liao et al., 2006), and was selected for precasting all of the coupling beams for both experimental phases of this study and for the second story of Specimen CW-2. The HPFRC used in the first story of Specimen CW-2 was ordered from a local supplier and delivered to the laboratory, where fibers were added, to accommodate the larger volume of concrete required.

The first mixture, used for precasting of the coupling beams, is a highly flowable HPFRC with a 1.5% volume fraction (v_f) of high-strength hooked steel fibers. The properties of the selected fibers, as specified by the manufacturer, are summarized in Table 3.1. The mixture proportions, as reported by Liao et al. (2006), are shown in Table 3.2. For each batch of this mixture, students and technicians worked together to blend the required quantities using a drum mixer at the University of Michigan mixing facility. A team of students with buckets placed the concrete, with close attention being paid to properly vibrating the fresh concrete when necessary. Placement of this HPFRC was done with little difficulty.

For each batch, companion 6 by 6 by 20 in. (150 by 150 by 500 mm) flexural specimens conforming to ASTM C1609/C1609M-05 and 4 by 8 in. (100 by 200 mm) cylinders conforming to ASTM C39/C39M-03 were cast. Average results from tests of both cylinders and flexural specimens performed 28 days after casting and from cylinders

Table 3.1 – High-strength hooked steel fiber properties (specified by manufacturer)

Length (in./mm)		Diameter (in./mm)		L/d	Minimum Tensile Strength (ksi/MPa)	
1.2	30	0.015	0.38	80	333	2300

Table 3.2 – HPFRC mixture proportions by weight

Cement (Type III)	Fly Ash	Sand	Agg. Max dia. 0.5 in. (13 mm)	Water	Super-plasticizer (Glenium 3200HES)	Viscosity Modifying Agent (Rheomac VMA 362)	Steel Fiber
1	0.875	2.2	1.2	0.8	0.005	0.038	0.32

tested on the same day as the structural specimen are shown in Table 3.3. For the flexural tests, the equivalent bending stress at first crack (σ_{fc}), peak (σ_{peak}), and at deflections of $L/600$ ($\sigma_{\delta=600}$) and $L/150$ ($\sigma_{\delta=150}$) are reported. The peak compressive stress (f_c') is reported from the tests of cylinders.

For design purposes, compressive and tensile constitutive responses were assumed for the HPFRC used to precast the coupling beam specimens. These assumed relationships, shown in Figs. 3.34 and 3.35, were based on previous tests of cylinders and tensile "dogbone" specimens described in greater detail by Liao et al. (2006). The assumed compressive constitutive response consisted of a parabolic ascending branch defined by Eq. 3.2 (Hognestad, 1952), up to a specified peak compressive stress of 6 ksi (41 MPa) occurring at a strain of 0.002. A linear descending tail defined by Eq. 3.3 (Kent and Park, 1971) represented the post-peak response. In these equations, f_c' is the peak compressive stress, assumed to be 6 ksi (41 MPa), ε_c is the strain in the concrete, ε_o is the strain at which $f_c = f_c'$, assumed to be 0.002, and Z is the slope of the descending branch. Z was assumed to be 50 (rather than 150, which is often used for unconfined concrete) to account for the more gradual loss of strength due to the confinement provided by the transverse reinforcement and fibers. Moment curvature analyses were terminated when ε_c reached 0.008, which was considered to be the maximum useable strain of the HPFRC although, given the amount of confinement, a larger compressive strain capacity could reasonably be expected. These assumptions were used in design, but the test day values of f_c' were used for analysis of results.

Table 3.3 – HPFRC properties 28 days after casting and on the day of specimen testing (specified $f_c' = 6$ ksi; 41 MPa)

	Location of Pour	28-Day Tests										Test Day		Age in days
		f'_c (ksi;MPa)		ASTM 1609 Flexural Tests								f'_c (ksi;MPa)		
				σ_{fc} (psi;MPa)		σ_{peak} (psi;MPa)		$\sigma_{(\delta=L/600)}$ (psi;MPa)		$\sigma_{(\delta=L/150)}$ (psi;MPa)				
Phase 1	CB-1	5.5	38	640	4.4	930	6.4	950	6.6	600	4.1	6.5	45	78
	CB-2	6.1	42	630	4.3	890	6.1	810	5.6	400	2.8	7.5	52	48
	CB-3	5.0	34	690	4.8	860	5.9	750	5.2	330	2.3	5.0	34	41
Phase 2 CW-1	Beam-1	5.5	38	710	4.9	1030	7.1	970	6.7	520	3.6	10.3	71	299
	Beam-3	5.5	38	710	4.9	1030	7.1	970	6.7	520	3.6	10.3	71	299
	Beam-4	6.0	41	830	5.7	1120	7.7	1050	7.2	600	4.1	10.8	74	302
Phase 2 CW-2	Beam-1	6.0	41	830	5.7	1120	7.7	1050	7.2	600	4.1	10.4	72	562
	Beam-3	5.5	38	710	4.9	1030	7.1	970	6.7	520	3.6	10.4	72	559
	Beam-4	6.0	41	830	5.7	1120	7.7	1050	7.2	600	4.1	10.4	72	562
	Wall 1st lift (a)*	2.7	19	-	-	-	-	-	-	-	-	2.7	19	113
	Wall 1st lift(b)	7.2	50	800	5.5	1090	7.5	1040	7.2	740	5.1	7.4	51	112
	Wall 2nd lift	6.7	46	835	5.8	1050	7.2	1010	7.0	570	3.9	7.3	50	105

CW: Coupled Wall (1 lift = 1 story)

*Supplied by contractor, not according to mixture proportions presented in Table 3.2

$$f_c = f_c' \left[\frac{2\varepsilon_c}{\varepsilon_o} - \left(\frac{\varepsilon_c}{\varepsilon_o} \right)^2 \right] \tag{3.2}$$

$$f_c = f_c' [1 - Z(\varepsilon_c - \varepsilon_o)] \tag{3.3}$$

Similarly, a constitutive tensile response was assumed based on previously conducted tensile tests of this mixture (Liao et al., 2006). The assumed piecewise tensile constitutive response is shown in Figure 3.35. It is represented by a peak tensile stress of 500 psi (3.4 MPa) occurring at 0.5% strain, which is 25% higher than the first cracking stress. This peak is followed by a gradual decrease in tensile stress capacity. On average, tensile specimens still resisted 50% of their peak tensile stress at 1.4% strain.

The first story of Specimen CW-2 was cast with two lifts consisting of different HPFRC mixtures. The first lift, which rose 42 in. (1050 mm) from the foundation, was

delivered to the laboratory by a local concrete supplier. A 6 ksi (41 MPa) concrete mixture with a maximum aggregate size of 0.5 in. (13 mm) was ordered with a slump of 8 in. (200 mm). After arrival at the laboratory, the high-strength hooked steel fibers described in Table 3.1 were added such that the volume fraction of fibers (v_f) was 1.5%. The addition of fibers to this mixture, which did not have an adequately high paste content to accommodate a $v_f = 1.5\%$ of hooked steel fibers, stiffened the fresh concrete considerably. Despite the addition of water to increase the slump, placement was still difficult. Furthermore, the addition of water to improve the flow characteristics of the concrete significantly affected the observed compressive strength of cylinders, which is shown in Table 3.3 for lift (a). Despite the placement difficulties, good consolidation was obtained due to the wider spacing of hoops provided in the fiber reinforced wall and due to considerable effort on the part of students and technicians.

As a result of the placement difficulties associated with the pouring of the first story of Specimen CW-2, the remaining HPFRC wall segments were poured with the first HPFRC mixture described previously, using the laboratory facility for batching all of the required concrete. Given the volume of concrete, this was a considerable undertaking for both students and technicians, but resulted in a far more flowable concrete with more reliable hardened properties.

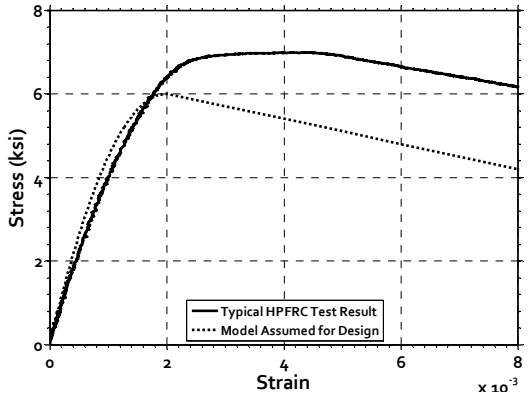

Figure 3.34 – Compressive constitutive model

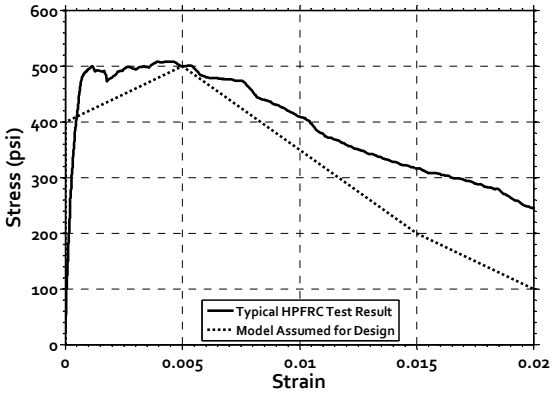

Figure 3.35 – Tensile constitutive model

3.3.2 CONVENTIONAL CONCRETE

Conventional concrete with a maximum aggregate size of 0.5 in. (13 mm) was used throughout this project. A compressive strength of 4 ksi (28 MPa) was specified for the simulated wall elements in Phase 1 and for the foundations, walls and slabs in Phase 2. A compressive strength of 6 ksi (42 MPa) was specified for the two reinforced concrete coupling beams incorporated in the coupled wall tests. Results from compressive tests on 4 in. by 8 in. (100 mm by 200 mm) cylinders at 28 days and near the test dates are shown in Table 3.4. Again, test day values of f'_c are used throughout this study for analysis of results.

Table 3.4 – Regular concrete properties 28 days after casting and on the day of specimen testing

	Location of Pour	Specified f'c (ksi; MPa)		28-Day f'c (ksi; MPa)		Test Day f'c (ksi; MPa)		Age in days
Phase 1	CB-1 End Blocks	4	28	3.9	27	4.0	28	57
	CB-2 End Blocks	4	28	5.3	37	4.8	33	37
	CB-3 End Blocks	4	28	5.0	34	5.0	34	17
Phase 2 CW-1	Beam-2	6	41	5.3	37	9.8	68	308
	Foundation	4	28	5.0	34	7.7	53	204
	Wall 1st lift	4	28	5.3	37	7.0	48	167
	Wall 2nd lift	4	28	4.1	28	6.7	46	149
	Slab #1	4	28	3.6	25	5.3	37	132
	Wall 3rd lift	4	28	5.5	38	6.6	46	125
	Wall 4th lift	4	28	6.9	48	9.5	66	118
	Slab #2	4	28	7.4	51	9.5	66	100
	Wall 5th lift	4	28	6.6	46	8.9	61	98
Phase 2 CW-2	Beam-2	6	41	6.6	46	9.2	63	566
	Foundation	4	28	7.2	50	7.6	52	127
	Slab #1	4	28	5.9	41	6.6	46	90
	Wall 3rd lift	4	28	7.9	54	8.3	57	84
	Wall 4th lift	4	28	6.5	45	7.0	48	78
	Slab #2	4	28	7.3	50	7.7	53	49
	Wall 5th lift	4	28	7.7	53	8.1	56	44

CW: Coupled Wall (1 lift = 1 story)

3.3.3 REINFORCING STEEL

Standard deformed mild-steel reinforcing bars were used for all reinforcement sized #3 and larger (10 mm and larger). Smaller 0.25 in. (6 mm) diameter reinforcement was used for transverse reinforcement where indicated in Section 3.2. This smaller diameter reinforcement was not deformed; however, 135-degree hooked anchorage was provided with sufficient development to prevent the pulling out of these bars, and to ensure adequate confinement was developed for the concrete core. Yield and ultimate stresses obtained from tensile tests of representative coupons are shown in Table 3.5.

Table 3.5 – Results from coupon tests of steel reinforcement

	Location	Bar Size	Yield Stress (ksi; MPa)		Ultimate Stress (ksi; MPa)	
Phase 1	CB-1	#3 (D10)	76.5	525	116	800
		#4 (D13)	72.5	500	107	740
		#5 (D16)	62.6	430	98.7	680
	CB-2	#3 (D10)	68.8	475	108	745
		#4 (D13)	63.5	440	99.6	685
		#5 (D16)	62.6	430	98.7	680
	CB-3	#3 (D10)	60.4	415	92.8	640
		#4 (D13)	63.5	440	101	695
		#5 (D16)	61.2	420	104	715
Phase 2 CW-1	Coupling Beams	#2 (D6)	64.1	440	73.3	505
		#3 (D10)	76.1	525	118	815
		#4 (D13)	76.0	525	115	795
	Structural Wall	#2 (D6)	64.1	440	73.3	505
		#3 (D10)	74.2	510	112	770
		#5 (D16)	67.2	465	109	750
		#6 (D19)	68.0	470	109	750
Phase 2 CW-2	Coupling Beams	#2 (D6)	64.1	440	73.3	505
		#3 (D10)	76.1	525	118	815
		#4 (D13)	76.0	525	115	795
	Structural Wall	#2 (D6)	64.1	440	73.3	505
		#3 (D10)	67.3	465	117	810
		#4 (D13)	60.1	415	97.0	670
		#5 (D16)	67.2	465	109	750
		#6 (D19)	68.0	470	109	750

3.3.3.1 Estimating Steel Stresses from Recorded Strains

The strain gauges applied to the reinforcing steel of each specimen provided a record of the cyclic strain history that each of the bars was subjected to at the gauge location as the structural element was displaced. These recorded strains are most useful for identifying the drift at which the reinforcement first yielded, the range of strains experienced during cycles of increasing specimen drift, and the maximum strains experienced by the reinforcement.

For some analysis purposes, approximating the level of stress corresponding to the recorded strain was required. Once steel reinforcement has yielded, developing a realistic constitutive model that captures the hysteretic behavior of steel, including an accurate description of the variation of loading and unloading slopes with the level of plastic strain, can be very difficult. It is beyond the scope of this project to either develop or improve existing models. Although several existing models were considered, a relatively simplistic model reported in Sakai and Mahin (2004) was adopted. An example implementation is shown in Figure 3.36. Figure 3.36(a) is a plot of the relationship between specimen drift and strains recorded by gauge L1 of Specimen CB-1 (see Figure 3.8), which was located on the primary flexural reinforcement near the precast beam-to-wall interface. The stresses predicted by the model are plotted versus the recorded strains in Figure 3.36(b).

3.3.3.2 Behavior of Mechanical Splices

The longitudinal reinforcement in the coupled wall specimens was spliced near mid-height of each specimen using mechanical splices (pictured in Figure 3.23). Although plastic deformations were not expected to occur at the location of the splice, the post-yielding response of the splice, compared to a continuous bar, was of interest. A spliced coupon specimen representing a #6 (D19) bar ready for testing is shown in Figure 3.37. The markers fixed to the coupon above and below the mechanical splice measured the separation of the two fixed points. This separation can be converted into an apparent average splice strain for comparison with a straight bar. The stress applied to the splice was calculated as the applied force divided by the area of the solid bar, neglecting the

changes in cross-section that occur over the splice length. Figure 3.38 is a plot of the apparent stress-strain responses of straight and spliced bar coupons.

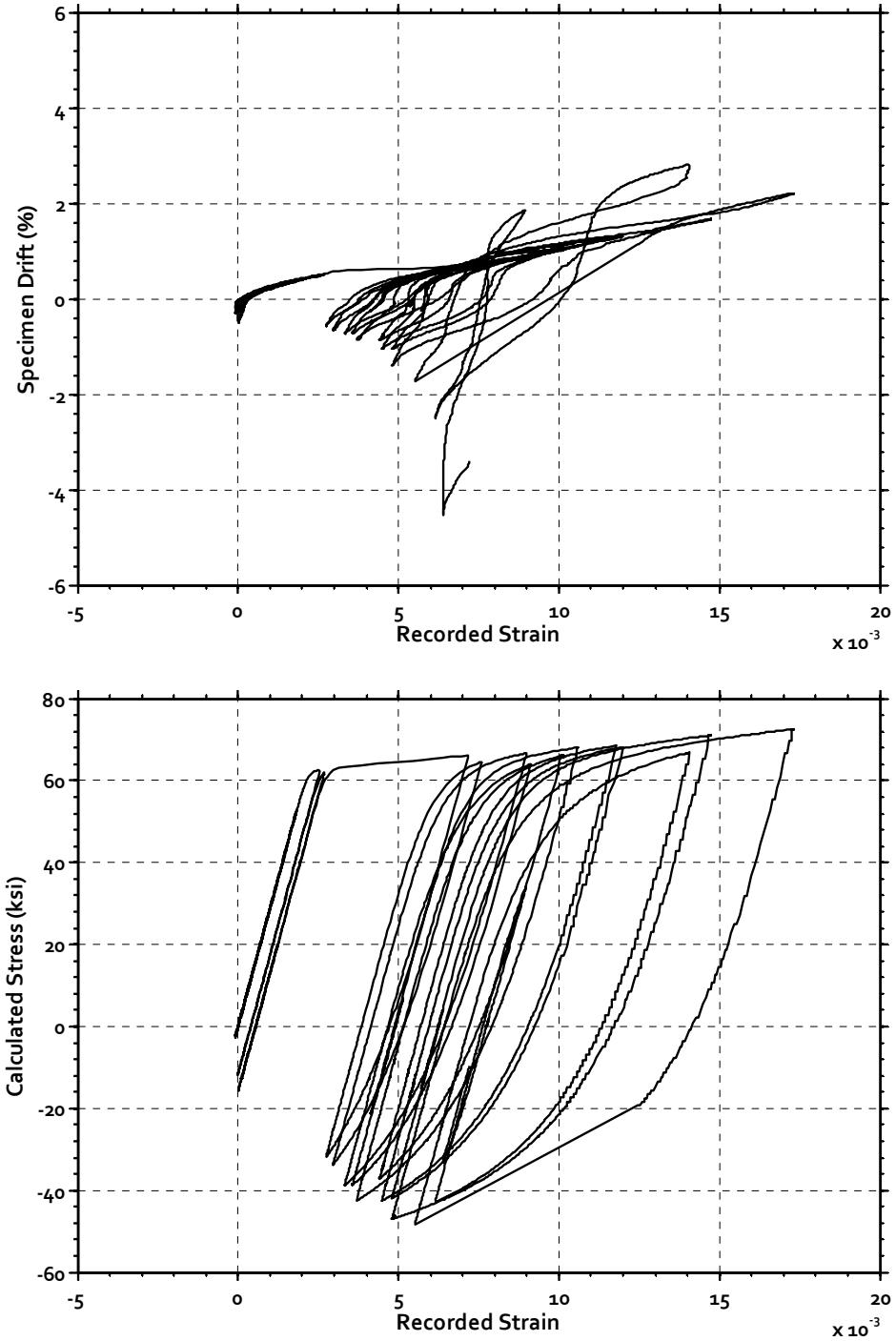

Figure 3.36 – (top figure) Recorded strain from gauge L1 of Specimen CB-1; (bottom figure) Calculated stress versus recorded strain for strain gauge L1 of Specimen CB-1

Overall, the spliced coupons behaved well and developed initial stiffness, yield stress and ultimate strength characteristics comparable to the straight bar coupons. The apparent post-yield stiffness, however, is much larger for the spliced bar. This should be expected, because only the short pieces of bar on either side of the spice yielded within the gauge length. Accordingly, the spliced coupon exhibited an ultimate strain capacity of approximately 4.8%, compared to over 10% for the straight bar coupons.

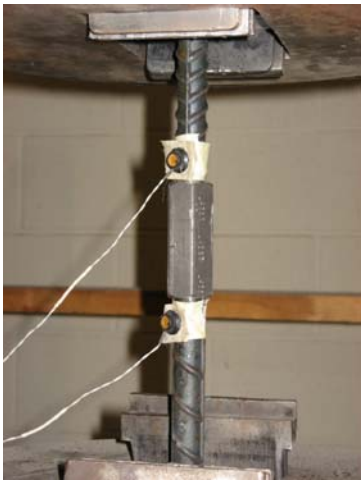

Figure 3.37 – Mechanically spliced bar coupon ready for testing

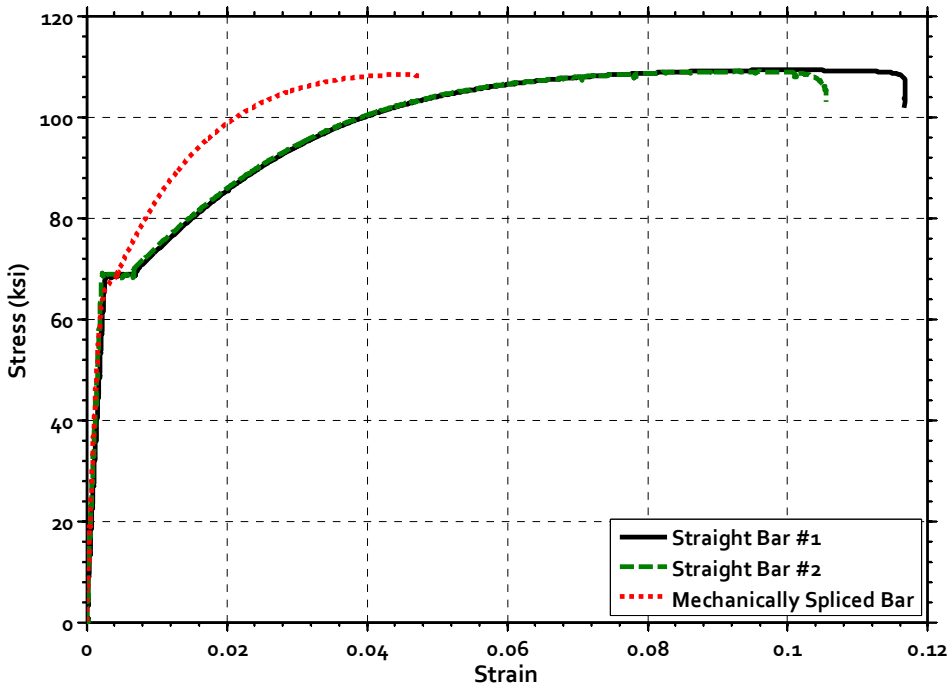

Figure 3.38 – Effective stress versus apparent average strain relationship for straight and mechanically spliced coupons of #6 (D19) reinforcing bars

CHAPTER 4:
COUPLING BEAM COMPONENT TEST RESULTS

4.1 CRACKING AND GENERAL DISCUSSION OF SPECIMEN RESPONSE

The three coupling beam specimens described in Chapter 3 were designed to resist high shear stresses that exceeded the upper limit of $10\sqrt{f_c'}, [psi]\left(0.83\sqrt{f_c'}, [MPa]\right)$ permitted by the ACI Building Code (ACI 318-08). Each of the specimens was subjected to the loading history shown in Figure 3.2. The resulting hysteresis relationship for each specimen, plotted as the average shear stress (calculated based on an area of bh, where b and h are the width and height of the coupling beam, respectively) versus specimen drift, is shown in Figs. 4.2, 4.4 and 4.6. Throughout this document, drift is used to describe the chord rotation referenced in ASCE/SEI 41 (2007), as calculated by Eq. 4.1 with variables shown in Figure 4.1. A discussion of the response of each specimen, and the observed progression of cracking, follows.

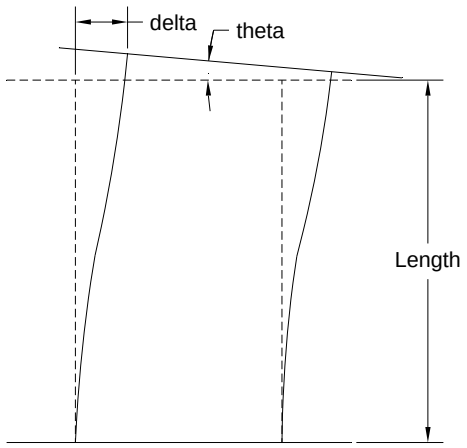

Figure 4.1 – Calculation of drift (chord rotation) from specimen deformation

$$Drift = \frac{delta}{Length} - \frac{theta}{2} \tag{4.1}$$

4.1.1 SPECIMEN CB-1 RESPONSE

The normalized shear stress versus drift response of Specimen CB-1 is shown in Figure 4.2. Moderately wide hysteresis loops, indicative of yielding of the flexural and diagonal reinforcement, indicate good energy dissipation in early cycles. The peak shear stress of $12.8\sqrt{f_c'}, [psi]\left(1.07\sqrt{f_c'}, [MPa]\right)$ near 2% drift in the positive loading direction is a very high shear stress for a concrete member. It should be emphasized that in the design of Specimen CB-1, the diagonal reinforcement accounted only for approximately 1/3 of the shear strength. Therefore, the shear capacity of the specimen indicates that other mechanisms are active in resisting the applied shear forces.

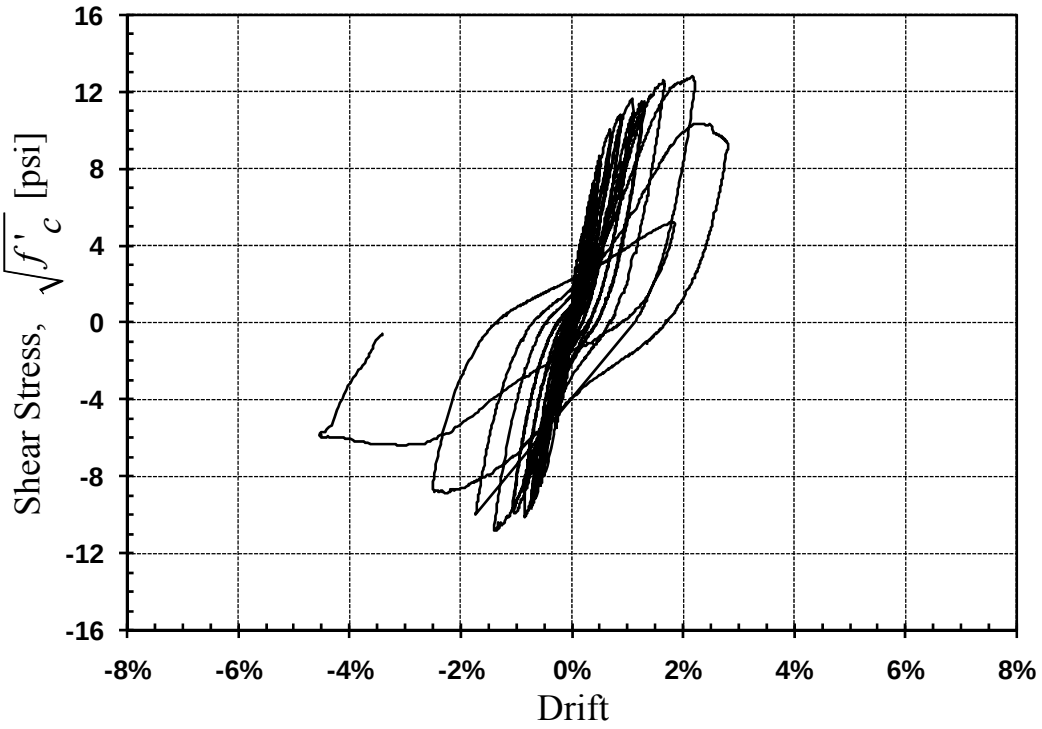

Figure 4.2 – Specimen CB-1 shear stress versus drift response

Despite the initially favorable response, the ability of the coupling beam to resist shear degraded substantially beyond a drift of 2%, which is not adequate for coupling beams that may be subjected to very large drift demands in a seismic event. To

understand the detailing issue that caused the premature degradation of the response near 2% drift, it should be kept in mind that the diagonal reinforcement was bent within the precast HPFRC member before entering the wall (see Figure 3.3a). This was done for two reasons: 1) to ease placement of the precast section through the densely reinforced wall boundary element, and 2) to increase the efficiency of the diagonal reinforcement for resisting shear by increasing the angle of inclination with respect to the longitudinal axis of the beam. This bend resulted in an inclined force component that would tend to burst through the top and bottom of the coupling beam if not adequately restrained by stirrups. In design, this inclined force component was estimated as $9.5kip$ $(42.3kN)$ based on the area of one diagonal bar, the angle of inclination (24º), and an estimated yield stress of $75ksi$ $(515\ MPa)$. The two #3 (D12) stirrups located near the bend had a tensile yield strength of $26.5kip$ $(118\ kN)$, assuming a yield stress of $60ksi$ $(415\ MPa)$. This is nearly 3 times the burst out force, so the stirrups were expected to resist the bursting force from the diagonal reinforcement with enough spare capacity remaining to effectively work with the HPFRC to confine the plastic hinge. However, the limited ductility achieved experimentally indicates that the HPFRC and transverse reinforcement provided were not sufficient to confine the plastic hinge region. In subsequent tests, this deficiency was addressed by providing a tighter spacing of ties with 135º bends throughout the plastic hinge region, and by providing additional tie legs through the center of the hinge to restrain lateral expansion.

Throughout the test, a group of students used markers to carefully identify and record the development of cracks. The first observed cracks, beyond those caused by concrete shrinkage, were web-shear cracks that developed near 0.75% drift. As the specimen was pushed to 1.0% drift, additional web-shear cracks developed that were joined by flexural-shear cracks near the ends of the beam, where moments were highest. At 1.25% drift, only a few new web-shear cracks were observed at mid-span. At this stage of loading, the development of flexural and flexural-shear cracks near the ends of the specimen became more prominent. Up to this point, all cracks were kept narrow by the fibers and mild steel reinforcement. Further loading led to wider flexural cracks as yielding of the flexural reinforcement became more severe. The widest flexural cracks formed along the stirrup located approximately 3 in. (75 mm) away from the face of the

wall. When the beam was first pushed beyond 2.2% drift in the positive direction, sliding was observed along the stirrup where the most severe flexural cracking had created a crack plane across the entire beam cross-section. Further loading quickly forced a second failure plane to develop along the stirrup located 9 in. (225 mm) from the face of the wall. In addition to pronounced sliding shear displacements, the final failure of the specimen showed severe transverse expansion of the coupling beam. This transverse expansion indicates that insufficient lateral confinement was provided to the plastic hinge region. The failure of the plastic hinge region is shown in Figure 4.3. Severe damage is evident, as is the primary sliding plane. Similar, but less severe, damage was observed at the opposite end of the specimen.

Figure 4.3 – Ultimate damage state of Specimen CB-1: insufficient confinement and sliding are evident

4.1.2 SPECIMEN CB-2 RESPONSE

As shown in Figure 3.3b, Specimen CB-2 was reinforced with additional confinement reinforcement over a length of $h/2$, measured from the face of the wall, which was assumed to encompass the plastic hinge region. This change resulted in a significantly more stable hysteresis behavior (shown in Figure 4.4) than that observed in Specimen CB-1. Despite the high shear stresses imposed on this specimen, which exceeded $11.5\sqrt{f_c'}, [psi]\left(0.87\sqrt{f_c'}, [MPa]\right)$ in the positive loading direction, Specimen CB-2 performed in a stable manner. The response was characterized by minor pinching of the shear stress versus drift hysteresis loops and retention of 80% of the peak shear force to drifts of approximately 5% in both directions.

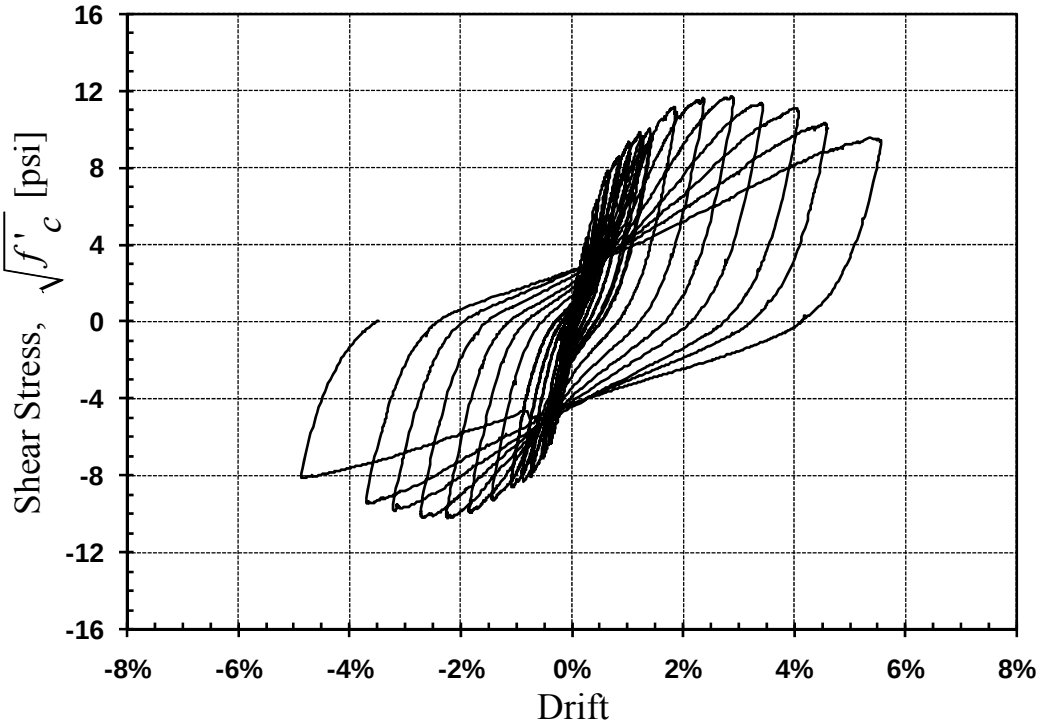

Figure 4.4 – Specimen CB-2 shear stress versus drift response

As with Specimen CB-1, diagonal steel was provided to resist approximately 1/3 of the shear force applied to the section. The high shear capacity, bolstered by the observation that diagonal cracks remained narrow throughout the test, supports the assertion that stirrups and HPFRC were both active and efficient at resisting shear forces,

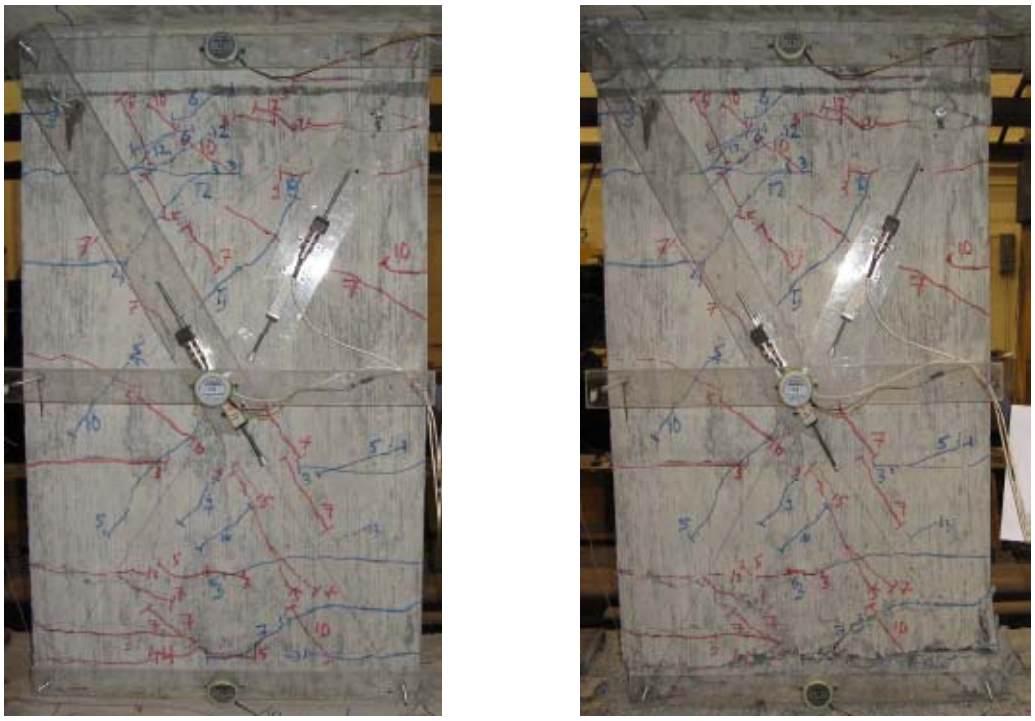

Figure 4.5 – Damage of Specimen CB-2 at 3.5% and 5.5% drift, left and right, respectively

even at large drifts. This allowed for plastic hinges to develop near both ends of the coupling beam, as intended. The special column-type confinement provided in the plastic hinge region complemented the confinement provided by the HPFRC to allow for a ductile and stable flexural mechanism to control the behavior. Late in the test, flexural cracks from opposing half-cycles of drift coalesced along a stirrup in the plastic hinge region, creating a plane with a reduced ability to resist sliding shear. Failure ultimately occurred along this plane at drifts exceeding 5%.

Specimen CB-2 developed cracking in the early drift cycles that closely matched the crack patterns observed during the test of Specimen CB-1. Web-shear cracks were observed at drifts of 0.75%, and continued to develop until a drift of approximately 1.0%, beyond which no further web-shear cracking was observed. Also near 1.0% drift, flexural and flexural-shear cracks were observed forming near the ends of the coupling beam. These flexural and flexural-shear cracks continued to form and extend until approximately 1.5% drift, beyond which very little new cracking was observed. At 2% drift, flexural cracks began to widen, and were measured to be approximately 0.04 in. (1

mm) in width. When Specimen CB-2 reached approximately 3.5% drift, superficial flaking was observed as fibers near the surface dislodged small flakes of concrete. At this point in the test, flexural cracking had become severe enough that a probable failure plane location could be identified at each end of the coupling beam; however, no deterioration of the behavior was yet observed. A photo of the beam at 3.5% drift is shown in Figure 4.5. Further drift cycles were dominated by the opening of a few (3 or 4) flexural cracks within the plastic hinge region at both ends of the coupling beam. At 4% drift, flexural crack widths of approximately 0.1 in. (2.5 mm) were observed, along with minor sliding along the crack faces. These flexural cracks opened to approximately 0.15 in. (3.5 mm) at a specimen drift of 4.5%. Finally, at approximately 5.5% drift in the positive loading direction, appreciable sliding was observed along flexural cracks in the plastic hinge region, resulting in a relative movement of nearly 0.25 in. (6 mm). This amount of sliding led to some splitting and spalling of the compression zone, which led to ultimate failure of the coupling beam. A photo of the beam at 5.5% drift is also shown in Figure 4.5.

4.1.3 SPECIMEN CB-3 RESPONSE

A simpler connection detail was evaluated through the testing of Specimen CB-3. This detail consisted of straight dowel bars placed across the beam-to-wall interface to encourage plastic hinging to occur within the beam, replacing the U-shaped dowel bars used in Specimens CB-1 and CB-2. The shear keys at the precast beam-to-wall interface of Specimens CB-1 and CB-2, intended to prevent sliding, were also eliminated in the design of Specimen CB-3. Finally, the transverse reinforcement ratio at midspan was reduced by 25% relative to the previous specimens, thus forcing the HPFRC to resist a higher percentage of the applied shear stress. Despite an unforeseen problem with a potentiometer that measured slip of the base block, which resulted in an asymmetric loading regimen, the response of Specimen CB-3 showed minor pinching of the shear stress versus drift hysteresis loops and retention of 80% of the peak shear force to a drift of 5% in the negative loading direction. Figure 4.6 shows that shear stresses of up to $14\sqrt{f_c'}, [psi](1.17\sqrt{f_c'}[MPa])$ were imposed in the negative loading direction. As in the

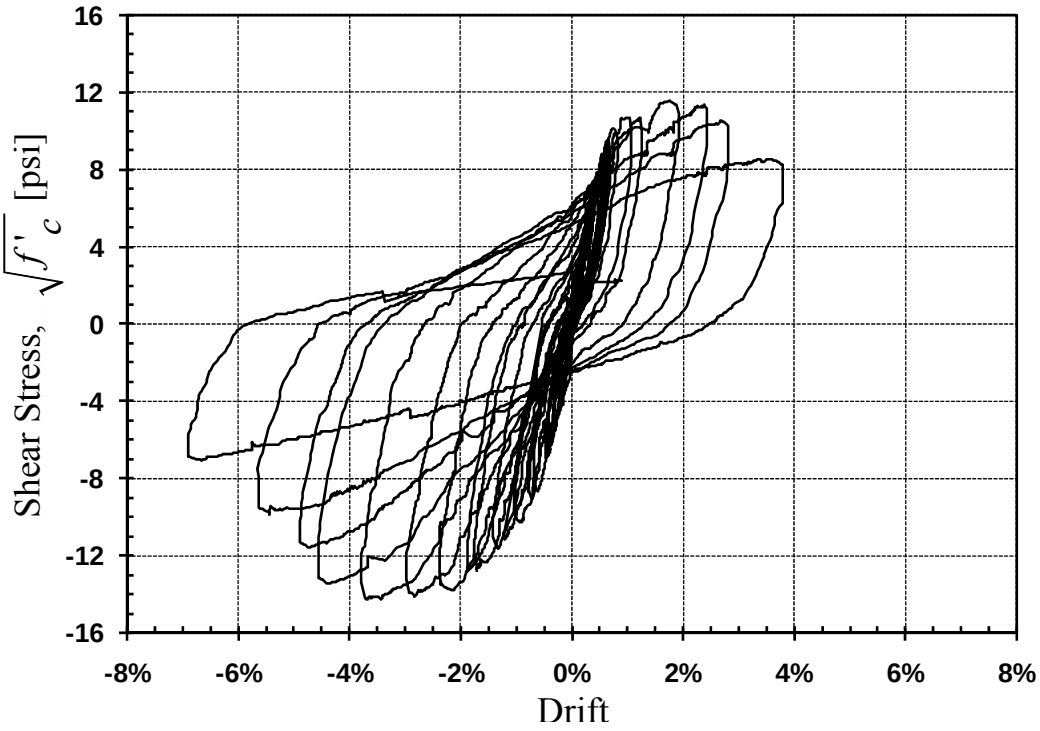

Figure 4.6 – Specimen CB-3 shear stress versus drift response

other two tests, the response of Specimen CB-3 was dominated by flexural rotations near the ends of the coupling beam. This ultimately led to the development of a sliding shear failure plane at drifts near 5% in the negative loading direction. Despite the relatively small drifts imposed in the positive loading direction, the larger demands in the negative loading direction led to large rotations and the development of a few wide flexural cracks. These flexural cracks were wide enough to allow sliding to develop under the large shear stresses imposed on the specimen ($14\sqrt{f_c'}, [psi]$($1.17\sqrt{f_c'}[MPa]$)). Similar to Specimens CB-1 and CB-2, diagonal cracking near midspan was limited, despite the 25% reduction in the stirrup area provided.

The development of cracking during the testing of Specimen CB-3 followed the same general pattern observed in previous tests. Although the transverse reinforcement ratio at mid-span was reduced by 25%, no opening of wide diagonal shear cracks was observed during the test. The modified connection detail did not have an observable effect on the pattern of cracking in the end region of the coupling beam. Like Specimen CB-2, the failure of Specimen CB-3 was initiated by sliding across a plane defined by

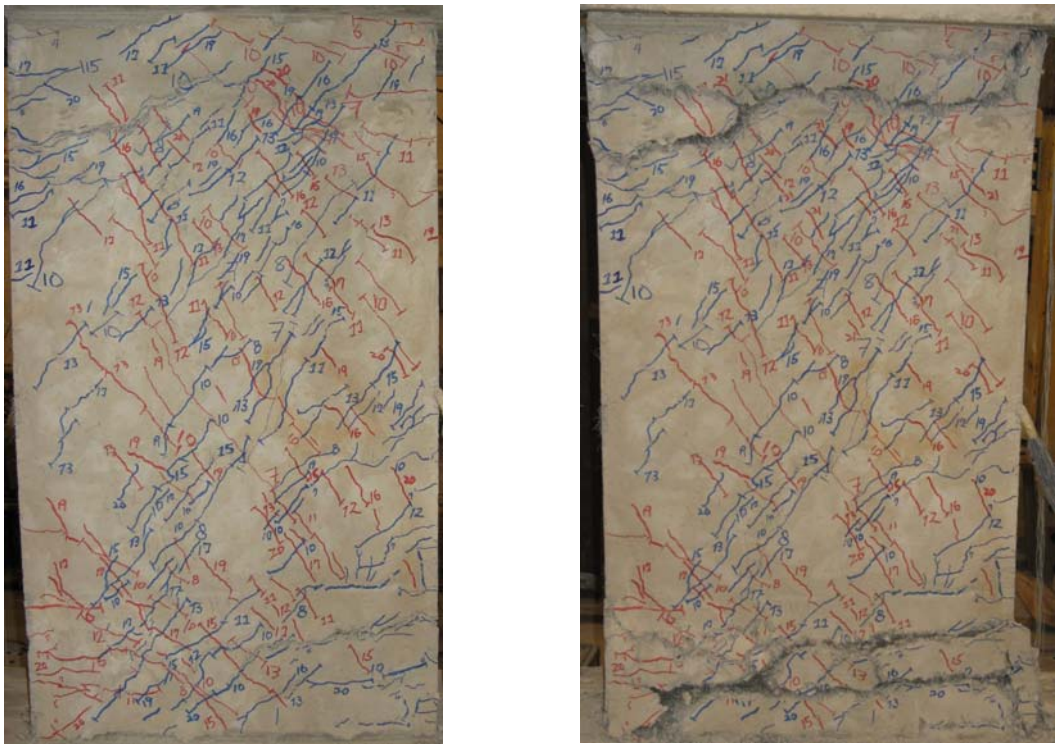

Figure 4.7 – Damage of Specimen CB-3 at 3% and 6% drift, left and right, respectively

flexural cracks that had formed along a stirrup approximately 3 in. (75 mm) from the face of the wall. Figure 4.7 shows the crack pattern at 3% and 6% drift. The higher density of marked cracks relative to previous specimens is due to greater access to the surface of the specimen permitted by reduced external instrumentation, rather than to a difference in behavior.

4.1.4 Elongation and Development of Axial Force in HPFRC Coupling Beams

When reinforced concrete members are subjected to cyclic displacements large enough to cause significant cracking and yielding of the reinforcement, it is widely acknowledged that the cracks will not close completely upon reversal of the loading direction. This is due to permanent (plastic) deformations in the steel reinforcement and the fact that cracks do not close perfectly. As a result, reinforced concrete members have a tendency to expand longitudinally when subjected to earthquake-type cyclic displacements. In most design cases, the resulting axial strain is either small or insufficiently restrained to cause significant axial forces to develop. However, the large

drift demands placed on short coupling beams result in a strong tendency to expand longitudinally, and the adjacent structural walls and surrounding slab should provide non-negligible resistance to this expansion, as identified by Teshigawara et al. (1998a).

In component tests, few researchers have addressed longitudinal expansion of coupling beams and the possible axial forces that may develop as a result. Most experimental work has allowed for unlimited axial growth, which has been reported to be on the order of 3.0% of the beam span (Kwan and Zhao, 2002; Zhao and Kwan, 2003; Naish et al., 2009). In the current series of tests, longitudinal expansion was partially restrained, which resulted in maximum average axial strains between 0.6-1.4%, as shown in Figure 4.8.

The importance of predicting the coupling beam elongation would be negligible if structural walls were not present to restrict this elongation and cause the development of axial forces within the coupling beam. In this series of tests, restricting the elongation of

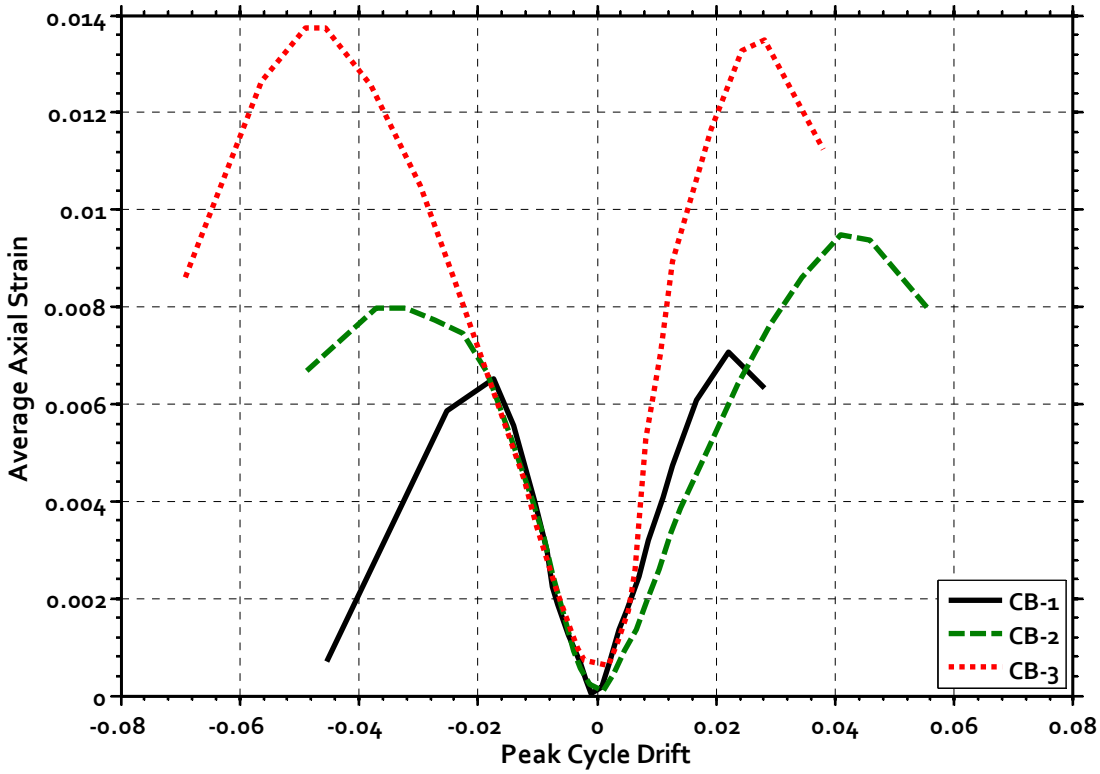

Figure 4.8 – Average axial strain in coupling beam specimens at the peak drift of each loading cycle (positive strain is elongation)

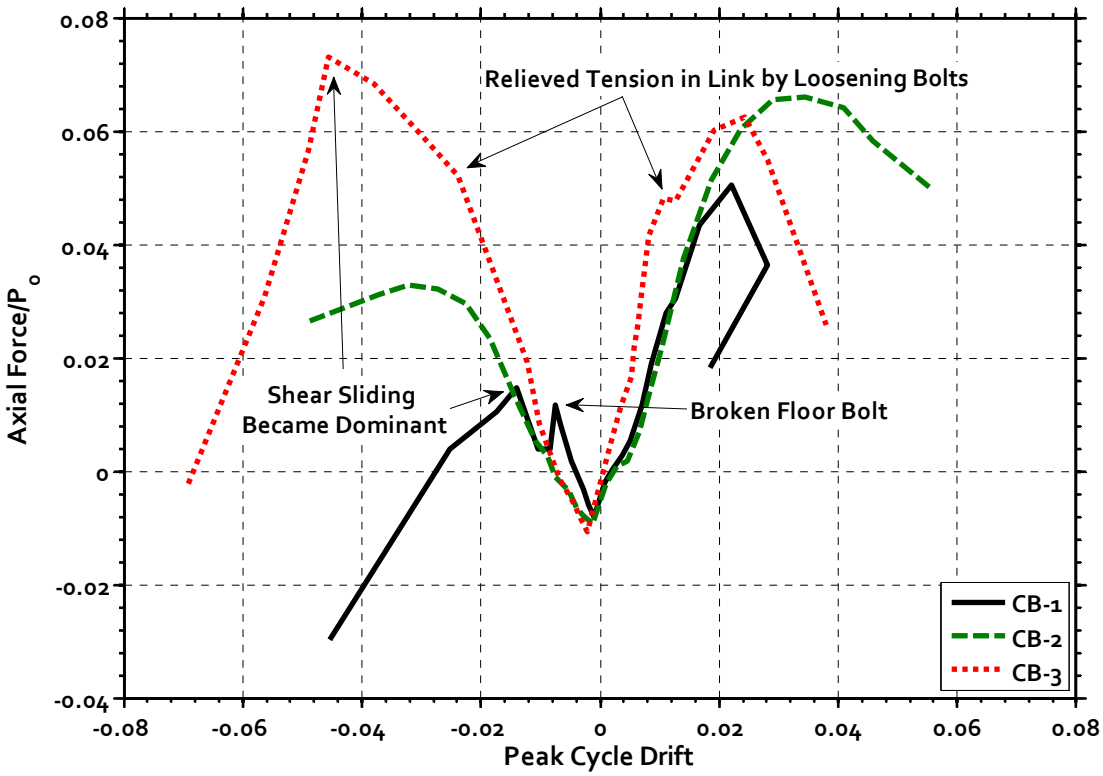

Figure 4.9 – Axial force developed in coupling beam specimens at the peak drift of each loading cycle, normalized by the axial force capacity

the coupling beams resulted in axial forces on the order of 4-7% of the axial force capacity, as shown in Figure 4.9. For the purpose of this discussion, the axial force capacity was calculated as $P_o = f_c'(A_g - A_{st}) + f_y A_{st}$, where f_c' is the compressive strength of the concrete, f_y is the measured yield stress of the steel reinforcement, A_g is the gross cross-sectional area of the beam, and A_{st} is the total area of longitudinal steel, including the longitudinal component of the diagonal steel. The 0.85 factor usually applied to f_c' was neglected because the specimens were horizontally cast.

Abrupt changes in the magnitude of the developed axial force are apparent for Specimens CB-1 and CB-3 that coincide with test setup issues (labeled in Figure 4.9) that resulted in lower test frame stiffness. The axial load in the beam quickly diminished once sliding became a dominant factor in the behavior of the specimen.

As mentioned earlier, the observed axial force was on the order of 4-7% of the beam's axial force capacity. Although this is a low level of axial force compared to more

typical compression members, these axial forces will have the effect of moderately increasing the flexural and shear capacity of coupling beams. For this reason, the observed axial forces are considered in the analysis of the coupling beam results and were necessary for accurately predicting the ultimate moment resisted by the specimens.

To further investigate the mechanisms that best correlate with the observed elongation, a number of coupling beam deformation parameters were plotted against the recorded elongation. Elongation best correlated with the maximum drift due to flexural rotations previously imposed on the specimen. In other words, for any given point in the loading regimen, the elongation of the coupling beam correlated best with the largest drift due to flexural rotations that had been imposed on the specimen at any time preceding that point in the loading regimen. This correlation implies some degree of dependence between elongation and flexural deformations. Relatively close correlation was also observed between elongation and the maximum previously imposed drift, which is largely comprised of flexural rotations. These relationships are shown in Figs. 4.10 and

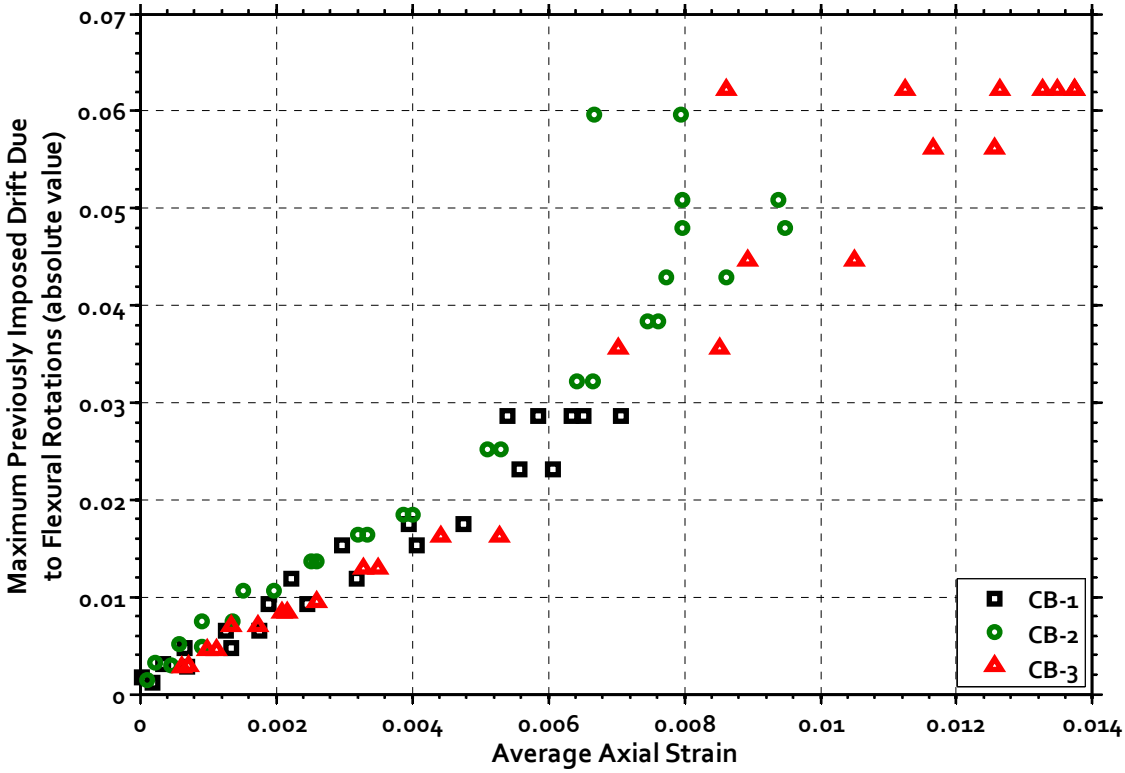

Figure 4.10 – Relationship between the maximum previously imposed drift due to flexural rotations and average axial strain (positive is elongation)

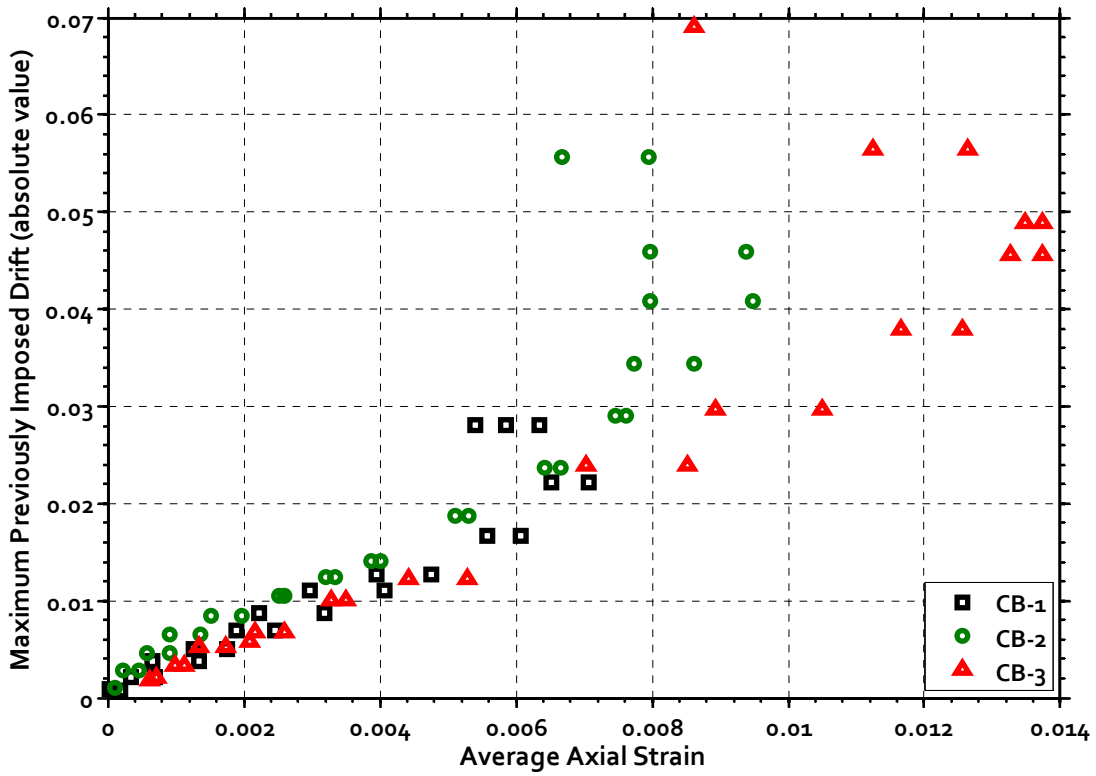

Figure 4.11 – Relationship between the maximum previously imposed drift and average axial strain (positive is elongation)

4.11. Conversely, shear deformations showed little correlation with the elongation, supporting the assertion that for these specimens it is the opening and then only partial closing of flexural cracks that provides the primary mechanism forcing axial elongation of coupling beams.

Fig 4.12 shows the elongation of the coupling beams as a function of the loading cycle number. Three important trends can be gleaned from these plots. First, it is again evident that the elongation increases as the imposed drift increases. Second, the step-like nature of the curves, caused by the repetition of loading cycles at the same drift level, shows that little axial growth was caused by the repeated cycles. Therefore, it seems the amount of elongation is more strongly dependent on the amount of inelastic deformation previously imposed than on the number of repeat cycles. Finally, the plots also show that the axial elongation decreases in the last few loading cycles. This coincides with the point of the test when shear sliding became a major contributor to beam drift.

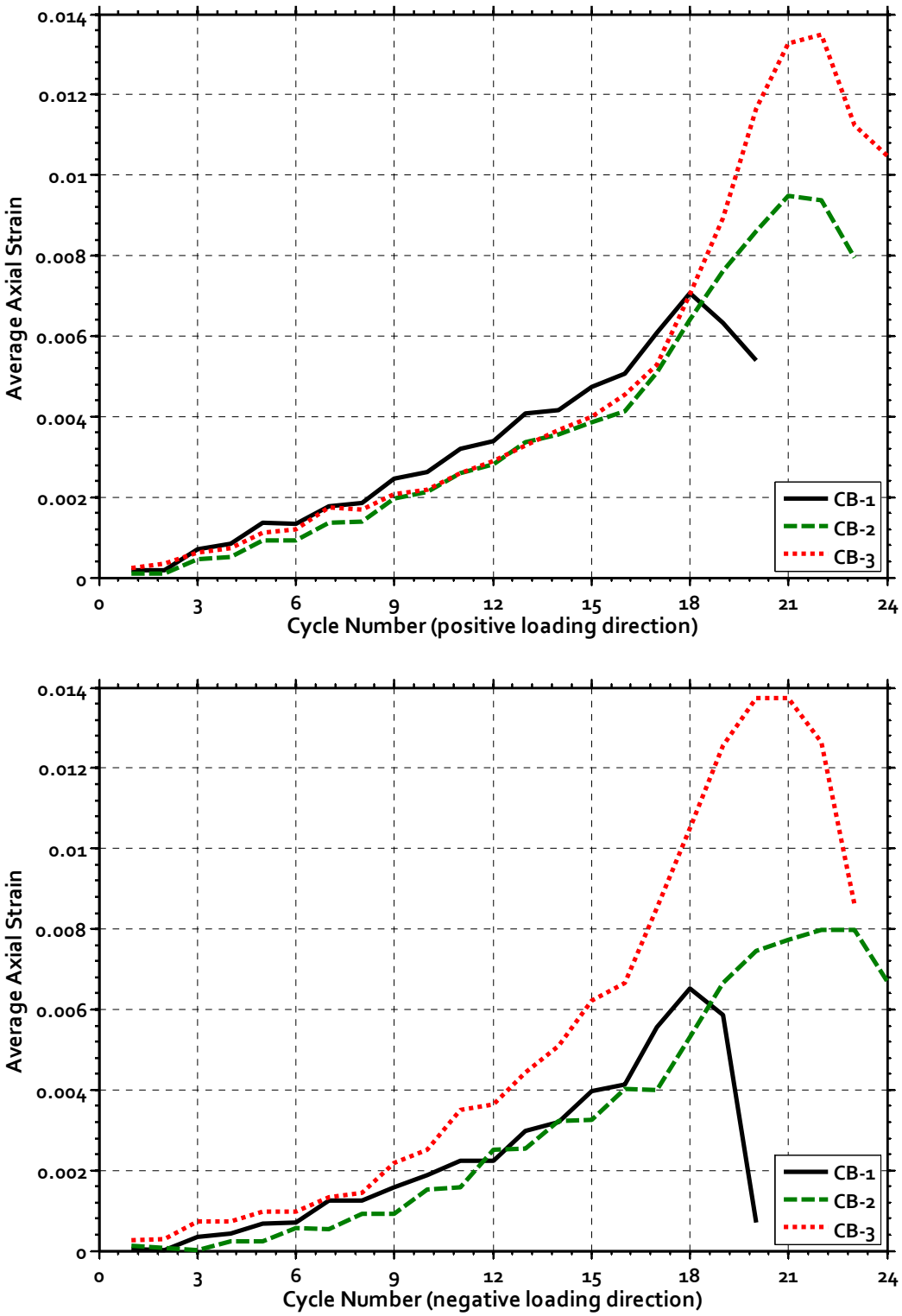

Figure 4.12 – Average axial strain of coupling beam specimens at the peak drift of each loading cycle plotted against the loading cycle number in the positive and negative loading directions

With additional data, a model could be developed to estimate the axial force expected to develop in a coupling beam. Such a model would include a measure of the maximum flexural deformations previously imposed on the beam, either in the form of maximum drift or maximum flexural rotations. The aspect ratio of the coupling beams, which impact the relative importance of flexural and shear deformations and the percentage of beam length affected by plastic deformations, would very likely have an impact on the elongation and should be considered as a variable in such a model. Finally, the tendency to elongate only results in an axial force when resisted by adjacent walls, so an estimation of the stiffness of the adjacent walls is required in such a model. Unfortunately, the given set of specimens was designed to investigate other parameters, so only one aspect ratio and test frame stiffness is represented by the given data set. This prevents a meaningful evaluation of these other important factors.

Until a more rational model for estimating coupling beam axial forces is developed, an approximate method for estimating this axial force is required for

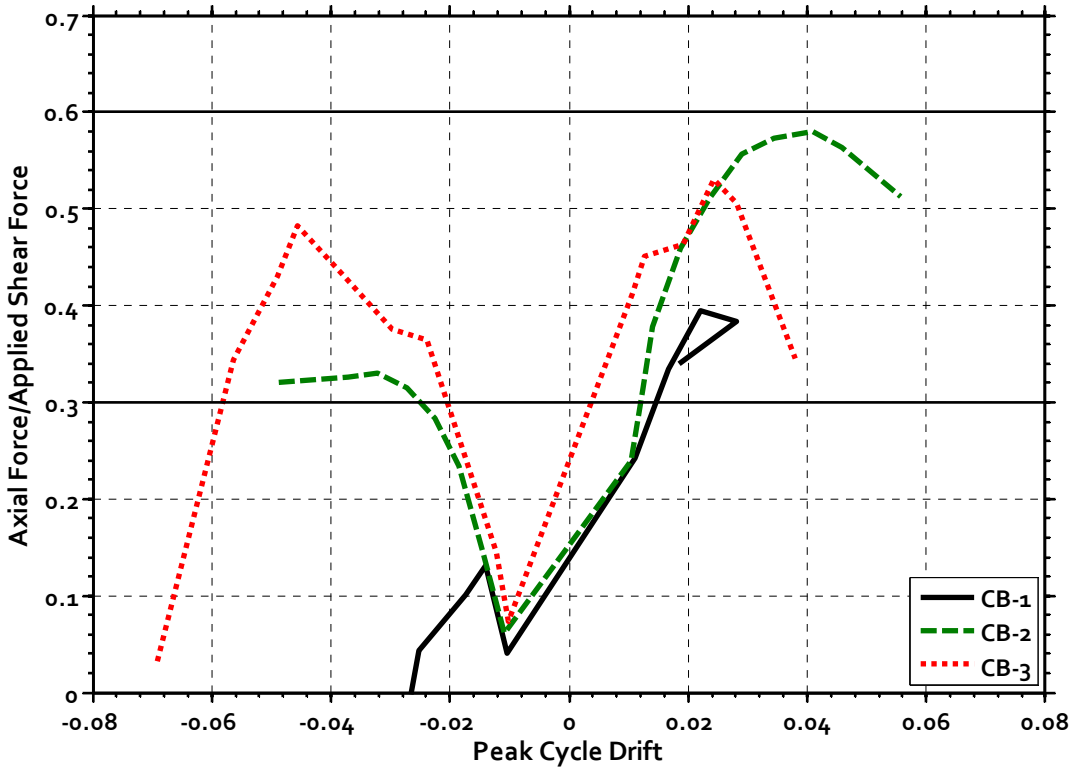

Figure 4.13 – Axial force in coupling beams normalized by the applied shear force

calculating an upper-bound flexural capacity of the coupling-beam. It is suggested that an axial force calculated as a fraction of the expected ultimate shear force can be used in design. The axial force developed in the tested coupling beams, normalized by the applied shear force, is plotted in Figure 4.13 versus the applied drift. The quotient of axial force developed and the applied shear force is roughly bounded by 30% and 60% at drifts greater than 2%. Despite significant variability, it is suggested that approximating the axial force in coupling beams as 40% of the expected shear force at the development of a flexural mechanism may be appropriate for calculating an upper-bound flexural capacity. Defining the axial force as a fraction of the shear capacity does imply the need for iterations; however, the solution converges relatively quickly.

4.1.5 Location of Inflection Point

It is reasonable to assume that coupling beams are subjected to very small gravity loads compared to the forces associated with seismically induced deformations. Therefore, distributed gravity-type loads are typically not applied in tests of coupling beams. Rather, a state of double curvature consistent with the deformations imposed by adjacent structural walls subjected to lateral deformations is imposed. Theoretically, the result is a constant shear force over the length of the coupling beam specimen, and equal but opposite moments at both ends with an inflection point located at midspan.

To evaluate the success of the test setup used for this series of tests at imposing the desired boundary conditions, it is useful to compare the actual location of the inflection point in each specimen with the theoretical inflection point location. To determine the location of the inflection point throughout the tests, the forces recorded by the actuator and the load cells mounted in each of the steel links were used to calculate the moment imposed at both ends of the coupling beam through equilibrium. By assuming that the moment varied linearly from one end to the other, the actual location of the inflection point could be determined using similar triangles. Figure 4.14 shows the location of the inflection point, measured from the face of the wall at the top end of the beam (in inches), plotted against the coupling beam drift. The actual inflection point location was within 6 in. (150 mm) of the theoretical inflection point (21 in., or 525 mm,

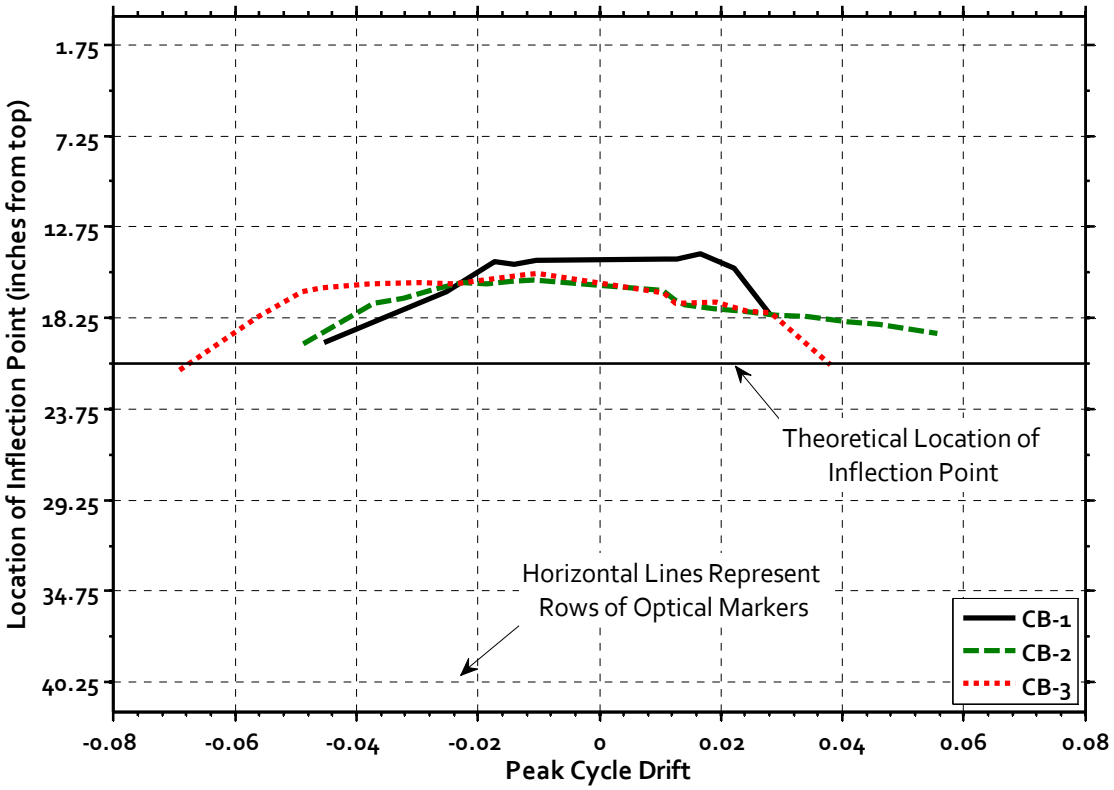

Figure 4.14 – Location of inflection point, calculated at the peak drift imposed in each loading cycle, measured from the face of the wall

from the face of the wall) throughout all three tests. As drifts increased and flexural rotations became dominant, the inflection point tended to drift nearer to midspan.

Some asymmetry in the development of damage can be expected (and was observed) as a result of this slight shift in inflection point location. However, the proximity of the actual and theoretical inflection point locations shows that the desired boundary conditions were generally imposed on the specimens – particularly as drift demands became more severe. Unfortunately, calculation of the inflection point location becomes increasingly unstable as the applied force approaches zero, so it will be assumed in subsequent discussions that the imposed inflection point was at midspan.

4.2 FLEXURAL BEHAVIOR OF HPFRC COUPLING BEAMS

4.2.1 FLEXURAL STRENGTH

For the design of each specimen, a moment-curvature analysis was performed at several points along the length of the coupling beam span, from the precast beam-to-wall interface to the inflection point at midspan. Multiple analyses were required because at each location along the span of the coupling beam the position of the diagonal reinforcement and the presence (or lack) of dowel reinforcement affected the magnitude of the expected yield and ultimate moment capacities. Figure 4.15 shows the result of this analysis for Specimen CB-2, which is typical of the analyses performed. The predicted cracking moment, yield moment, and ultimate moment capacity at several points along the span are shown. The abrupt decrease in flexural capacity at approximately 5 in. from the face of the wall is caused by the termination of the U-shaped dowel reinforcement. Material models presented in Section 3.3 were used for the moment-curvature analyses.

Due to the presence of a constant shear force along the beam span, the moment-demand distribution at any given deflection varied linearly along the span length from a maximum at the wall-face to zero at the inflection point. In theory, as displacements increase, the slope of the moment-demand line increases until it intersects the ultimate moment-capacity curve. Once the moment-demand line and the moment-capacity curves have intersected, the specimen has reached its full flexural capacity. As shown in Figure 4.15, Specimen CB-2 was designed such that the ultimate moment capacity curve and the moment demand line at ultimate intersect twice; once near the precast beam-to-wall interface and once at the cutoff point for the dowel bars. This was done to better distribute plastic rotations throughout the plastic hinge. However, it was anticipated, and experimentally verified, that the termination of the dowel reinforcement would create a modestly weaker plane that encourages damage to concentrate near the end of the dowel reinforcement rather than at the cold joint between the precast beam and wall when the ratio of moment demand to capacity is approximately equal at both locations. This phenomenon facilitated the relocation of the plastic hinge away from the interface and into the more damage tolerant HPFRC region. Testing proved that the intended relocation of the plastic hinge away from the interface was successful.

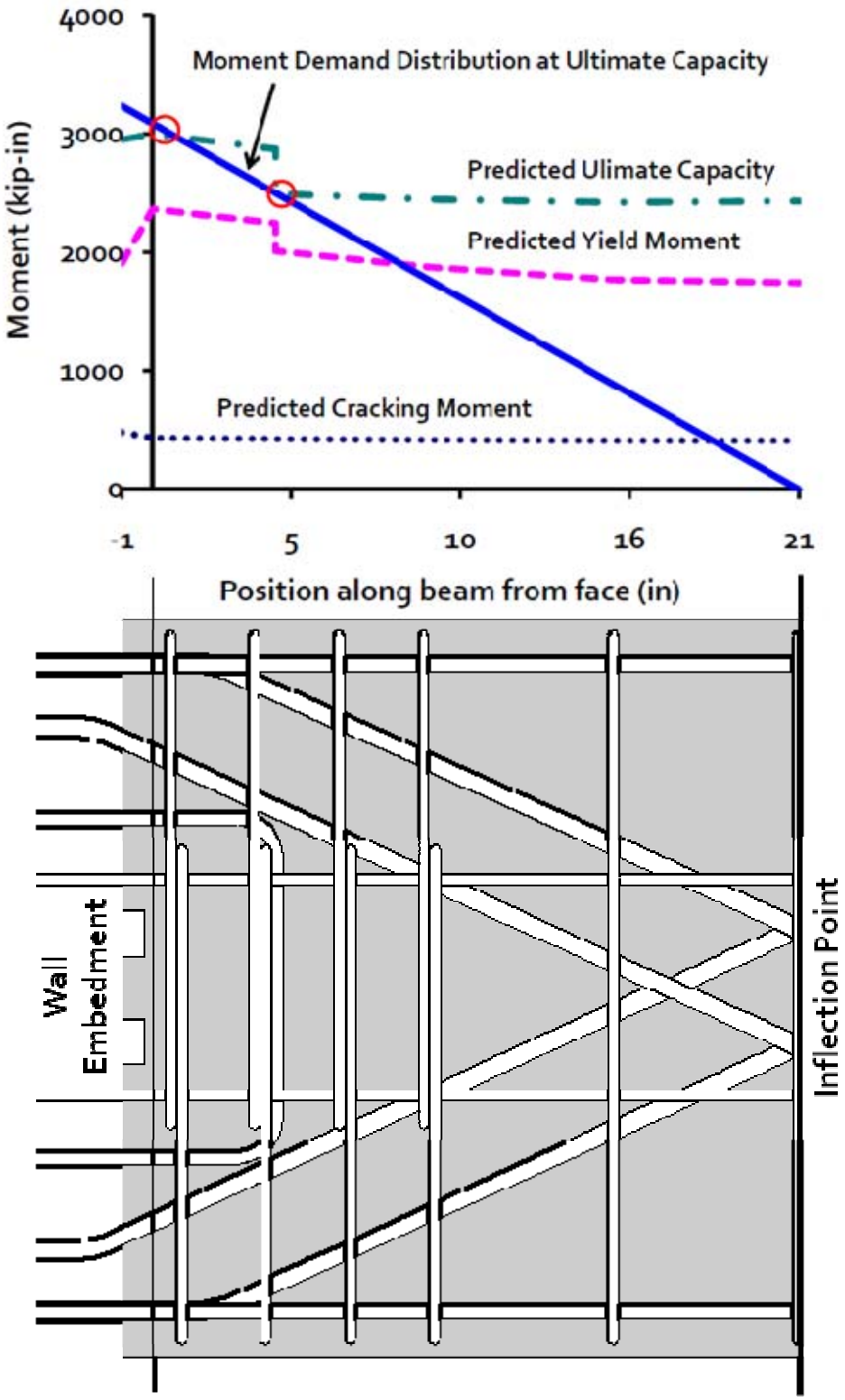

Figure 4.15 – Moment-curvature analysis used for design of specimens. Circled points indicate likely locations for ultimate failure planes to develop (example is for Specimen CB-2)

With the capacity of the coupling beam controlled by flexural hinging, accurately predicting the flexural capacity at the anticipated failure planes was critical. Although performing a moment-curvature analysis is a relatively straight-forward process, it could potentially become a cumbersome step in an iterative design procedure. The following sectional analysis appears to provide reasonably close agreement with observed capacities, and could be employed to simplify the design process by eliminating the need to perform moment-curvature analyses. Table 4.1 shows a comparison of the experimentally obtained ultimate shear demand (V_{exp}) and the probable shear (V_{pr}) corresponding to the ultimate flexural strength predicted by a sectional analysis at the point of dowel bar termination. For this sectional analysis, an axial force equal to 40% of V_{pr} was assumed to act on the section, which is consistent with the magnitude of axial force observed experimentally. When an effective yield stress of $\alpha \cdot f_y$ was assumed, where $\alpha = 1.25$, V_{exp} and V_{pr} did not differ by more than 6%. It is therefore proposed that a sectional analysis with an axial force of $0.4 \cdot V_{pr}$ acting on the coupling beam and an effective yield stress of $1.25 \cdot f_y$ for the longitudinal and diagonal reinforcement be used for calculating an upper-bound coupling-beam capacity.

A similar sectional analysis can be used to approximate a lower bound coupling beam capacity. For calculation of the lower bound capacity, no axial force and an effective yield stress of $\alpha \cdot f_y$, where $\alpha = 1.0$, were assumed. These assumptions resulted

Table 4.1 – Upper-bound capacity predicted by sectional flexural analyses performed at the dowel cutoff point with $P = 0.4 \cdot V_{pr}$

Specimen #	$V_{exp,\,max}$		Assumed f_y		P = 60k (approx. 40% of V_{pr} *)				
					M_{pr}		V_{pr} *		$V_{exp,max}/V_{pr}$
	kip	kN	ksi	MPa	kip-in	kN-m	kip	kN	
CB-1	148	660	60	415	2300	260	135	600	1.10
			75	515	2640	300	155	690	0.96
CB-2	147	655	60	415	2060	230	120	540	1.22
			75	515	2350	265	140	615	1.06
CB-3	146	650	60	415	2080	235	120	545	1.19
			75	515	2370	265	140	620	1.05

* $V_{pr} = 2M_{pr}/\ell$, where ℓ is the clear span length between dowel cutoff points

Table 4.2 – Lower-bound capacity predicted by sectional flexural analyses performed at the dowel cutoff point, with $P = 0kip$

Specimen #	$V_{exp,max}$		Assumed f_y		P = 0kip				
					M_{pr}		V_{pr} *		$V_{exp,max}$ / V_{pr}
	kip	kN	ksi	MPa	kip-in	kN-m	kip	kN	
CB-1	148	660	60	415	1790	200	105	465	1.41
			75	515	2170	245	130	570	1.16
CB-2	147	655	60	415	1520	170	90	400	1.64
			75	515	1860	210	110	485	1.35
CB-3	146	650	60	415	1660	190	100	435	1.49
			75	515	1980	225	115	515	1.25

* $V_{pr} = 2M_{pr}/\ell$, where ℓ is the clear span length between dowel cutoff points

in under-prediction of the ultimate capacity of the specimens, but could be useful to the designer as a conservative estimate of coupling beam capacity. The V_{pr} predicted by this analysis was reached at a drift of approximately 0.75%, and sustained in both loading directions until termination of the test. Table 4.2 shows the predicted lower-bound coupling-beam capacity compared to the experimentally obtained ultimate capacity. A designer may employ this lower-bound capacity to conservatively calculate the overturning-moment capacity of the coupled-wall system and to estimate structural drifts. Figure 4.16 shows the shear force versus drift response of all three specimens, along with the lower- and upper-bound capacities predicted by this sectional analysis approach.

4.2.2 ROTATIONS

The grid of optical markers fixed to the face of the specimens allowed an analysis of the distribution of flexural deformations over their length. To perform this analysis, the rotation of a row of markers throughout the test was subtracted from the rotation of an adjacent row of markers to obtain the rotation for the given "strip" of the beam specimen. The average curvature in that strip was calculated by dividing this differential rotation by the distance between the rows of markers. A special calculation, however, was required for the strips that encompassed the beam-to-wall interface. For these strips, an effective curvature was calculated by dividing the rotation of the strip by the distance between the

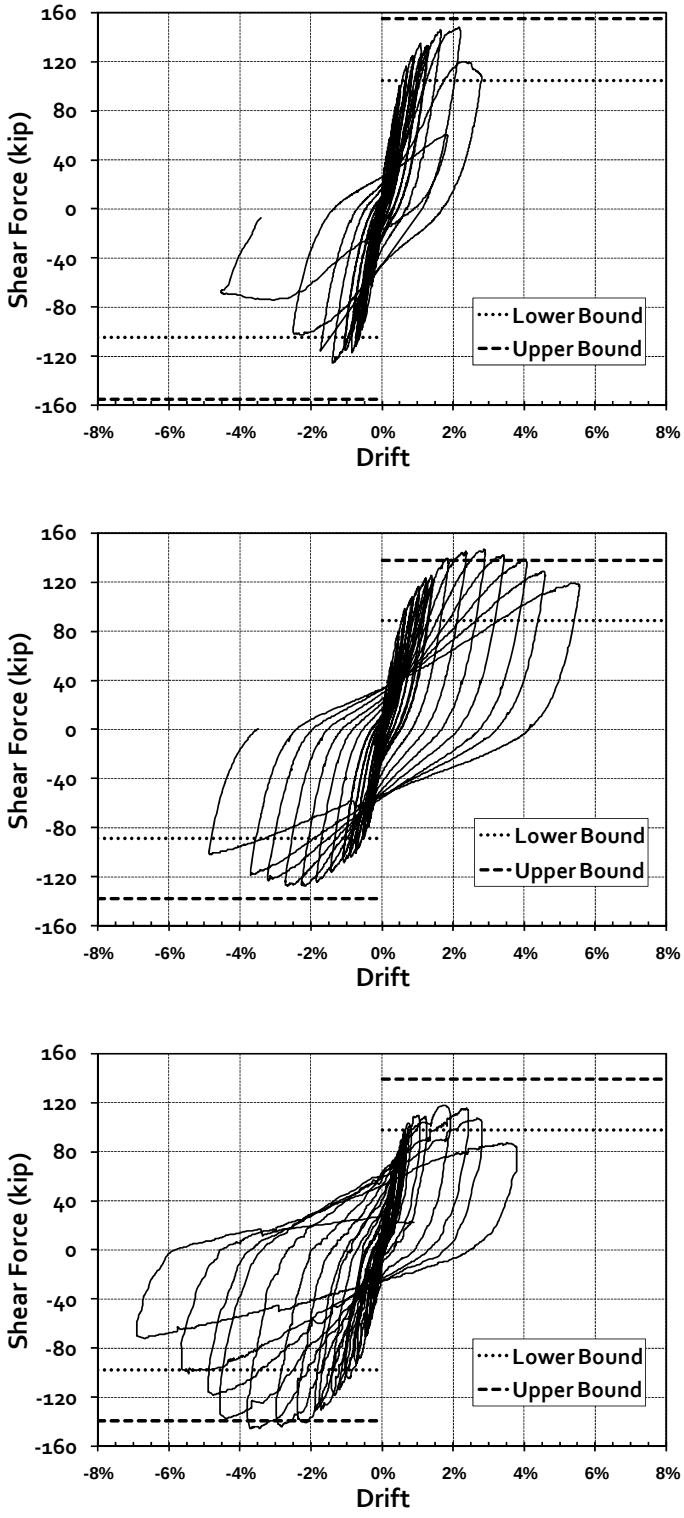

Figure 4.16 – Shear force versus drift response for Specimens CB-1, CB-2 and CB-3, with capacity bounds predicted by simplified sectional analysis

last row of markers on the beam and the face of the wall itself. This effective curvature included the effect of crack opening at the wall face.

Figure 4.17 shows the location of each of the nine strips for which this analysis was performed. In this section the experimentally observed moment-curvature relationships for each strip (consisting of the set of moment-curvature coordinates taken at the peak drift of each loading cycle) are plotted with a set of analytically derived curves representing expected moment-curvature relationships for axial forces ranging between $0 - 60$ kip (approximately $0 - 40\%$ of V_{exp}). The analytically derived moment-curvature relationships are linked by equal compressive strain curves identifying where each analytical curve reaches compressive strains in the extreme compression fiber of 0.003, 0.005, 0.007, 0.009 and 0.011.

The middle strips, numbered 4, 5 and 6 in Figure 4.17, covered the portion of the span nearest the inflection point. An example of an experimentally determined moment-curvature relationship for strip 4 of Specimen CB-2, which is typical of the behavior of the other middle strips, is shown in Figure 4.18. The middle strips were subjected to low levels of moment that were well below the flexural capacity of the coupling beam near midspan. Although no inelastic flexural deformations would be expected with such low moment demands, some non-linearity was observed at large drifts as yielding of the flexural reinforcement in adjacent strips extended into the middle portion of the beam.

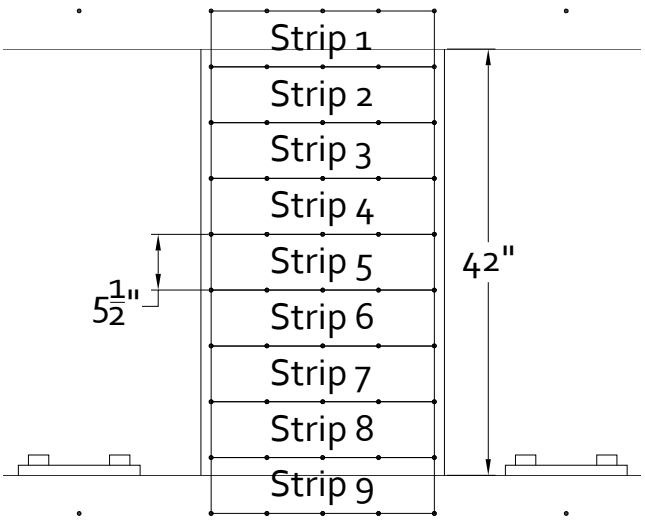

Figure 4.17 – Beam "strips" defined by adjacent rows of markers

The remaining strips, near the ends of the coupling beam, were subjected to much larger moment demands. Figure 4.19 shows the experimentally determined moment-curvature relationship for strip 2 of Specimen CB-2, which is typical of the behavior of strips 2 and 8 in all three specimens. Considering the high shear stresses imposed on the specimens and the repeated load reversals, remarkably close agreement can be seen between the experimentally obtained moment-curvature relationships and the theoretically derived curves. In particular, both the analytical cracked stiffness and first yield point are in close agreement with the experimental curves. This is also true of the behavior of strips 3 and 7, which generally remained within the cracked-elastic range throughout the test. The experimentally obtained moment-curvature relationship shown in Figure 4.19 also shows curvatures associated with compression strains significantly greater than 0.003. Curvatures associated with compression strains on the order of 0.007-0.009 were observed in strip 2, the first strip away from the wall face.

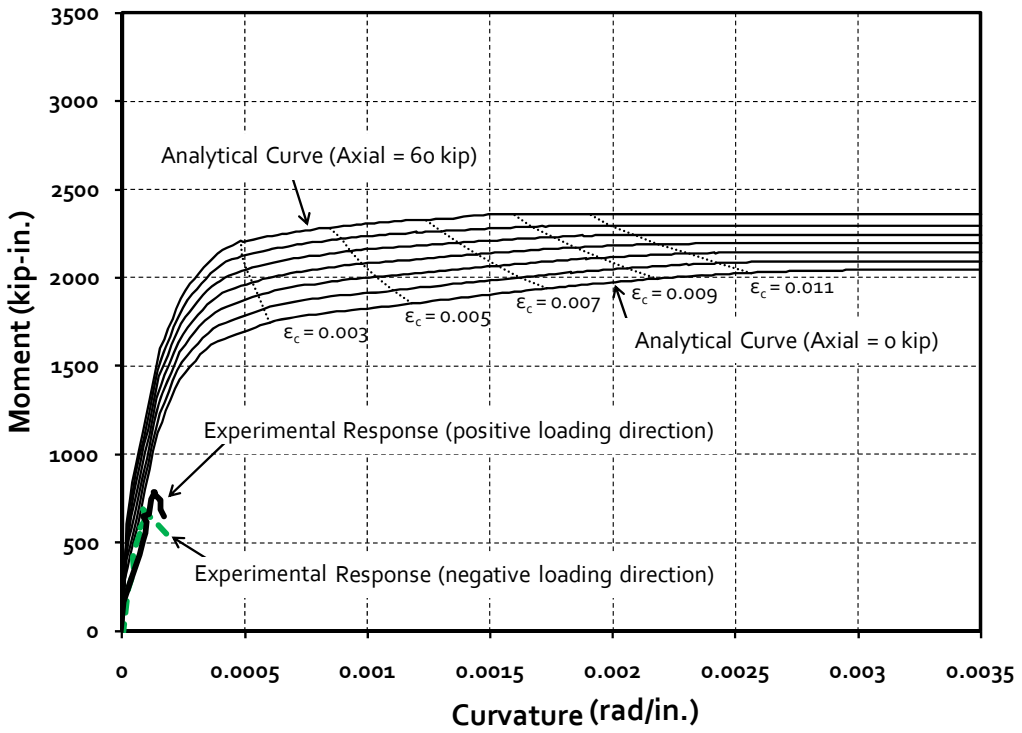

Figure 4.18 – Moment-curvature relationship for strip 4 of Specimen CB-2 (typical of middle strips)

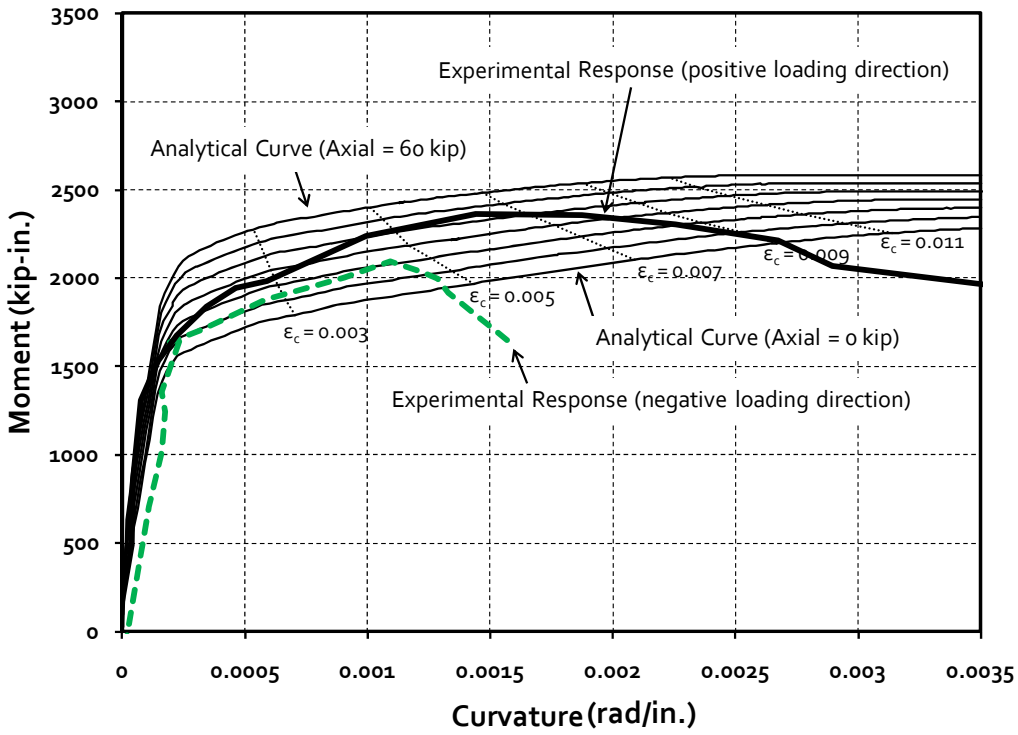

Figure 4.19 – Moment-curvature relationships for strip 2 of Specimen CB-2 (typical of end strips)

Figure 4.20 shows the experimentally obtained moment-curvature relationship for strip 9 of Specimen CB-2, which is typical of the behavior of the strips incorporating the precast beam-to-wall interface. For these strips that capture the rotation at the beam-to-wall interface, the experimentally obtained moment-curvature relationship deviates significantly from the predicted relationships. This deviation is most pronounced when comparing the initial stiffness of the curves. The experimentally obtained relationship is significantly less stiff than predicted by moment-curvature analyses, which is due to the fact that the cold-joint was "pre-cracked" as well as elongation and slip of the flexural and diagonal reinforcement over the development length of those bars into the wall.

A number of models have been proposed to account for the flexibility at a connection due to elongation of reinforcement over the development length (Rehm and Eligehausen, 1979; Alsiwat and Saatcioglu, 1992; Harajli, 2009). These models do a reasonably good job estimating rotations, but are rather complicated for implementation into a building system analysis. For the specimens tested, very good agreement was observed between the initial slope of the analytical and experimentally observed moment-

curvature relationships at the connection when a relatively simple adjustment was made to the effective length of the interfacial strip. If the effective length of the first strip is assumed to extend a distance of 8 times the diameter of the largest coupling beam reinforcing bar beyond the precast section into the wall, the predicted stiffness at the face of the wall closely agrees with test results. This adjustment successfully accounted for the softening at the interface due to the penetration of bar strains into the connection. Figure 4.21 shows the same predicted moment-curvature relationships as shown in Figure 4.20, but the experimentally obtained curvatures were calculated from the measured rotations at the interface with the modified strip thickness. Thus, assuming the coupling beam extends into the wall a distance equal to the precast embedment length $+ 8 * d_{b,largest\ bar}$ provided a good approximation of the observed trends.

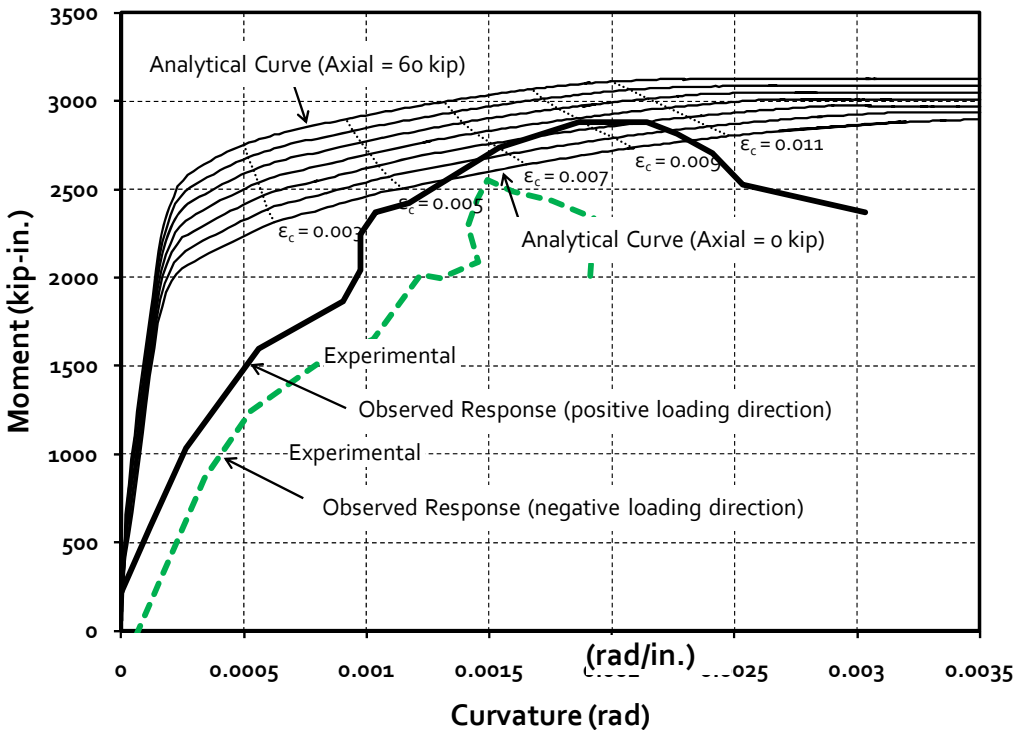

Figure 4.20 – Moment-"apparent curvature" relationships for strip 9 of Specimen CB-2 (typical of strips 1 and 9)

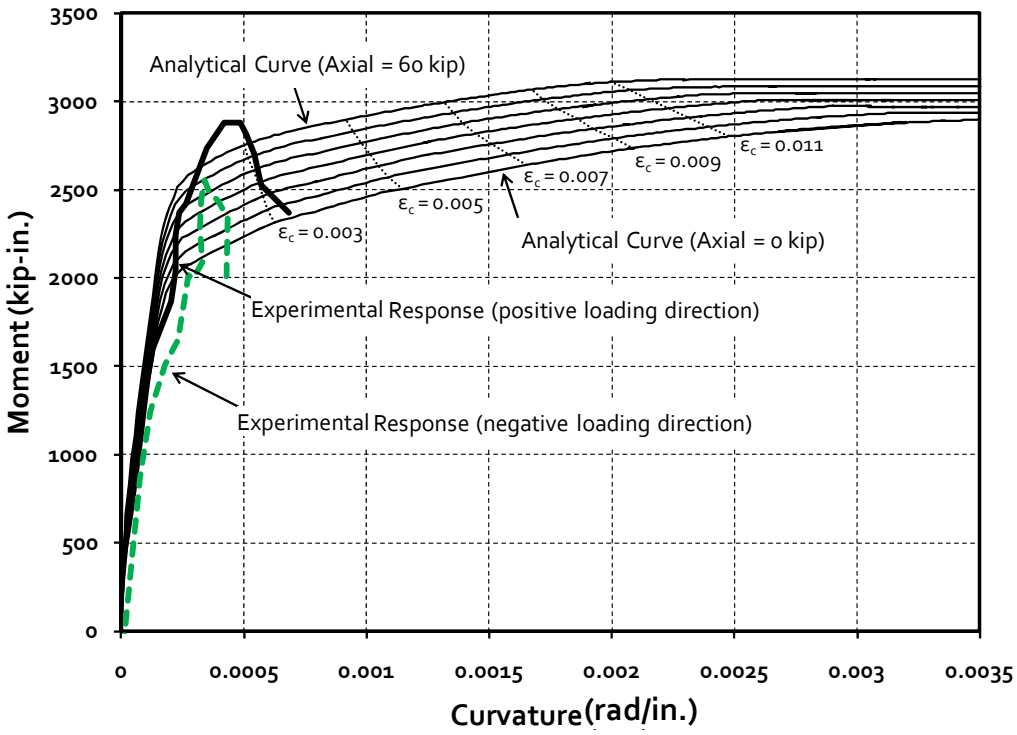

Figure 4.21 – Moment-curvature relationships for strip 9 of Specimen CB-2 adjusted for effective strip thickness (typical of strips 1 and 9)

4.2.3 Longitudinal Strain Distribution

The validity of the discussion of flexural rotations and curvatures for given strips is largely dependent on the assumption that general beam theory reasonably approximates the behavior at the ends of the coupling beam specimens. In beam theory, plane sections are assumed to remain plane as the specimen is loaded in bending. This assumption is generally valid for slender frame members, but questionable for short coupling beams where shear deformations are important. If plane sections remained plane throughout the test, then within a given beam strip (as defined in Figure 4.17), the longitudinal strain in each adjacent square should vary linearly across the depth of the coupling beam section. This was the case in all three coupling beams prior to yielding of the flexural reinforcement. Figure 4.22 shows the distribution of longitudinal strains in all three coupling beam specimens at the end of the loading cycle to 0.5% drift, which is the cycle when flexural yielding initiated. The number on either side of each strip is the strain in the outermost square, where tensile strains are positive.

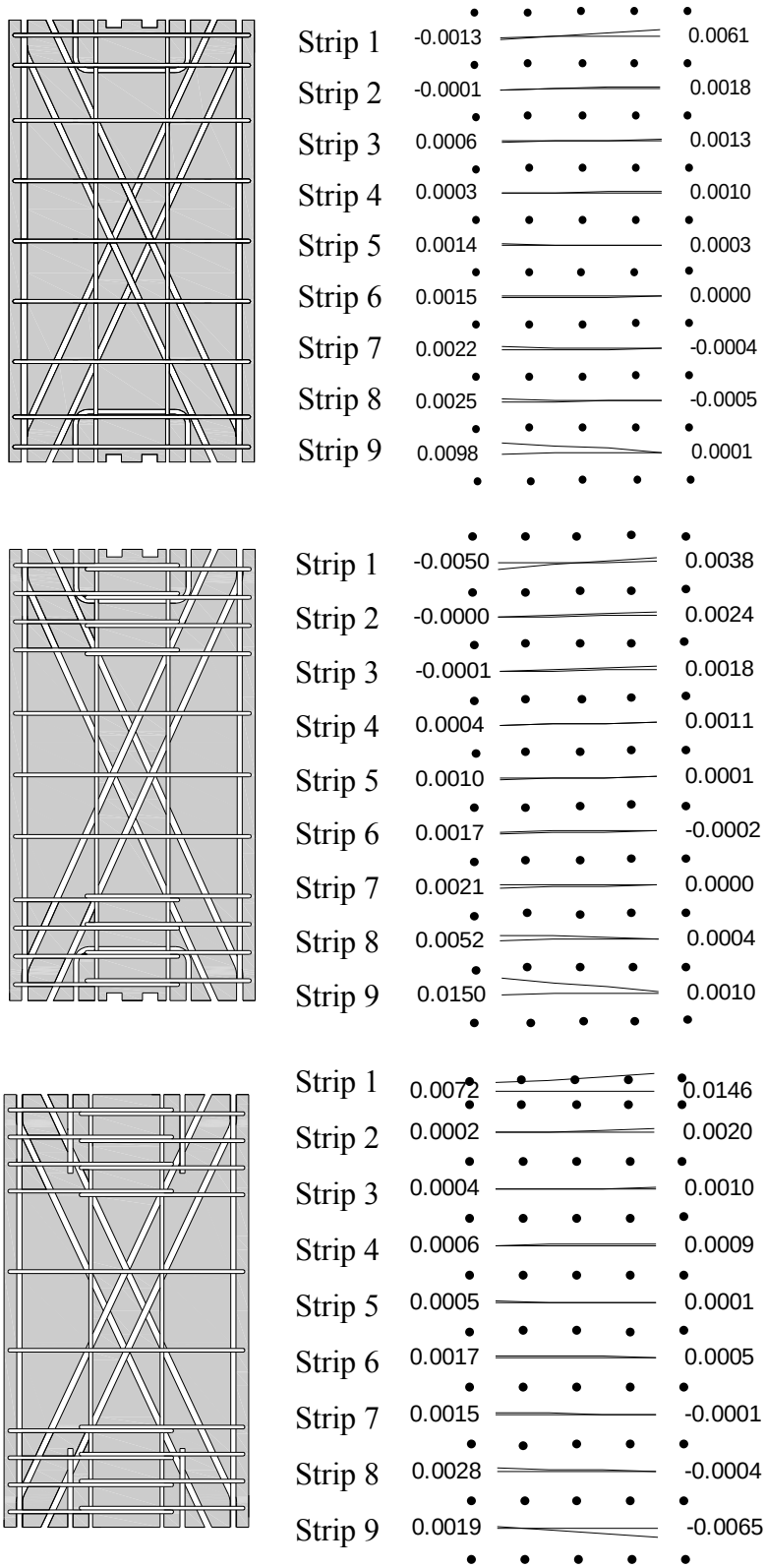

Figure 4.22 – Longitudinal strain distribution at 0.5% drift in Specimens CB-1, CB-2 and CB-3 (top to bottom, respectively), at initiation of flexural yielding. Tension is positive.

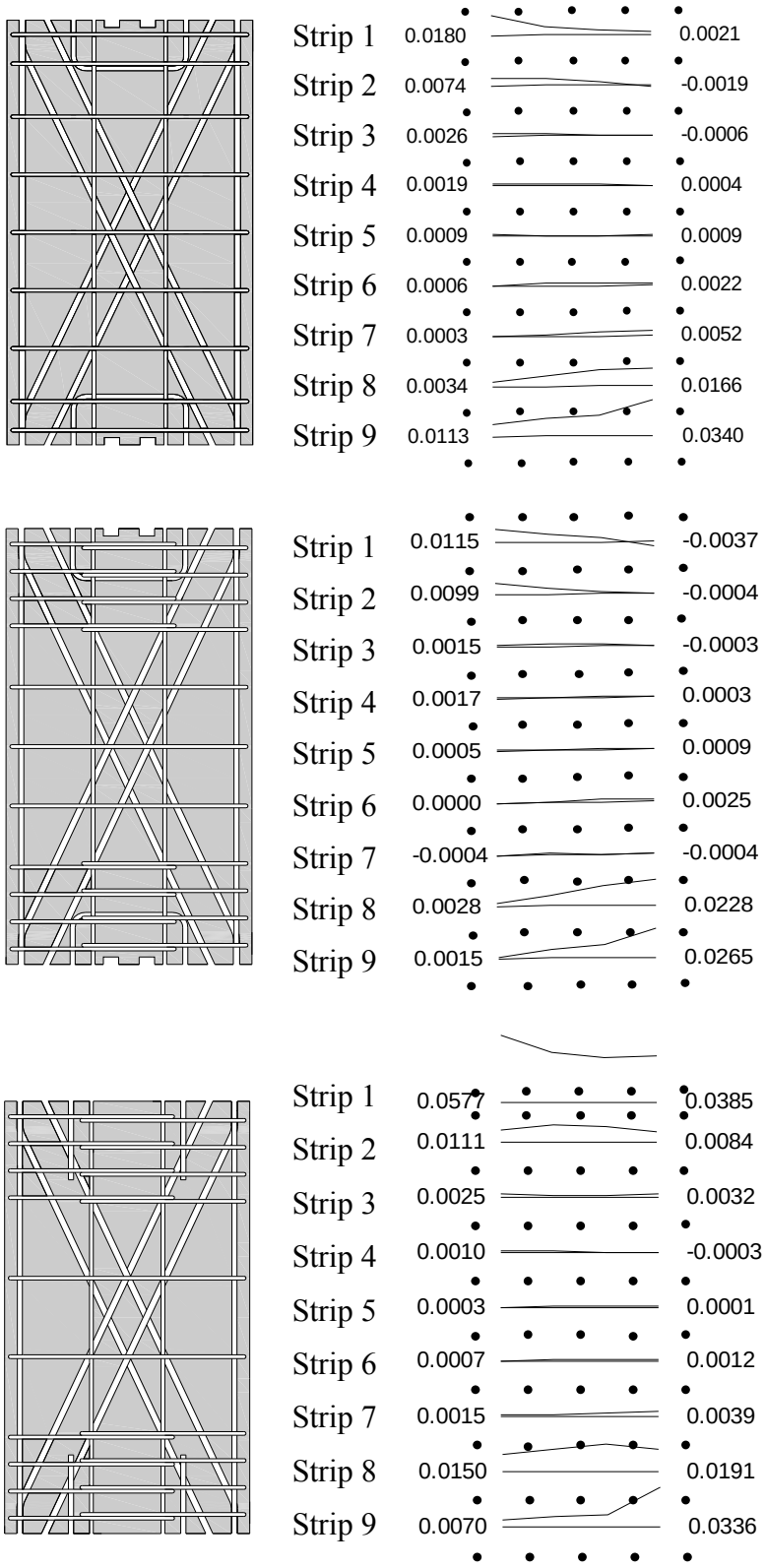

Figure 4.23 – Longitudinal strain distribution at 1.5% drift in Specimens CB-1, CB-2 and CB-3 (top to bottom, respectively). Tension is positive.

Figure 4.23 shows the same longitudinal strain distribution, but at the end of the loading cycle to a drift of 1.5%. At this drift, the distributions of longitudinal strains across the depth of the member were only approximately linear, indicating that plane sections did not remain plane. However, the non-linearity was primarily confined to the region near the termination of the dowel reinforcement. Otherwise, longitudinal strains generally varied linearly along the depth of the coupling beam. This supports the use of conventional moment-curvature analysis for the design of coupling beams with aspect ratios as low as 1.75.

At a drift of 1.5%, the largest observed compression strain was approximately 0.002, which occurred in strip 2 of Specimen CB-1. Otherwise, the longitudinal strains shown in Figure 4.23 are almost all tension (positive) strains, even though large curvatures and a compression force were imposed on the specimen. This elongation of the beam was what led to the axial forces discussed in Section 4.1.4. As shown in Figure 4.23, the tensile strains were significantly larger in the strips near the ends of the beam, where flexural rotations were at their maximum values.

The impact each connection detail, consisting of either U-shaped or straight dowel bars, had on the distribution of rotations near the ends of the beams is also shown in Figure 4.23. All of these dowel bars provided clamping action at the interface that forced elongations of similar magnitude to develop in the first and second strips of the beams. Within strips 1 and 9, the distribution of longitudinal strains tended to be smaller in the middle squares, where the dowels were more effective, than at the edges of the beam. Although less pronounced, the reverse was generally true within strips 2 and 8, where longitudinal strains tended to be relatively large in the middle squares compared to the squares along the edges of the beam.

4.2.4 Plastic Hinge Length

A different way to visualize the distribution of curvatures over the length of the coupling beam is shown in Figure 4.24. The figure shows the distribution of curvatures in each specimen, per strip, at select drift levels in both loading directions. General trends are that larger curvatures developed nearer the ends of the beam and that larger curvatures were associated with larger drifts, as expected. Apparent inconsistencies, such

as curvatures opposite in sign to moment demands within the same strip, are the result of load reversals where significant plastic deformation in one loading direction caused large curvatures that did not fully reverse when the specimen drift reversed.

Along with the observed curvature in each strip, the theoretical yield curvature is also plotted in Figure 4.24. Strip 5, which incorporates the theoretical inflection point of the coupling beam, showed average curvatures below the yield curvature in all cases. Strips 4 and 6, referred to previously as "middle strips," were also near the inflection point. The average curvatures calculated for these strips did, in some cases, surpass the theoretical yield curvature when the specimen was subjected to very large displacement demands. However, the flexural response in these strips was largely within the cracked-elastic range throughout the test. Strips 2, 3, 7 and 8 were all subjected to average curvature ductility demands greater than or equal to 2. Strips 1 and 9, which included the precast interface, exhibited significantly larger apparent curvatures; however, these curvatures are not included in Figure 4.24 because of the distorting effect slip and extension over the development length of the flexural reinforcement had on the curvatures calculated in these strips. Therefore, plastic flexural deformations were largely concentrated within the three beam strips nearest the connection. The boundary between strips 3 and 4 was located 12.75 in. (320 mm) from the face of the wall. It is therefore proposed that the plastic hinge length can be approximated as $h/2$ for coupling beams with $\ell_n/h \approx 1.75$, where $h/2 = 12\ in.\ (300\ mm)$ for the specimens tested. In order to account for the effect of concentrated rotations at the wall face, however, Eq. 4.2 is proposed for calculating total plastic hinge length. It is the sum of the plastic hinge length within the beam and the length of plastic deformation penetration into the wall, proposed in Section 4.2.2.

$$PH_{length} = \frac{h}{2} + emdement\ length + 8 * d_{b,largest\ bar} \tag{4.2}$$

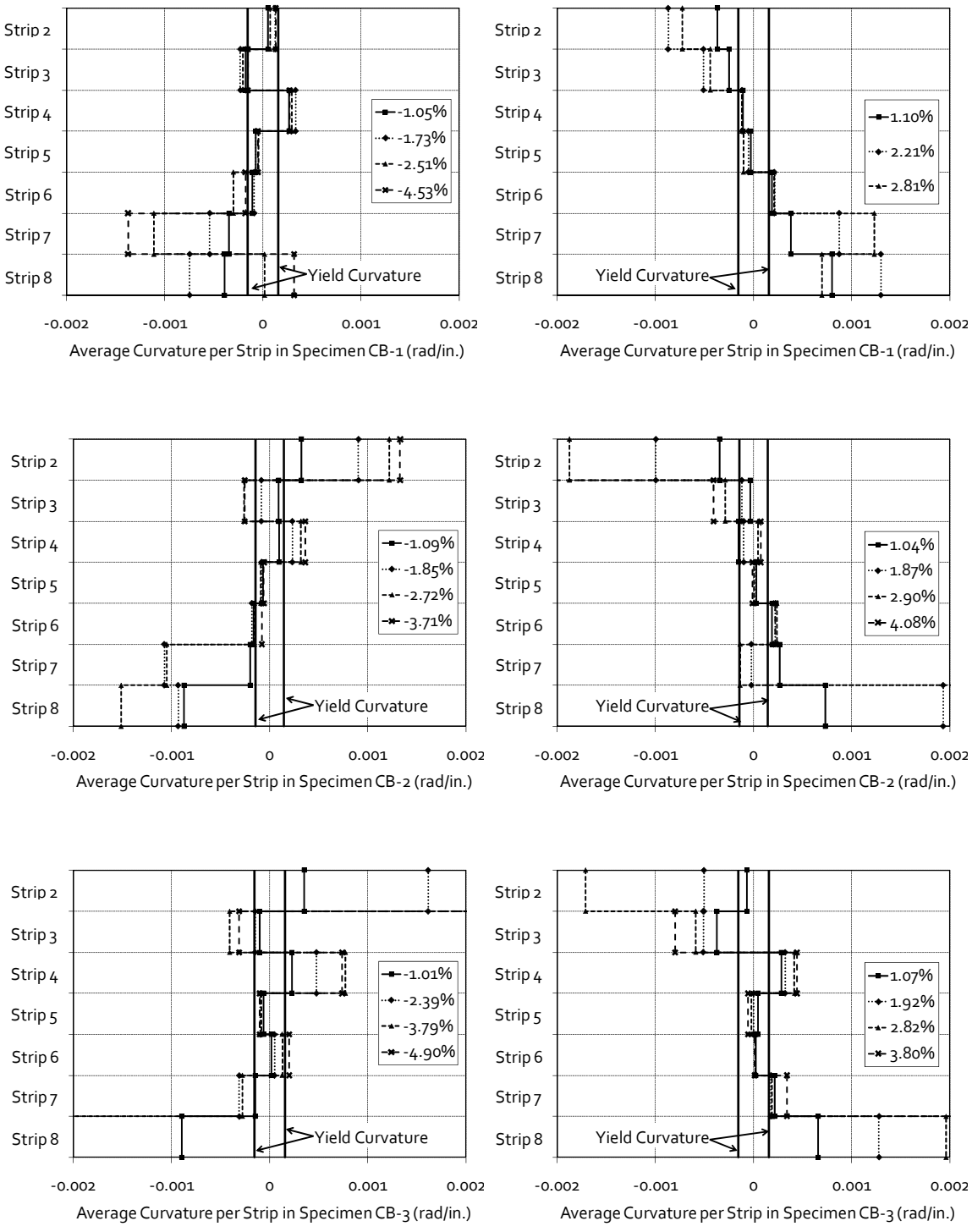

Figure 4.24 – Curvature distribution for strips 2-8 of all three coupling beam specimens in the negative and positive loading direction (left and right plot, respectively)

4.3 SHEAR BEHAVIOR OF HPFRC COUPLING BEAMS

4.3.1 SHEAR STRENGTH

The maximum shear force in all three coupling beams was controlled by the flexural strength of the plastic hinges that formed near each end of the specimens. However, to develop the full flexural capacity of these plastic hinges, significant shear stresses had to be sustained by each specimen throughout the test. Diagonally oriented steel reinforcement, transverse stirrups, and HPFRC were all active in resisting these shear stress demands.

For the purposes of the following discussion, the stresses developed in the transverse and diagonal reinforcement were approximated from strains recorded by gauges placed near mid-span using the algorithm presented in Section 3.3.3.2. Assuming diagonal cracking in the web of the coupling beam develops at an inclination of 45 degrees, which is consistent with observed crack patterns, the total shear force resisted by the transverse reinforcement was approximated. The total contribution from reinforcement, V_s, can be calculated by Eq. 4.3. The remaining shear force applied to the specimen is assumed to be resisted by shear mechanisms relying on the HPFRC.

$$V_s = V_{stirrups} + V_{diagonal\ steel} \tag{4.3}$$

The HPFRC contributes to resisting applied shear forces in three important ways: 1) buckling is prevented in the diagonal reinforcement, allowing for both the tension and compression diagonal steel to resist shear, 2) damage in the beam due to shear is limited to multiple narrow cracks, resulting in a section whose integrity is maintained, which results in a more active stirrup participation, development of direct strut action from one wall face to the other, and enhanced aggregate interlock, and, 3) fibers bridging cracks contribute directly to tensile stress transfer across cracks. Although a study of the interaction of these mechanisms is of interest, reliably isolating the relative importance of each mechanism is beyond the scope of this study. Herein, the contribution of the HPFRC to shear resistance was lumped into a V_{HPFRC} term, where $V_{HPFRC} = V_{measured} - V_s$.

4.3.1.1 Shear Stress at Onset of Cracking

In very early drift cycles, before the onset of diagonal cracking, the stirrups and diagonal steel exhibited a negligible amount of strain, as expected. At this early stage of testing, v_{HPFRC} was $2.1\sqrt{f_c'}, [psi]\left(0.17\sqrt{f_c'}, [MPa]\right)$, $2.2\sqrt{f_c'}, [psi]\left(0.18\sqrt{f_c'}, [MPa]\right)$ and $2.6\sqrt{f_c'}, [psi]$ $(0.22\sqrt{f_c'}, [MPa])$ for Specimens CB-1, CB-2 and CB-3, respectively. As drifts approached 0.5%, diagonal steel and stirrups became active, indicating that narrow diagonal cracks had begun to develop within the web of the coupling beams. By the time diagonal cracking was visually observed, which occurred at approximately 0.75% drift in all three tests, the calculated contribution of the HPFRC to shear resistance, v_{HPFRC}, exceeded $3.5\sqrt{f_c'}, [psi](0.29\sqrt{f_c'}, [MPa])$ in all specimens.

4.3.1.2 Relative Contribution of Shear Resistance Mechanisms at Peak Force

Table 4.3 shows the values of V_{HPFRC}, $V_{diagonal\ steel}$ and $V_{stirrups}$ for each of the three coupling beam specimens at the peak applied shear force in each loading direction. These values provide a reasonably good estimate of the relative contribution of each mechanism, but this estimate has its limitations. First, the contribution from both the diagonal steel and stirrups is based on the approximate model presented in Section 3.3.3.2 for relating recorded strains to stresses. It is emphasized that this is an approximate

Table 4.3 – Contributions to shear resistance at peak shear force, normalized by $\sqrt{f_c'}$

CB #	Source of Resistance	Positive Drift			Negative Drift		
		$\sqrt{f_c'}A_{cw}$, (psi)	$\sqrt{f_c'}A_{cw}$, (MPa)	% of total shear	$\sqrt{f_c'}A_{cw}$, (psi)	$\sqrt{f_c'}A_{cw}$, (MPa)	% of total shear
1	V_{HPFRC}	4.9	0.41	40%	4.9	0.41	46%
	$V_{diagonal\ steel}$	2.4	0.20	19%	2.3	0.19	21%
	$V_{stirrups}$	5.1	0.42	41%	3.5	0.29	33%
2	V_{HPFRC}	5.7	0.47	50%	4.9	0.41	48%
	$V_{diagonal\ steel}$	2.4	0.20	21%	2.4	0.20	24%
	$V_{stirrups}$	3.4	0.28	29%	2.8	0.23	28%
3	V_{HPFRC}	5.5	0.46	51%	6.7	0.56	50%
	$V_{diagonal\ steel}$	2.8	0.23	26%	3.0	0.25	23%
	$V_{stirrups}$	2.5	0.21	23%	3.6	0.30	27%

model, and that the resulting stress values are estimates. Also, dowel action provided by longitudinal reinforcement is not included in this estimate. Furthermore, the strains measured in the stirrups used to estimate the stirrup stresses are not only caused by shear, but also by the confinement that the stirrups are providing to the whole coupling beam section. Therefore, the contribution from the stirrups to shear through a truss mechanism is overestimated in Table 4.3, resulting in an underestimation of the shear stress resisted by the HPFRC. Finally, because shear failures were prevented in all three specimens, it is not possible to measure the peak shear capacity of the HPFRC through these tests. For these reasons, it is proposed that $5\sqrt{f_c'}, [psi]\left(0.41\sqrt{f_c'}, [MPa]\right)$ be used in design as a conservative approximation of the shear stress capacity of HPFRC in coupling beams with aspect ratios near 1.75.

4.3.2 Shear Stress/Shear Distortion Relationship

The grid of markers placed on the surface of the coupling beams allowed for an analysis of the distribution of shear deformations over the surface of the specimens. To perform this analysis, the model described below was adopted from Athanasopoulou (2010), who attributed it to Oesterle et al. (1976).

Figure 4.25 shows a typical arrangement of four optical markers fixed to the surface of the specimen. Given the initial location of the markers, $(x1, y1)_o, \dots, (x4, y4)_o$, the outside dimensions of the quadrilateral are determined. $L1$ and $L2$ are averaged to determine the mean length, L, of the polygon, and $H1$ and $H2$ determine H, the mean height of the polygon. The initial lengths of the diagonals, A_o and B_o, are calculated, as well as the lengths of each diagonal, A and B, throughout the loading regimen. With these quantities, Eq. 4.4 is used to calculate the average shear distortion exhibited by a given quadrant of the specimen.

$$\gamma = \frac{-(A - A_o)A_o + (B - B_o)B_o}{2HL} \tag{4.4}$$

Using this equation, the shear distortion was calculated for each of the 36 quadrants in the marker grid, and then averaged to obtain the mean shear distortion per

strip for each of the nine strips shown in Figure 4.17. Unfortunately, this approach does not directly differentiate true shear distortion from sliding shear deformations along flexural cracks, which occurred during the larger drift cycles, as discussed in Section 4.3.2.1.

Figure 4.26 shows the envelope of the shear stress versus average shear distortion curve for strip 4 of Specimen CB-2, plotted with the shear distortion envelope curves for each of the squares within the same strip. The result shown is generally typical of strips where no sliding was observed across flexural crack faces. A few notable observations can be made from this plot. First, there is a change in slope near a shear stress of 200 – 300 psi (1.4 – 2.1 MPa), corresponding to a normalized shear stress of $2.3 - 3.5\sqrt{f_c'}, [psi]\left(0.19 - 0.29\sqrt{f_c'}, [MPa]\right)$, which signals the initiation of diagonal cracking. Diagonal cracking was not visibly noted during testing until larger shear stresses had been imposed, indicating that the HPFRC, stirrups and diagonal reinforcement were effective in resisting the opening and propagation of diagonal cracking.

It is also observed that within any given strip, the squares at mid-depth of the coupling beam showed higher shear strains than the squares at the edges of the beam.

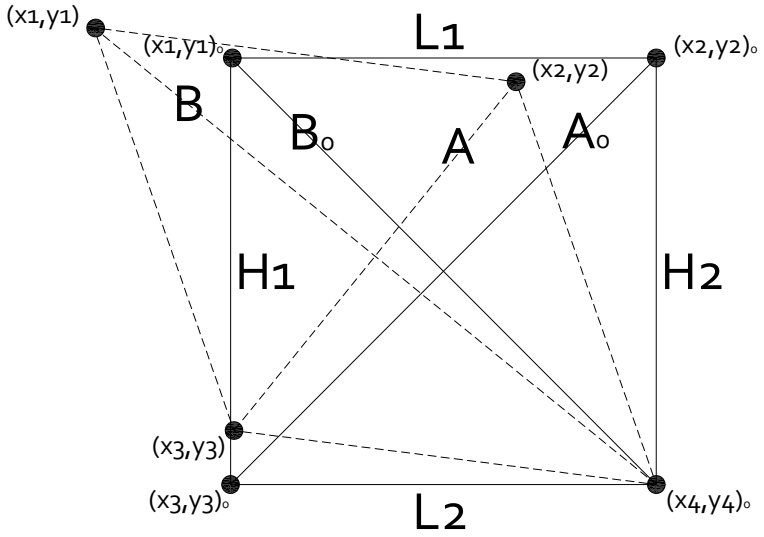

Figure 4.25 – Typical region of the marker grid with quantities for determining shear distortion

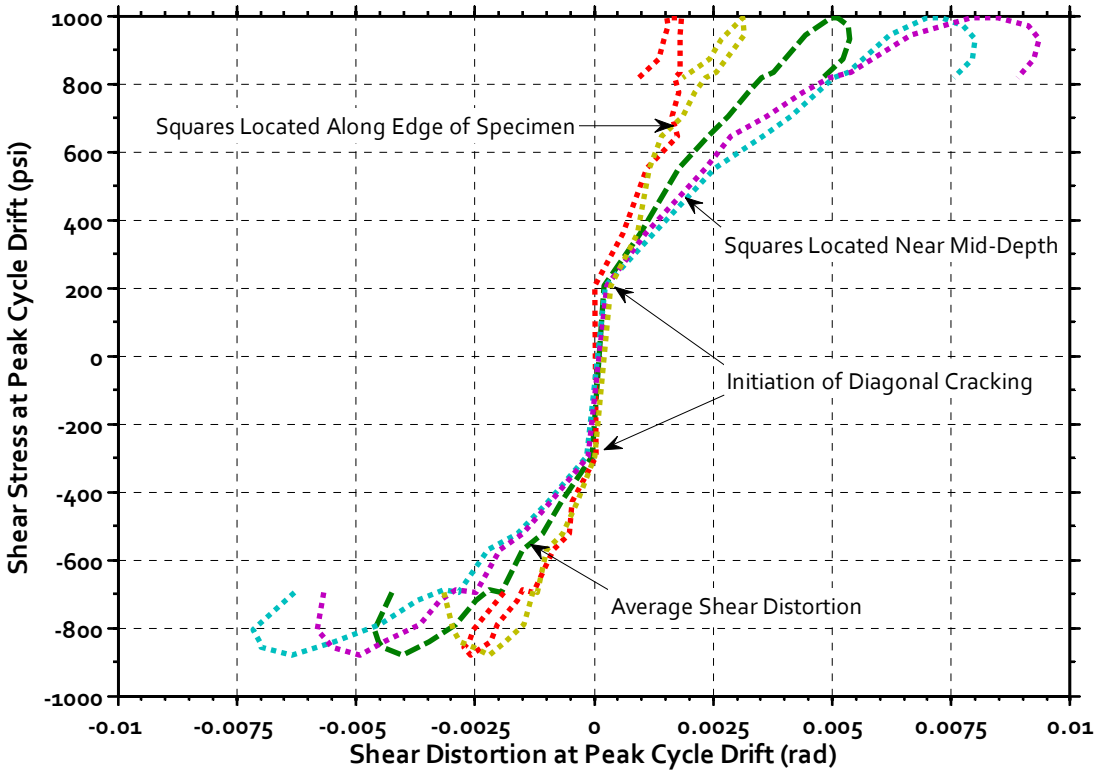

Figure 4.26 – Envelope shear stress versus shear distortion for strip 4 of Specimen CB-2

This is consistent with the shear stress distribution over the depth of a beam element predicted by an elastic solution. It was observed experimentally that the ratio of shear strains in the middle squares to the edge squares generally ranged between 1 and 3, which is on the same order as the ratio of 1.8 predicted by the elastic solution for the geometry of the squares used. It was also observed that for the strips closest to the inflection point, strips 4, 5 and 6, this ratio was usually higher than for the end strips where flexural demands were higher and shear distortion was more evenly distributed across the depth of the member. This result could be attributed to the interaction of shear and flexural cracking that softened the shear stiffness of the edge squares.

4.3.2.1 Sliding Shear Displacements

As stated previously, the shear distortion calculated by Eq. 4.4 does not differentiate "true" shear distortion from sliding shear displacements that developed across flexural cracks. However, distinguishing between these mechanisms is important.

It was observed during testing that sliding occurred at the most dominant flexural cracks near the ends of the specimens and dominated the eventual failure of the specimens. To study this sliding as a mechanism distinct from "true" shear distortion, the point at which sliding initiated in each strip must be identified. Figure 4.27 shows the shear stress applied to Specimen CB-1 plotted against the calculated shear strain in strip 8, where sliding was visually observed. Through most loading cycles, the hysteresis is confined to shear distortions less than 0.01. However, once this strain value was exceeded, the calculated shear strain in strip 8 began to significantly increase with repeated cycling, even as the imposed shear stress decreased. When this pattern was identified in a strip, it was assumed that sliding had begun to play an important role, and all shear strains larger than the strain at which the change occurred were attributed to sliding along flexural crack faces. For strip 8 of Specimen CB-1, all calculated shear strains larger than 0.01 were attributed to sliding shear. Table 4.4 lists the specimen drift levels at which sliding

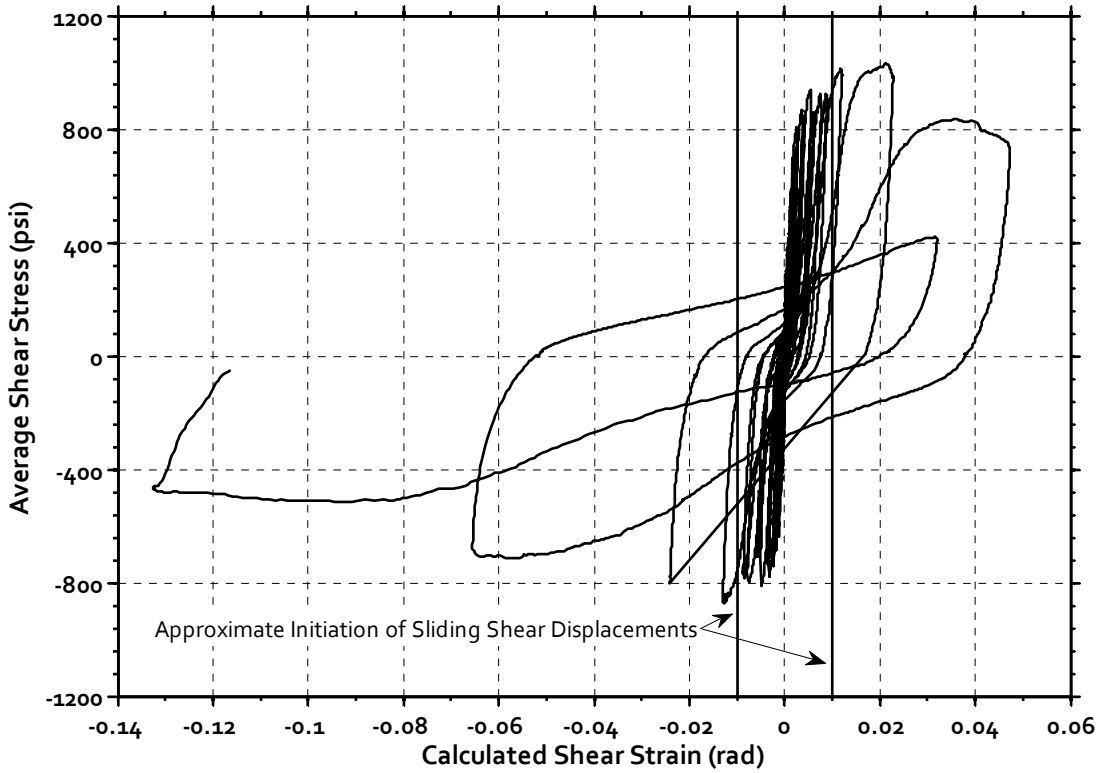

Figure 4.27 – Identification of initiation of sliding shear displacements in strip 8 of Specimen CB-1

Table 4.4 – Drift at which sliding was first identified

CB #	Loading Direction	% Drift at Which Sliding was First Observed in Each Strip							Max. Drift with 80% peak force
		2	3	4	5	6	7	8	
1	+	none	none	none	none	none	2.20	1.75	2.2%
	-	none	none	none	none	none	2.00	1.25	2.5%
2	+	2.50	none	none	none	none	none	1.75	5.5%
	-	2.00	none	none	none	none	none	1.25	5.0%
3	+	1.25	none	none	none	none	none	1.25	3.0%
	-	2.00	none	none	none	none	none	1.00	5.0%

*shading indicates strip(s) where eventual failure localized

was first identified in each strip of the specimens by this analysis. Strips 1 and 9, which encompass the precast beam-to-wall interface, are not included in the table because all shear strains observed at this interface are assumed to be due to sliding.

The last column of Table 4.4 also shows the peak drift attained in each loading direction with strength retention of 80%. For the three tests, sliding was first observed within the strip that eventually controlled the failure of the specimen. However, the large increase in drift attained by each specimen beyond the initiation of sliding demonstrates that, as Paulay and Binney (1974) showed, the presence of diagonal reinforcement is effective at stabilizing potential sliding shear failures and allows the coupling beam to achieve larger drifts. This is true for HPFRC coupling beams detailed similarly to those tested, even with the large reduction of diagonal reinforcement.

Figure 4.28 shows the distribution of sliding shear displacements per strip over the length of the coupling beams. A comparison of Figure 4.24 with Figure 4.28 shows that sliding shear displacements are most pronounced in strips that undergo the largest flexural curvatures, but that these sliding shear displacements do not begin to develop until drift cycles larger than approximately 2% are imposed. Although not an exact measure, crack width measurements taken during testing indicated that, when subjected to shear stresses larger than $10\sqrt{f_c'}, [psi]\left(0.83\sqrt{f_c'}, [MPa]\right)$, flexural cracks wider than 0.04 in. (1 mm) generally coincided with the initiation of sliding displacements.

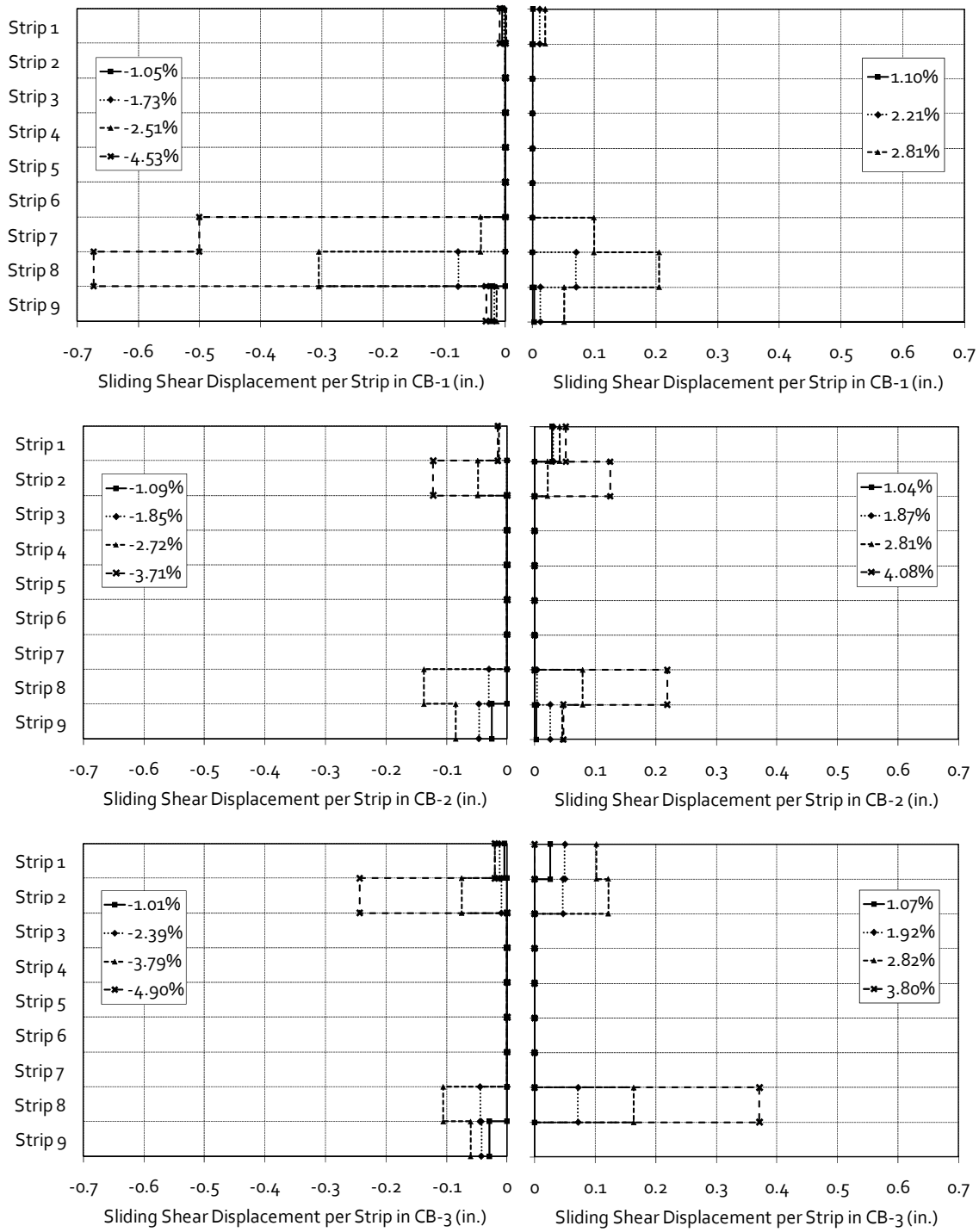

Figure 4.28 – Sliding shear displacement distribution for strips 1-9 of all three coupling beam specimens in the negative and positive loading direction (left and right plot, respectively)

Specimen CB-1 exhibited significantly larger sliding shear-displacements in the plastic hinge than Specimens CB-2 or CB-3. This indicates that, for Specimens CB-2 and CB-3, the combined effects of diagonal reinforcement, column-type confinement and HPFRC maintained the integrity of the plastic hinge and reduced and delayed sliding. Also, relatively small sliding shear displacements were observed in strips 1 and 9, which encompassed the precast beam-to-wall interface. For this analysis, all calculated shear distortion in strips 1 and 9 was assumed to result from sliding at this interface, as mentioned earlier. This assumption overestimates the influence of sliding in strips 1 and 9 because some true shear distortion did develop in the narrow strip of beam between the last row of markers and the face of the wall. Despite this, sliding displacements less than 0.1 in. (2.5 mm) were calculated, which indicates that the shear keys and dowel reinforcement were effective at controlling this sliding in Specimens CB-1 and CB-2. Specimen CB-3, which did not have shear keys, did not exhibit appreciably larger sliding at the interface, indicating that shear keys, although useful, are not required in the design of these types of elements.

For the specimens tested, there were two interfaces where the sliding shear capacity is critical in design: (1) at the precast beam-to-wall interface, and (2) along the stirrup nearest the termination of the dowel reinforcement, where intersecting flexural cracks create a potential plane of weakness. Table 4.5 shows the peak shear force applied to each of the three specimens, along with the sliding shear capacity predicted by the shear friction analogy adopted by the ACI Building Code (318-08). The ACI Building Code procedure uses a coefficient of friction to linearly relate the sliding shear resistance of an interface to the sum of the forces required to yield the reinforcement crossing the interface. For interfaces between two concrete elements (i.e. not steel-concrete), the coefficient of friction (μ) is to be taken as 1.4 for monolithically cast concrete, 1.0 for concrete cast against "intentionally roughened" concrete and 0.6 for concrete cast against concrete that does not qualify as "intentionally roughened." "Intentionally roughened" concrete has a surface that has been prepared such that the amplitude of surface roughness is greater than or equal to 0.25 in. (6 mm). Although it is not clear how effective compression reinforcement is at providing meaningful clamping action to the interface, it does provide some dowel action and is included in this prediction, as

permitted by ACI 318-08. Only the impacts of the compression diagonal and the transient axial force are ignored, per the ACI 318-08 commentary. The ACI 318-08 equations also have an upper limit for sliding shear capacity, which is shown in Table 4.5.

Table 4.5 shows that although the predicted sliding shear capacity was generally much higher than the shear forces developed experimentally, the upper limit for sliding shear capacity permitted by the ACI Building Code (318-08) provided a conservative estimation of the shear forces developed in every case except at the flexural crack faces in Specimen CB-2, where the strength limit slightly exceeded capacity. Therefore, the ACI Building Code (318-08) equations are appropriate for designing the precast beam-to-wall interface to resist sliding shear displacements.

Unfortunately, the shear friction model is not as useful within the precast element, where sliding shear displacements ultimately led to the failure of the specimens. In the tests of all three specimens, the dominant sliding shear displacements developed within the precast beam (see Figure 4.28) along a sliding plane created by intersecting flexural cracks, despite a sliding shear capacity at this location that was predicted to be 25-50% higher than at the precast beam-to-wall interface. This is because the shear stress at which sliding displacements developed within the plastic hinge was not controlled by conventional sliding shear friction principles. Rather, the flexural capacity of the hinge

Table 4.5 – Predicted versus experimentally obtained peak sliding shear capacity

Spec. #	Measured Peak Shear Capacity		Precast Interface					Flexural Cracks				
			μ	Predicted Sliding Shear Capacity*		ACI Code Upper Limit		μ	Predicted Sliding Shear Capacity*		ACI Code Upper Limit	
	kip	kN		kip	kN	kip	kN		kip	kN	kip	kN
CB-1	148	660	1.0†	230	1020	115	510	1.4	300	1330	145	640
CB-2	147	653	1.0†	200	890	125	560	1.4	250	1110	155	690
CB-3	146	649	0.6	120	530	115	510	1.4	240	1070	125	560

* Compression diagonal and transient axial force ignored, per ACI 318-08

† Interface with shear keys is assumed to qualify as "intentionally roughened" to warrant use of μ = 1.0 (shear keys and roughened surface were shown to be comparable in performance by Bass, Carrasquillo and Jirsa, 1989)

controlled the shear stress imposed on the specimen, and only after repeated cycling and significant crack opening did the interface sufficiently degrade to allow sliding displacements to develop. This highlights the strong negative influence that large curvature demands and repeated cycling have on sliding shear resistance along an interface within a plastic hinge, which has previously been studied extensively (Paulay, 1971; Bertero and Popov, 1975; Scribner and Wight, 1980; and many since). For the specimens tested, the ability of the interface created by intersecting flexural cracks to resist sliding shear is not well predicted by a shear friction model. Rather, the presence of diagonal reinforcement and ample confinement of the plastic hinge region were shown to be much more important factors for maintaining the integrity of the sliding shear resisting mechanisms and delaying the development of critical sliding displacements.

4.3.2.2 Initial Shear Stiffness

Before the specimens were subjected to shear stresses large enough to cause diagonal cracking, the stirrups and fibers did not have a meaningful participation in resisting shear stresses. At these early stages of loading, the response of the specimen to shear stresses was approximately linear. The slope of this response represents the effective initial shear modulus of the specimens. For comparison purposes, it is useful to eliminate the effect of different concrete compressive strengths between specimens by normalizing the observed initial shear stiffness by the theoretical shear modulus, G, where $G = 57000\sqrt{f_c'}/\big(2(1+\nu)\big)$, f_c' is the compressive strength of the concrete obtained from tests of cylinders (in psi), and ν is Poisson's ratio, assumed herein to be 0.15. Figure 4.29 shows the experimentally calculated shear modulus, measured from peak-to-peak of the first cycle to 0.25% drift, normalized by the theoretical shear modulus. Significant scatter is observed in Figure 4.29, which could be due to varying amounts of shrinkage and micro-cracking in the different specimens caused by differences in handling of the precast element. To reduce the effect of the scatter in the observed normalized shear modulus, the effective initial shear modulus was taken as $G_{eff,initial} = 0.6 * G$ in further analyses (Section 6.3).

4.3.2.3 Shear Distortion

Fig 4.30 shows the average shear distortion measured in each strip of the coupling beam specimens at various drift levels (in both positive and negative loading directions). To calculate the shear distortion plotted in Figure 4.30, the effect of sliding shear displacements plotted in Figure 4.28 was subtracted from the shear distortion calculated by Eq. 4.4. Therefore, Figure 4.30 represents a best-estimate of the "true" shear distortion exhibited by each strip. Although all strips were subjected to the same average shear stress, the middle strips, nearest the inflection point, generally exhibited the smallest shear strains. This indicates that flexural deformations soften the shear resistance of a section, as expected. That many of the strips continued to exhibit increasing shear strains with increasing drift demands, even as the shear stress demand remained approximately constant, is further evidence of this phenomenon. The formulation of a shear spring to model the shear behavior of coupling beams should account for this softening due to flexural deformations, particularly at the ends of the coupling beam.

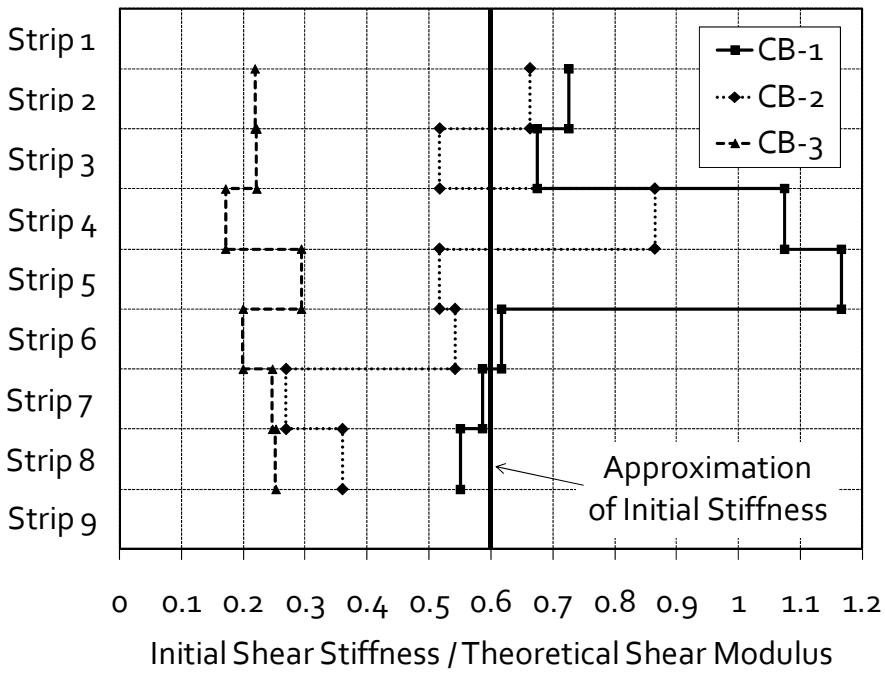

Figure 4.29 – Observed initial shear stiffness for individual strips, normalized by the theoretical shear modulus

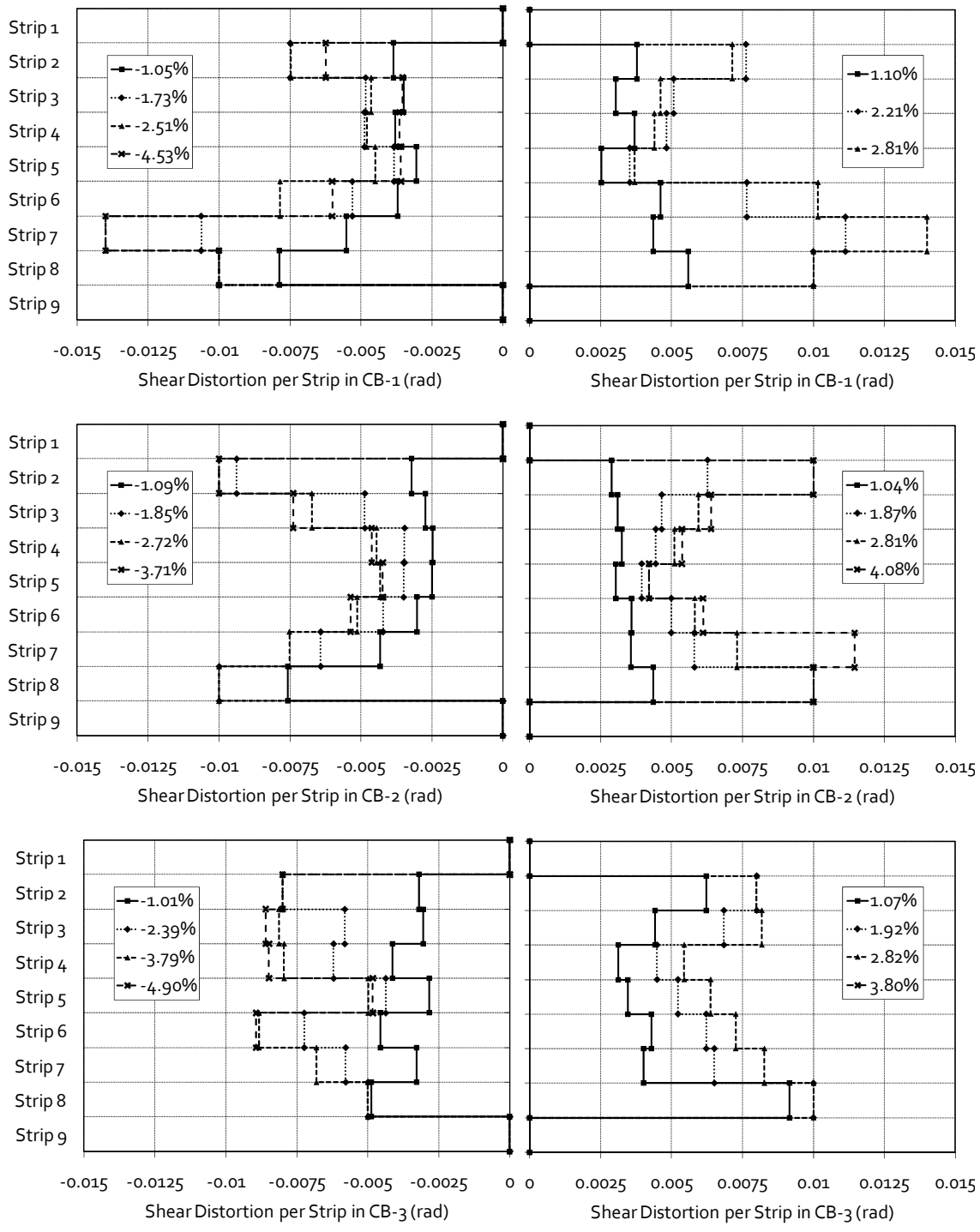

Figure 4.30 – Shear distortion distribution for strips 1-9 of all three coupling beam specimens in the negative and positive loading direction (left and right plot, respectively)

4.4 DRIFT COMPONENTS

During testing, the specimens had to deform to accommodate the imposed drift demands, but the relative contribution of various mechanisms to the total drift varied throughout the tests. Figure 4.31 shows the relative contribution of the primary mechanisms contributing to the deformation of the coupling beam specimens, calculated from measurements obtained by the grid of optical markers fixed to the surface of the specimens.

The contribution of flexural rotations was determined first. The procedure described in Section 4.2.2 was used to determine the rotation in strips 2-8 of the coupling beam, and then the second moment-area theorem was used to calculate the drift associated with these rotations. The same procedure was used for strips 1 and 9, which encompassed the interface between the precast beam and the wall; however, the contributions of the rotations at the interface are plotted separately from flexural rotations in Figure 4.31 to isolate the relative impact of strain penetration into the connection from "pure" bending of the specimen. The contribution of rotations at the interface to total drift is labeled "steel strain penetration" in Figure 4.31.

The penetration of strains into the connection was responsible for approximately 10-20% of the overall drift imposed on the specimens. This is considerably smaller than contributions reported by other researchers (Naish et al., 2009), and shows that the precast HPFRC specimen was itself responsible for accommodating more than 80% of the drift imposed on the specimens. The restraint of axial elongation, which resulted in the development of the axial forces discussed previously, may have complemented the dowel reinforcement and limited the importance of the penetration of strains into the connection. When the contribution of rotations within the beam and strain penetration into the connection are considered together as the total contribution of flexural mechanisms to drift, it is seen that approximately 60% of the total drift was due to flexural deformations. This is a large contribution for coupling beams with an aspect ratio of 1.75, and supports the use of flexural design principles in the design and analysis of these members.

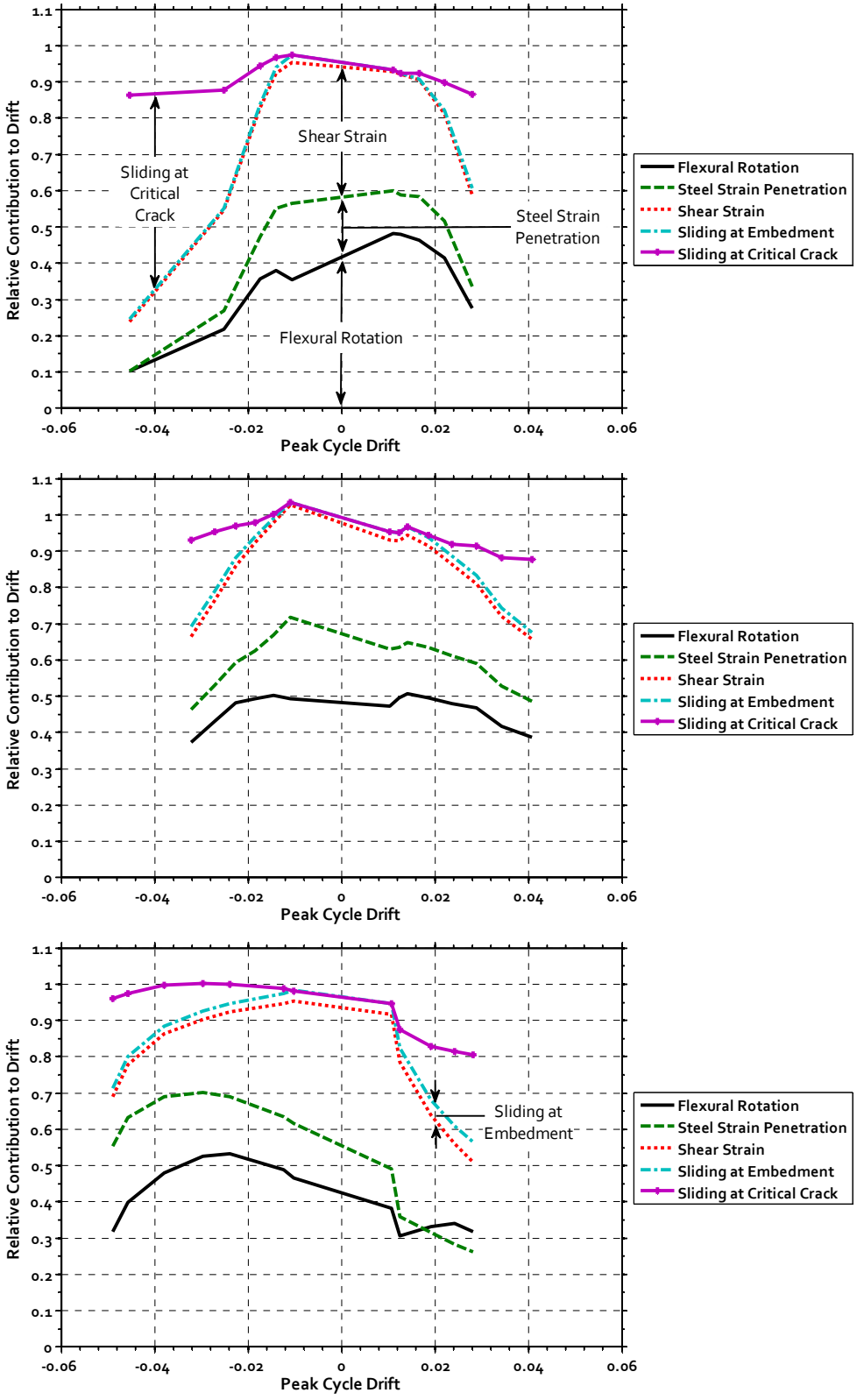

Figure 4.31 – Relative percentage contributions to specimen drift at the peak drift of each loading cycle (Specimens CB-1, CB-2 and CB-3, top to bottom, respectively)

The contribution of shear distortion was calculated using the process described in Section 4.3.2 to determine the shear distortion of each strip of the specimen, and then multiplying that shear distortion by the length of the strip to obtain a shear displacement per strip. These displacements were summed over the length of the coupling beam, and then normalized by the total imposed displacement to determine the fraction of drift resulting from shear distortions of the coupling beam. Sliding shear displacements were differentiated from "true" shear distortions by the process described in Section 4.3.2. Figure 4.31 shows that sliding displacements accounted for a very small fraction of the total drift imposed up to drifts of approximately 2%. Beyond 2% drift, shear sliding was a more important component of the overall drift. Of the three specimens, Specimen CB-1 exhibited the largest contribution from sliding shear displacements. The combination of high shear stresses and large rotation demands forced expansion of the inadequately confined plastic hinge region in Specimen CB-1. Column-type confinement reinforcement in the plastic hinge region of Specimens CB-2 and CB-3 maintained the integrity of the plastic hinge region sufficiently to support the diagonal reinforcement and allow for aggregate interlock to remain active in resisting sliding shear displacements across flexural crack faces until much larger drift demands were placed on the specimens. As a result, sliding was a less important contributor to the drift imposed on Specimens CB-2 and CB-3. Figure 4.31 also shows that the contribution of sliding at the precast beam-to-wall interface to the specimen drift was negligible throughout the tests, indicating that sufficient dowel resistance was provided across this interface to complement the shear capacity of the compression zone and limit sliding shear displacements.

4.5 ENERGY DISSIPATION

In addition to stiffening a coupled-wall system to limit system drifts, a primary function of coupling beams is to dissipate energy throughout the full height of a structure (Paulay and Santhakumar, 1976). This energy dissipation is primarily achieved through yielding of coupling beam reinforcement, and can be calculated for a given imposed drift

cycle as the area enclosed by the shear force versus displacement hysteresis loops. Figure 4.32 shows the energy dissipated per the first cycle for each new drift imposed on the coupling beam specimens. In this figure, the drift plotted on the x-axis is the average of the peak drift achieved in the positive and negative loading directions for the given cycle. Initially, all three specimens showed similar levels of energy dissipation. Specimen CB-1 deviated from the trend near 2% drift, which coincides with the loading cycle when sliding shear displacements became an important drift component in this specimen. The lower energy dissipated in this cycle is a measure of the pinching of the hysteresis loops caused by shear sliding. With more confinement reinforcement in the plastic hinge, Specimens CB-2 and CB-3 showed increasing levels of energy dissipation with increased drift demands until failure of the specimens. Figure 4.33 shows a close-up view of the smaller drift levels shown in Figure 4.32, along with the energy dissipated in repeat cycles, to allow a comparison of the energy dissipated during initial and repeat cycles for each of the three specimens. The energy dissipated in repeat cycles to the same drift level was, although smaller, generally similar in magnitude to the first loading cycle. This indicates that the mechanisms dissipating energy do not appreciably degrade with low numbers of repeat cycles.

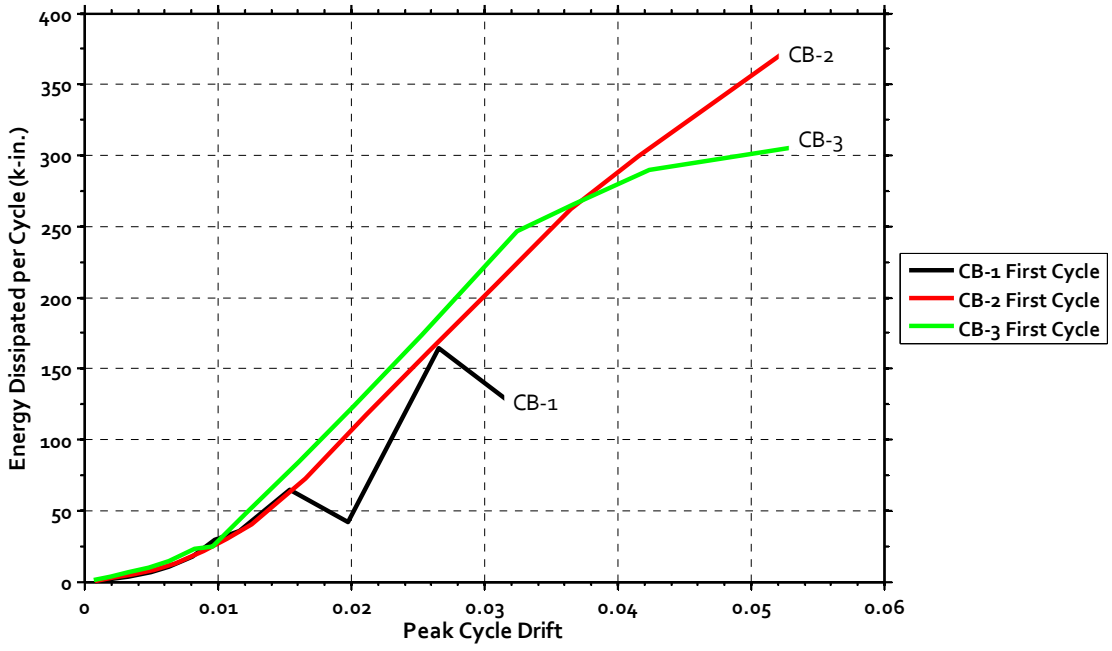

Figure 4.32 – Energy dissipated per loading cycle plotted against the average peak drift achieved in the positive and negative loading directions

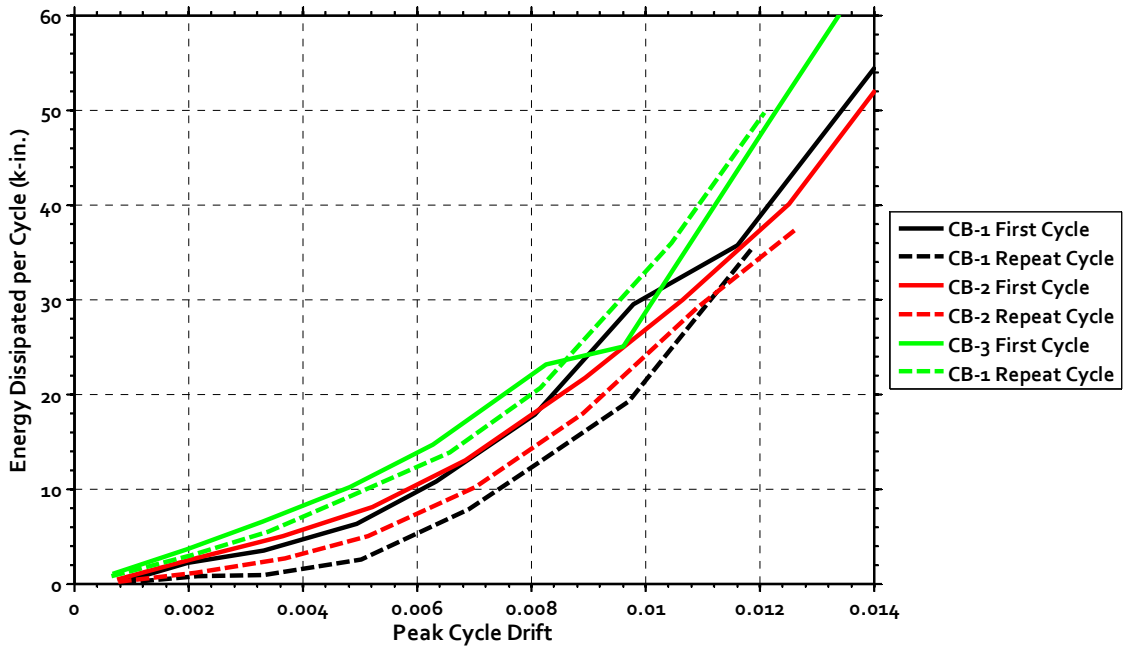

Figure 4.33 – Close-up of energy dissipated per loading cycle plotted against the average peak drift achieved in the positive and negative loading directions

To compare the energy dissipation capacity of the HPFRC coupling beams with other reinforced concrete coupling beam tests, it is useful to normalize the calculated energy dissipation capacity. Figure 4.34 shows the energy dissipated per cycle for Specimens CB-1, CB-2 and CB-3, normalized by the area of an equivalent elasto-plastic hysteresis loop to the same peak force and displacement (as shown in Figure 4.35). The loading and unloading stiffness of the equivalent elasto-plastic hysteresis loop was set equal to the secant stiffness of the first cycle to 0.5% drift. Figure 4.34 shows that a normalized energy dissipation of approximately 0.4 was generally exhibited beyond 1% drift. Specimen CB-1 showed reduced energy dissipation capacity at 2% drift, which was due to sliding shear displacements that caused pinching of the shear force versus drift hysteresis loops. Once sliding shear damage was severe enough to cause a large reduction in the shear capacity of Specimen CB-1, the normalized energy dissipated per cycle returned to approximately 0.4, even though the amount of energy dissipated was reduced (as shown in Figure 4.32). Column-type confinement and HPFRC combined to maintain the energy dissipation capacity of Specimens CB-2 and CB-3 until termination of the test.

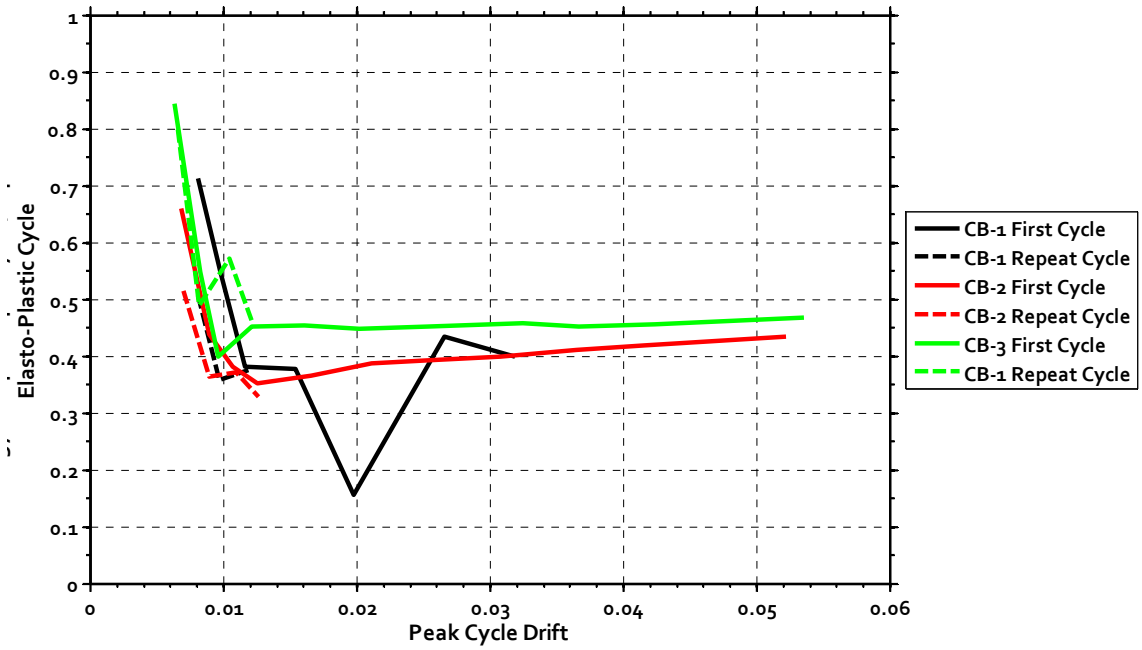

Figure 4.34 – Energy dissipated per loading cycle normalized by an equivalent elasto-plastic hysteresis loop and plotted against the average peak drift achieved in the positive and negative loading directions

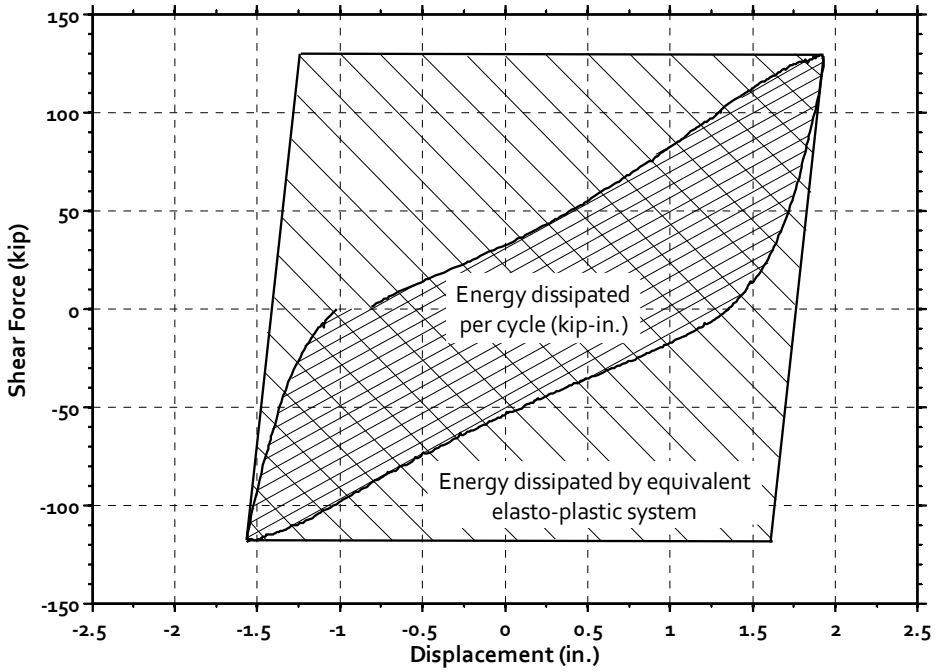

Figure 4.35 – Elasto-plastic hysteresis loop used for normalization of the energy dissipated per cycle, drawn to the peak force and displacement of each loading cycle (example taken from a late loading cycle from the test of Specimen CB-2)

Table 4.6 – Energy dissipated per loading cycle normalized by the energy corresponding to an elasto-plastic hysteresis loop for comparable reinforced concrete coupling beams

Researchers	Year	Aspect Ratio	Axial Force (Y/N)	HPFRC (Y/N)	Reinforcement Scheme	Normalized Energy Dissipation
Shiu et al.	1978	2.5	N	N	Diagonal	0.5
Naish et al.	2009	2.4	N	N	Diagonal	0.55
Tegos et al.	1988	2	Y	N	Diagonal	0.35
Current Study	2010	1.75	Y	Y	Diagonal	0.4
Galano et al.	2000	1.5	N	N	Diagonal	0.45
Tassios et al.	1996	1.5	N	N	Diagonal	0.35
Canbolat et al.	2005	1	N	N	Diagonal	0.4
Canbolat et al.	2005	1	N	Y	Diagonal	0.25

Unfortunately, few researchers report energy dissipation per cycle, and fewer report this value in a normalized fashion. For comparison purposes, the normalized energy dissipation per cycle was calculated for a sample of reported test data from the most comparable reinforced concrete coupling beam specimens reported in the literature. This analysis was done by digitizing published images of hysteresis plots, and calculating an approximate ratio between the area of a reported experimental shear force versus displacement hysteresis loop and an equivalent elasto-plastic loop. The results of this comparison are shown in Table 4.6. The results are sorted by coupling beam aspect ratio because there is a trend towards larger normalized energy dissipation for more slender coupling beams, where flexural deformations play a more prominent role. Despite the significant reduction in diagonal reinforcement area, this series of HPFRC tests exhibited an energy dissipation capacity similar to comparable reinforced concrete coupling beams with similar aspect ratios.

4.6 STIFFNESS

To achieve reasonable results from linear and nonlinear analyses of coupled wall systems, a reasonably accurate estimate of the flexural and shear stiffness of each of the coupling beams and wall components is required. For nonlinear analyses, an estimate of

the cracked flexural stiffness is required as part of the definition of a hysteresis model. This cracked stiffness can be estimated from experimental data as the slope of a secant drawn from the origin to the point of first yield, and is discussed below for the tested specimens. This same cracked flexural stiffness is appropriate for use in linear analyses of structures that will later use a factor to amplify elastic displacements to predict inelastic displacements. For structural models that attempt to capture non-linear system behavior based on an "equivalent" linear system, a flexural stiffness reduction factor must be assumed to modify the uncracked flexural stiffness to account for yielding as well as cracking. Appropriate flexural stiffness reduction values for such an analysis are proposed for coupling beams similar to the specimens tested.

In both linear and non-linear analyses, it is common practice to assume a constant value for shear stiffness. For the specimens tested herein, the observed shear stiffness was markedly lower than commonly assumed. It is also generally assumed that any resulting error will be small because shear deformations are a minor contributor to overall drift; however, shear deformations played an important role in the overall deformation of the tested specimens, so the resulting error would be non-negligible. Although both the flexural and shear stiffness are non-linearly related to the level of deformation demand, and increasingly interdependent as deformation levels increase, it is shown that merely adopting a more appropriate constant value for shear stiffness would be a marked improvement over current practice for the given test specimens. In the following sections the experimentally obtained secant shear stiffnesses of the tested coupling beams in the context of a commonly used stiffness reduction factor are discussed. A more appropriate value for use in modeling beams similar to those tested is then proposed.

4.6.1 Coupling Beam Flexural Stiffness

The uncracked flexural rigidity of a coupling beam, neglecting the reinforcing steel, should theoretically be $E_c I_g$, where $E_c = 57{,}000\sqrt{f_c'}$, f_c' is the compressive strength of the concrete (in psi), and I_g is the gross moment of inertia of the section. As the section cracks, this stiffness diminishes. To account for this, both linear and non-linear analyses assume a reduced "cracked-elastic" flexural stiffness. The ACI Building Code (318-08) suggests a reduced flexural stiffness of $0.35E_c I_g$ for flexural members,

but this reduction is not intended for coupling beams. ASCE/SEI 41/06 adopts a reduced flexural stiffness of $0.5E_cI_g$ for coupling beams, but in Supplement 1 of ASCE/SEI 41/06 it is proposed that this value should be reduced to $0.3E_cI_g$. A flexural rigidity of $0.3E_cI_g$ is consistent with effective stiffness values commonly used in practice for coupling beams (Harries, Moulton and Clemson, 2004), but still may not sufficiently account for penetration of strains into the connection at first yield. Elwood and Eberhard (2006) determined that the mean secant flexural stiffness at first yield for columns with axial forces less than $0.1E_cA_g$ is approximately $0.2E_cI_g$, based on a database of column tests. As shown in Figure 4.36, $0.2E_cI_g$ is a more representative estimate of the secant flexural stiffness at first yield of the coupling beams tested than the recommended $0.3E_cI_g$.

For "equivalent" linear analyses of coupled-wall systems, where components are modeled linearly using stiffness and damping characteristics that approximate non-linear component properties, further reduction of the flexural stiffness is required to account for yielding. The ratio of experimentally calculated flexural stiffness to theoretical uncracked

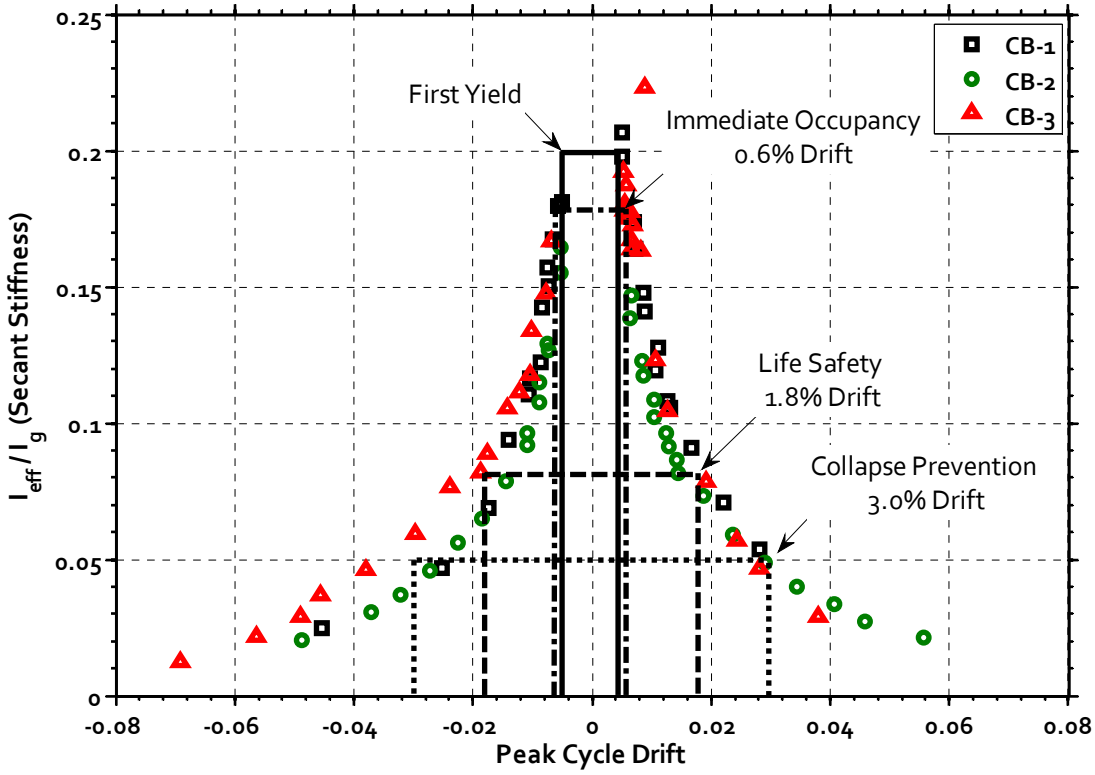

Figure 4.36 – Experimentally obtained secant flexural stiffness reduction factors

stiffness for the precast HPFRC specimens tested in this study is plotted in Figure 4.36 versus the peak drift imposed in each cycle. For these specimens, the experimentally obtained flexural stiffness is defined as the slope of the secant drawn from the origin to the point of peak force within each loading cycle after displacements are corrected to remove deformations due to shear. Lines are drawn on Figure 4.36 that correspond with the deformation levels expected of coupling beams for immediate occupancy, life safety and collapse prevention level seismic events, (0.6%, 1.8% and 3.0% drift, respectively) as defined by ASCE/SEI 41/06. It is shown that for the precast HPFRC specimens tested, an effective flexural stiffness of $0.18E_cI_g$, $0.08E_cI_g$ and $0.05E_cI_g$ correspond with immediate occupancy, life safety and collapse prevention demand levels, respectively. Tests reported by Naish et al. (2009) of diagonally reinforced concrete coupling beams exhibited flexural stiffness values on the order of $0.15E_cI_g$ at deformation levels associated with immediate occupancy (0.6% drift) and as low as $0.05E_cI_g$ at deformation levels associated with structural collapse prevention (3.0% drift). The observed effective flexural stiffnesses are consistent with those observed by Naish et al. and would be more appropriate for use in "equivalent" linear system models than cracked stiffness values intended for non-linear analyses. The close correlation between the stiffness of the specimens in the current study and those reported by Naish et al. shows that the precast embedment details used herein did not lead to a noticeable reduction of the flexural stiffness.

4.6.2 Coupling Beam Shear Stiffness

ASCE/SEI 41/06 adopts a constant value of $0.4E_cA_w$ for the shear rigidity of coupling beams. In this expression, A_w is included to convert the shear force to an average shear stress. The $0.4E_c$ term might appear to represent some degree of softening to account for diagonal shear cracking; however, $0.4E_c \approx E_c/2(1+\nu) = G$. Therefore, the shear stiffness adopted in ASCE/SEI 41/06 is essentially the theoretical uncracked shear modulus, G. For coupling beams, which are often expected to sustain high shear stresses as large as $10\sqrt{f_c'}, [psi]\left(0.83\sqrt{f_c'}, [MPa]\right)$, neglecting the softening effect of diagonal and flexural cracking on the shear stiffness will lead to overestimating the shear

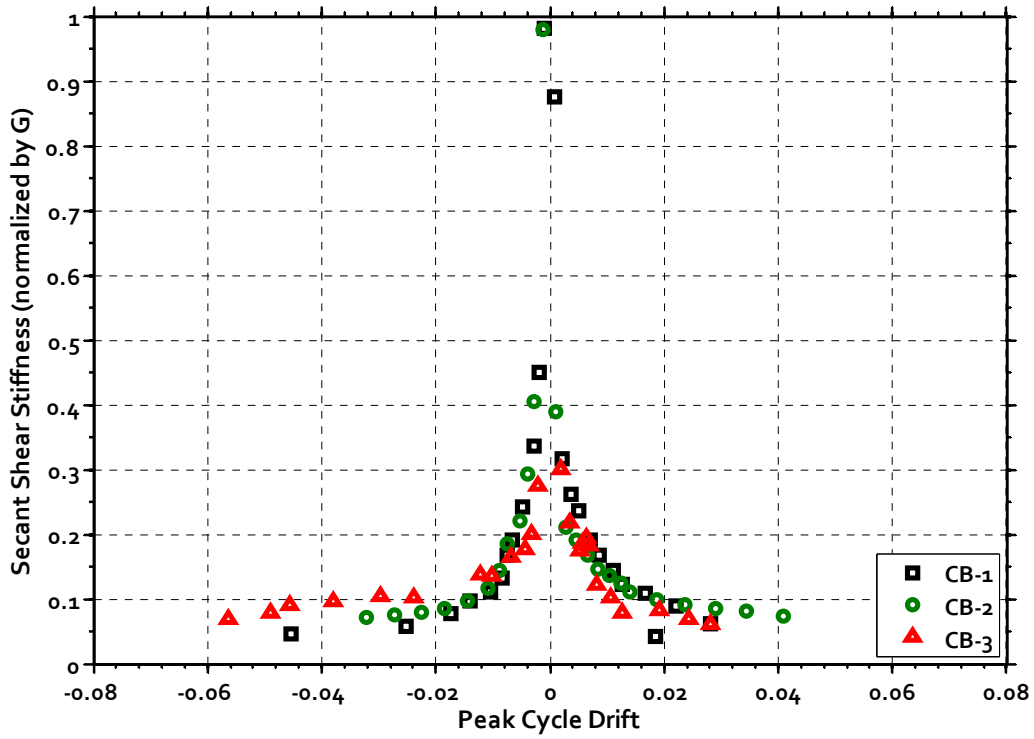

Figure 4.37 – Experimentally obtained secant shear stiffness, normalized by G

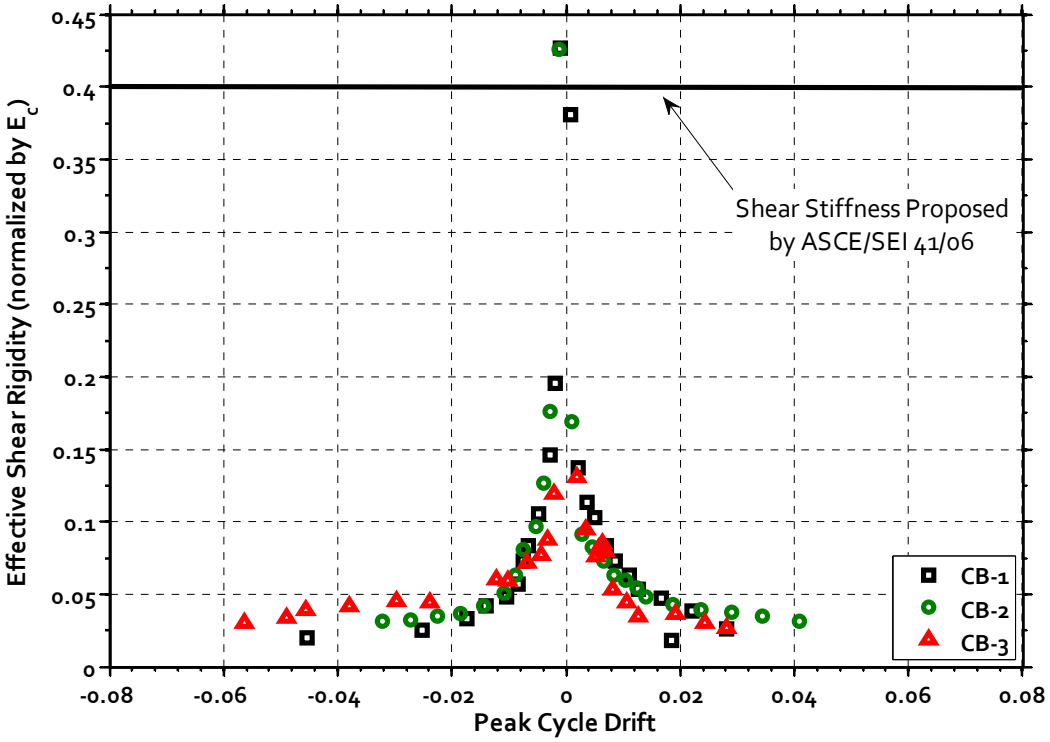

Figure 4.38 – Experimentally obtained secant shear stiffness, normalized by E

stiffness. This effect is likely non-negligible, as shear deformations accounted for approximately 40% of the deformations of the specimens tested at all levels of drift demand. Figure 4.37 shows the secant shear stiffness exhibited by each specimen at various drift levels, normalized by the theoretical shear modulus, assuming that $\nu = 0.15$. The effect of sliding shear deformations was removed in Figure 4.37, so the effective shear stiffness would need to be further reduced if sliding is to be included.

Once diagonal cracking occurred there was an appreciable reduction in the experimentally observed shear stiffness to approximately $0.1G$ at drifts beyond 1.5%. To be more consistent with ASCE/SEI 41/06, Figure 4.38 shows the same observed shear stiffness, as a function of drift demand, but normalized by E_c, where $E_c = 57{,}000\sqrt{f_c'}$ (in psi). Assuming a shear stiffness of $0.4E_c$ would significantly overestimate the shear stiffness of coupling beams designed similarly to the specimens tested (by a factor of 10).

4.7 REINFORCING STEEL STRAINS

Strain gauges were fixed to the longitudinal, diagonal and transverse steel reinforcement in Specimens CB-1, CB-2 and CB-3. The data from these strain gauges were then compared with results from monotonic tests of representative coupons to estimate the point at which each of the various reinforcing bars yielded. Figs. 4.39-4.41 show the location of every strain gauge that functioned properly throughout the tests of Specimens CB-1, CB-2 and CB-3, respectively. The gauge locations where yielding was detected are indicated by a black dot. For each specimen, three figures are shown. In the leftmost figure, labeled 0.5% drift, black dots are used to indicate the locations of strain gauges that had indicated yielding at any point in the test up to, and including, the loading cycles to 0.5% drift. The middle and rightmost figures show the same for 1% drift, and for the entire duration of the test, respectively.

In all three specimens, first yielding was observed in the longitudinal and diagonal reinforcement at the ends of the coupling beam near the precast beam-to-wall interface at approximately 0.5% drift. The testing of Specimen CB-1 also indicated

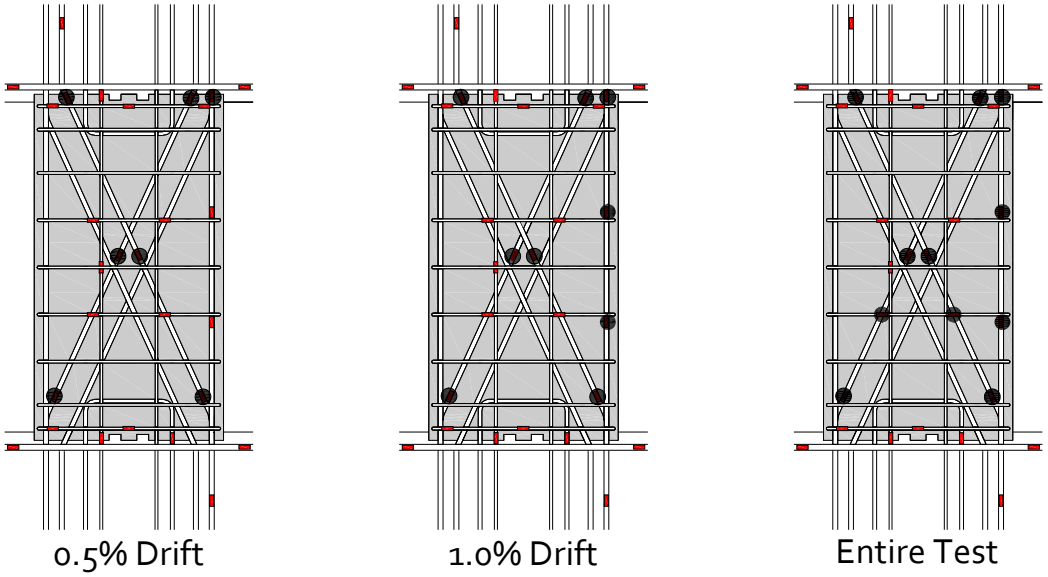

Figure 4.39 – Yield progression for Specimen CB-1. Rectangles mark the location of a strain gauge prior to yielding, black dots indicate a location where yielding had occurred.

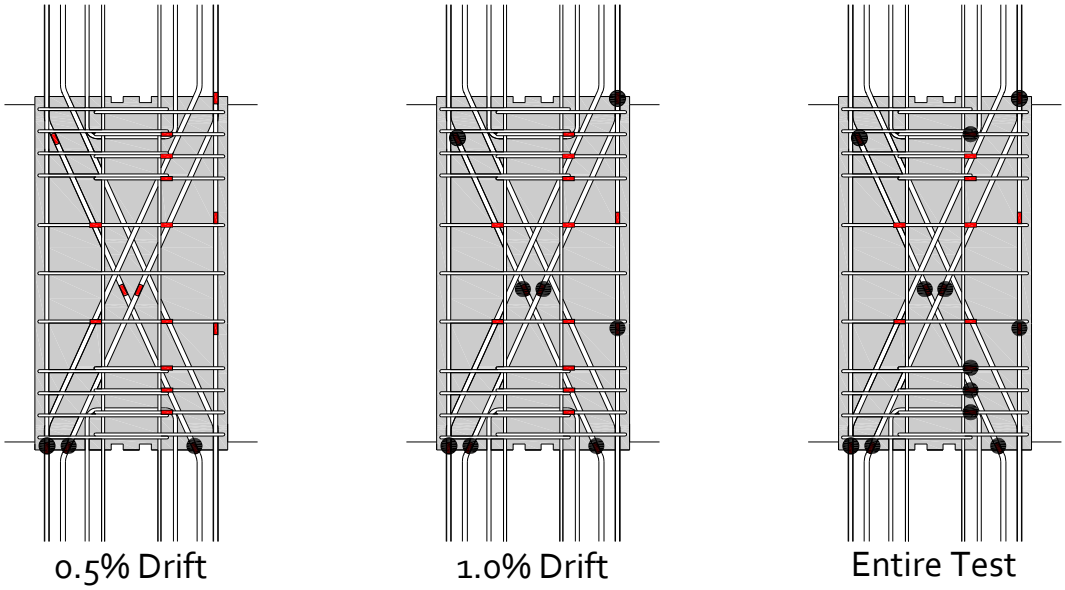

Figure 4.40 – Yield progression for Specimen CB-2. Rectangles mark the location of a strain gauge prior to yielding, black dots indicate a location where yielding had occurred.

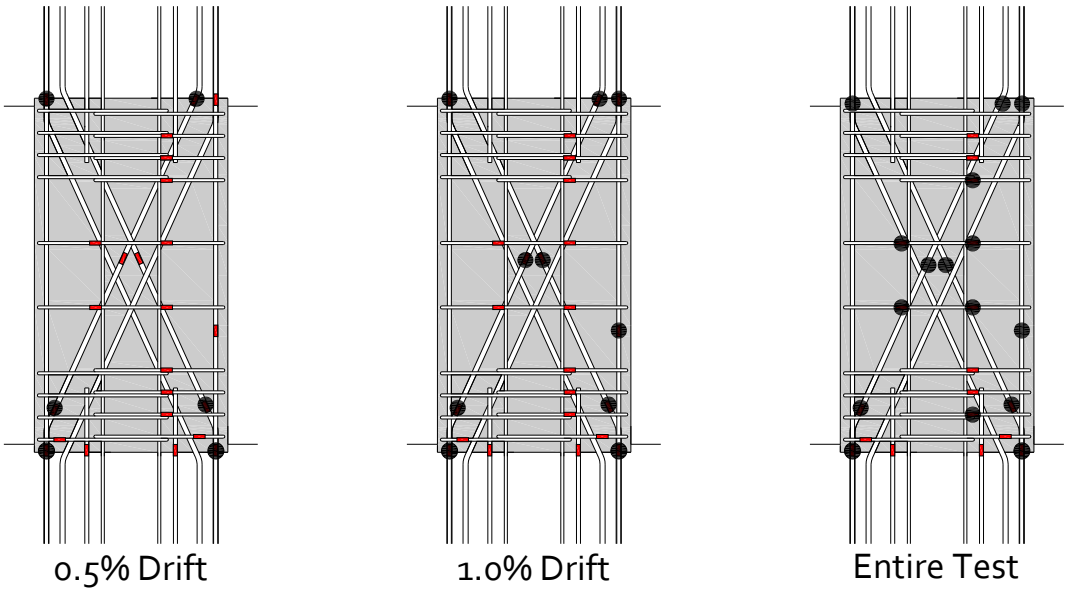

Figure 4.41 – Yield progression for Specimen CB-3. Rectangles mark the location of a strain gauge prior to yielding, black dots indicate a location where yielding had occurred.

yielding of the diagonal reinforcement near midspan at this stage of the test. By 1% drift, yielding had been indicated at some point by every gauge fixed to the longitudinal and diagonal reinforcement, but not simultaneously. Unlike tests of reinforced concrete coupling beams with no axial restraint that reported tensile strains of longitudinal reinforcement over the full length of the coupling beam (Paulay, 1971), these tests of HPFRC coupling beams with axial restraint simultaneously showed compression strains at the interface at one end and inelastic tensile strains at the other end of the same bar. At drifts near 1%, these inelastic tensile strains spread out to the gauges placed near midspan. The distribution of strains in the longitudinal reinforcement reflects a pattern that is more consistent with beam theory than previously tested coupling beam specimens and is most likely due to the improved bond capacity developed between HPFRC and deformed steel reinforcement.

Strain gauges attached to the dowel reinforcement placed near mid-depth of the coupling beam specimens across the precast beam-to-wall interface did not indicate yielding strains in any of the three tests. The dowel bars were effective enough at limiting deformations at this interface (as discussed in Section 4.2.3) that rotations large enough

to demand inelastic strains near mid-depth of the beams did not develop. The strains observed in the dowel reinforcement were, however, approaching yield, indicating that although a sufficient area of dowel reinforcement was provided to effectively move the primary inelastic deformations away from the interface, the dowel reinforcement was not excessive.

Strain gauges placed within the wall on the diagonal reinforcement, located 8 in. (200 mm), $13d_b$, from the face of the wall, did not indicate yielding at any point during the tests. This indicates that good bond developed between the reinforcement and the wall concrete, suggesting that the "elongation and slip" of the reinforcement described previously was properly characterized as normal strain penetration rather than undesirable anchorage failure.

The midspan transverse reinforcement, intended primarily as shear reinforcement, generally did not yield in Specimens CB-1 or CB-2, which had a transverse reinforcement ratio of 0.6%. Although some yielding was observed in the midspan stirrups in Specimen CB-1, it occurred late in the test and coincided with the loss of confinement of the plastic hinge at the bottom of the specimen. For this reason, it was felt that a reduction in the transverse reinforcement ratio to 0.45% would not be detrimental to the performance of Specimen CB-3. Although, as discussed previously, no detriment to the performance of this specimen was observed, yielding was recorded in all of the gauged midspan stirrups, indicating that further reduction of the transverse reinforcement would not have been advisable.

The column-type transverse reinforcement distributed through the plastic hinge region, which resisted both shear forces and lateral beam expansion, was fully utilized in both Specimens CB-2 and CB-3, as yield-level strains were recorded by most of the gauges. The only stirrups within the plastic hinge that were instrumented in Specimen CB-1 were those closest to the wall faces. These gauges did not indicate yield-level strains despite the obvious need for more confinement of the plastic hinge after failure of the specimen. It is likely that the strains recorded near the wall face remained elastic due either to confinement provided by the wall to the end of the precast section or some opening of the stirrups, which were mistakenly fabricated with 90º hooks.

4.8 SUMMARY AND CONCLUSIONS

Three precast HPFRC coupling beams with an aspect ratio of 1.75 were subjected to earthquake-type displacement reversals. The behavior of all three specimens was dominated by flexural hinging that developed at both ends of the specimen. Shear stresses exceeding $10\sqrt{f_c'}, [psi]\left(0.83\sqrt{f_c'}, [MPa]\right)$ were imposed on all three specimens. The behavior of Specimen CB-1 indicated insufficient confinement of the plastic hinge that limited the ductility of the specimen; however, additional confinement of the plastic hinges in Specimens CB-2 and CB-3 allowed both specimens to continue to resist more than 80% of the peak shear force up to and beyond 5% drift. Given that flexural yielding was first observed prior to 0.5% drift, 5% drift represents a displacement ductility of approximately 10. For comparison purposes, a review by Harries (2001) of coupling beam tests summarizes that well detailed diagonally reinforced coupling beams can be expected to exhibit a maximum displacement ductility of 7, showing that the HPFRC specimens performed similarly to comparable reinforced concrete specimens, despite reduced diagonal and confinement reinforcement.

The following conclusions regarding the design and behavior of these specimens can be drawn:

- Precasting the HPFRC coupling beam and embedding the concrete section only as deep as the wall cover proved to be an effective design alternative. The development of the diagonal, longitudinal and dowel reinforcement was shown to be adequate to transfer the moment capacity, and associated shear, of the coupling beam into the wall. Shear keys at the beam-to-wall interface slightly reduced sliding, but were found to not be required. This precast method is believed to simplify the construction of coupled-wall systems and limit the use of HPFRC to where it is most effective.
- Axial restraint of coupling beams resulted in axial forces on the order of $0.4V_{max}$. The axial elongation that developed in the coupling beams was shown to be proportional to the maximum drift due to flexural rotations previously imposed on the specimen.

- For design, a flexural analysis is appropriate for calculating the capacity of hinges at both ends of the coupling beam that ultimately control the beam shear demand. Assuming $f_s = f_y$ and $P = 0k$ resulted in a lower-bound coupling-beam capacity that was achieved at 0.75% drift and sustained until termination of the test. Assuming $f_s = 1.25f_y$ and $P = 0.4V_{max}$ resulted in an upper-bound coupling-beam capacity that was close to the measured peak shear force.
- Diagonal reinforcement provided 20-30% of the resistance to applied shear force, and stirrups and HPFRC effectively resisted the remaining shear force. Assuming that $v_c = 5\sqrt{f_c'}, [psi]\left(0.41\sqrt{f_c'}, [MPa]\right)$ appears to provide a conservative estimate of the contribution of the HPFRC to shear stress capacity under drift reversals.
- HPFRC provides adequate confinement of diagonal reinforcement, so no special confinement is required to provide stability to these bars. Special column-type confinement is, however, required throughout the flexural plastic hinge at each end of the coupling beam to ensure stable behavior.
- The plastic hinge length can be approximated as $h/2$ from the face of the wall at each end of an HPFRC coupling beam. Strain penetration into the connection can be accounted for by assuming the plastic hinge extends a length of approximately $precast\ embedment\ length + 8 * d_{b,largest\ bar}$ into the wall.
- Sliding shear deformations initiated near 2% drift along dominant flexural cracks, and became important contributors to total drift at large drift demands before eventually leading to the failure of each specimen. The reduced area of diagonal reinforcement, supported by HPFRC and column-type confinement, was effective at controlling the impact of sliding shear displacements until large drifts were imposed.
- Energy dissipated per cycle, when normalized by the energy corresponding to an equivalent elasto-plastic system with the same peak shear force and drift, and with a loading and unloading stiffness equal to the secant stiffness measured in the first cycle to 0.5% drift, was approximately 0.4 at drifts larger than 1%. This level of energy dissipation is comparable to well-detailed diagonally reinforced concrete coupling beams with similar aspect ratios.

- A flexural stiffness of $0.2E_cI_g$ provides a better estimate for calculating cracked stiffness for use in non-linear analyses than the $0.3E_cI_g$ adopted by Supplement 1 of ASCE/SEI 41/06. For "equivalent" linear analyses, assuming an effective flexural stiffness of $0.18E_cI_g$, $0.08E_cI_g$ and $0.05E_cI_g$ to account for cracking and yielding seems appropriate for drift demands associated with immediate occupancy, life safety and collapse prevention, respectively, as defined by ASCE/SEI 41/06. These effective flexural stiffness values are consistent with results from tests of diagonally reinforced concrete coupling beams, indicating that the proposed precast embedment does not appreciably reduce the flexural stiffness of the element.
- The specimens exhibited a shear stiffness of approximately $0.04E_cA_g$ at drifts beyond 1%, which is only ten percent of the $0.4E_cA_g$ proposed in ASCE/SEI 41/06 for modeling coupling beams. The $0.4E_cA_g$ value does not account for reduction of shear stiffness as a result of diagonal or flexural cracking and thus, is not appropriate for coupling beams that may be subjected to large shear stresses.

CHAPTER 5:
COUPLED WALL SYSTEM TEST RESULTS

The two coupled wall specimens described in Chapter 3, which are referred to as Specimen CW-1 and CW-2, were built at approximately 1/3 scale and pseudo-statically subjected to the loading history shown in Figure 3.16. Both specimens consisted of four coupling beams linking two T-shaped structural walls. Slabs were included at the second and fourth levels to facilitate application of lateral displacements. Three of the coupling beams were precast with high-performance fiber reinforced concrete (HPFRC) and one was precast with regular concrete. The design of the coupling beams was based on the coupling beam component tests discussed in Chapters 3 and 4. The same coupling beam designs were used in Specimens CW-1 and CW-2, with one important difference. The longitudinal reinforcement of the coupling beams used in Specimen CW-1 was terminated 3 in. (75 mm) into the wall to be more consistent with current design practice, whereas all coupling beam reinforcement was fully developed into the walls in Specimen CW-2.

The reinforcement of the first two stories of the walls also differed. In Specimen CW-1, the walls were designed and detailed to satisfy the requirements of the ACI Building Code (318-08). For comparison purposes, HPFRC was used in the first two stories of the structural walls in Specimen CW-2. In the HPFRC walls, the boundary element confinement reinforcement was reduced and a higher shear stress was assumed to be resisted by the concrete. Also, dowel bars were placed along the cold joint at the wall-to-foundation interface to account for the lack of fibers crossing this cold joint. In addition to the axial compression applied to the lower two stories of the coupled wall specimens to simulate gravity loads, each wall was alternately subjected to compression and tension caused by coupling of the walls. Accordingly, the walls will often be referred

to as either the "compression" or "tension" wall with the understanding that this terminology refers to both walls at various times in the loading regimen.

Drift, which is used throughout this document as a measure of the deformation of the wall specimens, was calculated using Eq. 5.1 with the variables defined in Figure 5.1. Rigid body rotation of the entire specimen resulting from uplift of one foundation relative to the other needs to be subtracted from the calculated drift so that only deformations causing internal forces to develop within the coupling beams are considered. The θ shown in Figure 5.1 accounts for this uplift of one foundation relative to the other. It is calculated as the relative vertical displacement between the foundations, measured at the centroid of each wall, divided by the distance between the centroids of the wall areas.

$$Drift = \frac{\Delta - \left(\frac{\lambda_1 + \lambda_2}{2}\right) - \left(\frac{CB4_L - CB4_{L(inital)}}{2}\right)}{Height} - \theta \tag{5.1}$$

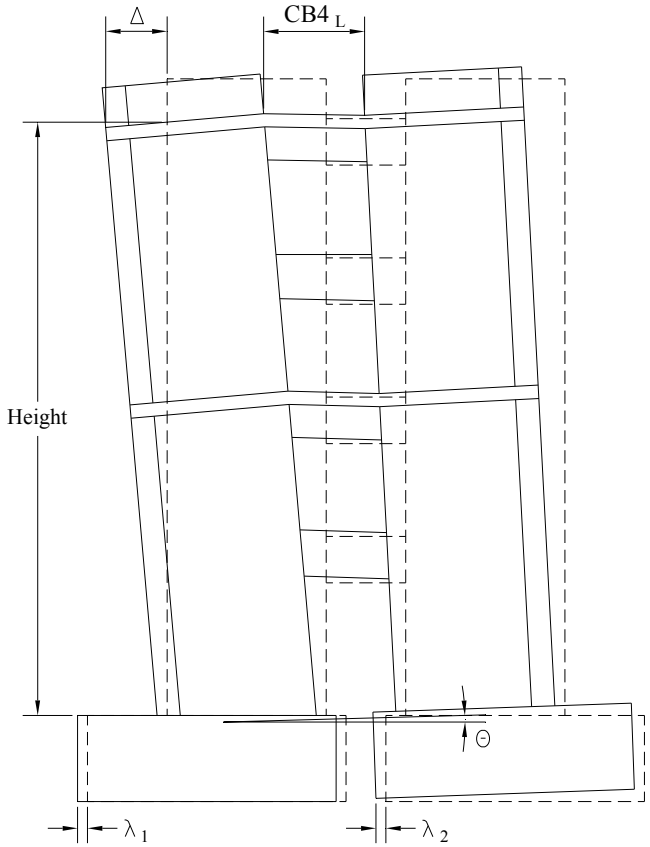

Figure 5.1 – Definition of terms used to calculate wall drift

This formulation of the drift equation assumes that rotation of the compression wall foundation is negligible. It underestimates the deformation demands placed on the compression wall, but accurately captures the system deformations that cause deformations in the beams and slabs.

5.1 CRACKING AND GENERAL DISCUSSION OF SPECIMEN RESPONSE

5.1.1 SPECIMEN CW-1 RESPONSE

A plot of the overturning moment versus drift response of Specimen CW-1 is shown in Figure 5.2. More than 90% of the ultimate overturning moment capacity of the system was maintained in both loading directions up to 2.3% drift, and more than 80% was maintained when the test was terminated at -2.8% drift. This is a significant level of deformation for coupled reinforced concrete shear walls. When the system drift exceeded 2.5%, the coupling beams all exhibited drifts exceeding 6.0%, with some exceeding 7.5%. As in previous chapters, coupling beam drift is used herein to describe the chord rotation referenced in ASCE/SEI 41/06 (2007), and is discussed further in Section 5.3. The very large coupling beam drift demands emphasize the need for highly ductile coupling beams. The full hysteresis loops in Figure 5.2 for Specimen CW-1 show no appreciable pinching, indicating good energy dissipation capacity. The wall reinforcement, which satisfied ACI Building Code (ACI 318-08) requirements, provided sufficient shear resistance and confinement to longitudinal reinforcement to allow for a stable flexural mechanism to develop in the base of both walls.

Throughout the test, a group of students used lamps and markers to identify and label cracks at various drift levels. The first cracks were identified after the drift cycle to 0.25% drift. At this early stage of loading, fine diagonal cracks were observed in all four of the coupling beams. Fine diagonal cracks were also observed in the first story of the structural walls, but only in the compression wall.

At a system drift of 0.5%, additional diagonal cracking was observed in the coupling beams. Diagonal cracks were also observed in the third and fourth wall stories, but only in the tension wall. This would be expected in situations where the principal

tensile stress is increased due to the net tension in the wall, leading to earlier diagonal cracking in the tension wall than in the compression wall. More obvious diagonal cracking was observed in the second wall story, in the tension wall, and in the first story of the compression wall. This is indicative of a transfer of shear stresses in the lower stories to the compression wall, which is a well recognized phenomenon in coupled wall systems. At this level of drift, some minor diagonal cracking was also observed in the first story of the tension wall.

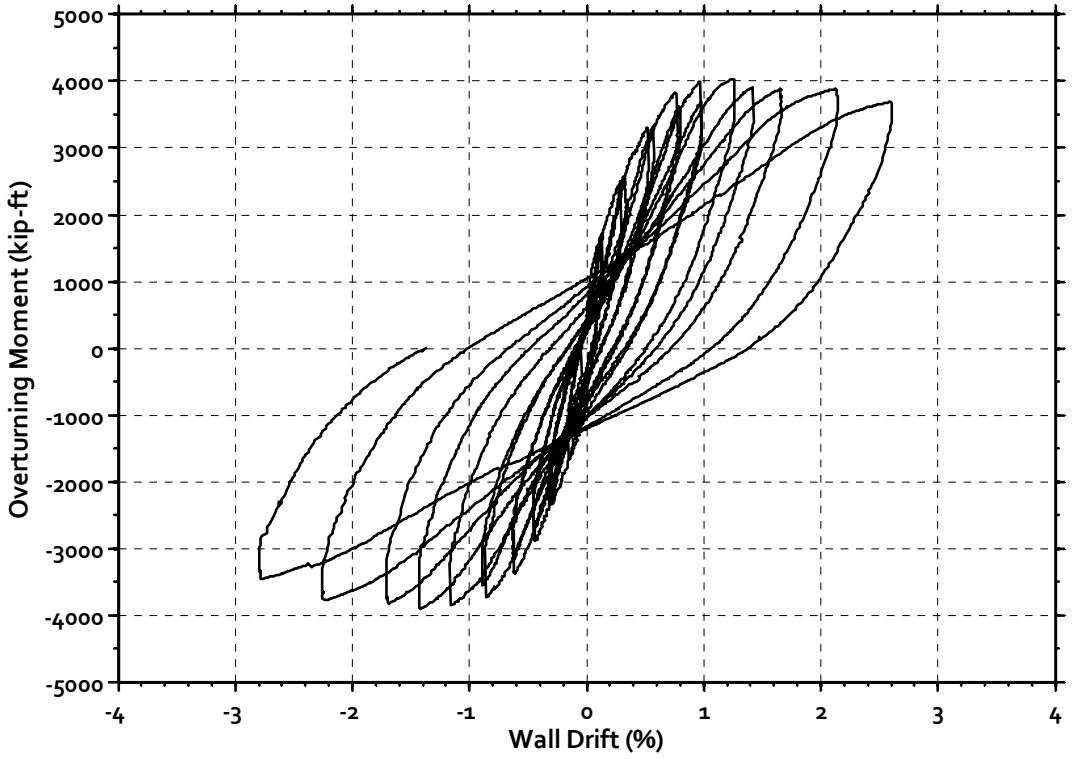

Figure 5.2 – Overturning moment versus wall lateral drift response for Specimen CW-1

At 0.75% drift, diagonal cracks in the first story of the compression wall extended and began to join with newly formed flexural cracks. Flexural cracks were also observed in the tension wall flange. The coupling beams continued to develop diagonal cracks, but no flexural cracks were observed. Instead, cracks were observed in the wall near the termination of the longitudinal beam reinforcement. Due to these cracks, it appeared that much of the flexural deformation was localizing at the beam-to-wall interface, instead of distributing throughout the beam. A picture of CB-4 at a system drift of 0.75% is shown

in Figure 5.3. The start of cracking within the wall, which was typical of the coupling beams at this drift, is evident on the right side of the figure. This damage was most obvious in the coupling beams located at the second and fourth floor levels.

At 1% drift, diagonal cracking in the walls was most pronounced in the first story of the compression wall, and in the second story of the tension wall. These diagonal cracks were measured to be approximately 0.04 in. (1 mm) wide, and spaced at approximately 5 in. (125 mm). The coupling beams did not exhibit much new cracking within the beam span, except for the coupling beam at the fourth story, which had developed some flexural cracks. The most notable cracks related to the coupling beams were in the wall near the interface with the beam, as shown in Figure 5.4, which were measured to be as wide as 0.25 in. (6-7 mm). Some spalling of the wall cover near the coupling beam at the fourth level was observed. A gap that was less than 0.04 in. (1 mm) wide was observed between the coupling beams in the second and fourth stories and the adjacent slabs, indicating that the responses of the slabs and coupling beams were likely to be increasingly independent of each other. This gap remained narrow and there was no measureable relative vertical displacement between the slab and beam at this drift level.

Loading cycles to 1.25 and 1.5% drift caused similar damage patterns, characterized by widening cracks along the beam-to-wall interface for the coupling beams at the third and fourth levels, spalling of cover concrete in the reinforced concrete

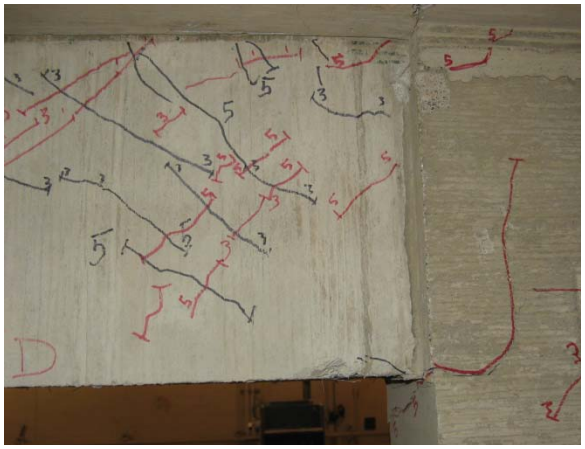

Figure 5.3 – Damage typical of coupling beams in Specimen CW-1 at a system drift of 0.75%. Cracking near the termination of the longitudinal beam reinforcement is evident in the wall.

Figure 5.4 – Damage localizing along termination of longitudinal coupling beam reinforcement at 1% system drift (Specimen CW-1).

Figure 5.5 – Final damage state at the base of Specimen CW-1 (left and right are east and west walls, respectively). Diagonal cracks occurred when each wall was in compression; flexural cracks predominantly occurred while each wall was in tension.

Figure 5.6 – Damage state of coupling beams in Specimen CW-1 after testing. Coupling beams from story level four down to one are shown from top to bottom, respectively.

coupling beam at the second level, intersecting diagonal cracks causing damage to the center of the coupling beam at the first level, and pronounced flexural cracks in the slabs near the inside faces of the walls. These flexural cracks in the slabs did not appear to result from interaction with the coupling beam. Rather, it appeared that plastic hinges were forming in each slab indicating that the slabs were acting as slender coupling beams, slightly increasing the coupling of the walls. No additional diagonal cracking and only a few new flexural cracks were observed in the walls beyond 1% drift.

Pushing the system to 1.75% drift caused further spalling of the wall cover concrete near the coupling beam-to-wall interfaces, which led coupling beam damage to concentrate along the interface rather than within the beams. Only the coupling beam at the first story continued to develop diagonal cracking in the central portion of the beam.

At 2% drift, some minor crushing was observed within the coupling beam compression zone at the fourth story. The coupling beams at the second and third levels appeared to be exhibiting primarily sliding shear displacements along the beam-to-wall interface rather than developing damage within the beam.

As shown in Figure 5.5, the structural walls had sustained only moderate damage by the end of the test; however, the integrity of the coupling beams had been severely compromised, as shown in Figure 5.6. The coupling beam at the first story had large cracks along the precast beam-to-wall interface, and significant shear related damage. The other coupling beams had little to no concrete remaining at the precast beam-to-wall interface. The test was terminated after the integrity of the structure had been compromised by what was recorded as fracturing of diagonal reinforcement in the coupling beams and flexural reinforcement in the walls.

5.1.2 SPECIMEN CW-2 RESPONSE

A plot of the overturning moment versus drift response of Specimen CW-2 is shown in Figure 5.7. More than 90% of the system's ultimate overturning moment capacity was maintained in both loading directions up to 2.1% drift. More than 80% was maintained up to 2.5% drift in the positive loading direction and 3.5% in the negative loading direction. These are significant deformations for coupled reinforced concrete shear walls. When the system drift exceeded 2.5%, the coupling beams exhibited drifts of

approximately 6.0%, with some exceeding 10% before termination of the test. The full hysteresis loops show no appreciable pinching, indicating good energy dissipation capacity. No buckling was observed in the wall longitudinal reinforcement, indicating that good confinement was achieved despite the significant reduction in the amount of ties provided for confining the wall boundary elements. A shear failure did occur in the base of the west wall that caused the drop in the coupled wall capacity evident in the last loading cycle in the positive loading direction. Upon reversal of the loading direction, a flexural mechanism dominated the response of the opposite wall, with a single dominant flexural crack located near the end of the dowel bars, which extended out of the foundation. This is shown in Figure 5.8.

A group of students used lamps and markers to identify and label cracks at various drift levels. The first cracks were identified after the drift cycle to 0.25% drift. Fine diagonal cracks were observed in all four of the coupling beams. The reinforced concrete coupling beam at the second floor level had the most cracks. Fine diagonal cracks were also observed in the structural walls at the first story level.

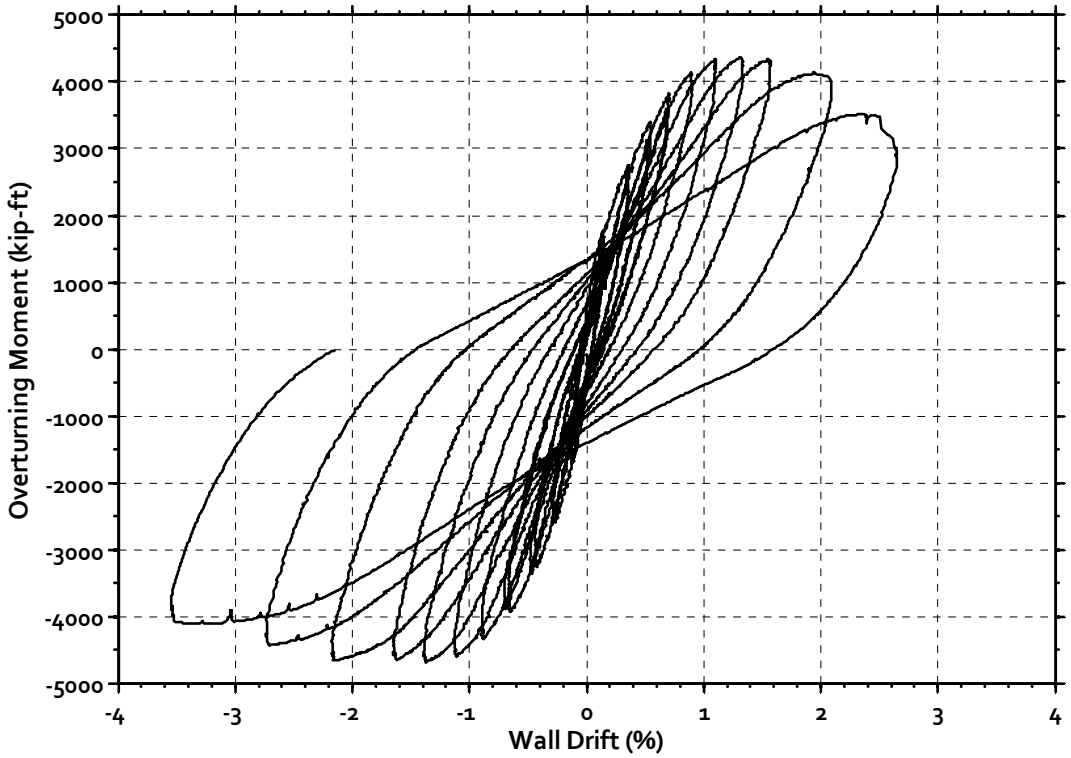

Figure 5.7 – Overturning moment versus wall lateral drift response for Specimen CW-2

Figure 5.8 – Photo of the base of the wall showing flexural cracking that localized at the termination of the dowel bars extending from the foundation

At a system drift of 0.5%, additional diagonal cracking was observed in all of the coupling beams. Diagonal cracks were observed in the second, third and fourth wall stories, but only in the tension wall, similar to Specimen CW-1. In the first story, diagonal cracking was observed primarily in the compression wall, which is indicative of a transfer of shear stresses in the lower stories to the compression wall. However, this force transfer was observed to a larger extent in the test of Specimen CW-1.

At 0.75% drift, it was observed that additional diagonal cracking had developed in both the compression and tension walls at the third and fourth stories. In the first story of the walls, diagonal cracks were still primarily observed in the compression wall. Unlike the observed cracks in Specimen CW-1, diagonal cracks had not yet begun to join flexural cracks in the first two stories at this drift level, at least not to an extent notable by visual inspection. Only minor flexural cracking had been observed at 0.75% drift, and was noted in the flange of the tension wall. It is likely that more cracks were present, but as a result of using steel fiber reinforcement, they would have been so fine that they could not be identified. The coupling beams continued to develop diagonal cracks, but only a few flexural cracks were observed. Also at a system drift of 0.75%, the reinforced concrete coupling beam at the second story began to exhibit a somewhat different crack pattern than the HPFRC coupling beams. The reinforced concrete beam exhibited numerous intersecting diagonal cracks that extended to the edges of the beam, giving it the appearance of having “shattered”. The HPFRC coupling beams also exhibited

predominantly diagonal cracks, but those wide enough to be visually identified were much less numerous and did not extend to the edges of the beam. A comparison of the HPFRC and reinforced concrete coupling beams at 0.75% drift is shown in Figure 5.9.

As with the test of Specimen CW-1, the diagonal cracking in the walls was most pronounced in the first story of the compression wall, and in the second story of the tension wall at a system drift of 1.0%. These diagonal cracks were just hairline cracks and were, on average, spaced at only 1 or 2 in. (25 or 50 mm). This is less than half of the spacing observed at this point in the test of Specimen CW-1, which had reinforced concrete structural walls. At this stage in the loading regimen, few new cracks were observed in the third and fourth stories of the walls, while the coupling beams exhibited some minor additional diagonal cracking. Unlike the test of Specimen CW-1, no major crack was observed to form along the precast beam-to-wall interface, indicating that the full development of the beam reinforcement was sufficient to prevent significant deformation at the cold joint between the precast beam and cast-in-place wall.

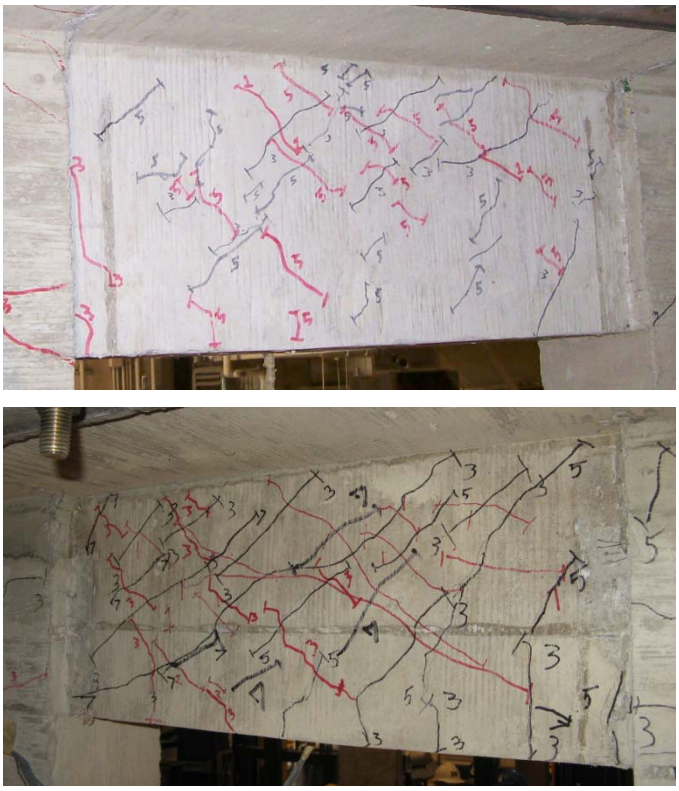

Figure 5.9 – Damage state of coupling beams at a system drift of 0.75%. HPFRC and reinforced concrete coupling beams are shown top and bottom, respectively.

During the loading cycle to 1.5% drift, diagonal cracks widened to approximately 0.04 in. (1 mm) in the third and fourth story walls. In the first story of the wall, flexural and diagonal cracks were interacting to form flexural-shear cracks. This phenomenon was first observed in the reinforced concrete walls of Specimen CW-1 at a drift of 0.75%. Some additional diagonal cracking and minor superficial flaking were observed in the HPFRC coupling beams at the first, third, and fourth levels, along with some opening of flexural cracks to approximately 0.04 in. (1 mm) within the third story coupling beam. Spalling of cover concrete, exposing the stirrups, was observed in the reinforced concrete coupling beam at the second level. Flexural cracks in the slabs indicated the development of plastic hinges, as was observed in the test of Specimen CW-1. At this point in the test, a thin gap (less than 0.04 in., or 1 mm, wide) was visible along the precast beam-to-slab interface, implying that the beam and slab were acting independently. However, there was no noticeable relative vertical displacement.

At 2% drift, the flexural crack near the base of the east wall at the point of termination of the dowel reinforcement crossing the wall-to-foundation interface widened to approximately 0.12-0.16 in. (3-4 mm). Upon reversal of the loading direction, the widening of several diagonal cracks in the compression wall (on the west side of the system) that extended from the lower corner of the first story coupling beam towards the wall compression flange was observed. This opening of diagonal cracks was not observed in the east wall. Pushing the system to 2% drift also caused further superficial flaking of the surface of the HPFRC coupling beams and opening of inclined cracks in these beams to a width of approximately 0.04 in. (1 mm). The widest cracks in the first and fourth story coupling beams were diagonal cracks, whereas flexural cracks were the widest cracks in the third story coupling beam. At this same drift level, spalling of the reinforced concrete coupling beam at the second story had progressed to the point of exposing three stirrups. Unlike the test of Specimen CW-1, no sliding shear displacements were visually observed between the coupling beams and the adjacent walls.

Further loading of Specimen CW-2 to approximately 2.5% drift in the negative (west) direction caused the west wall, which had exhibited widening diagonal cracks at 2% drift, to suddenly fail in shear as cracks stemming from the bottom of the first story coupling beam propagated through the web of the wall and penetrated the compression

flange. The result was a failed compression zone. Despite this, the system continued to resist more than 60% of the peak overturning moment capacity, indicating that some redistribution of base shear stresses to the tension wall likely occurred. Upon reversal of the loading direction, the wide flexural crack observed at 2% drift in the east wall along the end of the dowel bars continued to widen and led to a flexural failure mode characterized by failure of the compression zone at a system drift of 3.5%. The ultimate damage state of the first story of each wall is shown in Figure 5.10.

Although not apparent during testing, further investigation revealed that diagonal reinforcement in the coupling beam at the fourth level had buckled near midspan. The sparse instrumentation on the fourth story coupling beam makes it difficult to identify the point at which buckling initiated; however, consideration of the damage state in the beam through photographs can offer clues. Photographs taken of the fourth story coupling beam at system drifts of 2.5, 3.0, and 3.5% (which correspond to approximately 4.5, 6,

Figure 5.10 – Final damage state of the first story walls of Specimen CW-2 (left and right are east and west walls, respectively). Diagonal cracks occurred when each wall was in compression, flexural cracks predominantly occurred while wall was in tension.

(a) At coupling beam drift of 4.5%

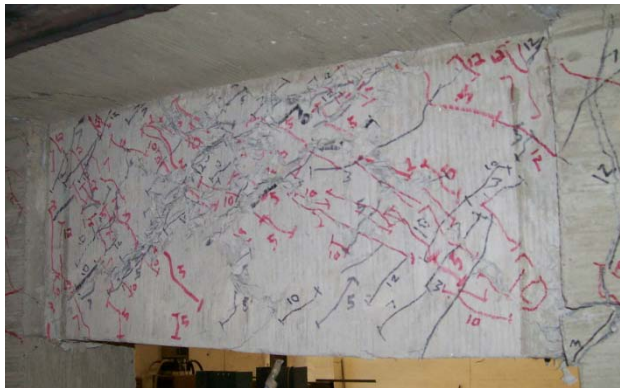

(b) At coupling beam drift of 6.0%

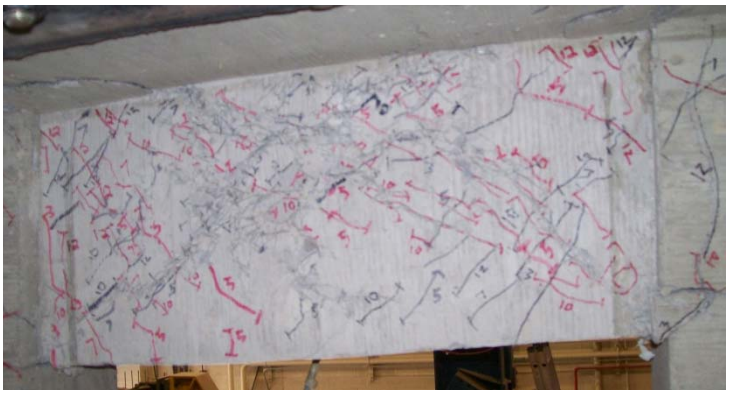

(c) At coupling beam drift of 9.0%

Figure 5.11 – Damage of coupling beam CB-4 in Specimen CW-2. Buckling may have begun by 6.0% drift

Figure 5.12 – Damage state of coupling beams in Specimen CW-2 after testing. Coupling beams from story level four down to one are shown from top to bottom, respectively.

and 9% coupling beam drift) are shown in Figure 5.11. At a coupling beam drift of 6%, significant damage in the middle of the coupling beam was evident, suggesting that buckling may have begun developing by this drift cycle. The first and third level HPFRC coupling beams remained sound throughout the test, and it was not possible to expose the diagonal reinforcement after termination of testing. Therefore, no buckling of the diagonal bars was believed to have occurred in these beams.

The final loading cycles caused severe spalling of the reinforced concrete coupling beam at the second floor level that exposed nearly all of the reinforcement, rendering the beam structurally nonfunctional. The HPFRC coupling beams exhibited slightly varied damage states, pictured in Figure 5.12, but generally remained sufficiently undamaged to contribute to the stiffness and strength of the coupled wall system.

5.2 WALL DEFORMATIONS WITHIN THE FIRST STORY

A dense array of instrumentation was placed on the first story of the coupled wall specimens, as described in Chapter 3. The data recorded throughout the tests was used to determine the distribution of flexural rotations, shear strains, and axial deformations in the first story of the walls. For many of the calculations the wall was divided into "strips", as shown in Figure 5.13. The following section discusses the measured deformations in the first story of each wall.

5.2.1 WALL CURVATURE

The average curvature exhibited by each strip of the wall was calculated using the difference between the rotations of the row of markers above and below the strip, divided by the initial thickness of the strip. Significant scatter, caused by cracking near individual marker locations, was observed and made trends difficult to identify. Averaging the recorded curvatures for each group of three strips (1-3, 4-6, and 7-9) reduced the scatter and helped clarify the trends. The resulting average curvature calculated for each group of three strips at various wall drift levels is shown in Figure 5.14(a)-(d). The theoretical

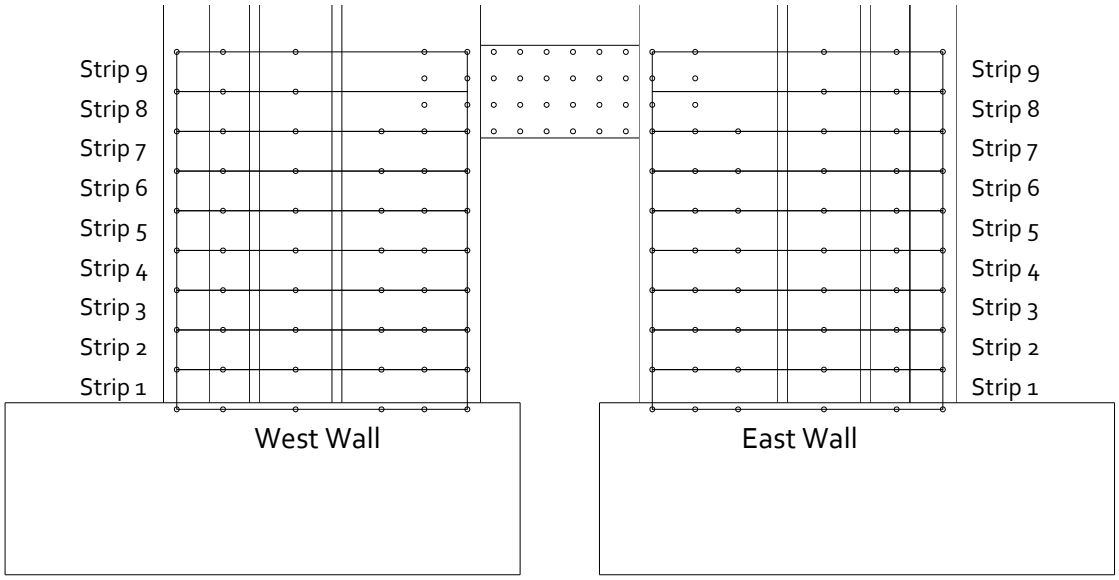

Figure 5.13 – Location of wall strips used in calculation of wall deformations

yield curvature is also plotted in each of the figures. The theoretical yield curvature was calculated using a moment curvature analysis with measured material properties as input and neglecting axial forces in the walls caused by coupling. Measured wall curvature at first yield would have been used, but inconsistent strain gauge data in the base of the walls made this difficult to estimate. Regardless, in every case but one, average curvatures exceed the theoretical yield curvature. This indicates that plastic flexural deformations generally developed throughout the first story. The extent to which the observed curvatures exceeded the theoretical yield curvature in the last loading cycle is indicated by the average curvature ductility for each group of three strips, shown in Figure 5.14 as μ_ϕ. Curvature ductility was calculated as the curvature at the peak drift divided by the theoretical yield curvature. In a few cases, the curvature ductility is given as "not a number," abbreviated as NaN, indicating that disruption of the instrumentation late in the test due to wall damage prevented calculation of the curvature in the last loading cycle.

Two important observations can be made on the basis of these plots. First, average curvatures large enough to cause flexural yielding were recorded throughout the first story (which corresponds to approximately one member depth). There is a clear trend of large curvature ductility near the foundation, and diminishing ductility demands

further up the wall. Although no instrumentation was placed above the first story that can be used to calculate curvature ductility demands, a rough projection of the trend of diminishing curvature demands away from the foundation indicates that curvature ductility greater than 1.0 was unlikely above the first coupling beam. Although approximate, this indicates that the plastic hinge length can be estimated as the depth of an individual wall. The second observation comes from comparing the curvatures calculated for the compression wall to those of the tension wall. In every case except one, larger curvatures were observed in the compression wall than in the tension wall throughout the first story. The only exception to this trend is the middle strip in the negative loading direction of Specimen CW-2, where very large curvatures close to the foundation in the compression wall lowered the curvature demands further up the wall.

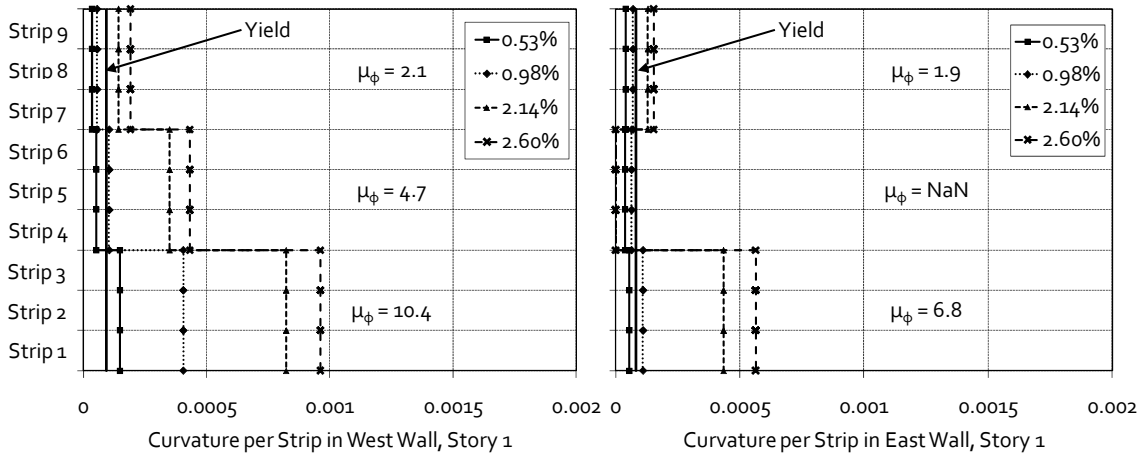

(a) Specimen CW-1, Positive drift (left = compression wall, right = tension wall)

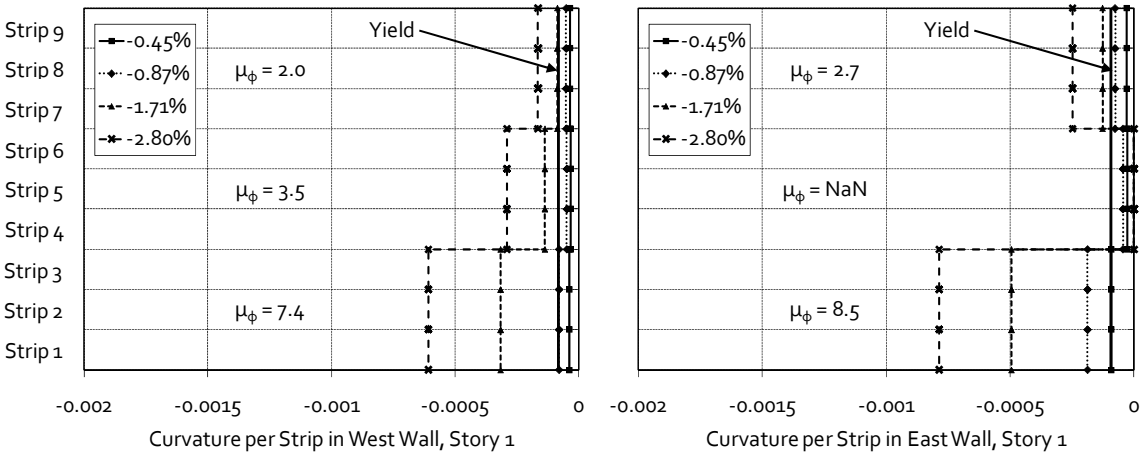

(b) Specimen CW-1, Negative drift (left = tension wall, right = compression wall)

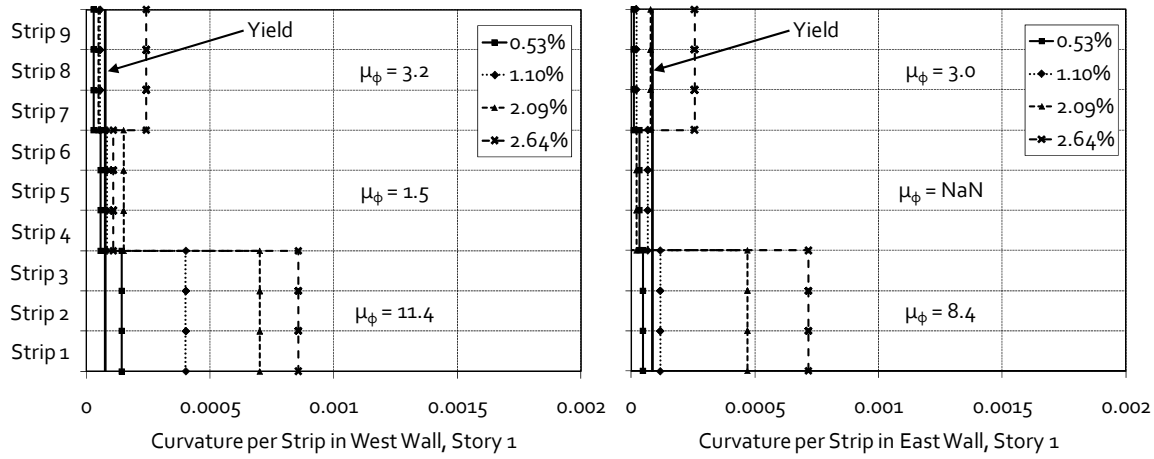

(c) Specimen CW-2, Positive drift (left = compression wall, right = tension wall)

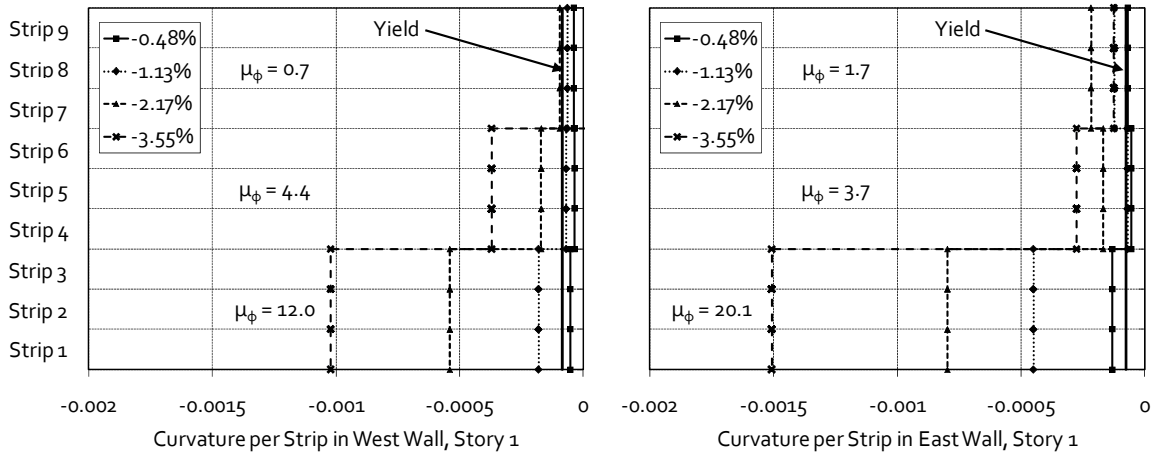

(d) Specimen CW-2, Negative drift (left = tension wall, right = compression wall)

Figure 5.14 – Average wall curvature for strips 1-3, 4-6, and 7-9 in the first story of the walls, with peak curvature ductility labeled

The primary explanation for the larger curvatures recorded in the compression walls is that the separate wall foundations allowed for the base of the tension wall to slide towards the compression wall. This sliding reduced the deformation demands placed on the tension wall and required the plastic hinge region in the compression wall to develop larger deformations than in the tension wall.

5.2.2 Shear Deformation

The average shear distortion calculated per strip of wall in the first story of the coupled wall system is shown in Figure 5.15. The same method described in Chapter 4

for calculating shear distortions in the coupling beam specimens was used. The plot of average shear distortion per strip in Specimen CW-1, shown in Figure 5.15(a) and (b), indicates that the average shear distortion generally increased closer to the foundation, even though the average shear stress within a wall did not vary between the bottom of the coupling beam (located in strip 7) and the foundation. The larger shear distortion near the foundation was primarily due to a reduction in the wall shear stiffness caused by larger flexural rotations near the base of the wall.

A general trend of larger shear distortion in the compression wall was observed in both loading directions of Specimen CW-1. For the drift cycle to approximately 2% drift, the average shear strains were 160% and 185% larger in the compression wall in the positive and negative loading directions, respectively. In general, larger shear strains in the compression wall could be caused by two interacting phenomena. The primary cause is the shift of shear force to the compression wall, which has been well documented in coupled wall systems. The reductions in shear stiffness associated with the larger flexural rotations that develop in the compression wall are a second reason for larger shear strains to be recorded. Both of these phenomena would be somewhat offset by the increase in shear stiffness expected in the compression wall due to axial compression forces. As with the discussion of flexural rotations in the walls, the extent to which these observations apply to real building systems is difficult to judge on the basis of these tests. This is because the deformation demands were larger in the compression wall than in the tension wall due sliding of the tension wall foundation towards the compression wall described in Section 5.2.1.

The average shear distortion per strip in Specimen CW-2, shown in Figure 5.15(c) and (d), is more erratic from strip to strip. This greater inconsistency from strip to strip is believed to be caused by diagonal cracks that cut across strips. This is especially true in later loading cycles on the west side of the system, where a shear crack dominated the failure of the specimen. Despite the erratic nature of the data, the same trend of larger average shear distortions in the compression wall can be observed, with average shear distortions 80% and 90% larger in the compression wall for the positive and negative loading directions, respectively. In Specimen CW-2, the largest shear deformations were measured in strip 2, where the termination of dowel bars from the foundation forced large

flexural rotations and a corresponding reduction in shear stiffness. In the final loading cycles, sliding shear displacements along flexural cracks within this strip were the primary contributors to the plotted shear distortion. The very large shear distortions in strips 6 and 7 of the west (left) wall captured the movement along the failure plane that led to failure of the wall. This failure is discussed further in Section 5.2.2.1.

Another way to visualize the distribution of shear distortion in the first story of the wall system is through the orientation of principal strains. Principal tensile strains (shown as outward pointing arrows) and compressive strains (shown as inward pointing arrows) for each rectangle in the grid of optical markers are shown in Figure 5.16. The principal strains are calculated from the normal and shear strains measured for each grid

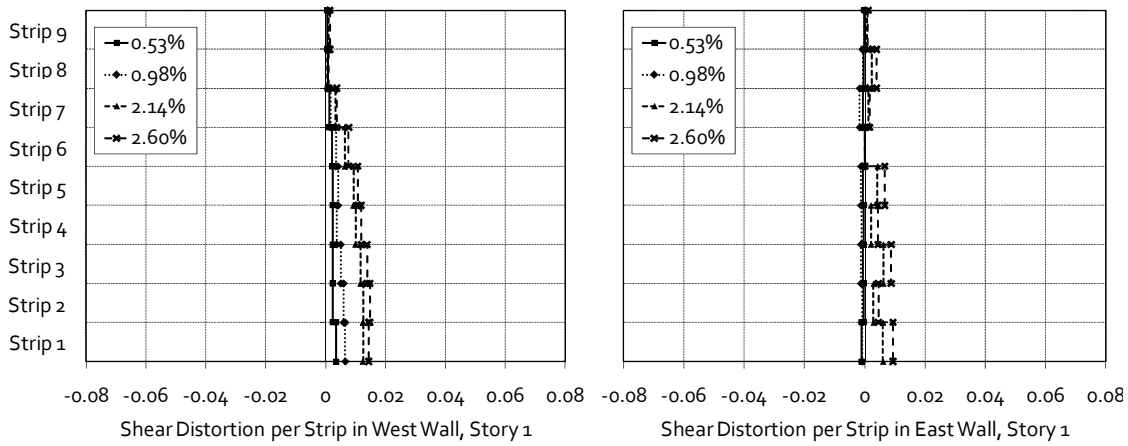

(a) Specimen CW-1, Positive drift (left = compression wall, right = tension wall)

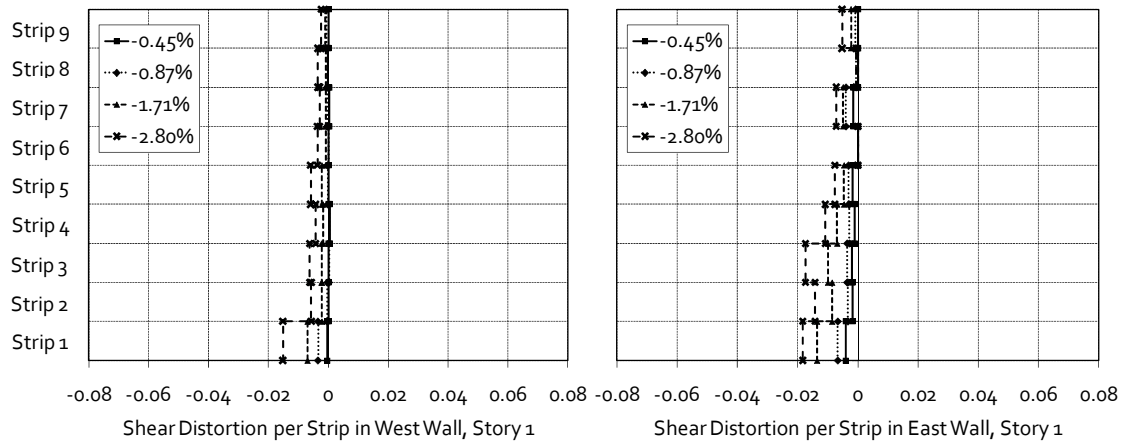

(b) Specimen CW-1, Negative drift (left = tension wall, right = compression wall)

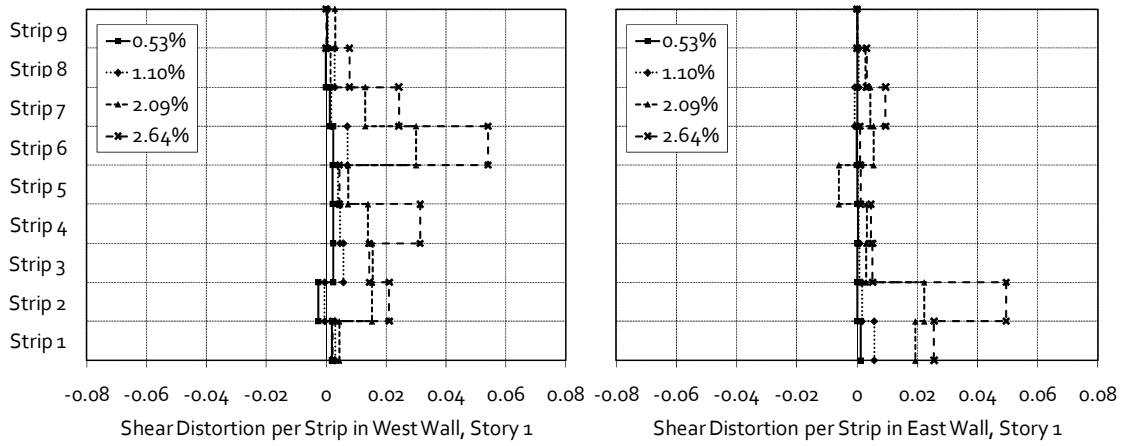

(c) Specimen CW-2, Positive drift (left = compression wall, right = tension wall)

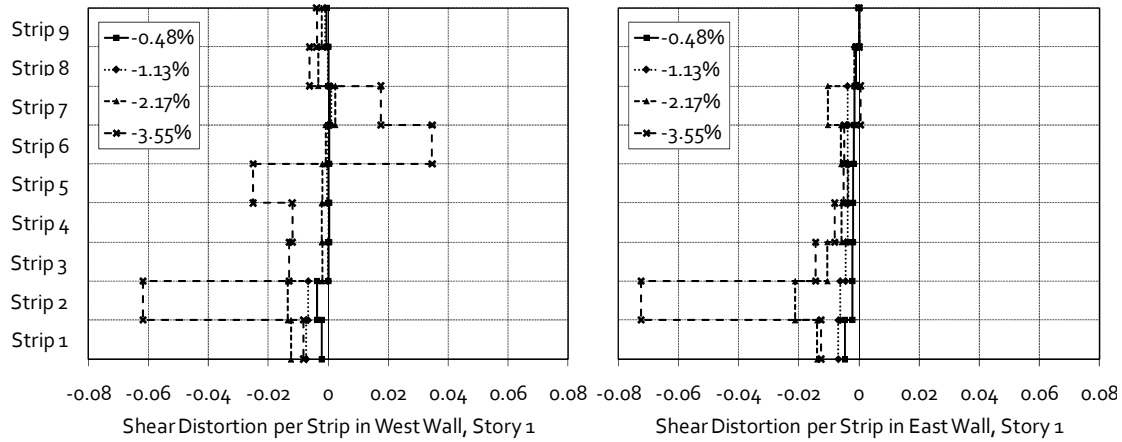

(d) Specimen CW-2, Negative drift (left = tension wall, right = compression wall)

Figure 5.15 – Average shear distortion per strip in the first story of the walls

unit using Mohr's circle. Principal strains plotted in-line with the horizontal and vertical axes represent zero shear strain, whereas, for a given average between the horizontal and vertical strains, a principal strain orientation closer to 45 degrees shows an increase in shear strain. The distribution shown in Figure 5.16 was measured in Specimen CW-2 at the peak drift of the loading cycle to -1% drift; however, this distribution is generally typical of both specimens and loading directions.

The wall subjected to tension, shown on the left of Figure 5.16, exhibited small principal strains compared to the compression wall. The principal strains observed in the leftmost column of grid units in the tension wall are approximately vertically oriented,

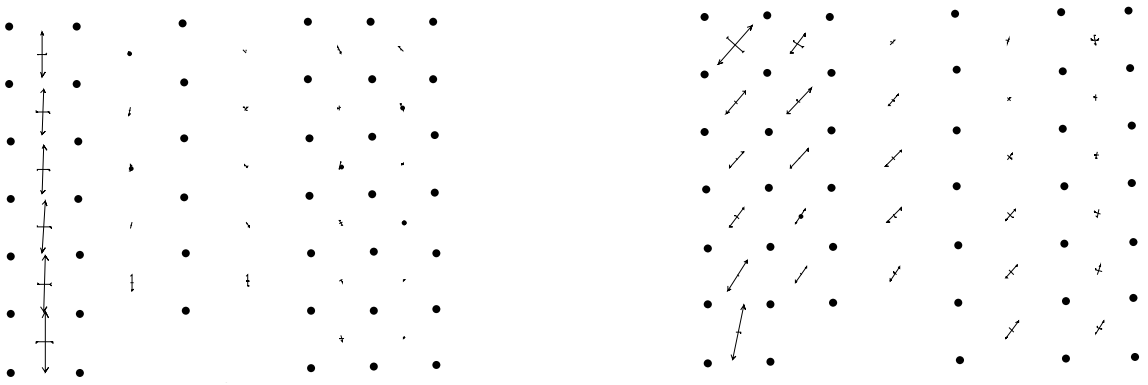

Figure 5.16 – Typical example of average principal strain distribution and orientation within the first story of the walls. Outward and inward pointing arrows indicate tensile and compressive strains, respectively. Arrow length is proportional to the magnitude of the principal strain.

indicating very little shear strain in these grid units. In these squares, the axial tensile strains caused by coupling added to the tensile strain demands from flexural rotations. Most of the rest of the principal strains in the tension wall were small in magnitude.

In contrast, the compression wall (on the right of Figure 5.16) exhibited principal tensile strains with larger magnitudes, caused by the combination of large flexural rotations and significant shear strains. Interestingly, if lines are drawn along the principal compression strains (or perpendicular to the principal tensile strains) and extended towards the compression zone of the wall, they appear to approximately come to a point near where the flange of the wall meets the foundation. This visually creates a "pinwheel" effect where principal tensile strains appear to encircle the union of the compression zone and the foundation. The magnitude of the principal tensile strains also appears to be approximately proportional to the distance from the center of the circle. This 'pinwheel' effect is observed from the foundation up to a line connecting the coupling beam to the union of the foundation and the wall flange. Beyond this line, principal strains are relatively small. This is consistent with a diagonal strut developing between the coupling beam and the wall compression zone near the foundation.

A comparison of the measured shear stiffness in the walls of Specimens CW-1 and CW-2 is also of interest because the presence of fibers is expected to increase the shear stiffness after cracking compared with regular reinforced concrete. Although this

comparison is problematic because the shear stress imposed on each individual wall is not known, an attempt was made by using an average shear stress taken over the full area of the wall webs. Strips 1 and 2 were ignored in this calculation because dowel bars in Specimen CW-2 affected the wall deformations in these strips. Strips 8 and 9 were also ignored to minimize the impact of the coupling beam at the first floor level on this comparison. Given these assumptions, the average shear stiffness in strips 3-7 of the compression wall was 15%, 60%, and 25% higher in Specimen CW-2 than in Specimen CW-1 at system drifts of 0.5%, 0.9% and 1.3%, respectively. Therefore, the results consistently indicate that the HPFRC walls exhibited larger shear stiffness than the conventional reinforced concrete walls. This is remarkable given that, for the same drift demands, larger shear stresses were imposed on the HPFRC wall system and that significantly lower strength concrete was used throughout the first story in Specimen CW-2. Both of these factors would be expected to reduce the shear stiffness in the walls of Specimen CW-2. Therefore, the measured increase in shear stiffness may have been higher had there been comparable shear stresses and concrete strengths. It is important to consider that these mean stiffness increase values have standard deviations (between the calculated stiffnesses of rows 3-7) of 55%, 60%, and 15%, respectively, so there is appreciable variability in the data. Comparisons at larger system drifts are significantly more variable, and are not reported. Although the shear stiffness in the tension wall was also larger in Specimen CW-2 than in Specimen CW-1, the values are not reported because of the significant variability in the test data.

5.2.2.1 Shear Failure in Specimen CW-2

Restricting the propagation and opening of diagonal shear cracking in coupled walls, such that a more ductile flexurally dominated response controls the behavior, is of critical importance when designing coupled wall systems. A flexurally dominated response was achieved in both walls of Specimen CW-1, which were reinforced with transverse and boundary element confinement reinforcement conforming to the ACI Building Code (ACI 318-08) requirements. The east wall of Specimen CW-2, which was designed assuming a higher shear stress contribution from the concrete, as described in Chapter 3, and boundary element confinement reinforcement spaced at $t_w/2$, developed

a similar ductile flexural mechanism. This demonstrates that HPFRC can be relied upon to provide confinement and to resist higher shear stresses than conventional reinforced concrete. Only the west wall of Specimen CW-2, which was designed with the same transverse reinforcement as the east wall but with boundary element confinement spaced at t_w, developed a brittle shear failure mode. This wall performed in a ductile flexural manner up to drift demands of 2%, but eventually failed in shear at 2.5% drift.

A photograph of both faces of the west wall, immediately after the shear-compression failure, is shown in Figure 5.17. It can be seen that the final failure plane extended nearly horizontally from the bottom of the coupling beam to approximately mid-depth of the wall. As it neared the flange, the failure plane followed a preexisting diagonal crack, which opened and eventually penetrated the compression zone. The failure of the compression zone destroyed the flange's ability to resist compression and shear stresses, and marked the point of wall failure in the positive loading direction.

The initial horizontal portion of the failure plane is interesting. Close inspection of the crack patterns marked prior to formation of the failure plane showed that horizontal flexural cracks were not observed in this portion of the wall. Rather, diagonal cracks, which were inclined more steeply than the final failure plane, formed a closely spaced network of cracks oriented so as to point from the coupling beam towards the foundation. It is likely, especially given the very poor quality concrete in this portion of the wall (the compressive strength was less than 50% of the design concrete strength), that the struts transferring compression stresses between the diagonal cracks became unstable and began to crush. This observation is supported by measured principal compression strains as large as 4% prior to the development of the shear failure. This web-compression type damage allowed for lateral displacement of the upper face of the failure plane with respect to the lower face. Subsequently, as the web-compression failure plane intersected a dominant diagonal crack near the flange, the wall web was no longer able to resist the very large diagonal tension stress demands, and began to pull apart. This led to the eventual failure of the compression zone.

This interpretation of the failure plane progression is corroborated by the distribution of shear strains within the west wall in the final positive loading cycle, which

Figure 5.17 – Photographs of the failure plane in Specimen CW-2 from both faces of the wall specimen

is shown in Figure 5.18. After multiple reversals of the loading direction, the shear strain distribution at 0% drift (shown in Figure 5.18(a)) indicates that large permanent localized shear distortions, on the order of 0.04-0.05 radians, had developed in the west wall near the bottom of the first story coupling beam. These large shear distortions were also observed along the horizontal portion of the failure plane and preceded any increase in distortions nearer to the compression zone. This indicates that the flange had not yet failed at this point in the loading sequence. The distribution of shear strains at 1.0% drift (shown in Figure 5.18(b)), shows that shear distortions had increased to approximately 0.06 radians along the horizontal portion of the failure plane, but still had not markedly increased in the compression zone. At a system drift of 2.3%, large shear deformations, on the order of 0.04 radians, finally developed in the compression zone after very large shear strains, on the order of 0.1 radians, had developed along the horizontal portion of the failure plane (Figure 5.18(c)). This shows that the combined web-crushing and diagonal tension failure in the web had compromised the ability of the web to resist shear forces. This resulted in a transfer of shear force to the compression zone (wall flange), which caused the large compression zone shear deformations recorded at 2.3% drift. These large compression zone shear strains are believed to have resulted in instability and

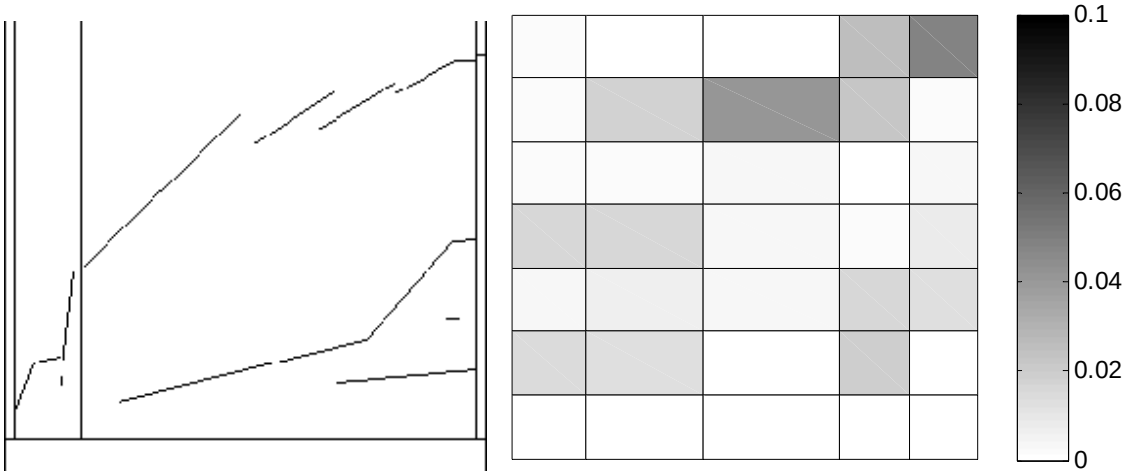

(a) 0% drift (after multiple reversals of loading)

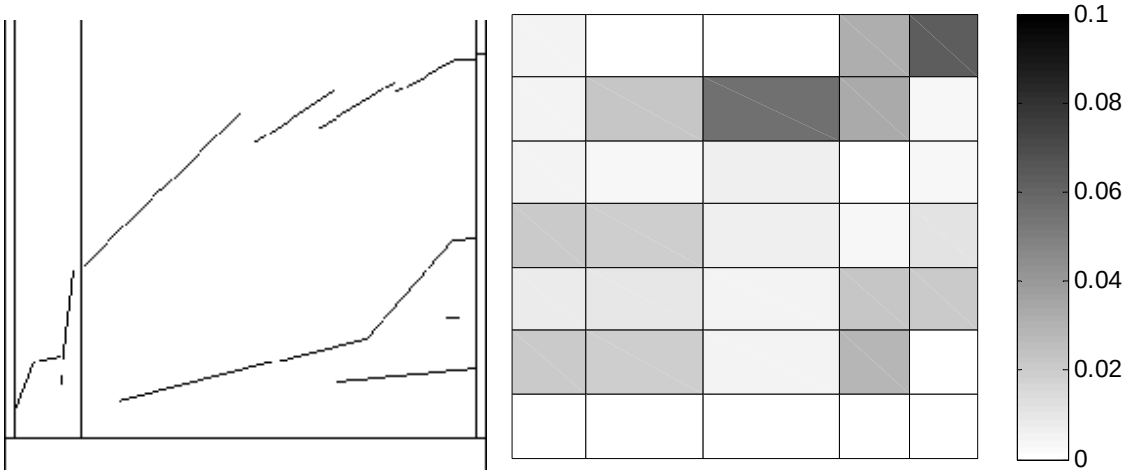

(b) 1.0% drift

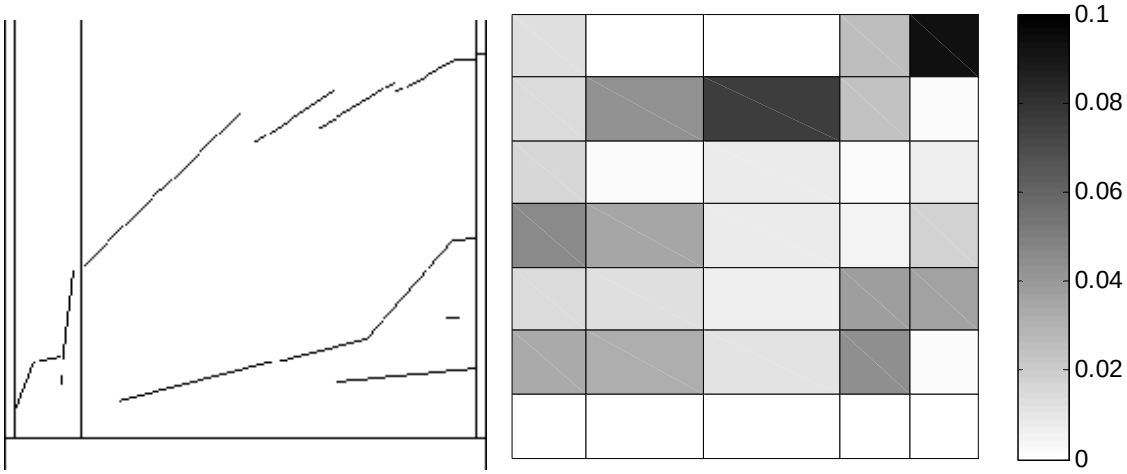

(c) 2.3% drift, the point of peak lateral force within the last positive loading half-cycle

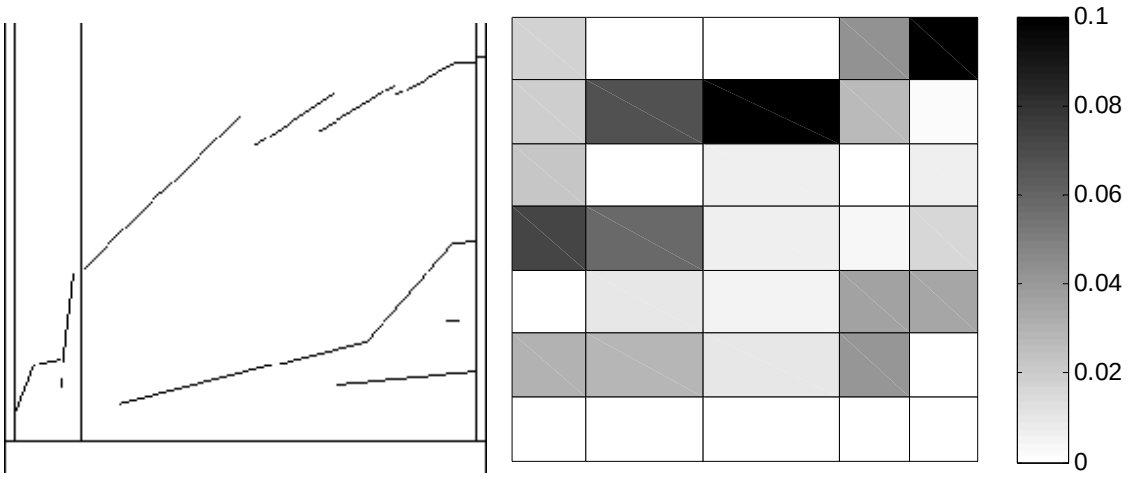

(d) 2.6% drift, the point of peak lateral drift within the last positive loading half-cycle

Figure 5.18 – Location of dominant cracks (left), and average shear strain in each instrumentation grid unit (in radians), calculated at various points within the final positive loading half-cycle

subsequent failure of the compression zone with a corresponding reduction in the system lateral force capacity in the positive loading direction. Therefore, instability of the compression zone was most likely caused by the shear failure and not the reverse.

Given the explanation presented above, it seems the (poor) concrete quality was most likely the root cause of the failure and not the spacing of horizontal or boundary element confinement reinforcement. The horizontal reinforcement in the wall did not prevent failure because the initial horizontal leg of the crack ran parallel to the reinforcement, so the reinforcement could not engage it. The boundary element confinement reinforcement was spaced more widely in this wall than in any other; however, the HPFRC appeared to provide good confinement despite the poor quality of the matrix. No indication of buckling of longitudinal bars was observed prior to the shear crack penetrating the compression zone, and all of the longitudinal reinforcement was still intact and active when the loading direction was reversed after the shear failure. It is impossible to know with confidence whether a more heavily confined compression zone would have provided a meaningful improvement in the failure mode, but it is doubtful.

Given the good response in the east (right) wall, and the determination that the source of the shear failure in the west (left) wall was web crushing due to poor concrete quality, the following can be said for the detailing provided in Specimen CW-2. It was reasonable to assume that the contribution of HPFRC to shear stress resistance is $4\sqrt{f_c'}, [psi]$ $\left(0.33\sqrt{f_c'}, [MPa]\right)$ when designing the walls. It was also shown that HPFRC coupled walls with relaxed boundary element confinement spaced at $t_w/2$ behaved favorably, even when subjected to large drift demands. Further relaxation of the boundary element confinement reinforcement spacing to t_w was not conclusively shown to be either safe or unsafe in design, although this wall did behave in a stable flexural manner up to drifts of 2%. Further testing is warranted, given the inconclusive nature of the test result for the two walls of Specimen CW-2.

5.2.2.2 Wall Twist

The algorithm employed for calculation of average shear distortion per strip initially led to unrealistically large shear distortion along the interface between the foundation and the walls that was not consistent with observations made during the tests. Further inspection of the data revealed that throughout the loading regimen the walls were twisting, or rotating about their vertical axis. This twisting led grid points fixed directly to the wall to move laterally relative to the points fixed to the foundation, which were 32.5 in. (813 mm) closer to the stationary infrared cameras (Figure 5.19). Once the twist of the walls was calculated and its effect on shear distortion accounted for, the average shear deformations in the strips nearest the foundation were more consistent with observed damage.

The twisting of the walls is believed to have had little impact on the overall performance of the coupled walls, aside from a need to be accounted for prior to interpretation of the data. A close look at the data indicates it is likely that the tension wall was the root cause of the twisting, as a slight uplift reduced the frictional forces between the base of the foundation and the laboratory floor. This allowed uneven horizontal reaction forces to act on the foundation, which consequently caused twisting of the wall. This twist travelled up the tension wall and forced some corresponding twist in

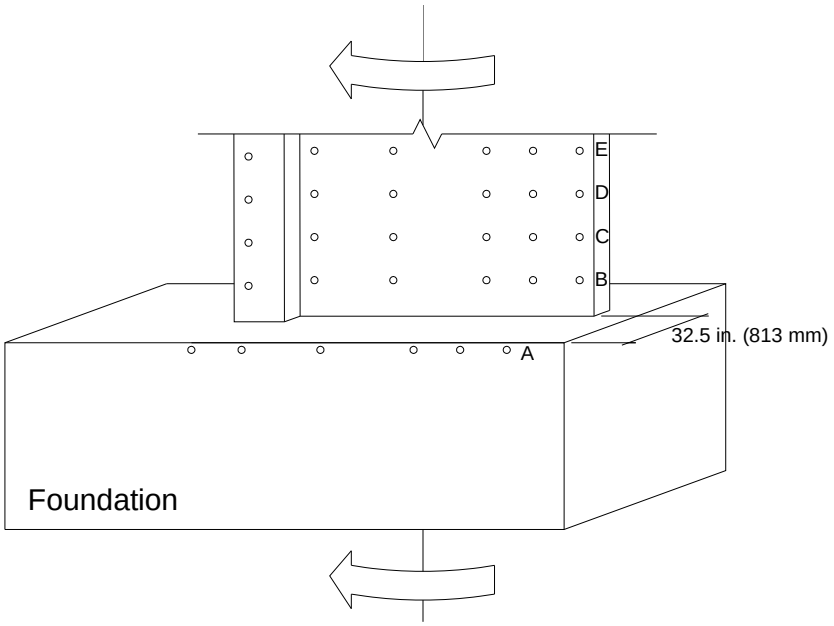

Figure 5.19 – The twist of individual walls about a vertical axis caused markers in row A (on the foundation) to move laterally relative to the markers in rows B through E (on the wall) due to their proximity to the stationary cameras

the compression wall in the opposite direction. For example, if the tension wall exhibited positive twist, the compression wall exhibited negative twist to satisfy compatibility of the coupled system (Fig 5.20). It is shown in Figure 5.21, which compares the twist observed in each of the walls at the level of CB-1 and at the foundation, that this phenomenon developed in the specimens tested. The twist of the individual walls was generally similar in magnitude (perhaps somewhat larger in the wall furthest from the loading frame), but opposite in sign. The twist was largest at the foundation and decreased further up the walls as the compression wall and out-of-plane flexural rigidity of the beams and slabs worked to limit the system to planar deformations. Fortunately, no indication of twisting or torsion related damage was observed during testing. This is likely because the relative twist between the foundation and first story coupling beam remained relatively small throughout the test. This relative wall twist was generally in the range of $0.002 - 0.004$ radians, and never larger than 0.009 radians. This corresponded to a maximum twist rate of 0.000167 radians/in.

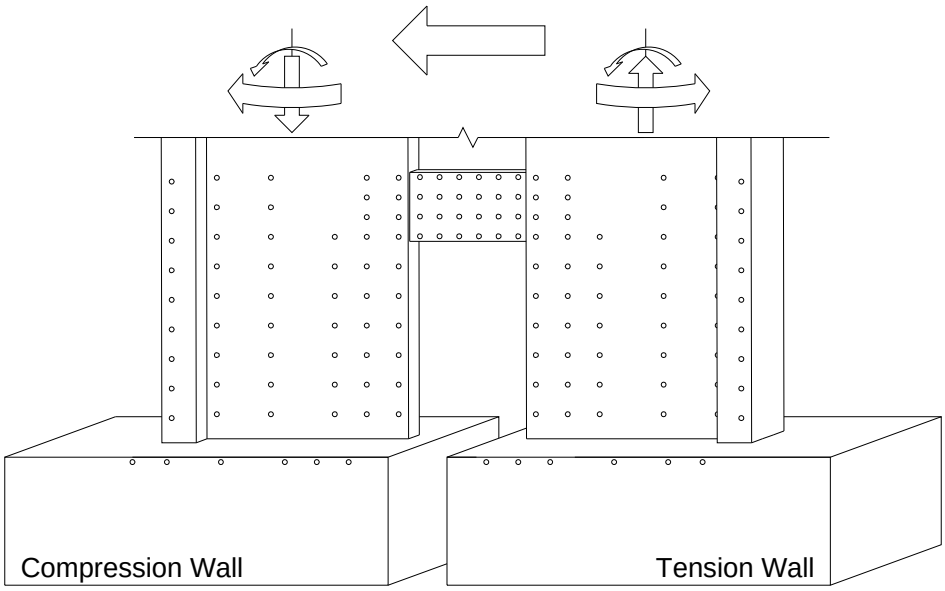

Figure 5.20 – Example of positive (or negative) twist in the tension wall forcing negative (or positive) twist to occur in the compression wall in order for out-of-plane compatibility to be maintained

5.2.3 AXIAL DEFORMATION

Throughout the testing of the coupled wall specimens, each of the walls was subjected to alternating tensile and compressive axial forces caused by the coupling action of the beams and (to a lesser extent) slabs. A gravity load applied at the second level offset some of the tensile force on one wall but increased the compressive force on the other. In addition to measuring rotations and shear distortions, the instrumentation placed on the first story of the walls allowed for an analysis of the impact these tensile and compressive forces had on the average axial deformation of the walls. Axial deformations per wall strip were calculated as the average change in vertical distance between markers above and below each strip.

It is reasonable to expect that the wall subjected to tension would exhibit larger average axial tensile strains than the wall in compression. However, the measured average axial strains per strip throughout the first story of the wall system, shown in Fig 5.22, deviate from this trend. It is shown that average tensile strains were generally larger in the compression wall than in the tension wall. A likely explanation for this unintuitive

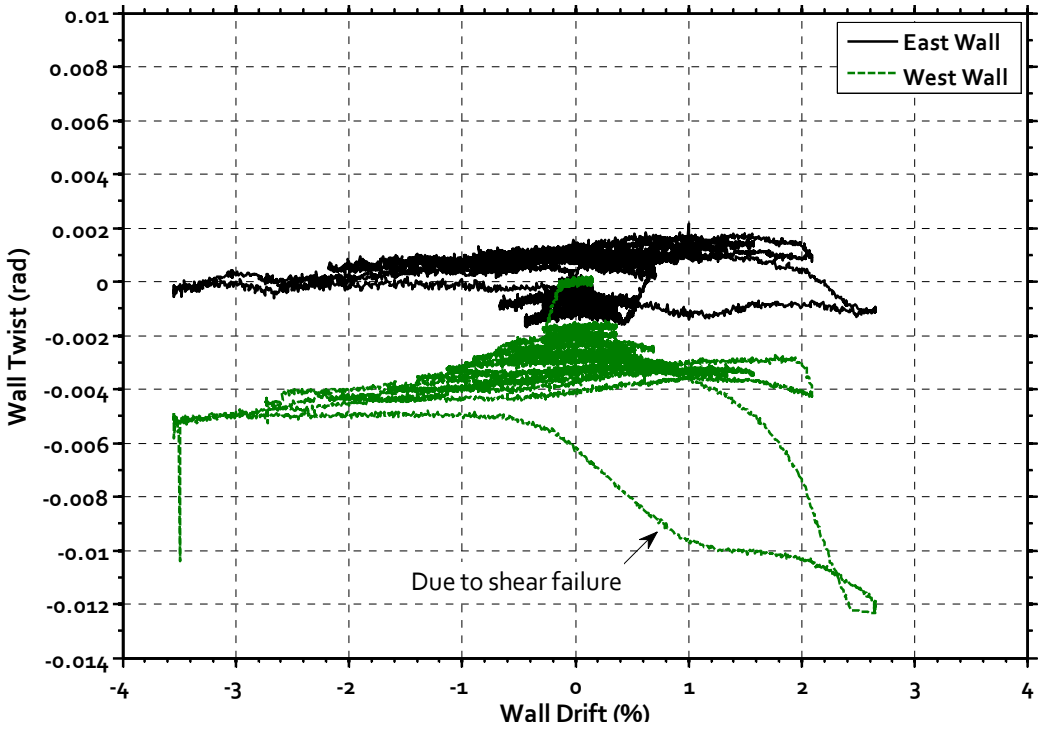

(a) Comparison of twist in walls of Specimen CW-2 at the level of CB-1

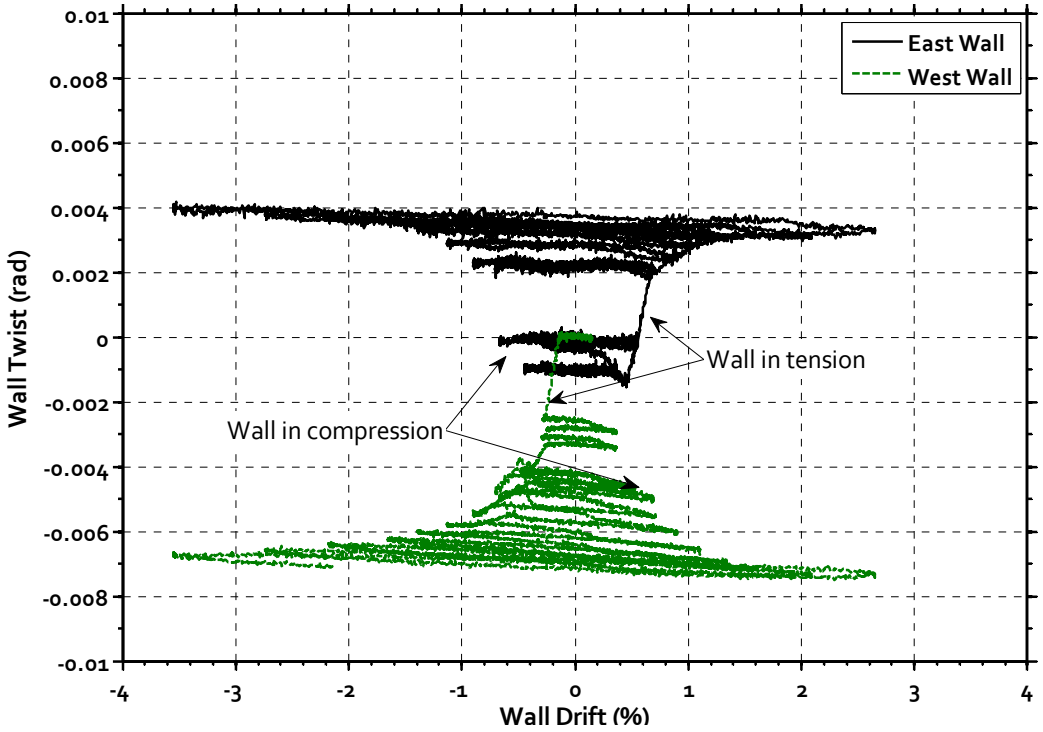

(b) Comparison of twist in walls of Specimen CW-2 at the level of the foundation

Figure 5.21 – Wall twist in Specimen CW-2 (typical of wall specimens)

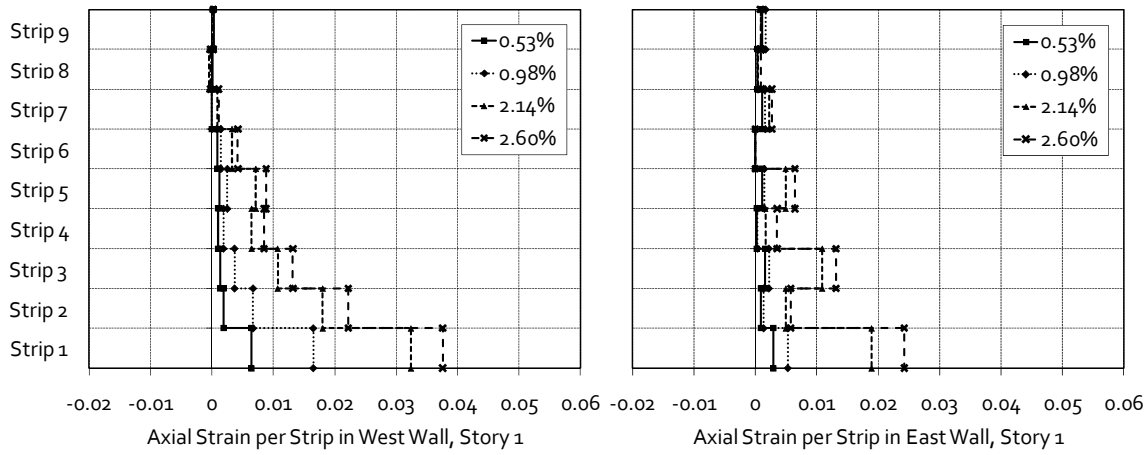

(a) Specimen CW-1, Positive drift (left = compression wall, right = tension wall)

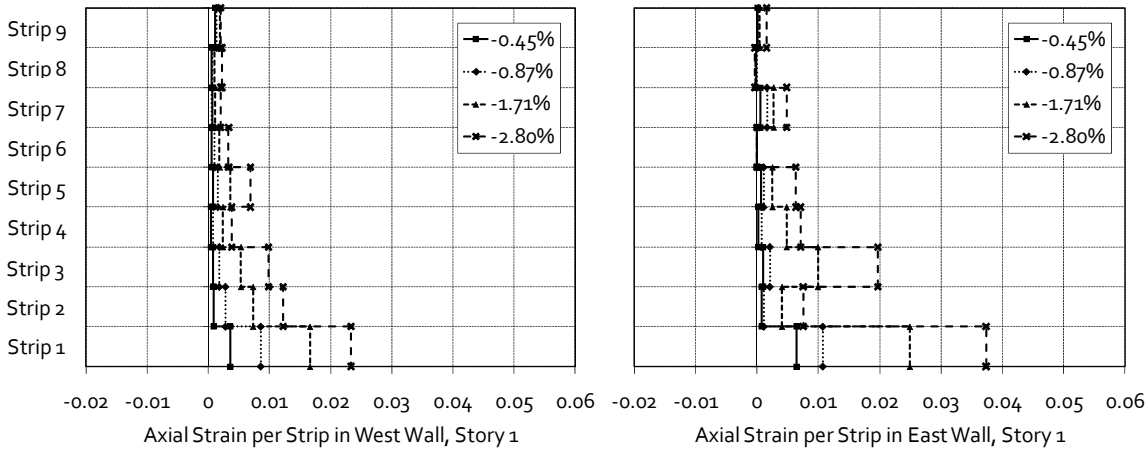

(b) Specimen CW-1, Negative drift (left = tension wall, right = compression wall)

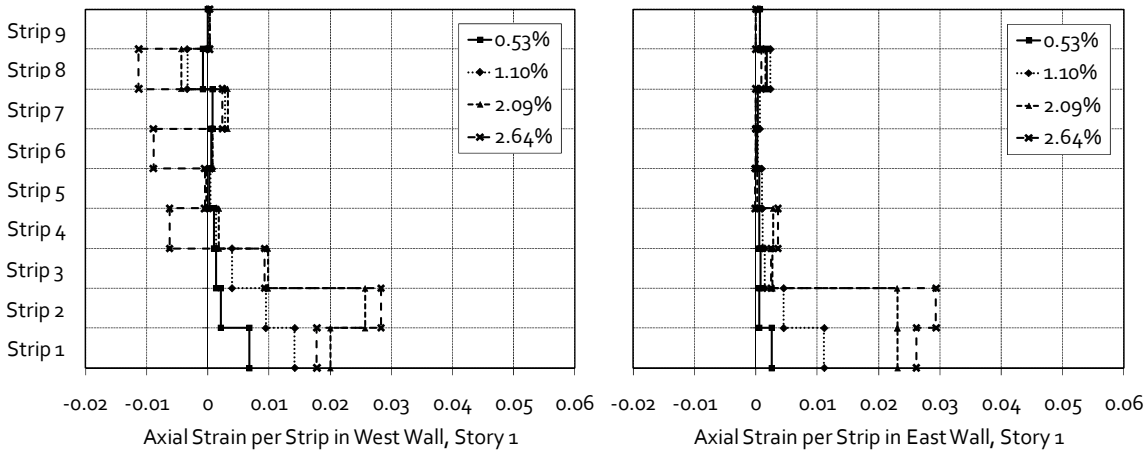

(c) Specimen CW-2, Positive drift (left = compression wall, right = tension wall)

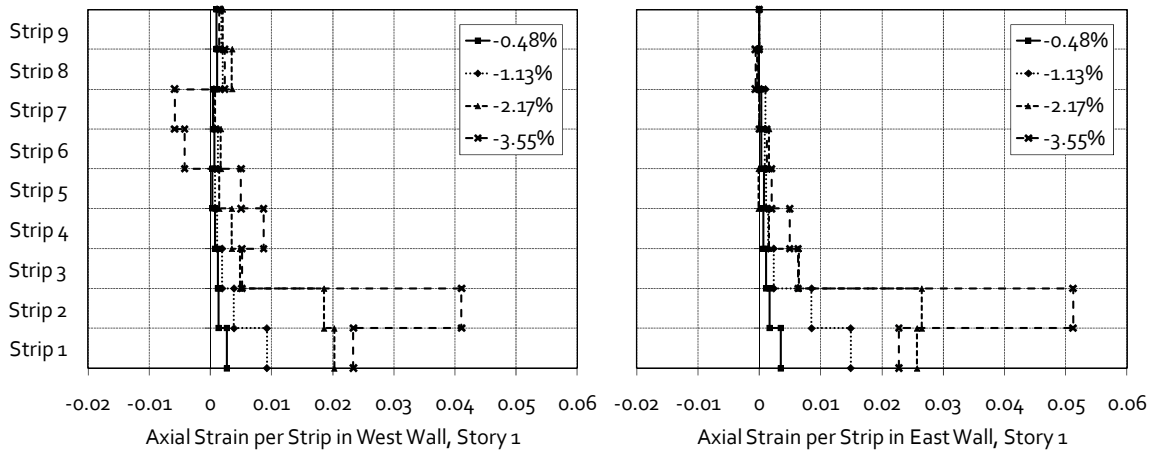

(d) Specimen CW-2, Negative drift (left = tension wall, right = compression wall)

Figure 5.22 – Average wall axial deformation for strips in the first story of the walls (positive indicates tensile strains)

response is that the tensile stresses, although large enough to approach the capacity of the tension reinforcement in the flange at yield, caused significantly smaller average elongation than did the opening of flexural and diagonal cracks in the compression wall. The large increase in average axial strain in the strips where wall curvature was largest is further evidence of the strong influence wall curvature has on the elongation of the walls. This suggests that it is quite reasonable for analytical models of coupled wall systems to ignore axial wall deformations due to axial forces in the walls, as they play a negligible role in the deformation of walls.

The only strips in which average compressive strains were measured were in Specimen CW-2. The compressive strains in strips 4, 6, and 7 coincide with the location of the severe horizontal and diagonal cracking that resulted in localized shortening of the wall along the failure plane after failure of the compression zone. The shortening of the wall in strip 8 of the left wall in Specimen CW-2 is harder to explain. This strip does incorporate a cold joint, but there is no obvious reason to believe this would permit the wall to shorten. Also, there is no reason to believe the instrumentation was questionable in this portion of the wall.

5.3 COUPLING BEAM DEFORMATIONS

Instrumentation was placed on each of the coupling beams, as described in Chapter 3, to record their deformation throughout the tests. At the first story, a grid of optical markers, similar to that used for the component tests reported in Chapter 4, was placed over the full length of the coupling beam to determine the distribution of flexural rotations, shear strains, and axial deformations in this coupling beam. At the third story, potentiometers were used to record average flexural rotations from the face of the wall to midspan of the coupling beam, average shear distortion within the span of the coupling beam, and average axial strains. The slabs located at the second and fourth story levels made the placement of instrumentation difficult, so only the axial deformation of these coupling beams was directly measured. The indeterminacy of the coupled system prohibited an accurate estimation of the shear stresses and moments developed in each coupling beam, but similar coupling beam reinforcement and drift demands allowed for some meaningful comparison of the coupling beam details within each system. The measured coupling beam deformations are discussed in the following section.

5.3.1 COUPLING BEAM DRIFT

Before discussing the individual contributions of flexural rotations and shear distortion to coupling beam drift, it is necessary to determine the drift demands that each coupling beam was subjected to throughout the tests. A network of optical markers and potentiometers was mounted along the outside edge of each wall to measure the relative vertical displacement, from the laboratory floor to each story level, throughout the test. This information, combined with measurements of the wall rotation taken by inclinometers mounted to the walls at each story level, was used to estimate the drifts imposed on each coupling beam. The inputs used in Eq. 5.2 for calculation of the coupling beam drift at each wall story are shown in Figure 5.23.

The coupling beam drift at each floor level, for both wall specimens, is plotted in Figure 5.24 against the interstory drift. Interstory drift is defined as the average of the wall rotations measured in each wall at a given floor level, and was used rather than

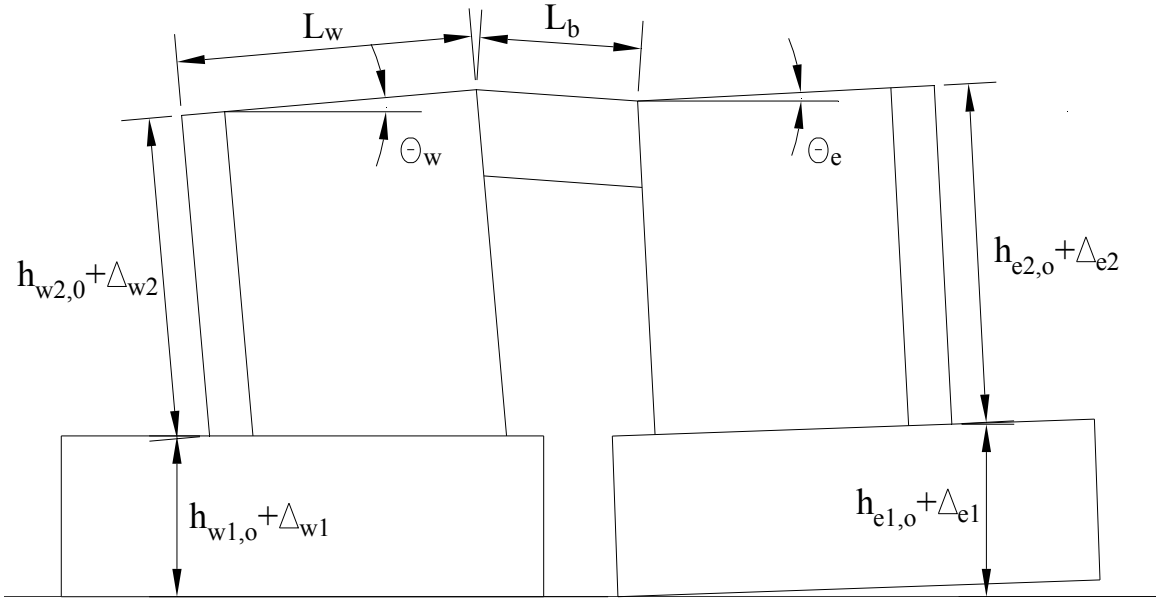

Figure 5.23 – Inputs for coupling beam drift calculation

$$CB_{Drift} = \frac{(\Delta_{w1} + \Delta_{w2} + \Theta_w L_w) - (\Delta_{e1} + \Delta_{e2} - \Theta_e L_w)}{L_b} + \left(\frac{\Theta_w + \Theta_e}{2}\right) \qquad (5.2)$$

system drift because the wall rotations varied over the height of the specimen. It is clear that the coupling beams were subjected to very large drift demands (as high as 8% and 10% in Specimens CW-1 and CW-2, respectively), requiring significant ductility from the coupling beams to ensure stable system behavior at large interstory wall drifts. It is common to limit design level drifts for structural systems dependent on coupled walls for lateral stiffness to 1.0 to 1.5% (ASCE/SEI 41/06, 2007). In the wall specimens tested, the coupling beams were subjected to drift demands on the order of 3.0 to 4.5% when the system was subjected to drifts of 1.0 to 1.5%. This is still a large drift demand, but within the drift capacity of HPFRC coupling beams with aspect ratios near 1.75, as described in Chapter 4. It is also shown in Figure 5.24 that the coupling beam drift demand was approximately linearly related to the interstory drift. The only deviation from this trend was observed in the last positive loading half-cycle of Specimen CW-2, where a shear failure in the first story of one of the walls affected the distribution of deformation demands throughout the system.

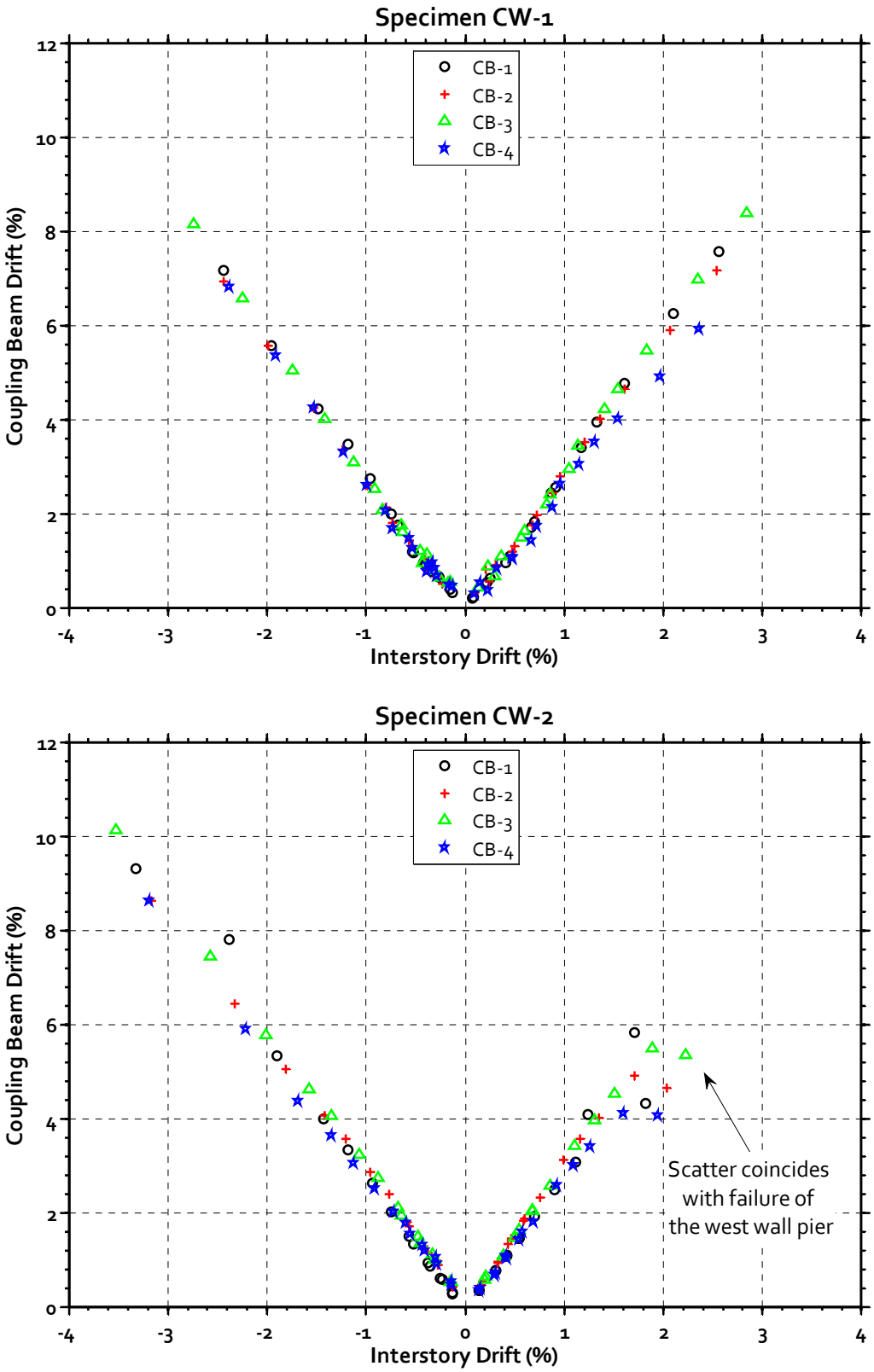

Figure 5.24 – Coupling beam drift versus interstory wall drift

5.3.2 AXIAL DEFORMATION

The average axial strain calculated for each of the coupling beams in Specimens CW-1 and CW-2 is shown in Figure 5.25. This figure is a corollary to Figure 4.8, which shows the axial strains calculated for the coupling beam component specimens. In both wall specimens, the average axial strains in the coupling beam at the first floor level, CB-1, were less than 0.005 throughout the test (where positive strains represent elongation), with negative axial strains recorded in CB-1 for Specimen CW-1. These negative strains represent shortening of the coupling beam as the test progressed, which indicates that a large axial force was being transferred through this beam. In previous tests of coupled wall systems (Teshigwara et al., 1998a; 1998b), this phenomenon has been directly measured and can be attributed to the shift of base shear force to the compression wall. The first story coupling beam in Specimen CW-2 did not shorten, suggesting that less shear force was transferred to the compression wall in this test. Some appreciable axial force must still have transferred through this beam, however, because it exhibited much less elongation than any of the coupling beams further from the foundation.

With the exception of CB-1, the coupling beams in the coupled wall specimens exhibited average axial strains between 0.005 and 0.017 at coupling beam drifts exceeding 2%. This is consistent with the axial strains that developed in the coupling beam component tests, which ranged between 0.007 and 0.014 for the same range of coupling beam drifts. For CB-3 and CB-4 in Specimen CW-1, and for CB-2, CB-3, and CB-4 in Specimen CW-2, the axial strain exhibited by the coupling beams was approximately proportional to the imposed drift. This trend did not extend to CB-2 in CW-1, which elongated to a strain of approximately 0.007 near 3% beam drift and then remained at that axial deformation level as drift demands increased.

Although coupling beam CB-2 in Specimen CW-1 eventually developed a sliding shear failure mode, which could reasonably be assumed to limit the tendency to elongate, this mode of failure did not develop until later in the test, suggesting that it was not the primary cause for the limited elongation in this beam. Furthermore, CB-3 in the same specimen developed the same sliding failure mode, yet continued to elongate throughout the duration of the test. It is more likely that the redundancy of the coupled wall system

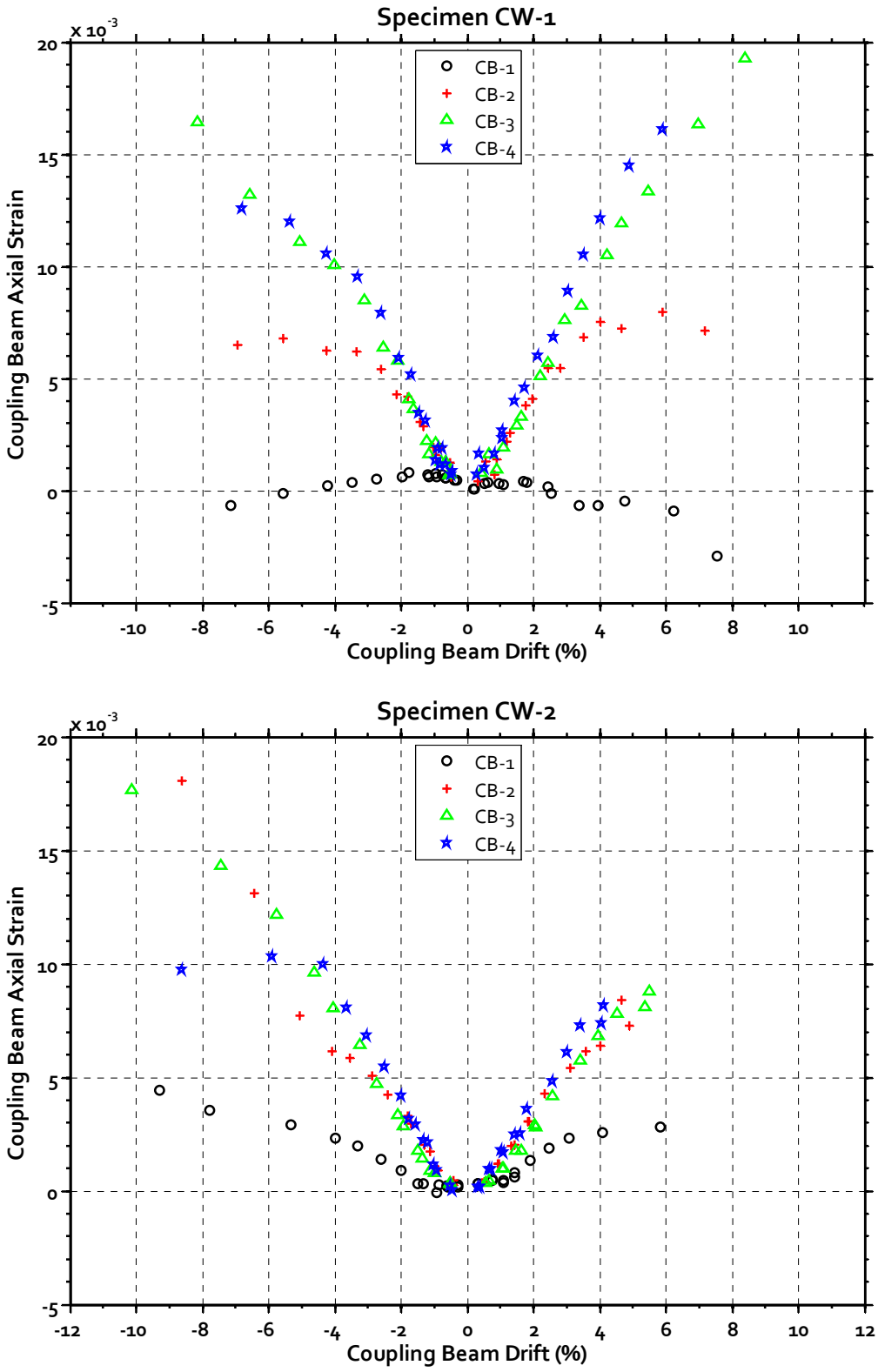

Figure 5.25 – Axial strain in coupling beams plotted versus coupling beam drift for Specimens CW-1 and CW-2 (top and bottom plot, respectively)

was responsible for limiting the growth of CB-2. The small tensile strains, and even shortening, of CB-1 in Specimen CW-1, constrained the potential for CB-2 to elongate more than in Specimen CW-2. For beams further from the foundation, this effect was less pronounced, which allowed CB-3 and CB-4 in Specimens CW-1 and CW-2 to exhibit similar axial deformations.

Although the axial strain of coupling beams is of interest, the axial forces that develop within the coupling beams in association with these recorded strains are perhaps more critical to the design and analysis of coupling beams. Unfortunately, developing a reliable correlation between coupling beam strains and axial forces is not straightforward. It is likely that these axial forces moderately increase the shear and flexural capacities while potentially limiting the ductility of coupling beams. However, studying the effects of the axial forces is difficult when the mechanisms leading to their development are not well understood. The following statements can, however, be made. First, coupling beam axial forces result from two distinct phenomena: 1) the shift of wall shear force to the stiffer compression wall near the foundation requires coupling beams and slabs linking adjacent walls to sustain axial forces, and 2) the accumulation of plastic deformation in coupling beam reinforcement and the opening and only partial closing of cracks forces coupling beams to elongate as drift demands increase. This is resisted by stiff walls and floor slabs, and results in axial compression forces in response to tensile axial strains in the coupling beams. Second, the average axial strains developed in each coupling beam, and thus the resulting axial force imposed on each beam, is also dependent on the axial strain in nearby coupling beams due to the indeterminate nature of the system. This phenomenon was demonstrated by the different axial strains exhibited by CB-2 in each of the coupled wall specimens, which was attributed to different behavior in CB-1 between the specimens. This interdependency of coupling beam elongations complicates the prediction of axial deformations and forces in coupling beams in a coupled wall system.

5.3.3 Shear Deformation

As described in the introduction to Section 5.3, only the coupling beams at the first and third levels were sufficiently instrumented to estimate the shear and flexural deformations exhibited by the coupling beam. Furthermore, the anchorage of the

instrumentation at the third level, shown in Figure 3.31, was compromised by spalling of cover concrete, and is of little use for analyzing beam deformations throughout the loading sequence. Therefore, only the first story coupling beam was sufficiently instrumented to provide a detailed record of the distribution of rotations and shear distortions over the length of the coupling beam. To calculate the distribution of deformations over its length, the beam was divided into the seven strips shown in Figure 5.26. The rotation and shear distortion exhibited by each strip were then calculated.

The average shear distortion exhibited by CB-1 in each of the two coupled wall specimens, calculated for each of the strips shown in Figure 5.26, are plotted in Figure 5.27 for various coupling beam drift levels. No sliding shear displacements were observed within the beam span, so all of the measured shear distortion is attributed to "true" shear distortion. It is likely, however, that some sliding developed across the precast interface that was hidden by the cover. Therefore, the shear distortion measured across this interface (captured by strips 1 and 7) was assumed to be attributable to sliding shear displacements and are plotted separately in Figure 5.28.

The plots of shear distortion within the beam span, shown in Figure 5.27, indicate that very large shear distortions developed in the first story coupling beam. At coupling beam drifts exceeding 4.0%, shear distortions larger than 1% were generally measured over the full beam length for both loading directions. In both specimens, the shear distortions were considerably larger in the negative loading direction, particularly in Specimen CW-1, where shear distortions were larger by a factor of three. The most

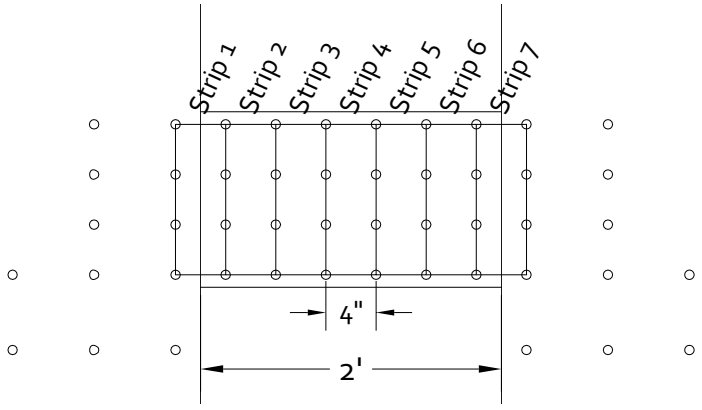

Figure 5.26 – "Strips" of the coupling beam at the first wall story used for calculating the distribution of deformation over the length of the coupling beam

probable explanation for this markedly asymmetric response is an unintended difference in the way that lateral forces transferred from the actuators into the specimen. In the positive loading direction, the actuators were pushing the specimen. It is likely that much of this lateral push was transferred into the slab closest to the actuator fixture (i.e. the tension wall). This lateral force would then have had to transfer through the first story coupling beam into the first story of the compression wall. The development of a diagonal strut from the second story on the tension side down to the base of the compression wall was supported by the crack patterns developed during the test, as well as by slightly smaller axial strains in the first story coupling beam in the positive loading direction. Upon reversal of the load, as the actuators pulled away from the specimen, it is likely that more of the lateral force transferred directly into the compression wall,

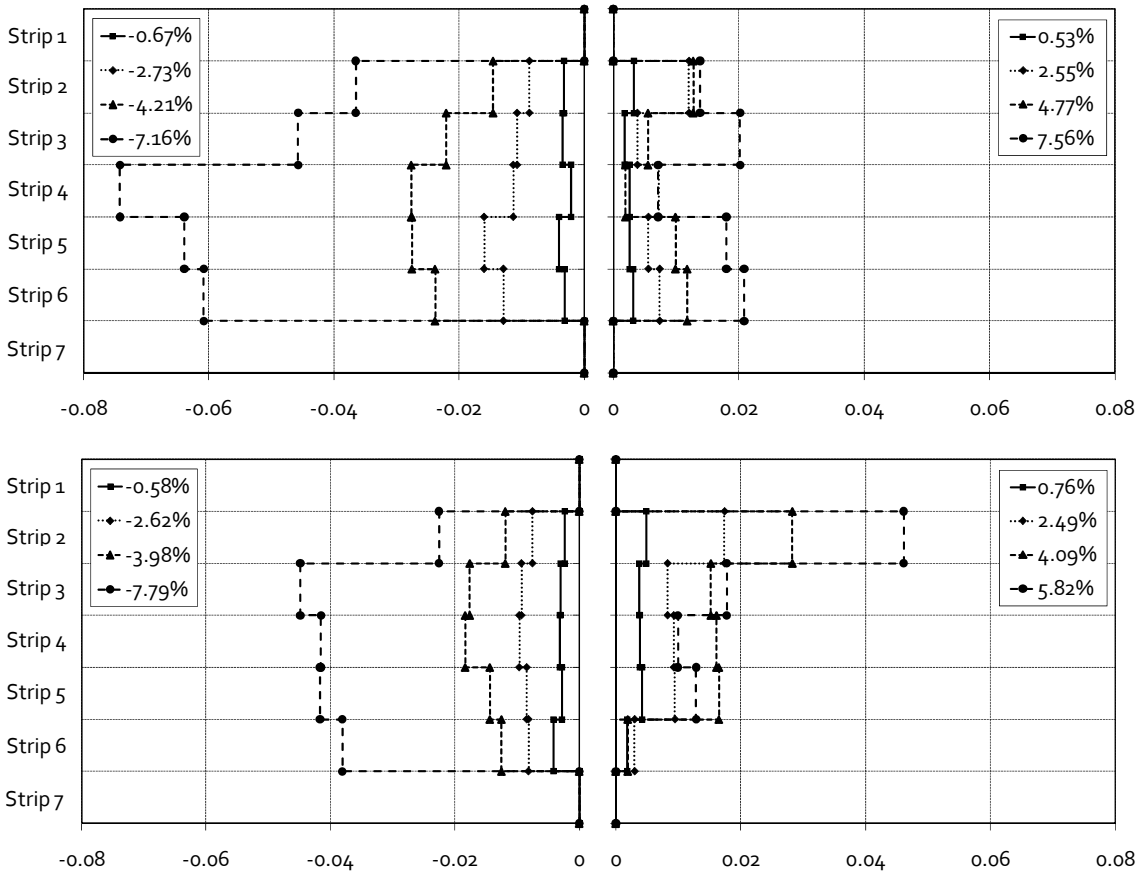

Figure 5.27 – Average shear distortion (rad), per strip, in the coupling beam at the first story for Specimens CW-1 and CW-2 (top and bottom, respectively). Left and right plot represent negative and positive drift, respectively.

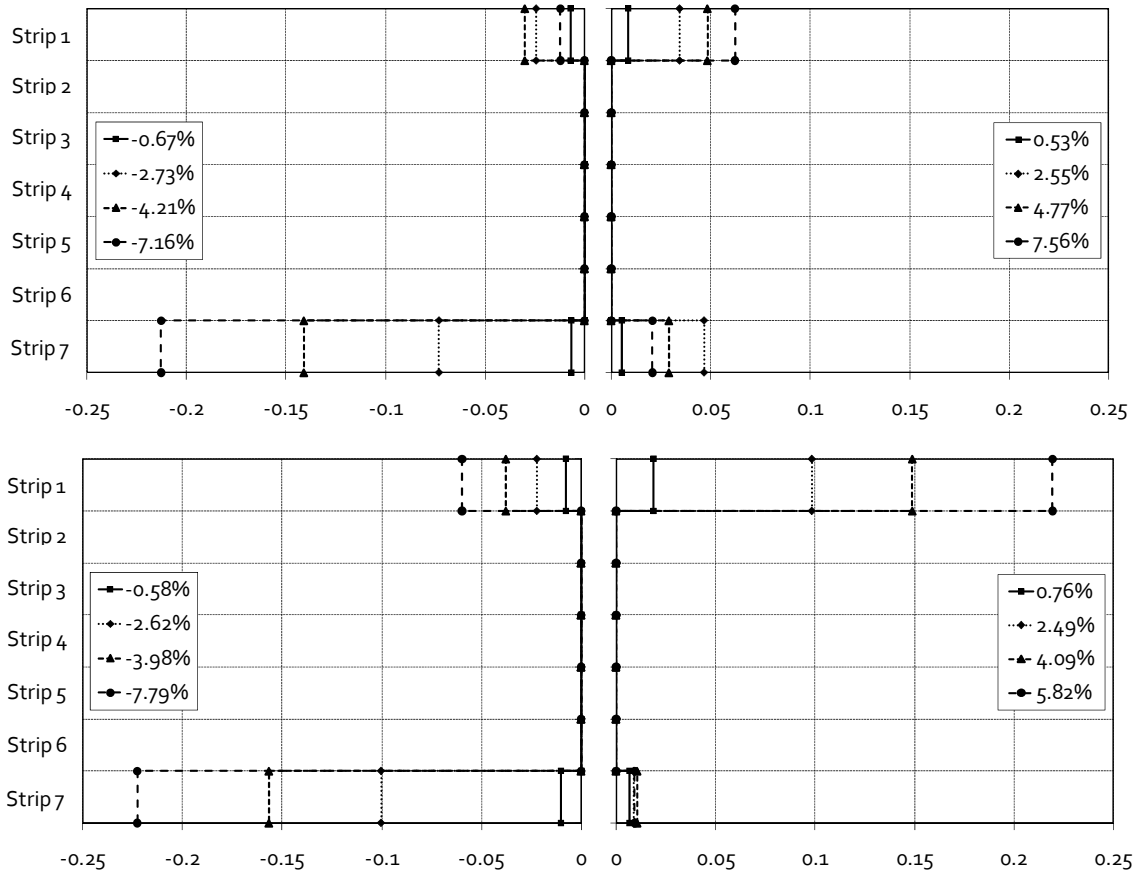

Figure 5.28 – Sliding displacements (in.), per strip, in the coupling beam at the first story for Specimens CW-1 and CW-2 (top and bottom, respectively). Left and right plot represent negative and positive drift, respectively.

requiring less transfer of shear force through the first story coupling beam as an axial force. The larger axial force in the first story coupling beam that developed during positive load cycles would have increased the shear stiffness of the beam, thereby resulting in comparatively smaller shear strains developing during positive drift cycles.

The displacements caused by the combined effects of sliding shear across the beam-to-wall interface and shear distortion in the section of beam captured in strips 1 and 7 at various coupling beam drifts are shown in Figure 5.28. Large relative displacements, on the order of 0.2 to 0.25 in. (5 to 6.3 mm), were recorded in some cases, whereas displacements of less than 0.05 in. (1.25 mm) were measured in other cases. This large disparity, particularly in the case of strip 7 of Specimen CW-2, was the result of large

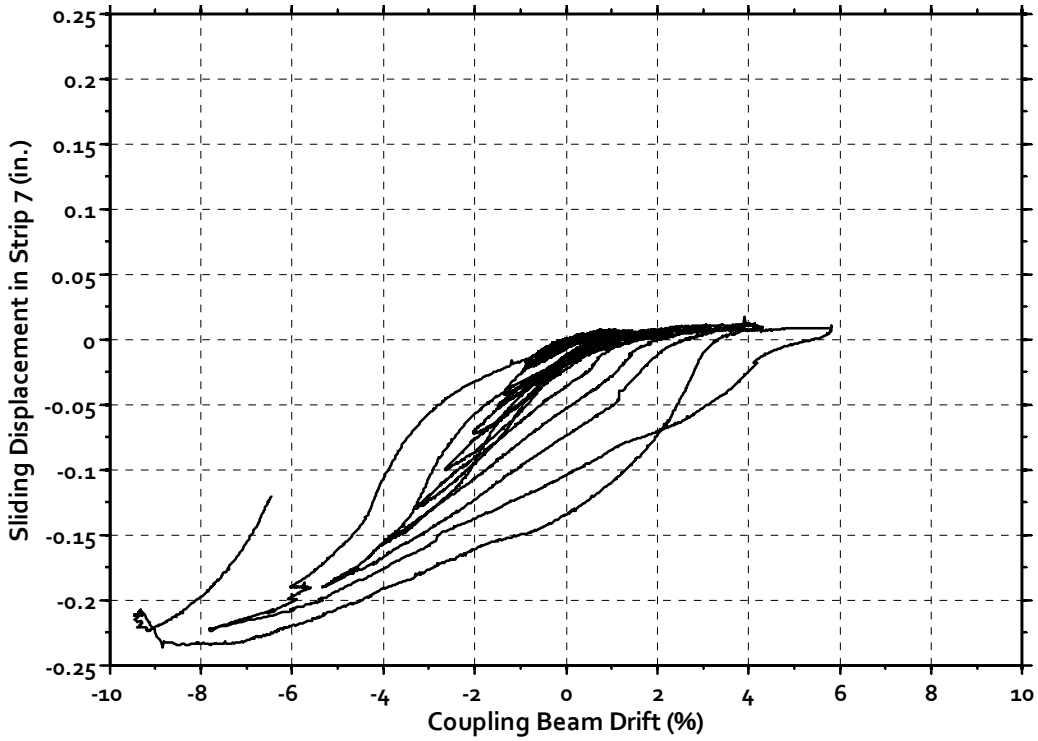

Figure 5.29 – Sliding displacement in strip 7 of CB-1 in Specimen CW-2 versus coupling beam drift.

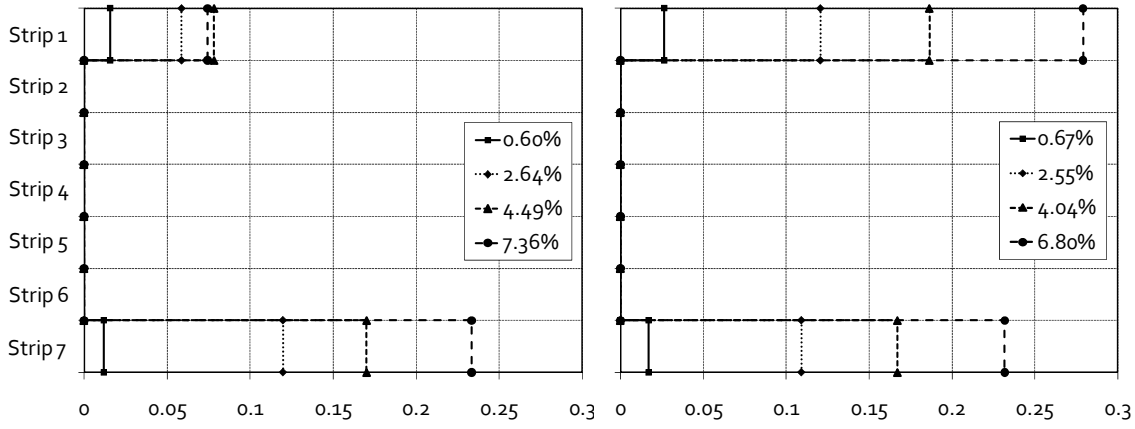

Figure 5.30 – Peak-to-peak sliding displacements (in.), per strip, in the coupling beam at the first story for Specimens CW-1 and CW-2 (left and right, respectively).

sliding displacements that did not fully reverse upon reversal of the loading direction (Figure 5.29). The full range of sliding displacements in each strip, measured from peak-to-peak, was much less disparate, as shown in Figure 5.30. Of the strips exhibiting sliding shear displacements, only strip 1 of Specimen CW-1 did not exhibit total peak-to-peak sliding displacements on the order of 0.25 in. (6.3 mm) at the end of the test.

5.3.4 CURVATURE

The average curvature measured in each strip of the first story coupling beams at the peak displacement of various loading cycles is shown in Figure 5.31. The curvature reported for strips 1 and 7 includes the rotations that concentrated at the cold joint between the precast beam and the wall. As a result, the largest apparent curvatures developed in strips 1 and 7, at the ends of the beam. This phenomenon was most pronounced in Specimen CW-1, where longitudinal reinforcement was cutoff near the end of the precast section, increasing the flexibility of the connection. Full development of the longitudinal reinforcement in Specimen CW-2 may have reduced the curvatures calculated in the strip with the cold joint somewhat, but did not prevent this phenomenon. This is because the elongation that develops over the bonded length of a well-anchored bar will still manifest as rotation at the connection. The development of the longitudinal reinforcement did, however, reduce the flexibility of the connection, which forced larger curvatures into the other strips within the beam span. The result was curvature ductility demands of up to 51 in strips 2-6 of the coupling beam in Specimen CW-2. These values can be compared to the curvature ductilites observed in Specimen CW-1, which did not exceed 8.0 in strips 2-5. Strip 6 of Specimen CW-1 was an exception to this trend. Large curvatures developed in this strip, likely in response to the very large curvatures developed in the opposite loading direction in strip 7, which did not fully reverse. This required strip 6 to accommodate the rotation demands placed on the end of the beam.

A comparison of the curvature distributions in CB-1 of Specimens CW-1 and CW-2 shows that curvature demands were generally larger in response to positive system drifts than negative drifts. The increased shear stiffness in the positive loading direction discussed in Section 5.3.3, which resulted in smaller shear distortions, required that larger flexural curvatures develop to accommodate the imposed drifts.

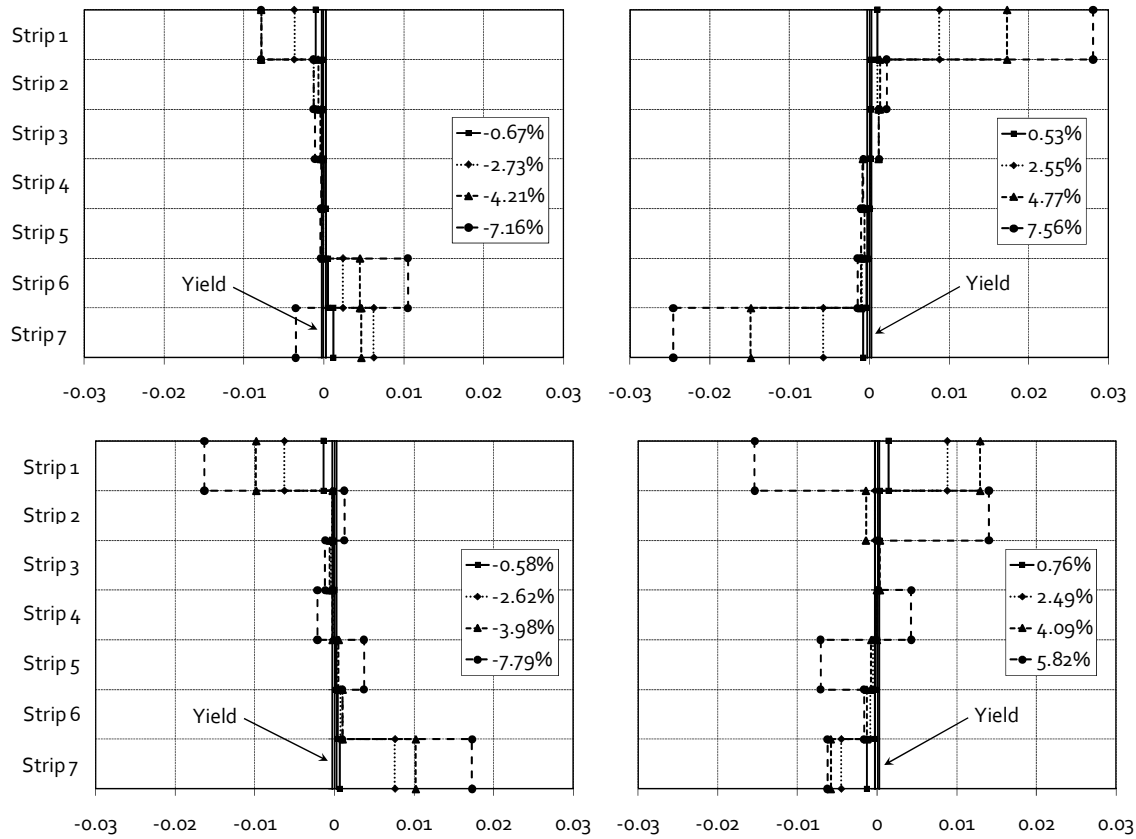

Figure 5.31 – Coupling beam curvature (rad/in.), per strip, in the first story coupling beam for Specimens CW-1 and CW-2 (top and bottom, respectively). Left and right plot represent negative and positive drift, respectively.

5.3.5 Coupling Beam Drift Components

On the basis of the calculations of flexural and shear deformations, it is possible to determine the relative contribution of various mechanisms to the total drift of the coupling beams at the first and third wall stories.

In the first story coupling beam, the contribution of rotations within the coupling beam and at the beam-to-wall interface due to steel strain penetration were computed along with the contribution of shear distortions within the span and sliding shear displacements at the beam-to-wall interface. The relative contribution of each of these mechanisms to coupling beam drift at the first story at various drifts is shown in Figure 5.32. For Specimen CW-1, 60 to 70% of the drift in the positive loading direction was due to the combined effects of flexural rotations within the span and rotations at the

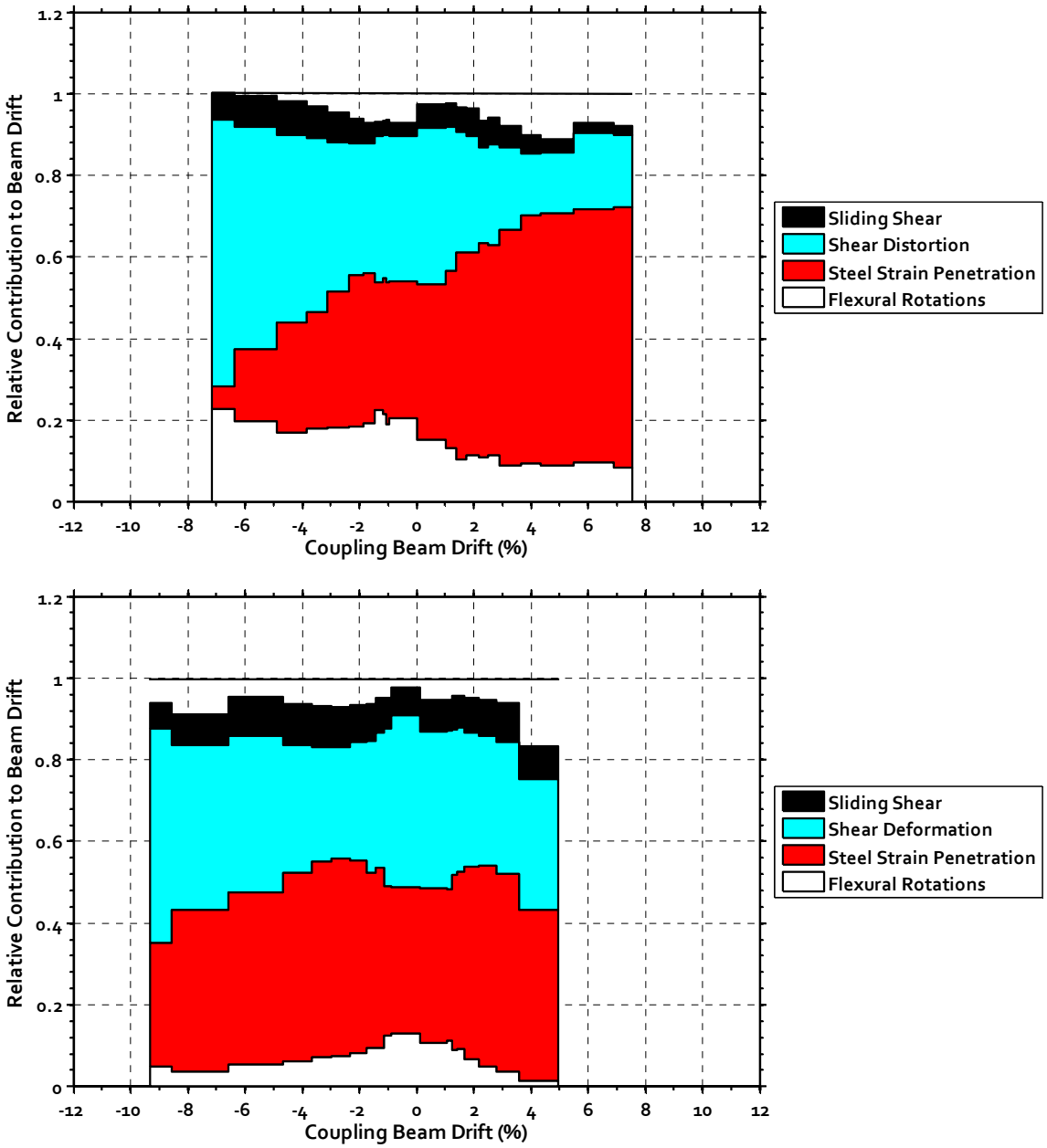

Figure 5.32 – Relative contribution to the total drift of the first story coupling beam in Specimens CW-1 and CW-2 (top and bottom, respectively)

beam-to-wall connection. In the negative loading direction, only 30 to 40% of the drift was due to flexural mechanisms, leaving shear distortion and sliding shear displacements to account for the remaining 60 to 70% of the imposed drift. In general, the shear related mechanisms contributed between 30-60% of the total drift of this beam, with this contribution being near 40% through most of the loading. It is worth mentioning that the

drift contribution from shear related mechanisms calculated for the component tests described in Chapter 4 was generally on the order of 40%.

Specimen CW-2 showed a more symmetric response. The combined effects of flexural rotations within the span and rotations at the beam-to-wall interface contributed approximately 50% of the drift, with shear deformations and sliding shear contributing the remaining drift. This indicates a somewhat larger influence from shear deformations than was observed in Specimen CW-1 or in the component tests described in Chapter 4. The full development of the flexural reinforcement in Specimen CW-2 increased the connection stiffness and required shear related mechanisms to play a more important role than in Specimen CW-1.

5.4 SYSTEM STRENGTH

The sources of overturning moment resistance for a solid wall, an uncoupled pair of walls, and a coupled wall system, are identified in Figure 5.33. For the coupled wall system, the total overturning moment capacity of the system, $M_{o(coupled)}$, is calculated with Eq. 5.4. First, the probable moment capacity of each wall is calculated, accounting for the effect of the axial forces that result from gravity loads and the sum of the shears developed in each of the coupling beams. This calculation gives the first two terms of Eq. 5.4, $M_{pr,C}$ and $M_{pr,T}$, representing the probable moment capacity of the compression and tension walls, respectively. $M_{o(coupled)}$ also includes the coupling moment consisting of the sum of the probable shear forces of each coupling beam, $V_{pr,beam}$, multiplied by the distance between the centroids of the walls, ℓ. For a more accurate estimation of $M_{o(coupled)}$ the coupling provided by slabs, $V_{pr,slab} \cdot \ell$, should also be included, as shown in Eq. 5.4. In a full system, selecting the effective width of slab to be considered for this calculation requires some judgment; however, the full width of the narrow slab strips incorporated in the coupled wall specimens was active and was considered in calculating $M_{o(coupled)}$ for the tested specimens. This formulation of the influence of slabs on

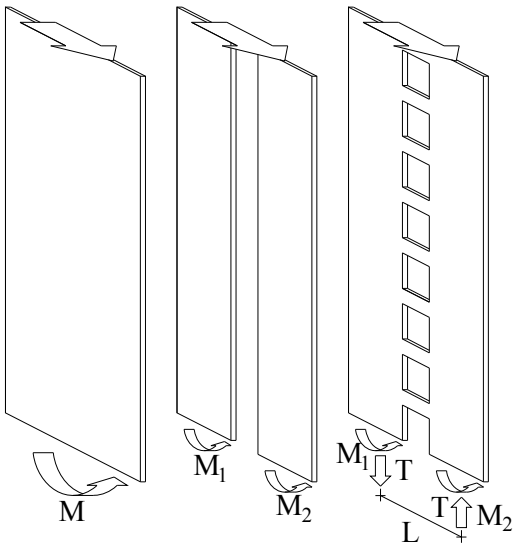

Figure 5.33 – Coupling of shear walls

$$M_{o(coupled)} = M_{pr,T} + M_{pr,C} + \sum V_{pr,beam}\ell + \sum V_{pr,slab}\ell \qquad (5.4)$$

$M_{o(coupled)}$ is valid for systems like the ones tested, which have precast coupling beams that are decoupled from the adjacent slabs. If the slabs and coupling beams are cast monolithically, the influence of the slabs should be included in the analysis of the coupling beams.

The overturning moment versus drift response of Specimens CW-1 and CW-2 is plotted in Figure 5.34 along with the predicted $M_{o(coupled)}$ using the material properties measured on the day of testing (reported in Chapter 3). This calculation assumes that a plastic mechanism develops with the coupling beams and walls all reaching their respective probable flexural capacities simultaneously. For the specimens tested, this approach resulted in a predicted capacity within 3% for both loading directions of Specimen CW-1 and for the negative loading direction of Specimen CW-2. The prediction for the positive loading direction of Specimen CW-2 was less accurate (it was over-predicted by approximately 6%). This was also the loading direction that ultimately developed a shear dominated failure in the base of the compression wall that was not consistent with the assumed flexural mechanism.

As discussed in Chapter 2, the degree of wall coupling, or coupling ratio, is often calculated for coupled wall systems to provide a general measure of the influence of the coupling beams on the strength of the system. This coupling ratio, *CR*, is the fraction of $M_{o(coupled)}$ that is due to the coupling action of the beams and slabs. Calculation of *CR* is straightforward once the terms in Eq. 5.4 are defined, as shown by Eq. 5.5. Generally, $0.2 \leq CR \leq 0.55$, where *CR* values below 0.2 result in a very lightly coupled system and *CR* values above 0.55 result in unacceptably high axial loads in the individual walls. For the two specimens tested, the theoretical *CR* was 0.43 and 0.52 for Specimen CW-1 and CW-2, respectively.

$$CR = \frac{\sum V_{pr,beam}\ell + \sum V_{pr,slab}\ell}{M_{o(coupled)}} \tag{5.5}$$

Also plotted in Figure 5.34 is the theoretical overturning moment capacity for the two individual walls neglecting wall coupling, or $M_{o(uncoupled)}$. For this calculation, the probable moment capacity of the walls, $M_{pr,T(uncoupled)}$ and $M_{pr,C(uncoupled)}$, was calculated assuming that the axial forces in the walls resulted only from gravity loads. Then Eq. 5.6 was used to calculate the uncoupled overturning moment capacity. It is important to note that $M_{pr,T\ or\ C(uncoupled)} \neq M_{pr,T\ or\ C(coupled)}$, as axial forces due to coupling impact the probable moment capacity of the walls.

$$M_{o(uncoupled)} = M_{pr,T(uncoupled)} + M_{pr,C(uncoupled)} \tag{5.6}$$

Although the coupling ratio, CR, is both straightforward to calculate and widely used, it does not provide a direct measure of the effect of coupling on the flexural strength of the walls. A different metric can be defined for this purpose, called the Wall Strength Index, or WSI, using Eq. 5.7.

$$WSI = \frac{M_{o(coupled)} - \left(\sum V_{pr,beam} + \sum V_{pr,slab}\right)\ell}{M_{o(uncoupled)}} \tag{5.7}$$

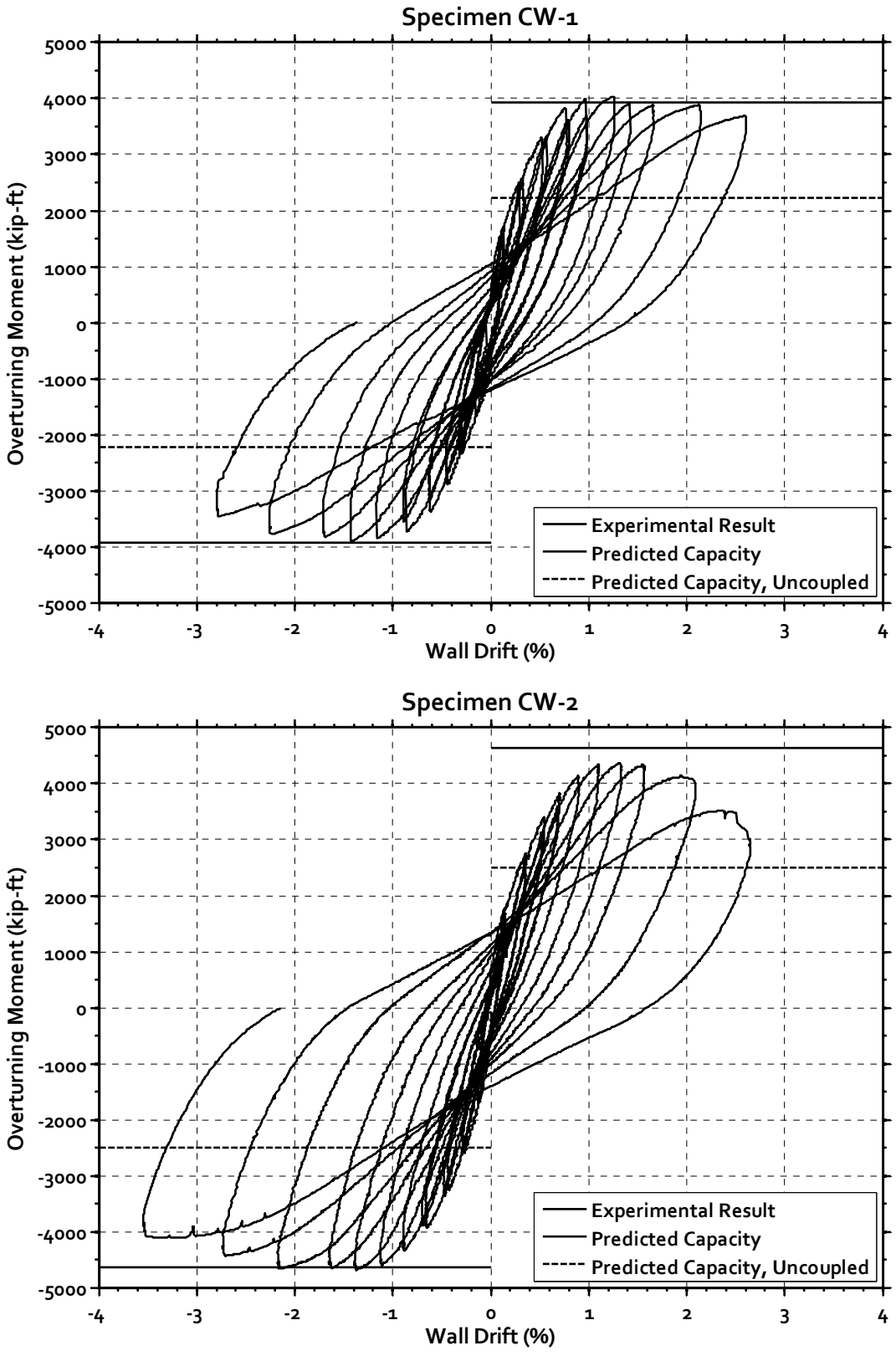

Figure 5.34 – Experimental result and predicted capacity

The WSI is a direct measure of the impact wall coupling has on the total flexural capacity of the walls. For low coupling ratios, where the detriment to the flexural strength of the tension wall is approximately offset by the increase in flexural strength of the compression wall, $WSI \cong 1.0$. This is desirable because further moderate increases in wall coupling will proportionally increase the overturning moment strength of the coupled system. However, for larger coupling ratios, where appreciable axial loads develop that may adversely affect the probable moment capacity of the walls, the value of WSI could decrease. This decrease in WSI would occur when either the tension wall is subjected to net tension forces or the compression wall is subjected to very large compression forces (above the balanced point). This is indicative of not only loss of wall flexural strength, but also of the compromised ductility associated with undesirable levels of axial load.

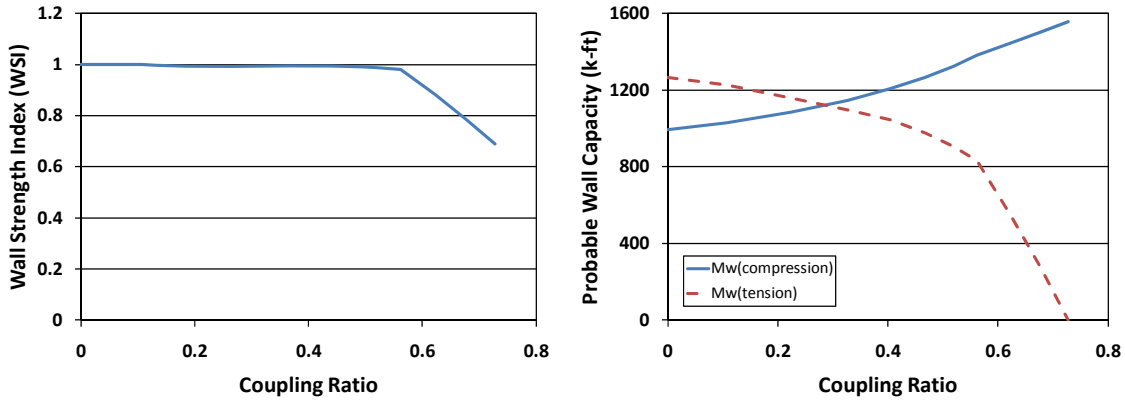

Figure 5.35 – Wall Strength Index (WSI) for coupled wall specimens versus coupling ratio and theoretical moment capacity of individual walls versus coupling ratio

For Specimens CW-1 and CW-2, $CR = 0.43$ and 0.52, and $WSI = 1.00$ and 0.99, respectively. This indicates that for both Specimens CW-1 and CW-2, the total moment capacity of the walls was negligibly influenced by the axial forces caused by the coupling beams. In this case, increasing the CR by strengthening the beams will proportionally increase $M_{o(coupled)}$, and is therefore an efficient way of increasing the strength of the system. However, as indicated by the plot of WSI versus coupling ratio shown in Figure 5.35, increasing the coupling ratio beyond approximately 0.55 will

cause a significant decline in the total flexural capacity of the walls in this coupled system, as the tension wall quickly looses flexural strength (shown on the right of Figure 5.35). Therefore, for $CR > 0.55$, the increases in coupling moment no longer proportionally increase $M_{o(coupled)}$, and is therefore not the most efficient way to increase the system strength. This concept is discussed further in Section 6.2.

5.5 REINFORCING STEEL STRAINS

Strain gauges were placed on reinforcement throughout the specimens, as discussed in Chapter 3. Figs. 5.36-39 show the location of the strain gauges within the walls and beams, and graphically indicate whether the strain gauges recorded strains larger than yield prior to 0.5% drift, 1.0% drift, or at any later point in the test. Yield strain was determined through direct tensile tests performed on bar coupons, which are described in Chapter 3. Although damage to some of the strain gauges in the first story of Specimen CW-2 limited the comparisons between the specimens, important observations could still be made.

5.5.1 PROGRESSION OF YIELDING

In Specimen CW-1, yield strains were first measured in the diagonal reinforcement of the coupling beams and at the first floor of the walls during the drift cycles preceding 0.5% drift. Interestingly, yield strains were not yet recorded in the walls immediately above the foundations, where moment demands were theoretically the largest. Rather, yield strains were first recorded half-way up and at the top of the first story, with yielding at the foundation recorded in later cycles. By the time the system had been pushed to 1.0% drift, yield strains had developed throughout most of the first story, the diagonal coupling beam reinforcement, and even some of the cutoff coupling beam longitudinal bars. Further cycling of the system yielded most of the remaining flexural bars within the first wall story, more of the cutoff coupling beam reinforcement, and some of the intermediate longitudinal wall reinforcement. The only yielding recorded in coupling beam transverse reinforcement was observed in the hoops confining the plastic

hinge region of the first story coupling beam. No yielding was observed in any of the instrumented coupling beam hoops within the midspan region, confirming that the premature failure of the beam-to-wall connections limited the shear demands placed on the coupling beams. Likewise, no yielding was observed in the horizontal wall reinforcement. Interestingly, the gauges placed on the wall flexural reinforcement in the flange at the base of the wall, which included a bar near the center of the wall flange (within the extended web) and a bar near the edge of the flange (see Figure 5.36), showed that the outside bars did not yield simultaneously with the bars within the web. This is a surprising result given that the flange width was only three times the web width.

The pattern of yield strain development was similar in Specimen CW-2. Again, the first yielding was observed in the first story of the walls, away from the foundation, and in the diagonal coupling beam reinforcement. With the longitudinal coupling beam reinforcement being fully developed in Specimen CW-2, these bars also exhibited yield strains prior to a system drift of 0.5%. Pushing the system to 1% drift caused yielding to spread throughout the first story walls. At this point in the test, the coupling beams were sufficiently activated that some of the midspan hoops in the HPFRC coupling beams had begun to show yield strains. Further cycling of the system caused yielding to spread to the intermediate longitudinal wall reinforcement and into more of the HPFRC coupling beam hoops. Unlike Specimen CW-1, yielding was recorded in the horizontal wall reinforcement prior to termination of the test, which is reasonable given that a shear failure developed in the wall near the gauged transverse reinforcement. Similar to Specimen CW-1, the flexural reinforcement in the flange of the wall farthest from the flange center did not reach the yield strain, even after bars within the flange nearer to the web of the wall had yielded. It is shown in Figure 5.39 that the strain gauges fixed to the midspan stirrup in the reinforced concrete coupling beam at the second story did not record strains indicative of yielding, despite extensive damage to the core of the beam pictured in Figure 5.12. This is likely a result of the order in which damage progressed through the beam. Beam damage began in the plastic hinge regions at the ends of the beam and spread towards the center of the span at larger drifts. This process did not fully engage the instrumented midspan hoops.

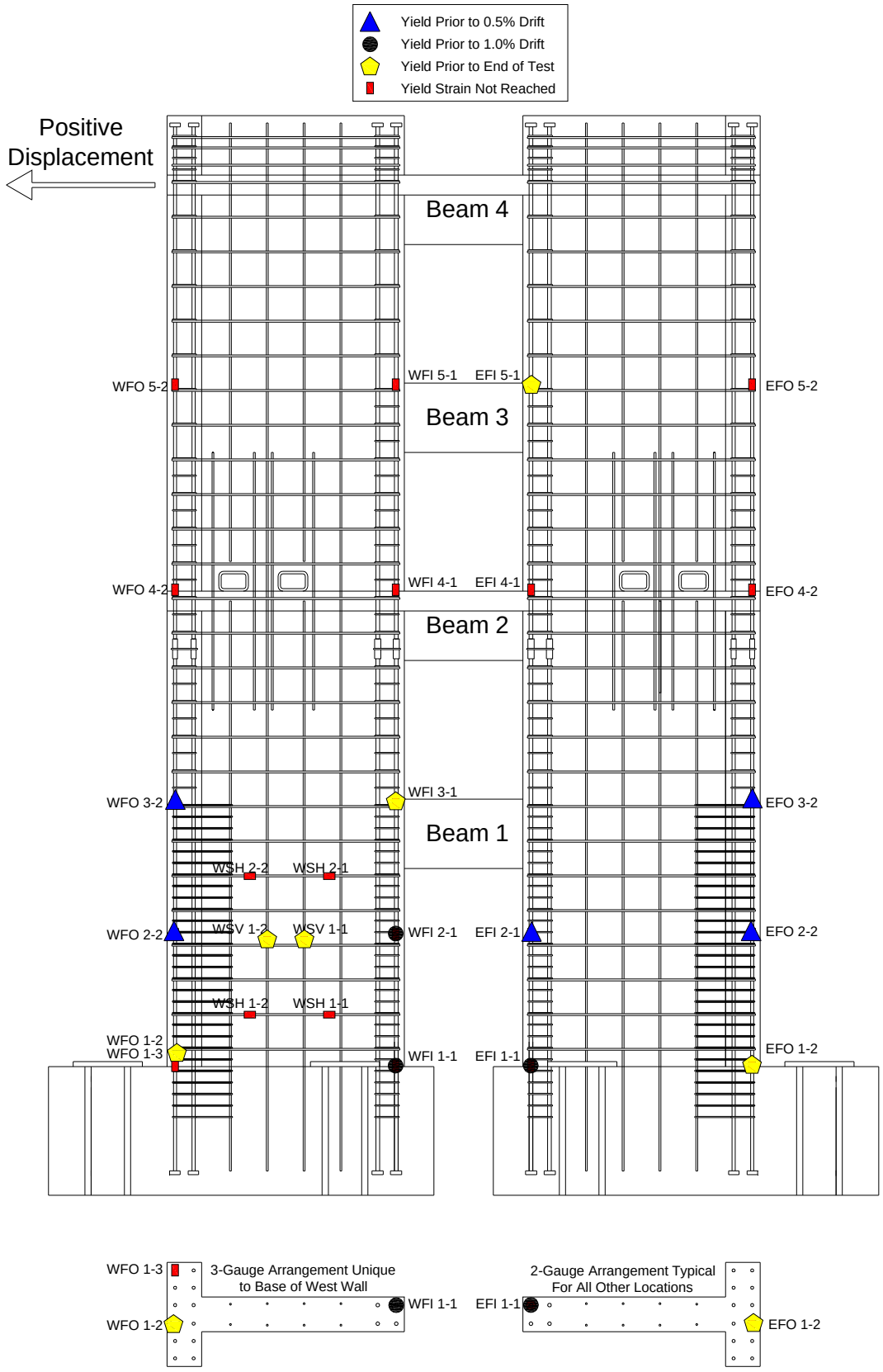

Figure 5.36 – Progression of yielding at strain gauge locations (Specimen CW-1, walls)

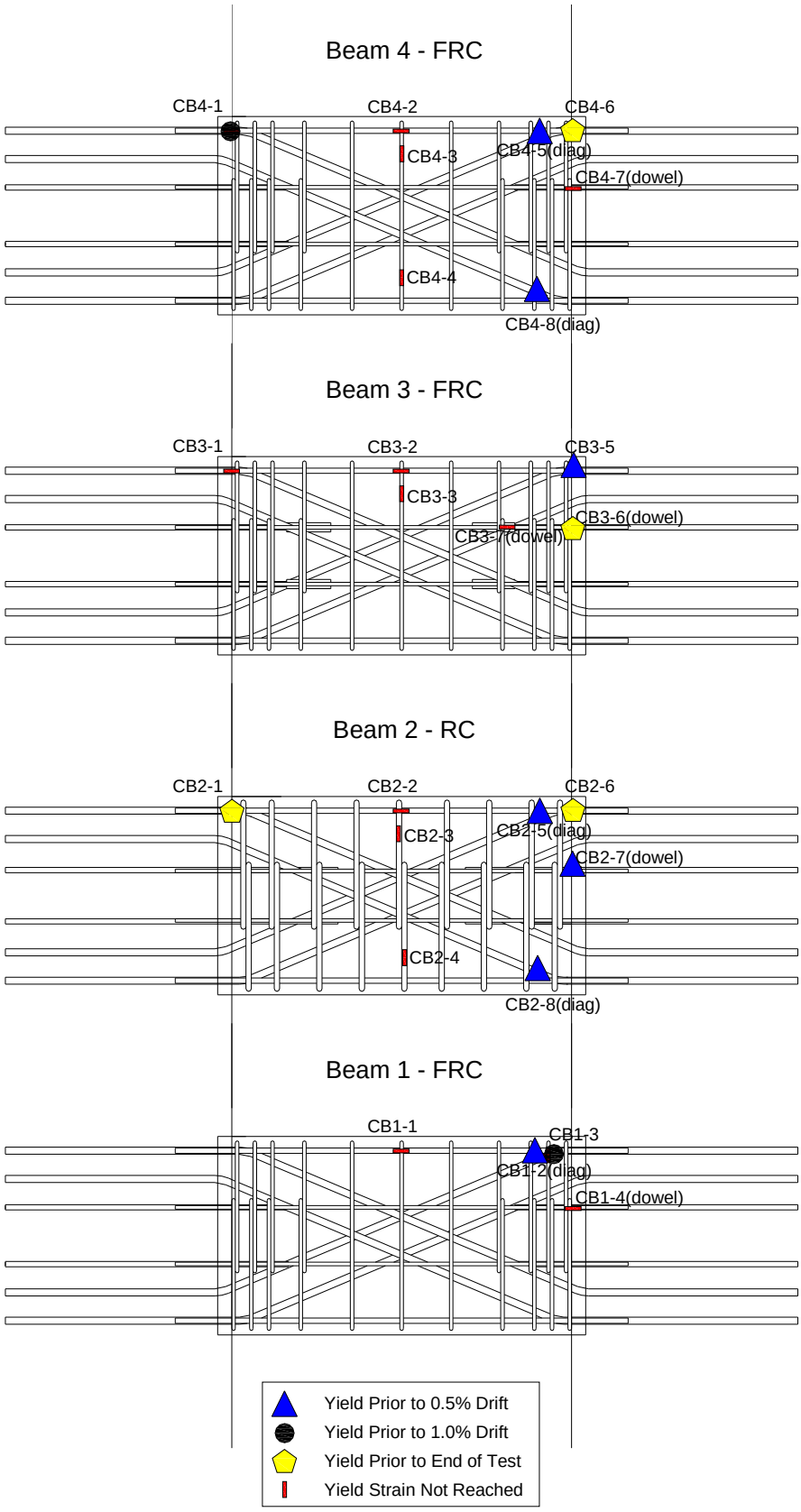

Figure 5.37 – Progression of yielding at strain gauge locations (Specimen CW-1, beams)

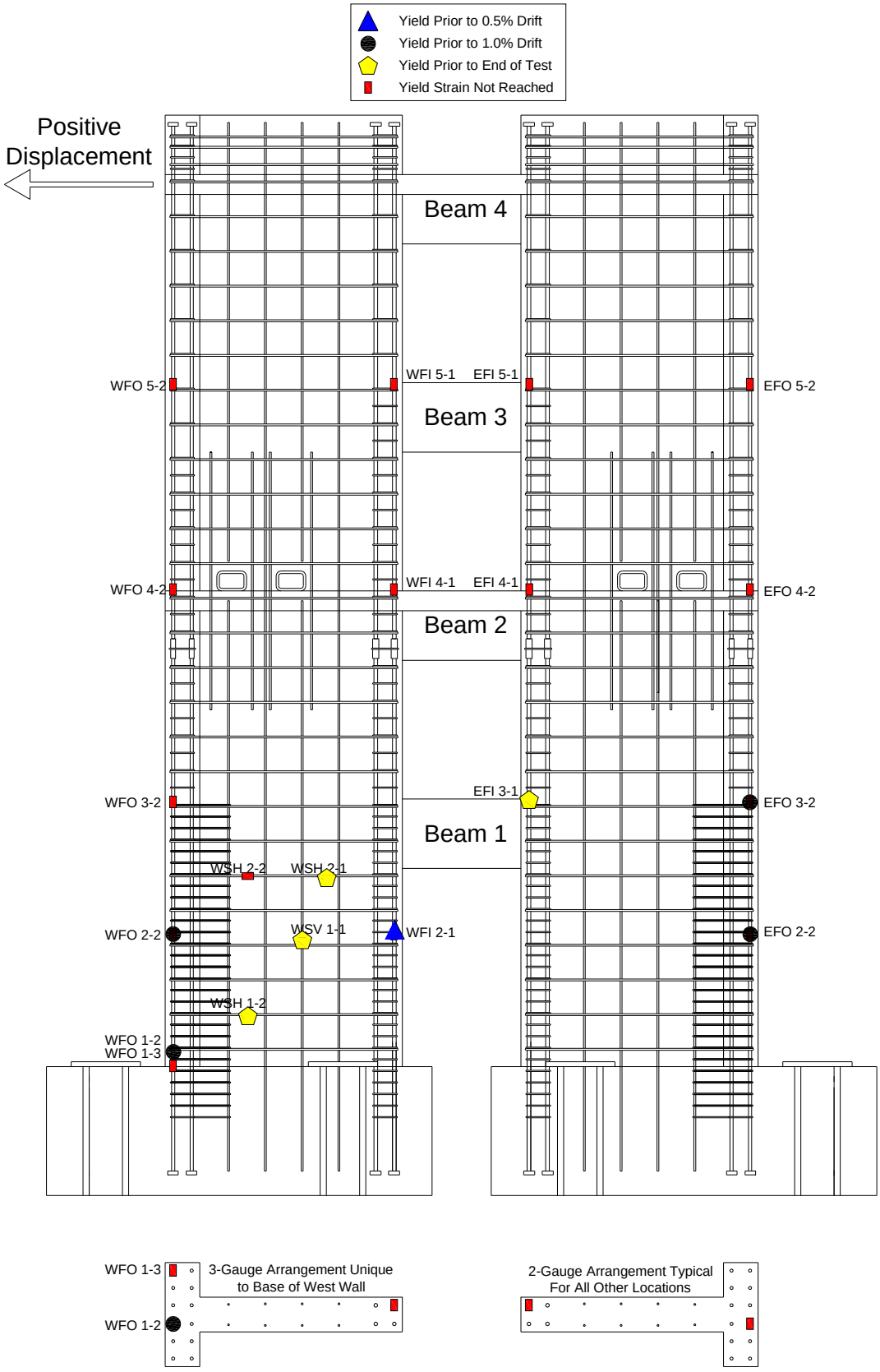

Figure 5.38 – Progression of yielding at strain gauge locations (Specimen CW-2, walls)

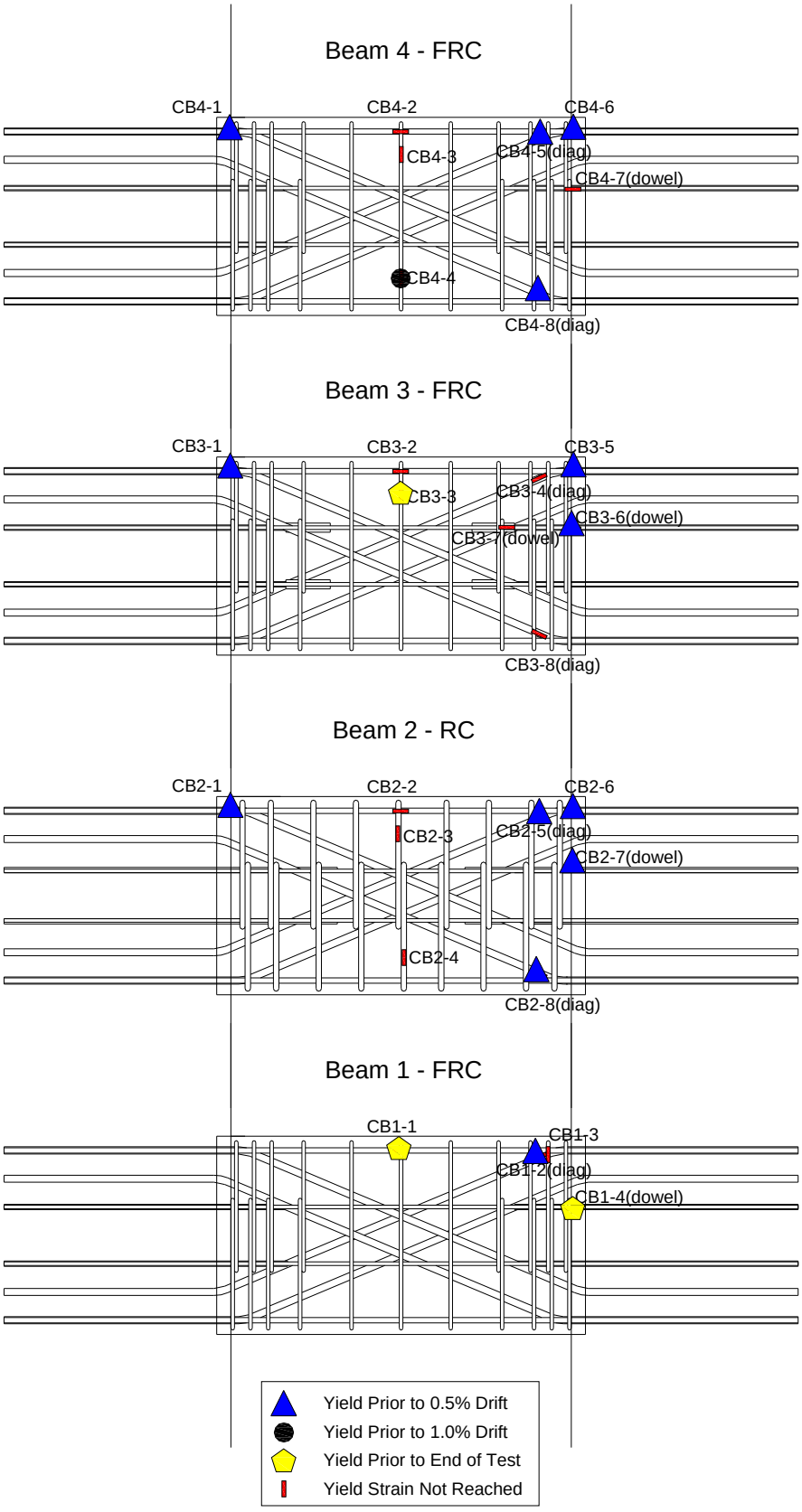

Figure 5.39 – Progression of yielding at strain gauge locations (Specimen CW-2, beams)

5.5.2 CUTOFF LONGITUDINAL BAR STRAINS

In Specimen CW-1, it was unexpected to record yielding strains in the longitudinal coupling beam reinforcement near the beam-to-wall interface that was terminated only 3 in. (75 mm), or $8d_b$, into the wall. The fact that yielding was recorded indicates that better bond was developed within the wall boundary element than expected. The calculated bar stresses corresponding to the measured bar strains for strain gauge CB3-5 in Specimens CW-1 and CW-2 (using the procedure described in Chapter 3) are plotted versus the coupling beam drift in Figure 5.40. The higher stress and fuller hysteresis loops exhibited by the fully developed bar from Specimen CW-2 demonstrate the improved strength and hysteretic characteristics achieved by the full development length. The shorter embedment length used in Specimen CW-1 did not withstand the cycling as well, showing pinching of the calculated stress versus coupling beam drift hysteresis curves. It is clear that the bar was slipping along its embedment length as a result of load reversals.

5.5.3 COUPLING BEAM SHEAR STRESSES

Given the indeterminate nature of the coupled wall system, it was not possible to determine the average shear stresses acting on each of the coupling beams. The beams were designed to have similar ultimate capacities, but the exact distribution of forces within the system cannot be determined. However, it is possible to use strain gauges fixed to the coupling beam reinforcement to estimate the contribution of hoops and diagonal reinforcement to resisting shear forces in each of the beams. It can be assumed that the difference between the probable beam shear force and the shear resistance provided by stirrups and diagonal reinforcement provide an approximation of the contribution of the concrete or HPFRC to the beam shear strength. Although the calculated values should not be considered exact, they do provide a sufficiently reasonable comparison between the beams to support a discussion of beam drift capacity. For the purpose of this discussion, the probable (or expected) shear force in the coupling beam, V_{pr}, is defined as the shear force theoretically required to develop a flexural hinge at both ends of the coupling beam. It was assumed that the strains recorded in a hoop at midspan were approximately

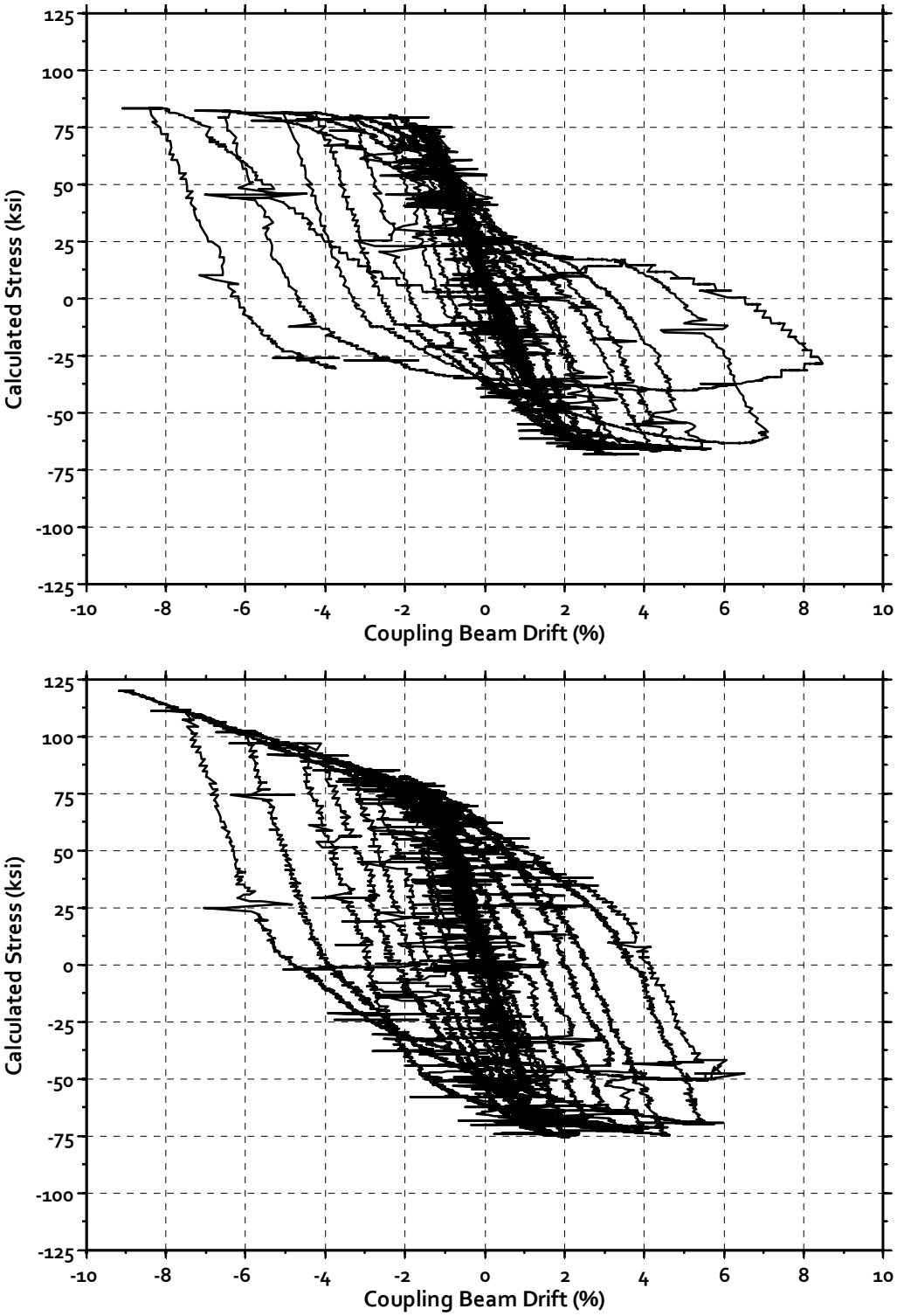

Figure 5.40 – Calculated bar stresses corresponding to the strains measured by strain gauge CB3-5 in Specimens CW-1 and CW-2 (top and bottom, respectively), plotted versus coupling beam drift

representative of the strains in all of the midspan hoops, and were used to estimate the shear force resisted by hoops. Likewise, it was assumed that strains recorded in one or two diagonal bars were adequately representative of the strains in all of the diagonal bars to reasonably estimate the total shear force resisted by diagonal reinforcement. Finally, it was assumed that the shear failure surface had a horizontal projection equal to the effective depth, d.

The approximate relative contribution of the midspan hoops to the expected shear force in the coupling beams of Specimens CW-1 and CW-2 is shown in Figure 5.41. This estimate likely overestimates the contribution of the midspan hoops to the shear capacity, because the hoops are providing confinement to the core of the beam in addition to shear strength. In Specimen CW-1, where the flexural reinforcement was terminated 3 in. (75 mm) into the wall, V_{pr} was approximately 50 kips (220 kN). The fully developed reinforcement in Specimen CW-2 increased V_{pr} in the beams to approximately 80 kips (350 kN). It is shown that the coupling beam hoops resisted approximately 15-25% of V_{pr} in Specimen CW-1, which is consistent with the observation that the beams were not fully active during this test. This is especially true at larger drifts, as sliding shear damage at the connections largely disconnected the beams from the walls. In Specimen CW-2, the hoops were generally more active in resisting shear, particularly in CB-2, the reinforced concrete beam.

The relative contribution of diagonal bars to V_{pr} is shown in Figure 5.42. The strain readings indicate that the contribution of the diagonal bars to V_{pr} was approximately 40% and 30% in Specimens CW-1 and CW-2, respectively. This corresponds to approximately 25 kips (110 kN) of shear force resisted by the diagonal reinforcement. The results indicate fully active diagonal reinforcement in every coupling beam except for CB-3 in Specimen CW-2. The reason for the different response in this beam is not clear.

Finally, the sum of the relative contributions of hoops and diagonal reinforcement to the probable shear force in each beam is shown in Figure 5.43. Although this sum could not be estimated for every coupling beam due to damaged or missing strain gauges, it is presented for all coupling beams where this sum could be reasonably approximated.

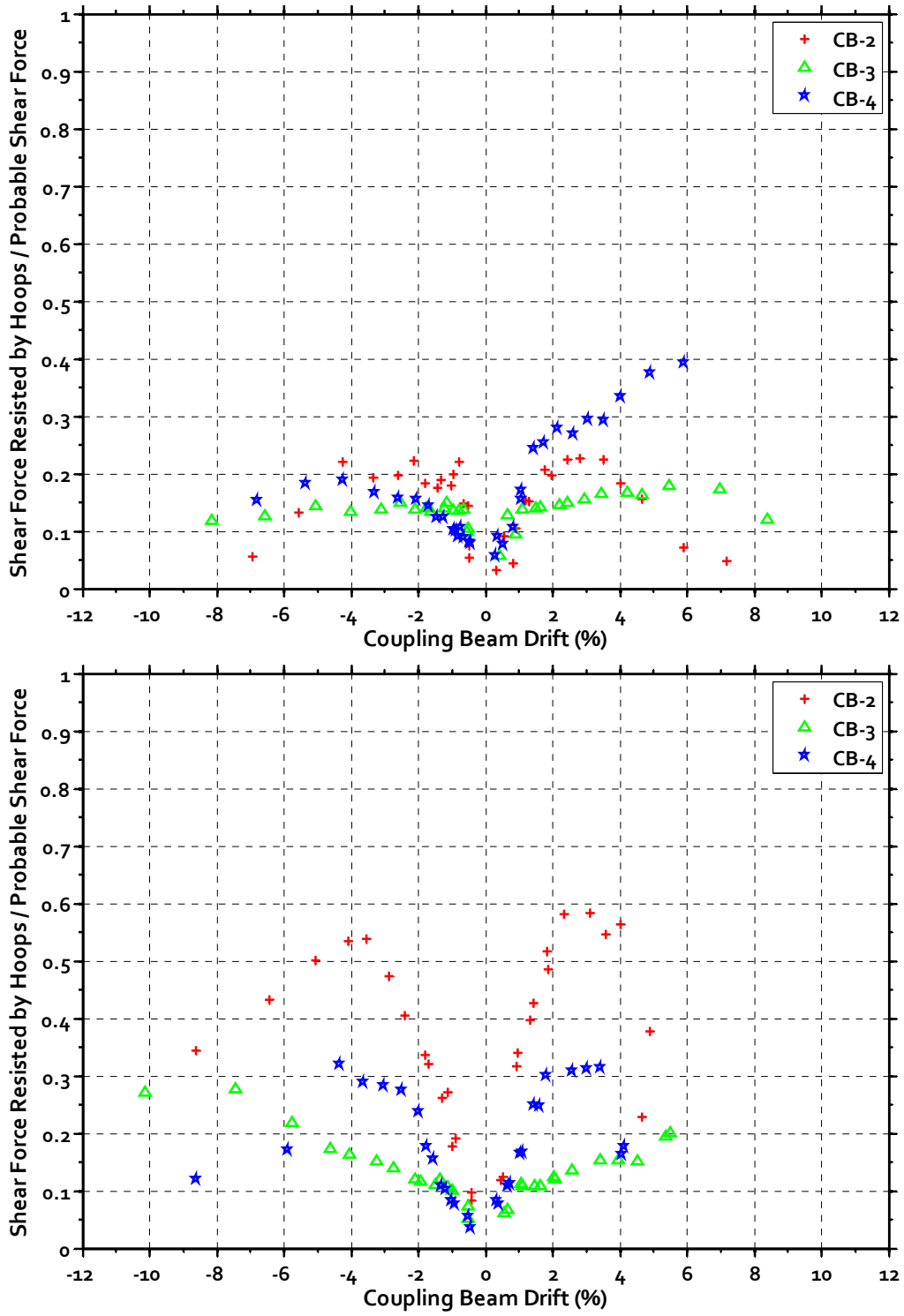

Figure 5.41 – Estimated shear force contributed by midspan hoops in the coupling beams of Specimens CW-1 and CW-2 (top and bottom, respectively)

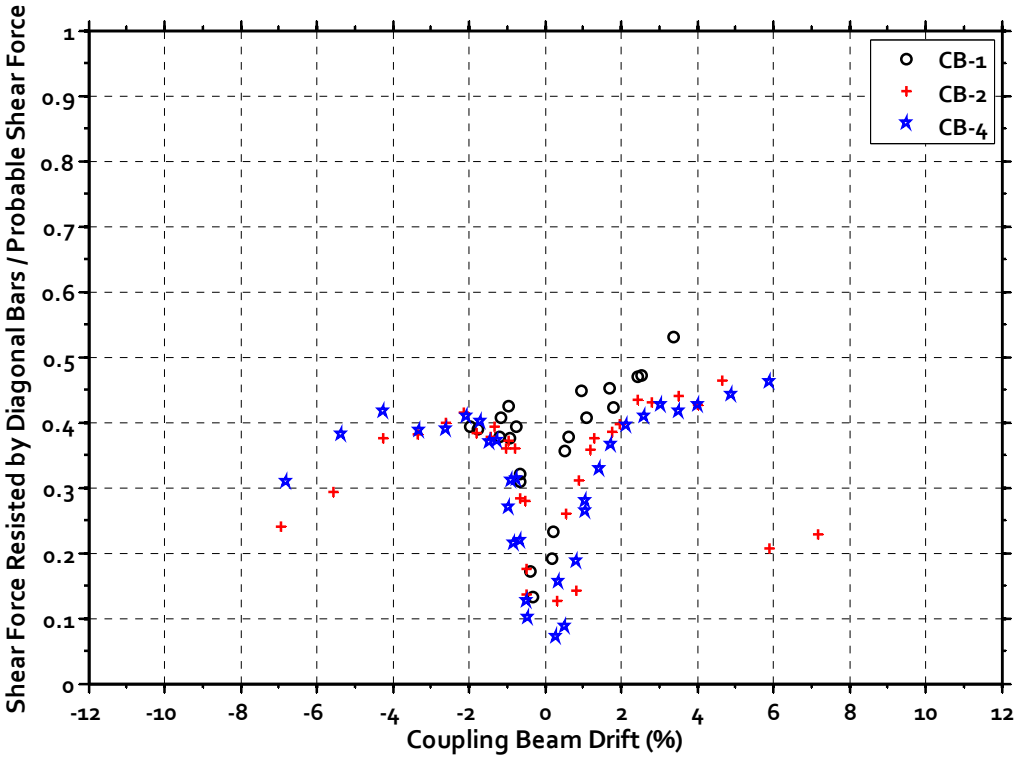

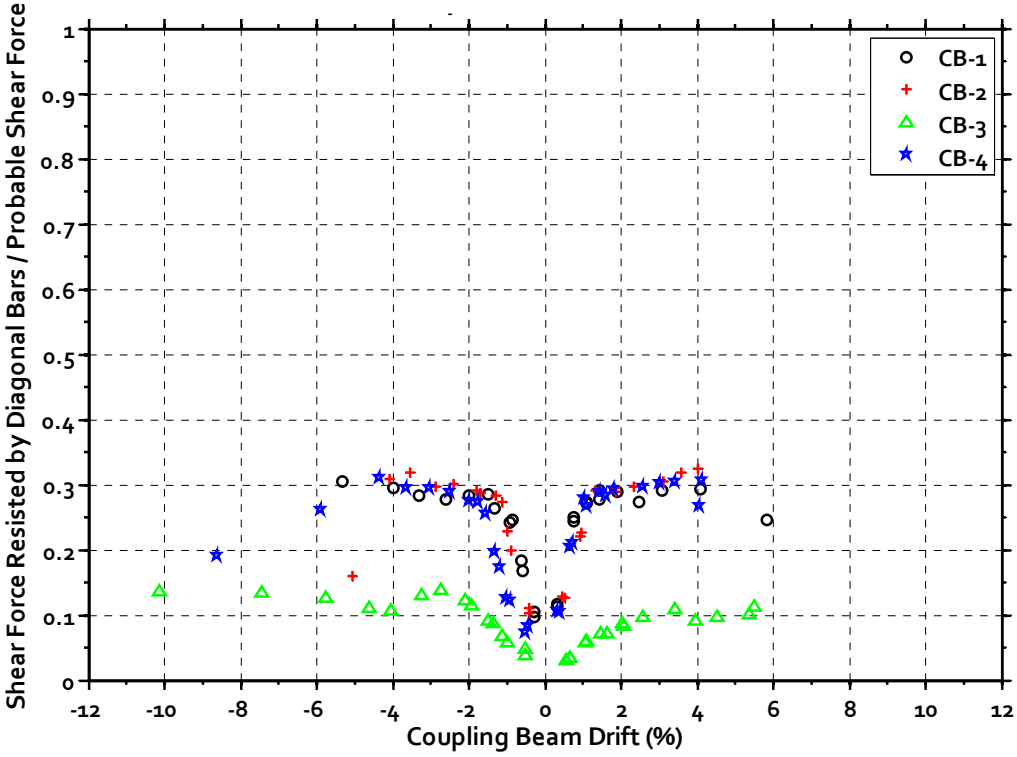

Figure 5.42 – Estimated shear force contributed by diagonal reinforcement in the coupling beams of Specimens CW-1 and CW-2 (top and bottom, respectively)

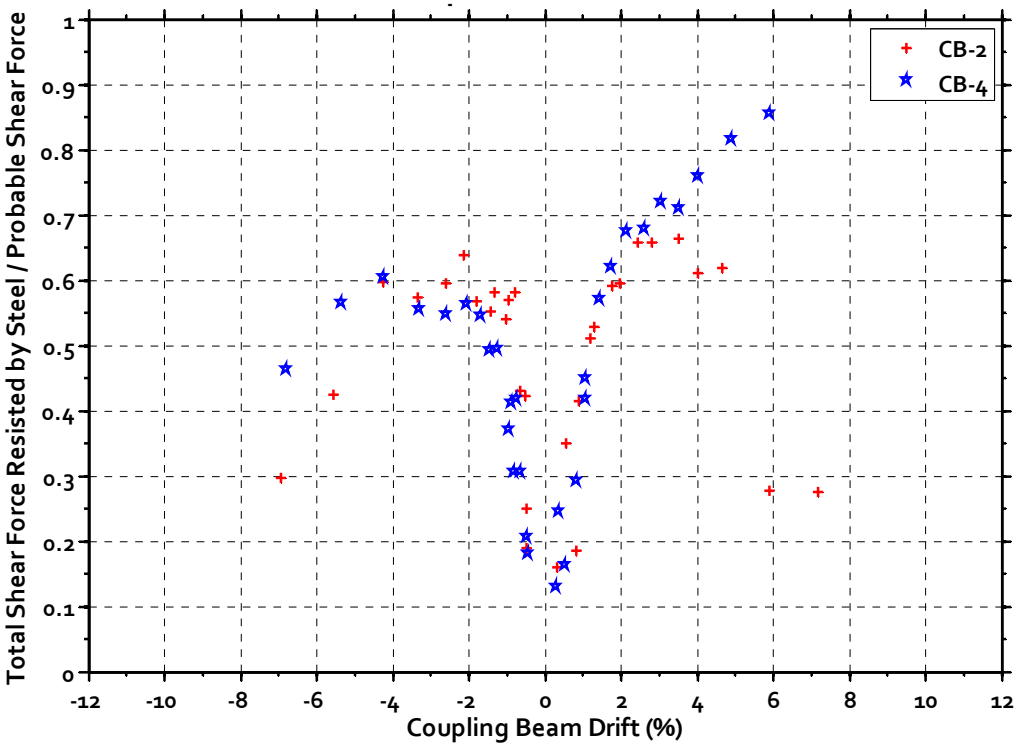

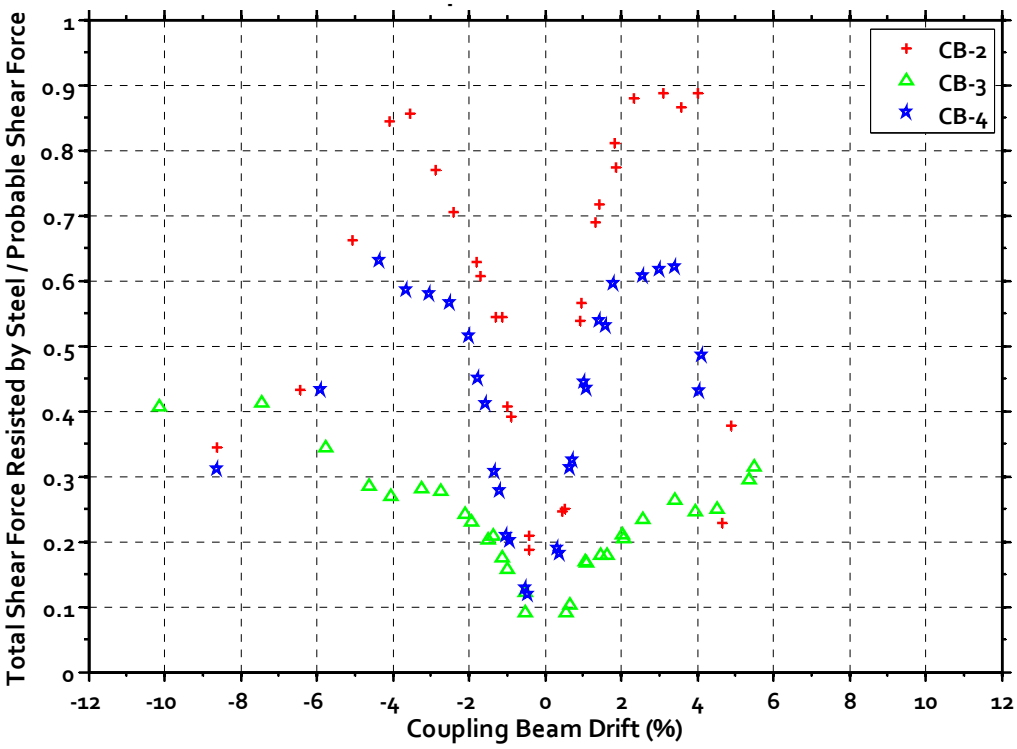

Figure 5.43 – Estimated total shear force contributed by diagonal and hoop reinforcement in the coupling beams of Specimens CW-1 and CW-2 (top and bottom, respectively)

It is shown that the shear demand in the coupling beams in Specimen CW-1 began to decrease at coupling beam drifts of approximately 3%, which corresponded to a coupled wall drift of approximately 1%. This is consistent with when damage to the beam-to-wall connection was noted, which appeared to limit the demands placed on the coupling beams. As previously discussed, full development of the beam flexural reinforcement in Specimen CW-2 prevented this premature localization of damage at the connection. The result was that the contribution of diagonal and hoop steel to V_{pr} in Specimen CW-2 showed different trends for different beams. The reinforced concrete coupling beam, CB-2, placed the largest demand on the diagonal reinforcement and hoops, as the concrete was unable to resist much of the applied shear stresses. The shear stresses resisted by the steel in CB-2 decreased significantly near a coupling beam drift of 4%, as the concrete section became severely damaged. It appears that the fourth story coupling beam, CB-4, began to lose its ability to resist the applied shear at coupling beam drifts of approximately 4%. This reduction in resisted shear forces after the loading cycle to 4% drift suggests that the buckling of the diagonal bars described in Section 5.1 initiated after this loading cycle. The third story HPFRC coupling beam showed no decrease in resisted shear force, even as drift demands surpassed 10%.

It is important to understand that this discussion is framed in relative terms given the limited instrumentation on the coupling beams above the first story level. It can generally be stated with confidence that the reinforced concrete beam relied more heavily on steel reinforcement to resist applied shear stresses than the HPFRC coupling beams, and that all of the HPFRC coupling beams sustained drift demands on the order of at least 4.0% before starting to lose shear capacity, with some far surpassing this drift capacity.

5.6 SUMMARY AND CONCLUSIONS

Two coupled wall specimens were built at approximately 1/3 scale and pseudo-statically subjected to earthquake-type displacement reversals. Both systems, which consisted of precast coupling beams linking two T-shaped structural walls, exhibited drift capacities larger than 2.5% with wide hysteresis loops. The test of Specimen CW-1

showed that the precast coupling beams, which had longitudinal reinforcement terminated near the beam-to-wall interface, developed premature localization of damage at the interface that limited the ability of the beams to couple the walls. The critical first wall stories in this specimen, detailed in accordance with the ACI Building Code (318-08), exhibited ductile flexural behavior. The fully developed coupling beam reinforcement in Specimen CW-2 moved damage away from the connection and into the beam spans, thereby taking full advantage of the toughness of the HPFRC beams and showing the improved damage tolerance of the HPFRC beams compared to the reinforced concrete beam. The HPFRC walls in Specimen CW-2, designed with a higher assumed concrete shear stress contribution and more widely spaced boundary element confinement reinforcement, exhibited a ductile flexural behavior in both loading directions, but ultimately failed in shear at approximately 2.5% drift in the positive loading direction.

The following conclusions regarding the design and behavior of these specimens can be drawn:

5.6.1 WALLS

- Assuming HPFRC could resist an average shear stress of $4\sqrt{f_c'}, [psi]\left(0.33\sqrt{f_c'}, [MPa]\right)$ in the design of walls was shown to lead to adequate resistance to shear. Two walls were designed with this assumption, resulting in a stable flexural mechanism in one and a shear failure in the other after substantial flexural yielding and multiple load reversals had taken place. Further analysis of the strain distribution within the failed wall indicated that initial crushing of poor quality concrete, not the transverse reinforcement ratio or hoop spacing, was the likely cause of failure.
- HPFRC coupled walls with a relaxed boundary element confinement spacing of $t_w/2$ behaved favorably when subjected to large drift demands (up to 3.5% drift), with no indication of buckling of wall longitudinal reinforcement throughout the test. A further increase of the boundary element spacing to t_w was not conclusively shown to be either safe or unsafe in design because of the diagonal

crack that failed the compression zone in that specimen. Further testing is warranted, given the inconclusive nature of the results.

- The walls detailed in accordance with the ACI Building Code (318-08) behaved very well.
- Dowel bars crossing the cold joint between the HPFRC wall and the foundation successfully prevented localization of damage along this interface. Late in the test, flexural rotations localized along the line where dowel bars were terminated. However, this occurred in the wall that achieved the largest drift capacity, so it was not considered a detriment to the performance of the test structure. This is further indication that dowel bars are advisable across cold joints in HPFRC structures.
- The plastic hinge length within each wall, estimated on the basis of the curvature distribution, was approximately one member depth.
- Average shear distortion was larger in the compression wall, which is consistent with a large shift of shear force to the compression wall. The flange in the tension wall, which accommodated more reinforcement along the outside edge of the system, did not appear to appreciably affect this shifting phenomenon. Although the indeterminate nature of the system prevented direct measurement of the shift of shear force, all evidence indicates that a dominant strut was active in both specimens that shifted shear force to the compression wall. Crack patterns indicate the presence of this strut through the first story coupling beam and in the walls, and the principal strains measured throughout the first wall story support this observation. Coupling beam measurements indicate that a large compression force was transferred between walls that shortened the first story beam in Specimen CW-1 and severely restrained its growth in Specimen CW-2.
- Axial deformations in the walls due to axial stresses were very minor compared to those due to rotations and thus, they did not play an important role in the deformation of the specimens tested.

5.6.2 COUPLING BEAMS

- HPFRC coupling beams were shown to be significantly more damage tolerant than comparable reinforced concrete coupling beams subjected to similar deformation demands, despite the use of substantially more transverse reinforcement in the reinforced concrete beams.
- When system drifts were large (on the order of 1.0 to 1.5%), the coupling beams were subjected to drift demands of 3.0 to 4.5%. The response of HPFRC coupling beams was shown to be stable at these drift demands. At even larger system drifts, coupling beam drifts continued to increase to beyond 10%, which highlights the significant drift demands coupling beams can be subjected to in response to seismic events.
- It was shown that coupling beam axial forces result from two distinct phenomena: 1) a shift of wall shear force to the stiffer compression wall near the foundation, and 2) resistance by stiff walls to beam elongation caused by the accumulation of plastic deformation in coupling beam reinforcement and the opening and partial re-closing of cracks as drift demands increase.
- Axial elongation of the beams above the first story were consistent with the elongation allowed in the component tests, indicating that the axial forces measured in the component tests are a reasonable approximation of the forces that might develop in a coupled system.
- In addition to affecting flexural and shear capacity of coupling beams, axial forces were shown to increase the beam shear stiffness. This had the effect of reducing shear deformations, but forced an increase in the curvature ductility demands to accommodate the imposed drift demands. This is an example of the potentially important role of axial forces on the behavior of coupling beams.
- Full development of the longitudinal reinforcement is required to develop the full capacity of the beams and to prevent localization of damage at the beam-to-wall interface. Although some cutoff bars yielded, their response was marked by lower ultimate stresses and more pronounced pinching than the fully developed bars.

- It was shown that the relative importance of shear and flexure mechanisms to the drift of the first story coupling beams was comparable to that exhibited by the component test specimens described in Chapter 4.

5.6.3 COUPLED WALL SYSTEM

- Incorporation of precast coupling beams into the construction sequence of the coupled system was shown to be a straightforward process and a viable alternative to current construction methods. Formwork easily supported the precast beam prior to casting the wall concrete, and wall boundary confinement reinforcement was successfully placed with little interference from beam reinforcement.
- The overturning moment capacity of the system was predicted to within 3% for both loading directions of Specimen CW-1 and for the negative loading direction of Specimen CW-2. This calculation assumed a flexural hinge would simultaneously form at the base of each wall, at the ends of each coupling beam, and in the slabs (which were treated independently from the coupling beams because they were cast adjacent to, but not connected with, the precast coupling beam). This method over-predicted, by approximately 6%, the capacity in the positive loading direction of Specimen CW-2 because the strength in this loading direction was governed by a shear failure that developed in the compression wall of this specimen.
- The thin slabs at the second and fourth levels were shown to develop plastic hinges and contribute to the coupling of the walls. Without considering this contribution, the overturning moment capacity of the system would have been under-predicted by between 5 and 9%.
- A Wall Strength Index (WSI), was proposed as a complement to the coupling ratio (CR). The WSI is defined as the sum of the flexural capacity of the walls considering axial forces due to coupling, divided by the sum of the flexural capacity of the walls without the axial forces due to coupling. WSI is a direct measure of the effect axial forces due to coupling have on the flexural strength of walls. For systems with $WSI < 1.0$, additional coupling reduces the flexural capacity of the walls, and thus increasing CR would not be the most efficient way

to increase the lateral capacity of the system. Furthermore, $WSI < 1.0$ indicates that the flexural ductility of the walls may be reduced by the axial forces from coupling.

CHAPTER 6:
DESIGN CONSIDERATIONS FOR COUPLED WALLS

6.1 FLEXURE-BASED COUPLING BEAM DESIGN

The precast HPFRC coupling beams described herein represent a change from the state of the art and require a different design approach than ACI Building Code (ACI 318-08) compliant beams. A flexure-based design approach was adopted, as discussed in Section 3.1.2, that considers the contribution of all longitudinal and diagonal reinforcement to the capacity of the beam. All of the transverse reinforcement and the concrete itself are considered when calculating the shear capacity of the beam because the HPFRC remains sufficiently sound through large displacement reversals to actively resist shear imposed on the coupling beam at the formation of a flexural mechanism. The specimens designed with this flexure-based design approach exhibited a ductile failure mode despite the short aspect ratio of the test specimens (1.75). The procedure used to design the specimens has been simplified and generalized for the design of precast HPFRC coupling beams with aspect ratios between 1.5 and 3.5. This recommended procedure is presented in Section 6.1.1.

The simplified flexure-based method (SFBM) relies on a calculation of the nominal moment strength, M_n, which governs the capacity of the beam. To simplify the calculation of M_n, the effects of axial forces and the contribution of the HPFRC to the flexural capacity are neglected. The accuracy of the SFBM is discussed in Section 6.1.2. It is shown that using the SFBM to calculate the capacity of HPFRC coupling beams is at least as accurate as the current ACI Building Code (ACI 318-08) method for code-compliant coupling beams. Furthermore, a review of relevant literature shows this SFBM may be more accurate for code-compliant coupling beams than the current code method.

6.1.1 Simplified Flexure-Based Design Method for HPFRC Coupling Beams

The following design procedure is intended for precast HPFRC coupling beams with aspect ratios between 1.5 and 3.5. It is based on the assumption that a flexural mechanism will control the capacity of the coupling beam. Because coupling beams are subjected to double curvature in an earthquake, and minimal non-earthquake related loading, the moment demand at the wall face is assumed to be a linear function of the shear demand, such that $M_{demand} = V_{demand}\ell_n/2$, where ℓ_n is the clear span length of the coupling beam. This design procedure assumes that an analysis of the structural system has been performed to determine V_{demand} in the coupling beams to achieve a target coupling ratio. The corresponding M_{demand} that develops in the coupling beam at the wall face is used for design, where a nominal moment capacity, M_n, is provided at the ends of the coupling beam so that $\phi M_n = M_{demand}$.

The coupling beam is subsequently designed with enough shear capacity to ensure that a shear failure will not occur when the beam reaches its probable flexural capacity, M_{pr}. For design, an R-factor is introduced to amplify M_n such that $RM_n \cong M_{pr}$. Based on experimental work, it is recommended $R = 1.4$ to account for strain hardening of the reinforcement, material overstrength, and axial forces that develop in the coupling beam.

The proposed step-by-step design procedure is as follows:

1) Determine the required coupling beam shear strength: From an analysis of the structural system, determine the target coupling ratio for the coupled wall system, and thus, the required shear (V_{demand}) for the coupling beam. Set $M_{demand} = V_{demand}\ell_n/2$, where ℓ_n is the clear span length of the coupling beam.
2) Select outer beam dimensions: Select cross-sectional beam dimensions that satisfy architectural requirements while ensuring that $V_{demand} < 8\sqrt{f_c'}A_{cw}$, [psi] $\left(0.66\sqrt{f_c'}A_{cw}, \text{[MPa]}\right)$, where A_{cw} is the cross-sectional area of the beam and f_c' is the specified compressive strength of the concrete. The beam is to be designed so that $\phi M_n = M_{demand}$. By sizing the beam such that $V_{demand} < 8\sqrt{f_c'}A_{cw}$, [psi] $\left(0.66\sqrt{f_c'}A_{cw}, \text{[MPa]}\right)$, it is ensured that the

maximum shear stress demand corresponding to the probable moment capacity will not greatly exceed $10\sqrt{f_c'}A_{cw}$, [psi] $\left(0.83\sqrt{f_c'}A_{cw}, \text{[MPa]}\right)$. This upper bound shear stress is appropriate based on experimental work that has shown that precast HPFRC coupling beams behave in a ductile manner when subjected to shear stresses as high as $14\sqrt{f_c'}A_{cw}$, [psi] $\left(1.17\sqrt{f_c'}A_{cw}, \text{[MPa]}\right)$, as in the test of Specimen CB-3 reported in Chapter 4.

3) Select diagonal reinforcement area and orientation (see Figure 6.1): It is recommended to set the shear force from diagonal bars to approximately 30% of V_{demand} for coupling beams with ℓ_n/h near 1.75. Less slender coupling beams should rely more heavily on diagonal reinforcement, and more slender coupling beams should place less reliance on diagonal reinforcement. At aspect ratios of approximately 3.5 and larger, the use of diagonal steel is no longer appropriate (Parra-Montesinos, Wight and Setkit, 2010).

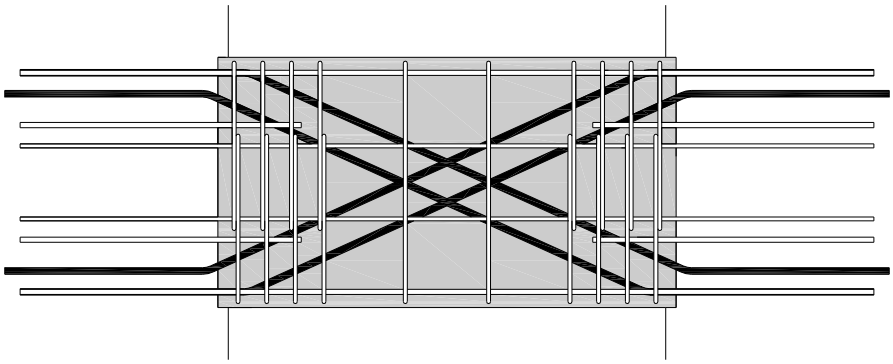

Figure 6.1 – Schematic of reinforcement (diagonal reinforcement is black)

4) Select longitudinal reinforcement, A_s, (see Figure 6.2): Select sufficient longitudinal reinforcement to ensure that $\phi M_n \cong M_{demand}$, where ϕM_n is calculated assuming that $\phi = 1.0$. The contribution of A_s and the diagonal reinforcement are to be included when calculating the flexural strength, M_n. A_s includes the total area of primary tension flexural reinforcement (top or bottom), intermediate depth reinforcement, and short dowel bars bridging the cold joint between the precast beam and wall (described further in Step 5). For preliminary selection of A_s, it is reasonable to assume that $(2/3)A_s$ is located at a depth of $h/2$ and that the remaining $(1/3)A_s$ is located at a depth, d_t

(Figure 6.3), that maximizes the contribution of these bars to flexural capacity. An assumed strain profile consistent with these recommendations is shown in Figure 6.3 along with the magnitude and location of the corresponding force resultants.

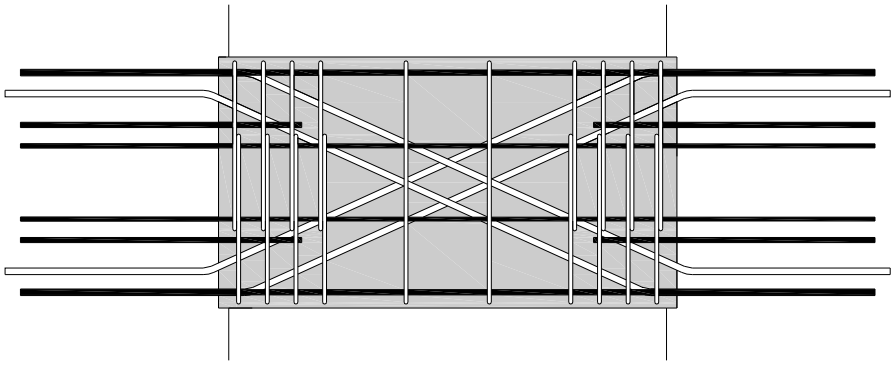

Figure 6.2 – Schematic of reinforcement (longitudinal reinforcement is black)

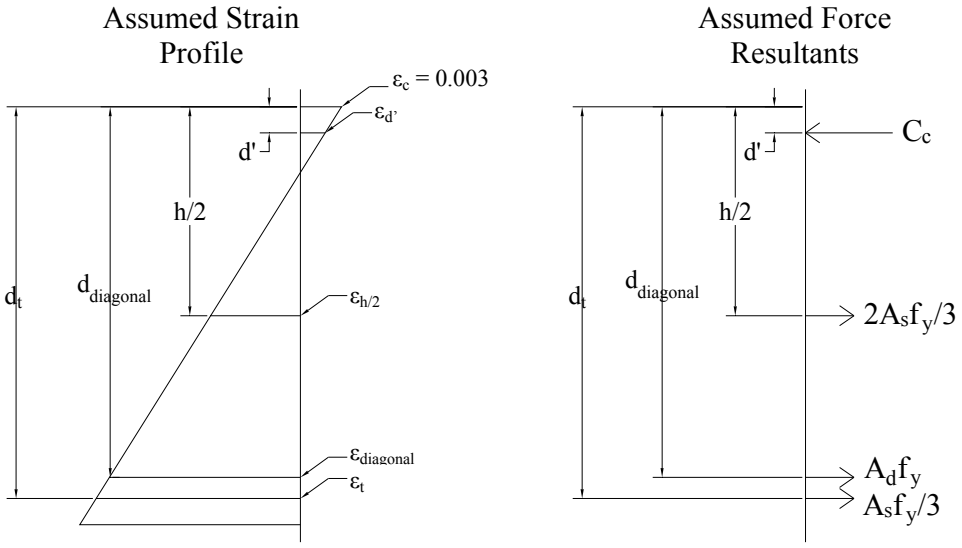

Figure 6.3 – Assumed strain profile and corresponding force resultants for determining A_s (A_d is the horizontal component of the force in the diagonal reinforcement)

5) Intermediate depth longitudinal reinforcement: Of the $(2/3)A_s$ whose force resultant is assumed to be located at mid-depth, some should be detailed as intermediate depth longitudinal reinforcement that is continuous over the entire length of the coupling beam, and some as short dowel bars to ensure

failure does not localize at the cold joint between the precast coupling beam and the wall.

a. Intermediate depth longitudinal reinforcement (see Figure 6.4): Two curtains of intermediate depth longitudinal reinforcement (one along each face of the beam) are recommended. These bars should be at least as large in diameter as the transverse hoops, and placed with a maximum vertical spacing of $d/3$. These bars are included in the calculation of M_n.

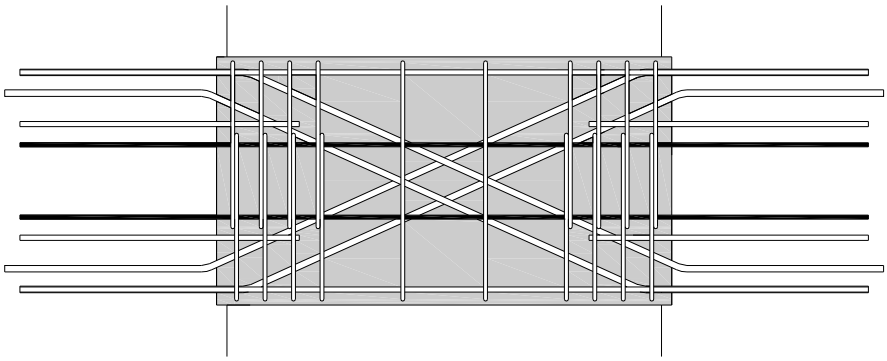

Figure 6.4 – Schematic of reinforcement (intermediate depth longitudinal reinforcement is black)

b. Dowel Bars (see Figure 6.5): Dowel bars must be placed across the cold joint where the precast beam meets the wall. For aspect ratios between 1.5 and 2.0, it is recommended that $A_{s(dowel)} \cong (0.4\ to\ 0.55)A_s$ and $\ell_{(dowel)} \cong h/3$, where A_s includes the total area of primary tension flexural reinforcement (top or bottom), intermediate depth reinforcement, and short dowel bars bridging the cold joint between the precast beam and wall. For aspect ratios larger than 2.0, it is recommended that $A_{s(dowel)} \cong (0.3\ to\ 0.4)A_s$ and $\ell_{(dowel)} \cong h/2$. Also, confirm that $\ell_{(dowel)} \geq \ell_{d(HPFRC)}$, where the use of $\ell_{d(HPFRC)} = 16d_b$ was shown to be sufficient to yield the dowel reinforcement in the specimens tested as part of this study. If the $\ell_{(dowel)} \geq \ell_{d(HPFRC)}$ condition cannot be

satisfied, U-shaped dowel reinforcement (as shown in Figure 3.3) is recommended.

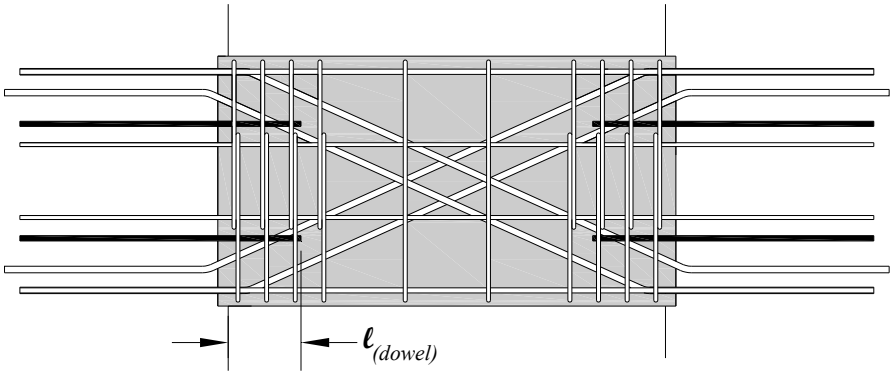

Figure 6.5 – Schematic of reinforcement (dowel reinforcement is black)

6) Shear Design: Calculate $V_{pr} = 2M_{pr}/\ell_n$, where $M_{pr} = RM_n$, and design the beam shear reinforcement so that $\phi V_n \geq V_{pr}$, where $\phi = 0.85$. For HPFRC coupling beams, $V_n = V_d + V_s + V_{cf}$, where V_d is the contribution from the diagonal reinforcement (taken as $V_d = 2A_{vd}f_{yd}\sin(\theta)$), V_s is the contribution from the stirrups (taken as $V_s = A_v f_{yt} d/s$), and V_{cf} is the contribution from the HPFRC (taken as $V_{cf} = 5\sqrt{f_c'}A_{cw}$, [psi] $\left(0.42\sqrt{f_c'}A_{cw}, \text{[MPa]}\right)$).
7) Final detailing recommendations:
    a. Beam embedment: Embed the precast coupling beam into the adjacent walls approximately as deep as the wall clear cover without imposing unreasonable construction tolerance demands.
    b. Confinement: No special confinement of the diagonal reinforcement is required when HPFRC is used. It is recommended that special column-type confinement (as defined in Chapter 21 of the ACI Building Code, 318-08) be provided at the ends of the coupling beam throughout the expected plastic hinge region, approximated as extending $h/2$ away from the face of the walls. Because the diagonal reinforcement is bent within the span of the coupling beam, a check must be made to ensure that closed hoops placed near the bend have sufficient strength to balance the full vertical (outward) force from the bent compression

diagonal reinforcement (see Figure 6.6 and satisfy Eq. 6.1). In Eq. 6.1, α is a factor accounting for material overstrength and strain hardening, often taken as 1.25, and the 1.5 factor ensures sufficient stirrup capacity remains to provide confinement and shear resistance after the force component from the diagonal reinforcement is accounted for.

$$\sum A_v f_{yt} \geq 1.5 \sum A_d \alpha f_{yd} sin(\theta) \tag{6.1}$$

8) Upper bound coupling beam capacity: For design of the walls, it is recommended that V_{pr}, calculated in Step 6, be used to estimate the maximum compression and tension forces the individual walls may be subjected to.

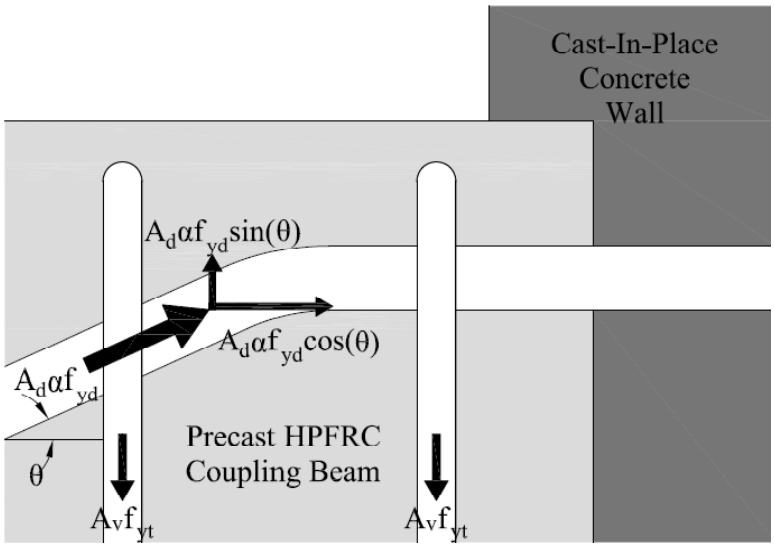

Figure 6.6 – Forces in steel reinforcement near the bent-diagonal detail

6.1.2 Comparison of Flexure- and ACI Code-Based Capacity Prediction

The flexure-based design procedure used to design and analyze the precast HPFRC coupling beams tested in this study was shown to provide an estimate of the peak capacity of the specimens that was within 6% of the actual capacity of the beams (see Section 4.2). In all three specimens, the shear capacity of the specimens was large enough to prevent a shear failure and force a flexural mechanism to control the capacity. To design these specimens, multiple moment-curvature analyses were performed that

accounted for the axial force in the coupling beams and the contribution of the HPFRC to the flexural capacity. Recognizing that it is unreasonable to expect this level of detail in a design office, particularly in preliminary design stages, a simplified flexure-based method (SFBM) for design was outlined in Section 6.1.1. In the SFBM, the contributions of axial force and HPFRC to flexural strength are neglected, and the moment-curvature analysis is replaced by a non-iterative nominal moment strength (M_n) calculation. The beam is then designed such that its shear strength exceeds the probable shear demand associated with the resulting flexural mechanism. To justify use of the SFBM, the accuracy of the method was compared to the current ACI Building Code (ACI 318-08) method, which requires the use of Eq. 6.2 to calculate the capacity of coupling beams, where A_{vd} is the area of steel in each group of diagonal reinforcing bars, f_y is the specified yield strength of the steel, generally taken as 60 ksi (415 MPa), and θ is the orientation of the diagonal reinforcement relative to the longitudinal axis of the beam. The results of this comparison are presented in this section.

$$V_n = 2A_{vd}f_y sin(\theta) \tag{6.2}$$

A database of 37 diagonally reinforced coupling beam component tests was compiled from the literature (Table 6.1). The only criteria for inclusion in the database were that some or all of the flexural capacity of the coupling beam was provided by diagonally oriented reinforcement and that sufficient information was provided describing the specimens that the capacity could be calculated and compared to test results. The database includes 13 diagonally reinforced coupling beams with all longitudinal reinforcement terminated near the beam-to-wall connection, 15 diagonally reinforced coupling beams with all longitudinal reinforcement fully developed into the adjacent walls, and 9 diagonally reinforced HPFRC coupling beams with all longitudinal reinforcement developed into the walls. Of the 28 reinforced concrete coupling beams, 27 were cast monolithically with the adjacent walls. The other reinforced concrete beam and the 9 HPFRC coupling beams were precast with varied embedment details. The database includes beams with aspect ratios ranging from 1.0 to 5.0, with the majority of specimens

Table 6.1 – Database of diagonally reinforced coupling beam specimens

Reference	Reinf. Type [1]	ℓ_n (in.)	ℓ_n/h	$V_{experiment}$ (kip)	$V_{predicted\text{-}1} = 2 \cdot A_{diag} \cdot f_y \cdot \sin(\theta)$	$V_{experiment} / V_{predicted\text{-}1}$	M_n	$V_{predicted\text{-}2} = 2M_n/\ell_n$	$V_{experiment} / V_{predicted\text{-}2}$
Sonobe et al. (1995)	RC - Dev	39.2	2.8	80.9	37.5 [2]	2.2	1240 [2]	63.3	1.3
Tassios, Moretti, Bezas (1996)	RC - Dev	20	1	63.6	30.3 [2]	2.1	610 [2]	60.8	1.0
Tassios, Moretti, Bezas (1996)	RC - Dev	20	1.7	38.2	23.1 [2]	1.7	330 [2]	33.1	1.2
Galano, Vignoli (2000)	RC - Dev	24	1.5	54.0	24.0 [2]	2.3	510 [2]	42.3	1.3
Galano, Vignoli (2000)	RC - Dev	24	1.5	53.3	24.0 [2]	2.2	510 [2]	42.7	1.2
Galano, Vignoli (2000)	RC - Dev	24	1.5	53.5	24.0 [2]	2.2	520 [2]	42.9	1.2
Galano, Vignoli (2000)	RC - Dev	24	1.5	53.5	24.0 [2]	2.2	520 [2]	42.9	1.2
Galano, Vignoli (2000)	RC - Dev	24	1.5	54.2	24.0 [2]	2.3	510 [2]	42.7	1.3
Galano, Vignoli (2000)	RC - Dev	24	1.5	53.7	24.0 [2]	2.2	510 [2]	42.3	1.3
Galano, Vignoli (2000)	RC - Dev	24	1.5	54.0	24.0 [2]	2.3	510 [2]	42.4	1.3
Kwan, Zhao (2002)	RC - Dev	28	1.2	77.8	28.6 [2]	2.7	920 [2]	65.5	1.2
Canbolat, Parra, Wight (2005)	RC - Dev	24	1	105.0	56.4 [2]	1.9	1160 [2]	97.0	1.1
Yun et al. (2007)	RC - Dev	24	1	143.0	37.2 [2]	3.8	1670 [2]	139	1.0
Fortney, Rassati, Shahrooz (2008)	RC - Dev	36	2.6	138.0	98.1 [2]	1.4	2470 [2]	137	1.0
Setkit (unpublished)	RC - Dev	66	2.75	126.0	28.9 [2]	4.4	2590 [2]	78.6	1.6
Mean		28.3	1.6			2.4			1.2
Min - Max		20.0-66.0	1.0-2.8			1.4-4.4			1.0-1.6
Paulay, Binney (1975)	RC - Cut	40	1.3	151.0	92.5 [3]	1.6	2110 [3]	106	1.4
Paulay, Binney (1975)	RC - Cut	40	1.3	130.0	92.5 [3]	1.4	2180 [3]	110	1.2
Paulay, Binney (1975)	RC - Cut	40	1.0	146.0	115 [3]	1.3	2580 [3]	129	1.1
Shiu et al. (1978)	RC - Cut	16.7	2.5	13.4	6.6 [2]	2.0	76 [2]	9.1	1.5
Shiu et al. (1978)	RC - Cut	33.3	5	7.5	4.5 [2]	1.7	76 [2]	4.6	1.6

Fortney, Rassati, Shahrooz (2008)	RC - Cut	36	2.6	93.4	74.5 [2]	1.3	1530 [2]	84.9	1.1
Naish et al. (2009)	RC - Cut	36	2.4	171.0	117 [2]	1.5	2500 [2]	139	1.2
Naish et al. (2009)	RC - Cut	36	2.4	160.0	117 [2]	1.4	2500 [2]	139	1.2
Naish et al. (2009)	RC - Cut	36	2.4	191.0	117 [2]	1.6	2510 [2]	140	1.4
Naish et al. (2009)	RC - Cut	36	2.4	212.0	117 [2]	1.8	2510 [2]	140	1.5
Naish et al. (2009)	RC - Cut	36	2.4	190.0	117 [2]	1.6	2510 [2]	139	1.4
Naish et al. (2009)	RC - Cut	60	3.3	124.0	92.0 [2]	1.3	3180 [2]	106	1.2
Naish et al. (2009)	RC - Cut	60	3.3	121.0	92.0 [2]	1.3	3180 [2]	106	1.1
Mean		38.9	2.5			1.5			1.3
Min - Max		16.7-60.0	1.0-5.0			1.3-2.0			1.1-1.6
Canbolat, Parra, Wight (2005)	FRC - Dev	24	1	180.0	43.7 [2]	4.1	1730 [2]	144	1.2
Canbolat, Parra, Wight (2005)	FRC - Dev	24	1	180.0	37.2 [2]	4.8	1670 [2]	139	1.3
Yun et al. (2007)	FRC - Dev	24	1	205.0	37.2 [2]	5.5	1670 [2]	139	1.5
Lequesne (this study)	FRC - Dev	42	1.75	148.0	30.6 [2]	4.8	2260 [2]	108	1.4
Lequesne (this study)	FRC - Dev	42	1.75	147.0	30.6 [2]	4.8	2000 [2]	95.4	1.5
Lequesne (this study)	FRC - Dev	42	1.75	146.0	30.6 [2]	4.8	1930 [2]	92.1	1.6
Setkit (unpublished)	FRC - Dev	66	2.75	129.0	28.9 [2]	4.5	3200 [2]	97.0	1.3
Setkit (unpublished)	FRC - Dev	66	2.75	116.0	28.9 [2]	4.0	2590 [2]	78.5	1.5
Setkit (unpublished)	FRC - Dev	66	3.3	115.0	23.0 [2]	5.0	2880 [2]	87.2	1.3
Mean		44.0	1.9			4.7			1.4
Min - Max		24.0-66.0	1.0-3.3			4.0-5.5			1.2-1.6

[1] RC – Dev, RC – Cut, and FRC – Dev, refer to coupling beams cast with either reinforced concrete or HPFRC, and reinforced with longitudinal reinforcement that was either fully developed into the wall or cutoff near the wall boundary

[2] Assumed $f_y = 60$ ksi

[3] Assumed $f_y = 40$ ksi

(90%) representing aspect ratios between 1.0 and 3.0. The specimens in the database were of reasonably large scale, with a mean clear span length of 36 in. (900 mm).

In Figure 6.7, the ratio between the experimental capacity of the coupling beams and the capacity calculated by Eq. 6.2 is plotted against the coupling beam aspect ratio. Similarly, in Figure 6.8, the ratio between the experimental capacity of the coupling beams and the capacity calculated by the SFBM (where $V_{predicted} = 2M_n/\ell_n$), is plotted against the coupling beam aspect ratio. For calculation of the beam capacity in both cases, it was assumed that $f_y = 60$ ksi (415 MPa), except for the tests performed by Paulay and Binney (1974) for which it was assumed that $f_y = 40$ ksi (275 MPa)). The three sets of beams (reinforced concrete with developed longitudinal bars, reinforced concrete with cutoff longitudinal bars, and HPFRC with developed longitudinal bars) are distinguished by different marker shapes. In the SFBM it is assumed that the shear capacity of each beam is great enough for the beam to reach its flexural capacity prior to failing, regardless of the eventual failure mode. Specimens that exhibited ductile flexural failure modes are identified with hollow markers, whereas solid markers indentify specimens that eventually developed other, generally brittle, failure modes.

Comparing Figs. 6.7 and 6.8 illustrates the significant improvement achieved when the SFBM is employed instead of the ACI method for calculation of coupling beam capacity. This improvement was most visible for HPFRC coupling beam specimens, which exhibited experimental capacities 4.0 to 5.5 times greater than calculated by Eq. 6.2, but only 1.2-1.6 times greater than calculated by SFBM. Because the HPFRC coupling beam specimens were designed using a flexure-based philosophy, this improvement, although significant, is not unexpected. Using SFBM for calculating the capacity of HPFRC coupling beam specimens resulted in an accuracy similar to that achieved by Eq. 6.2 for ACI Building Code-compliant coupling beams that have cutoff longitudinal reinforcement (compare a ratio of 1.2 to 1.6 using SFBM for HPFRC beams to a ratio of 1.3 to 2.0 using Eq. 6.2 for ACI Building Code-compliant beams). This indicates that using the SFBM for calculating the capacity of a coupling beam outlined in Section 6.1.1, which neglects axial forces and the flexural contribution from HPFRC, is at least as accurate as the current ACI method. Furthermore, the majority of the HPFRC coupling beams in the database were subjected to axial force that would tend to increase

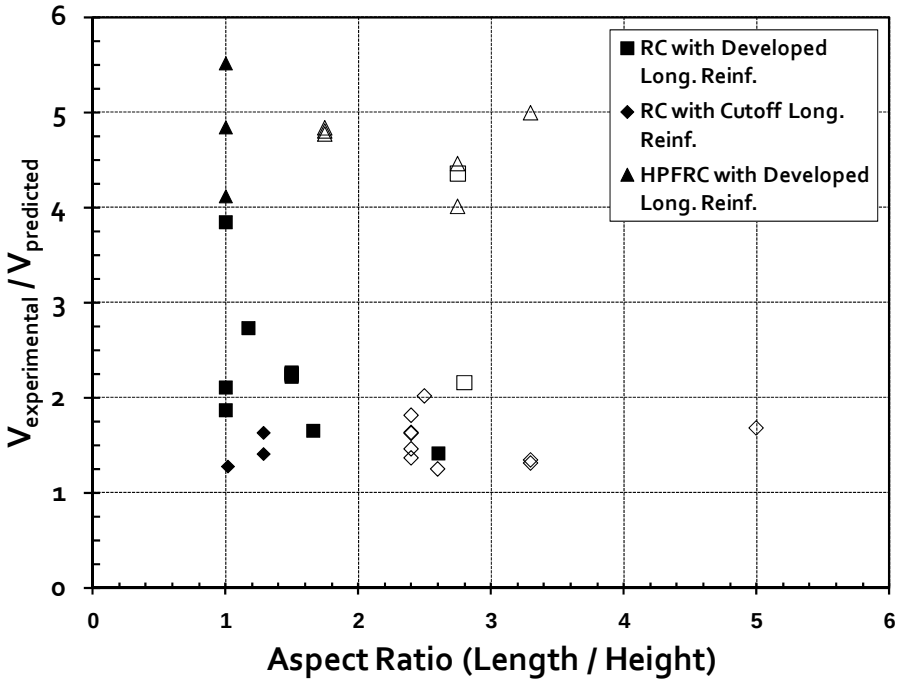

Figure 6.7 – Ratio of experimental and calculated coupling beam capacity versus coupling beam aspect ratio, where $V_{predicted} = 2A_{diag}f_y \sin(\theta)$. Hollow markers indicate a ductile flexural failure mode.

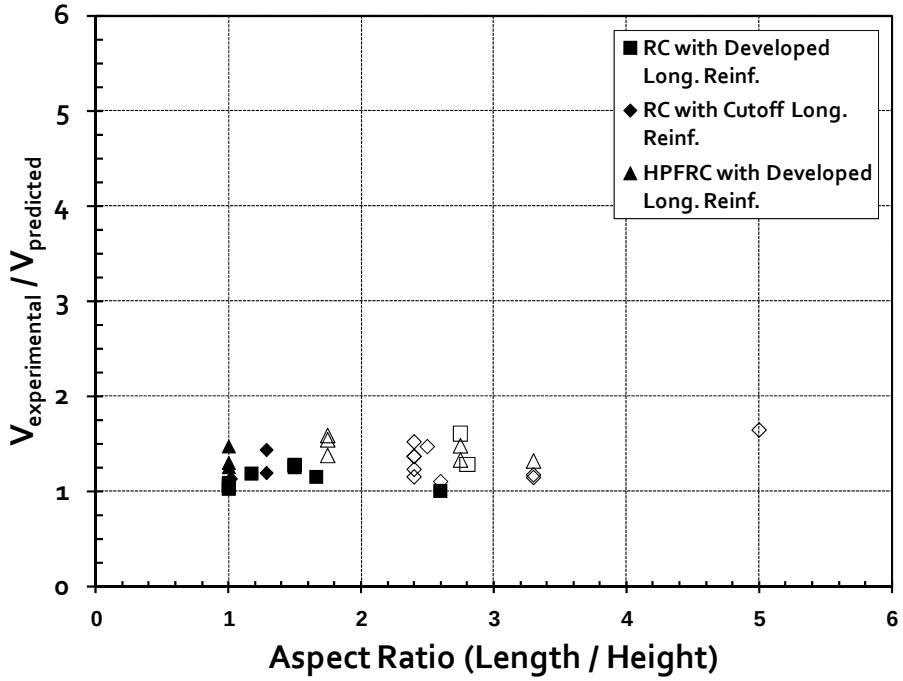

Figure 6.8 – Ratio of experimental and calculated coupling beam capacity versus coupling beam aspect ratio, where $V_{predicted} = 2M_n/\ell_n$. Hollow markers indicate a ductile flexural failure mode.

the ratio of experimental to calculated capacity, whereas the majority of the reinforced concrete coupling beams were not. It is likely that if the reinforced concrete coupling beams were subjected to axial force during testing, the apparent accuracy of the ACI method would be further compromised.

The data plotted in Figure 6.8 is also useful for evaluating the *R*-factor proposed in Section 6.1.1 for estimating M_{pr} for HPFRC coupling beams on the basis of M_n (where $M_{pr} = RM_n$). The proposed R value of 1.4 was based on the results of the three coupling beam component tests described in Chapters 3 and 4 of this document. Because $V_{pr} = 2M_{pr}/\ell_n \cong 1.4V_{predicted} = 2 * 1.4M_n/\ell_n$, the ratios plotted in Figure 6.8 can be divided by $R = 1.4$ to obtain the ratio of experimental to calculated ultimate capacity. For the HPFRC coupling beam specimens shown in Figure 6.8, this ratio has a mean of 1.0, and a range of 0.9-1.1. This is a good degree of accuracy, and indicates that this procedure is appropriate for use with HPFRC coupling beams until further testing provides additional data for an improved *R*-factor.

For reinforced concrete coupling beams with fully developed longitudinal reinforcement, the improved strength calculation was also substantial. The ratio of experimental to calculated capacity improved from between 1.4 to 4.4 using Eq. 6.2 to between 1.0 and 1.6 using SFBM. This significant improvement in accuracy, achieved by considering the longitudinal ("skin") reinforcement, indicates that it is imperative that all developed longitudinal reinforcement be considered when the coupling beam capacity is calculated. An illustration of the risks of under-estimating the coupling beam capacity is shown in both Figs. 6.7 and 6.8. In these figures it is shown that 13 of the 15 reinforced concrete coupling beams with fully developed longitudinal reinforcement ultimately failed in a non-flexural manner (i.e. shear, crushing, buckling). This undesirable behavior is the likely result when the designer considers only the diagonal reinforcement in calculating the shear and flexural capacity of the beam, but then permits longitudinal reinforcement to be developed into the walls. The inevitable result is that the flexural capacity of the coupling beam is increased, which increases the seismic shear demand on the coupling beam. Because the ACI Building Code (ACI 318-08) requires that the designer neglect the contribution of the concrete and transverse reinforcement to the shear capacity of the beam, the result is a coupling beam that, if pushed to develop a

plastic mechanism as a result of seismic demands, risks failing in shear prior to developing ductile flexural hinges at both ends. This leaves the engineer with two choices: (1) cutoff all longitudinal reinforcement near the beam-to-wall connection, or, (2) consider the contribution of the longitudinal reinforcement to the capacity of the coupling beam using the SFBM. Option (2) is not permitted in the current ACI Building Code for short coupling beams ($\ell_n/h < 2$) with moderate to high shear stresses ($v_u > 4\sqrt{f_c'}$ [psi], $0.33\sqrt{f_c'}$ [MPa]). For these beams, the engineer is not permitted to consider the contribution of concrete and transverse reinforcement to the shear capacity of the coupling beam. Therefore, the only way to increase the shear capacity of the coupling beam is to increase the amount of diagonal reinforcement, which also increases the flexural capacity, and thus, the seismic shear demand. This is a virtually unsolvable problem unless the longitudinal reinforcement is cutoff near the beam-to-wall connection.

Finally, a comparison of Figs. 6.7 and 6.8 also shows that non-negligible improvement in the accuracy of the calculated capacity was achieved for reinforced concrete coupling beams with all longitudinal reinforcement cutoff near the wall. For these beams, it is shown that using the SFBM improved the accuracy and reduced the scatter of the ratio of experimental to calculated coupling beam capacity when compared to the ACI method. This ratio improved from between 1.3 to 2.0 using Eq. 6.2 to between 1.1 and 1.6 using SFBM. A likely explanation for this improvement in accuracy is that although the concrete outside of the tightly confined diagonal reinforcement cages does degrade and spall at large drifts, it is sufficiently sound through the smaller drift cycles to resist compression, as assumed by the SFBM, leading to an increase in the flexural moment arm. It stands to reason that confining the full concrete section rather than just the diagonal reinforcement cages, which is permitted by the most recent ACI Building Code (ACI 318-08), will exacerbate this effect for the ACI method (Eq. 6.2). This trend was demonstrated in the recent tests reported by Naish et al. (2009).

This analysis of the database of coupling beam tests shows that using the SFBM to calculate the capacity of a coupling beam is appropriate for each of the three coupling beam designs considered (reinforced concrete with developed longitudinal bars, reinforced concrete with cutoff longitudinal bars, and HPFRC with developed longitudinal bars). For all three groups, a flexural analysis based on the nominal moment

capacity calculated at the ends of the coupling beam was shown to provide a more accurate prediction of the coupling beam capacity than the ACI Code equation (Eq. 6.2). Therefore, the SFBM should be considered appropriate for use in design, assuming sufficient diagonal and transverse reinforcement is provided to prevent a shear failure.

6.2 AXIAL LOAD EFFECTS IN COUPLED WALL SYSTEMS

After decades of experimental and analytical study, the collective understanding of coupled wall system behavior has greatly improved. However, despite these improvements, the exact distribution of forces within a coupled wall system is still not well understood. In particular, the cause and importance of axial forces within the coupling beams are only beginning to be investigated. Similarly, the potentially detrimental effect of under-estimating the ultimate capacity of coupling beams and the resulting axial forces they impose on walls has not been sufficiently explored. In the following section, the potential impacts that axial forces in coupling beams and walls have on the performance of a coupled wall system will be discussed. The intent is to highlight areas where increased attention from researchers and designers may be warranted.

6.2.1 AXIAL FORCES IN COUPLING BEAMS

Axial forces in coupling beams have received relatively little attention from researchers studying coupled wall systems. As a result, the approximate magnitudes, as well as the mechanisms causing the development of these axial forces, are not well understood. Thus, axial forces acting on coupling beams are difficult to estimate (and ignored in practice) and the potential impact of these axial forces on the performance of the coupling beams is also not well understood.

6.2.1.1 Causes of Axial Forces in Coupling Beams

However limited, there has been enough experimental work performed on coupling beam components and coupled wall systems to develop a qualitative sense of

the two primary mechanisms that lead to the development of axial forces in coupling beams. The first cause is the shift of base shear force to the compression wall. Although recognized for many years by researchers, the shift of base shear force to the compression wall was first measured experimentally by Teshigawara et al. (1998a). Their test of a 12-story coupled wall system indicated that the shift of base shear force is predominantly achieved by axial forces acting through the coupling beams in the lowest stories, resulting in some coupling beams being subjected to significant axial compression force demands. However, predicting the magnitude of these axial forces and their distribution throughout the coupled system (i.e. which beams are primarily affected) is challenging. Further research is needed to develop a sufficiently practical and accurate method for determining these axial forces. Furthermore, the systems tested by Teshigawara et al. (1998a) consisted of only walls and coupling beams, so research is needed to determine to what extent their results apply to complete building systems with slabs and adjoining frames.

The second cause of axial forces in coupling beams is the resistance that walls and slabs provide to growth of the coupling beams, which tend to elongate as flexural yielding and shear-related damage accumulate. Although tests of coupling beams restrained solely by post-tensioned slabs indicated that minimal restraint of the coupling beams is provided by slabs (Naish et al., 2009), tests of more complete coupled wall systems (Teshigawara et al., 1998a; Chapter 5 of this document) indicate that the walls do provide restraint and limit elongation of the coupling beams. The coupling beam specimens described in Chapters 3 and 4, which were partially restrained axially, developed axial strains consistent with those measured in the beams of the coupled wall specimens described in Chapters 3 and 5. The result was the development of axial forces in these coupling beams on the order of one third of the applied shear force, or approximately 5% of the axial force capacity of the beam. As discussed in Chapter 4, it is likely possible to develop a model for predicting coupling beam axial forces that considers the maximum deformations imposed on the beam, the beam aspect ratio, and the stiffness of the walls and slabs. However, further research is required to improve our understanding of these variables.

6.2.1.2 Axial Forces and Coupling Beam Strength

It is difficult to evaluate the potentially important impact these axial forces may have on coupling beams and coupled wall system performance because an accurate understanding of the causes of the axial forces in coupling beams does not exist. The purpose of the discussion in the following section is to conceptualize these effects with the intention of highlighting the need for improving our understanding of the mechanisms causing these forces.

If appreciable axial forces are shown to develop in the coupling beams throughout a structure, they will have an important effect on the coupling beam capacity, and thus, the performance of the entire coupled system. This is because, in general, axial forces with magnitudes between zero and approximately 30% of the compressive axial force capacity of a member (referred to as the balanced point) lead to increases in both the flexural and shear capacity of the member. Calculation of the flexural capacity of the coupling beam specimens described in Chapters 3 and 4, both considering and neglecting the axial force, showed that neglecting the axial force led to under-prediction of the capacity by 15-20%. Therefore, axial forces on the order of 5% of the axial force capacity of the member were shown to have an important impact on the capacity of the coupling beam specimens. If the capacities of all the coupling beams in a system are underestimated by 20%, the result is that axial forces developed in the walls due to coupling could be 20% larger than anticipated.

Underestimation of the coupling beam capacity due to axial forces is part of a larger problem with the current ACI Building Code (ACI 318-08) method for coupling beam strength prediction. It was shown in Figure 6.7 that the capacity of 13 diagonally reinforced concrete coupling beams with cutoff longitudinal reinforcement generally exceeded the capacity calculated by the current ACI Code equation (Eq. 6.2) by 30 to 100% when it is assumed that $f_s = 60$ ksi. Because most of these tests did not include the influence of axial forces, the increase in capacity due to axial forces will lead to further underestimation of strength by Eq. 6.2. Furthermore, the ACI Code requires that a phi-factor of 0.85 be applied to the nominal coupling beam shear capacity. This is presumably required under the pretense of introducing an element of conservativeness to the design process; however, it is likely that the reverse is true. When the underestimation

of the coupling beam capacity inherent in the ACI Code equation is considered together with the potential 15-20% increase in strength due to axial forces, and a phi-factor is subsequently applied, the result is that coupling beams designed in accordance with the ACI Building Code could potentially develop a peak capacity that is 75% to 180% greater than the "conservative" capacity given by ϕV_n. Although higher mode effects make it unlikely that all of the coupling beams within a coupled wall system will develop their peak strength at the same time, it is clear that a more accurate estimation of the coupling beam capacity is required. In particular, the following improvements to the ACI Building Code method are warranted:

(1) More accurate models for prediction of the coupling beam capacity are required. The SFBM presented in Section 6.1 is a modest improvement. This flexure-based model also has the advantage of readily incorporating the effects of axial forces, when they are better understood, through well understood axial force-bending moment (P-M) interaction diagrams,

(2) Improved understanding of the mechanisms that lead to the development of axial forces in coupling beams is required. Once coupling beam axial forces can be reliably estimated, their relative importance in the behavior of the system can be assessed, and,

(3) $\phi = 1.0$ should be applied to the calculation of the coupling beam capacity. If Eq. 6.2 is used to design a coupling beam, then $\phi = 1.0$ should be used instead of the $\phi = 0.85$ required by the ACI Building Code. If SFBM is used instead to design the coupling beam, it is suggested in Section 6.1 that $\phi = 0.85$ for designing the nominal shear capacity. However, because flexure is intended to control the capacity of the coupling beam, $\phi = 1.0$ is recommended for the flexural design.

6.2.2 Effect of Wall Axial Forces Resulting from Coupling

In general, the walls of a coupled wall system can be assumed to be subjected to an approximately constant axial force imposed by the tributary weight of the structure and super-imposed dead and live loads. At the wall base, these axial forces are usually on the order of 10% of the axial force capacity of the wall in compression (Wallace, 1995). In addition, there are axial tension and compression forces that develop in the individual

walls as a result of wall coupling, which alternately increase and decrease the net axial force on each wall. Some of the primary effects these axial forces have on the behavior of the walls is discussed in the following sections. The importance of accurately predicting these axial forces to ensure that appropriate reinforcement detailing is provided to achieve a ductile system response is emphasized.

6.2.2.1 Effect of Axial Force on the Distribution of Base Shear Force Between Walls

A cursory analysis of a coupled wall system might lead to the assumption that base shear force resistance is divided equally between the walls such that an average shear stress taken over the full wall area would reasonably approximate the shear stress magnitude in each wall. However, like a reinforced concrete beam, which resists a majority of the shear force applied to it through the compression zone after flexural yielding has initiated, a large percentage of the total base shear force applied to a coupled wall system tends to accumulate in the compression wall near the foundation. Analytically, this was shown to be the case for rectangular walls with tied column boundary elements by Aktan and Bertero (1984). Teshigawara et al. (1998a) measured this shift of force experimentally in a test performed on a 12-story coupled wall system with flanged walls through the use of load cells placed within each of the 12 coupling beams. Their results indicated that up to 90% of the base shear force was resisted by the compression wall (depending on the drift level). Although not directly measured, all observations and measurements indicated that a similar shift of shear force occurred in the coupled wall tests reported herein, as described in Chapter 5.

Results from analytical work by El-Tawil and Kuenzli (2002a; 2002b) have indicated that the presence of flanges along the outside edges of the wall system, which are a common feature of coupled walls found in practice, can cause the tension wall to be more active in resisting base shear force. The result is a more even distribution of shear force near the base of the coupled wall system. El-Tawil and Kuenzli indicated that for this to occur the effective width of the flange for the compression wall must be large enough to cause the compression zone to be contained entirely within the flange, thereby subjecting the entire web of the compression wall to tension. Furthermore, enough reinforcement must be placed in the flange of the tension wall to force a compression

zone to develop in the web of the tension wall that remains active throughout the imposed displacements. Neither of these conditions was met by the two series of tests of flanged coupled walls referenced previously. In both cases, the flange was not wide enough to keep the compression zone out of the web in the compression wall. Also, the reinforcement ratio for the tension wall was approximately 1.0%, calculated as the total area of longitudinal reinforcement in the wall flange divided by the area of the web (web width times length of wall). Therefore, experimental results on coupled walls with wide and highly reinforced wall flanges are not available to evaluate this analytically derived conclusion. Other system parameters, including coupling ratio and axial force due to gravity, will also have an important effect on how deep the compression zone is in the tension wall, and thus, impact the distribution of shear force between walls. It is likely that coupled wall systems with highly reinforced walls, walls with very large effective compression flange widths in the compression wall, walls with large gravity loads, and lightly coupled systems will all exhibit a more even distribution of base shear force between walls.

It is not recommended that the distribution of base shear force be considered in the design of coupled systems, given the complexities of predicting the distribution and the relatively sparse data on the topic. Rather, it is recommended that engineers consider an average base shear stress calculated over the area of the webs of the walls (ignoring the area of flanges) for determining the base shear capacity of the walls. In this spirit, all recommended design values for the shear stress capacity of HPFRC presented in Chapter 5 were determined on the basis of an average base shear stress.

6.2.2.2 Effect of Axial Force on Walls

The varying axial forces imposed on walls in a seismic event will have an impact on both the flexural capacity and ductility of the walls. A typical P-M interaction diagram for a reinforced concrete member, where P represents axial force on the y-axis and M represents the bending moment on the x-axis, is shown on the left of Figure 6.9 (Pfrang, Siess and Sozen, 1964). The diagram illustrates the typical interaction of axial force and moment capacity in reinforced concrete members, and shows that for elements loaded with axial forces greater than P_{bal}, increases in axial compression cause a decrease in the

moment capacity of the section. The same is true below the balanced point for decreases in axial forces (towards zero or into tension). Therefore, if wall coupling causes either wall to be subjected to more compression when $P > P_{bal}$, or less compression (or even tension) when $P < P_{bal}$, the contribution expected from the walls to the total overturning moment capacity of the system may be overestimated if the effect of axial forces is ignored. In addition to causing a reduction of the flexural strength, large axial forces from coupling will also reduce the curvature capacity of the walls. A typical relationship between axial force and curvature, which is shown on the right of Figure 6.9, illustrates how limited the curvature capacity is for axial forces larger than P_{bal}. Although the boundary element confinement that is required for walls in seismic regions will lead to additional ductility, designing coupled walls with coupling forces large enough to risk compromising both the strength and ductility of the walls is not recommended.

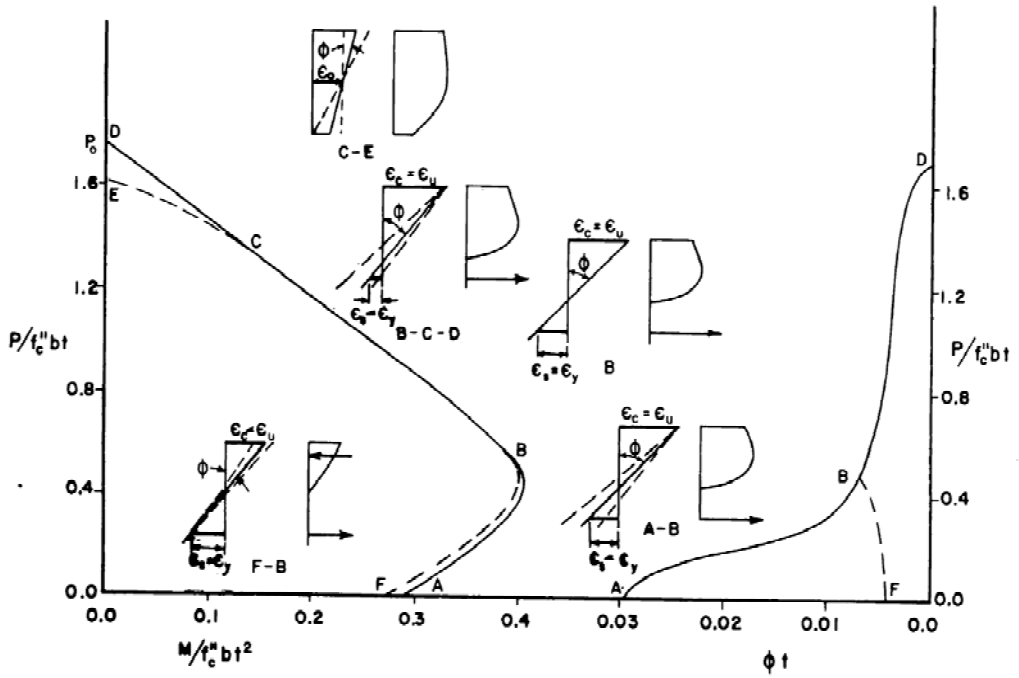

Figure 6.9 – Typical P-M and P-ϕ interaction diagrams (Pfrang, Siess and Sozen, 1964)

The Wall Strength Index, WSI, was proposed in Section 5.4 as a tool for identifying when the axial forces due to coupling compromise the sum of the flexural strength of the walls. WSI, as defined in Eq. 5.7, is the sum of the flexural capacity of the walls considering the axial forces due to coupling divided by the sum of the flexural

capacity of the walls without coupling. For coupled walls subjected to gravity loads below P_{bal}, $WSI \cong 1.0$ indicates that the sum of the flexural capacity of the walls is not being negatively affected by coupling, and thus implies that coupling is not likely to compromise the ductility of the walls. $WSI < 1.0$ indicates that coupling is causing a decrease of the sum of the flexural capacity of the walls and may also be compromising their plastic rotation capacity. Figure 5.35 showed that for the flanged walls of the specimens tested, which were subjected to an axial force of approximately 6% of the wall capacity, the theoretical WSI was close to 1.0 for coupling ratios up to 0.55. Beyond $CR = 0.55$, WSI was shown to decrease quickly with increasing CR. This indicates that for these specific flanged walls, coupling ratios up to approximately 0.55 will not impose detrimental axial forces on the walls for systems with low axial loads from gravity.

$$WSI = \frac{M_{o(coupled)} - \left(\sum V_{pr,beam} + \sum V_{pr,slab}\right)\ell}{M_{o(uncoupled)}} \tag{5.7}$$

To explore the usefulness of the WSI for evaluating the effect of axial forces from wall coupling on the performance of walls, a hypothetical system with rectangular walls was evaluated. First, the theoretical P-M diagrams were calculated for each wall. These results were manipulated to provide the theoretical flexural capacity of the walls as a function of coupling ratio for various initial levels of axial load due to gravity. The hypothetical system had identical walls with a cross section of 10 ft by 2 ft (3 m by 0.6 m), and a longitudinal reinforcement ratio of 1% grouped in boundary elements along each edge of the wall. Nominal vertical reinforcement was assumed in the web between the boundary elements such that $\rho_\ell = 0.0015$. The walls were assumed to be 4 ft (1.2 m) apart. The wall concrete was assumed to have a compressive cylinder strength of 6 ksi (41 MPa), and to be well confined such that the moment curvature analyses were not terminated until $\varepsilon_{cu} = 0.008$.

The resulting theoretical relationship between the flexural capacity of the tension and compression wall (normalized by $0.85f_c'bh^2$) and coupling ratio is shown in Figure 6.10 for axial loads due to gravity ranging from 5% to 25% of P_o, where $P_o = bhf_c'$. This

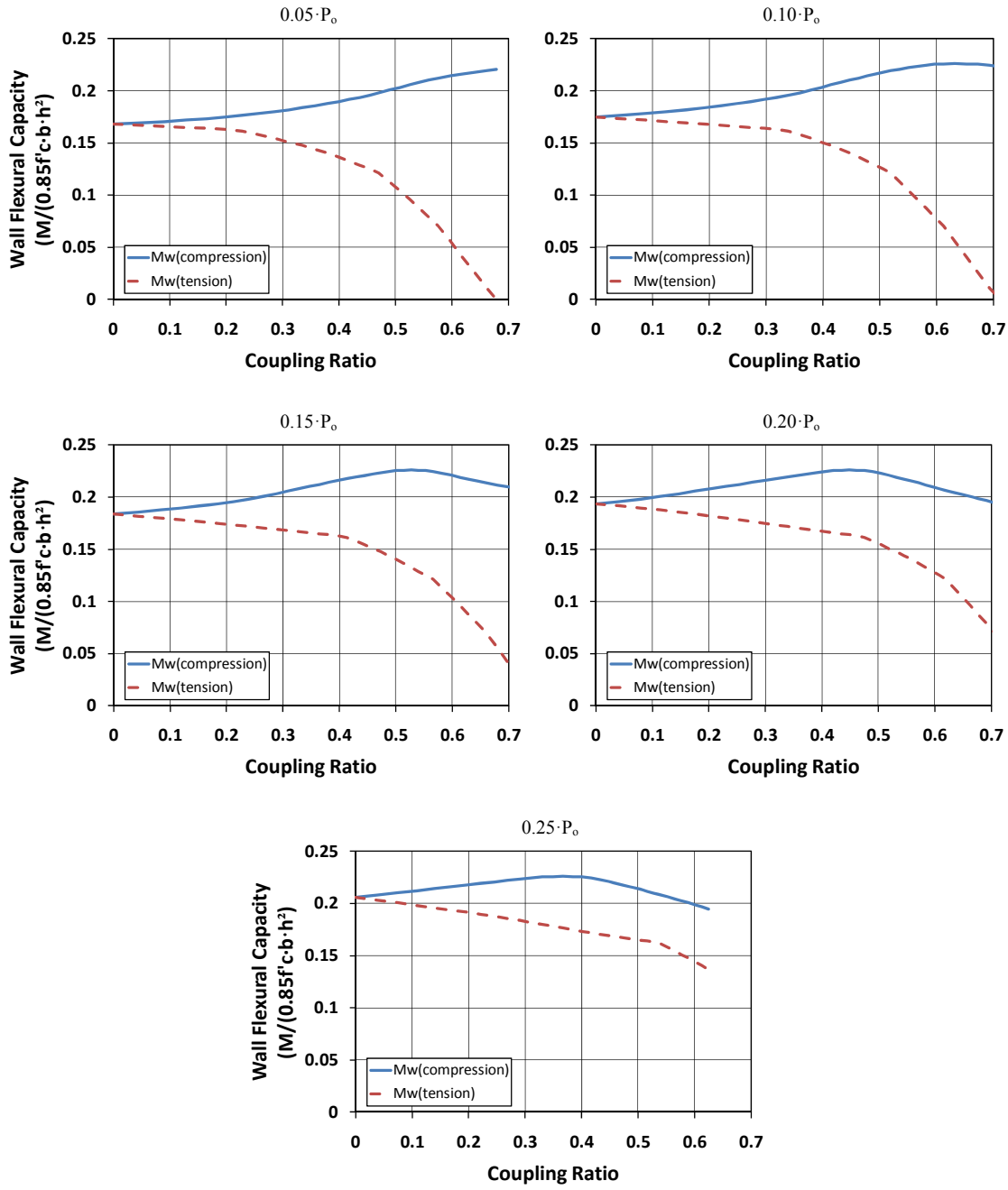

Figure 6.10 – Theoretical wall flexural capacity versus coupling ratio for a hypothetical coupled system with rectangular walls

figure shows that for small axial loads from gravity, the flexural capacity of the compression wall benefits from the axial forces from coupling. However, the flexural capacity of the tension wall begins to decrease more steeply than the capacity of the

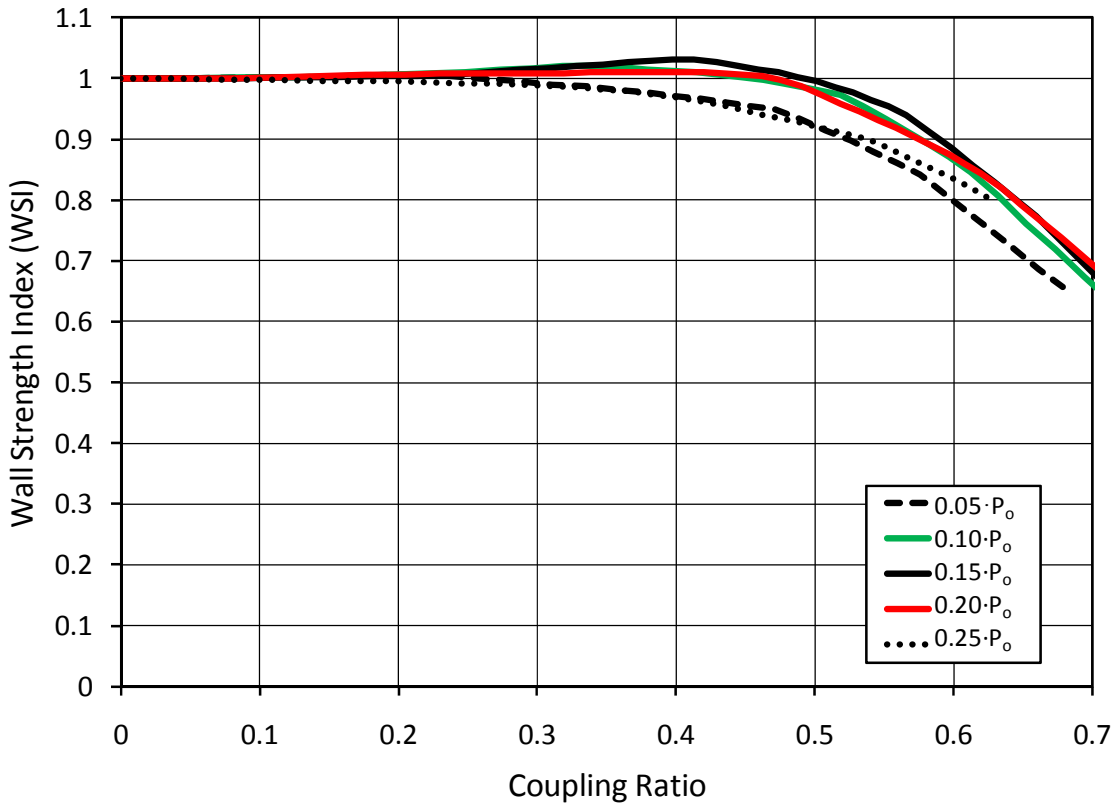

Figure 6.11 – Theoretical relationship between Wall Strength Index (WSI) and coupling ratio for a hypothetical coupled wall system with rectangular walls for various levels of axial loads from gravity

compression wall is increasing for coupling ratios greater than 0.3. For coupling ratios greater than 0.5, the flexural capacity of the tension wall is shown to be severely compromised. At the other extreme, for gravity axial loads equal to $0.25P_o$, the slope of the compression wall flexural capacity versus coupling ratio curve is shown to be negative beginning at a coupling ratio of 0.4. This indicates that coupling ratios of 0.4 and larger will cause a decrease in the flexural capacity of the walls, and worse, risk the reduction in wall ductility associated with axial loads above the balanced point.

With the values plotted in Figure 6.10, the theoretical WSI can be determined with Eq. 5.7. The theoretical WSI is plotted versus coupling ratio for axial loads from gravity ranging from 5% to 25% of P_o in Figure 6.11. It is shown in Figure 6.11 that when this system is subjected to axial loads from gravity equivalent to either 5% or 25% of P_o, the WSI is approximately 1.0 for coupling ratios up to 0.3. For larger coupling

ratios, WSI decreases, indicating that coupling is having a deleterious effect on the wall flexural strength and, likely, ductility. When the coupled wall system is subjected to axial forces from gravity between 10% and 20% of P_o, the WSI is shown to remain close to 1.0 until the coupling ratio exceeds 0.5. This analysis illustrates the important role that the combined effects of axial forces from coupling and gravity have on the flexural capacity (and, by association, ductility) of walls at coupling ratios between 0.3 and 0.5, which have long been deemed safe by researchers. Although there is no cause to indicate that a coupled wall system with $WSI < 1$ is categorically unsafe, it is recommended that when $WSI < 1$, the system should be carefully evaluated to ensure that the axial forces are accurately estimated and that the walls have appropriate reinforcement detailing to ensure adequate ductility for the axial loads.

6.2.2.3 The Need to Limit Coupling Ratio

Another way to minimize the detrimental impact of excessive axial forces on the flexural capacity and ductility of walls is to limit the coupling ratio. A limited coupling ratio will prevent the development of axial forces that compromise the strength and ductility of the individual walls in an earthquake.

In general, studies of coupled reinforced concrete walls have suggested an upper bound for coupling ratios on the order of 0.5-0.6. Shiu et al. (1981) first identified the deleterious effect of high coupling ratios on the ductility of the compression wall. Subsequent work by Aktan and Bertero (1984) led to a recommended limit of 0.6 for coupling ratio based on the risk for compression related failures in the walls. Kato, Sugaya and Nagatsuka (1996) proposed that coupling ratios range between 0.4 and 0.6 if the design goals of the system are to limit coupling beam drift demands to less than 2% drift and to prevent yielding of the walls. These design goals are not likely to be the design goals of typical coupled wall systems in the United States, but the risks associated with coupling ratios greater than 0.6 that were identified are transferable. Harries (2001) proposed coupling ratio limits ranging from 0.5-0.65, depending on the type of coupling beam selected, in recognition of the need to limit the coupling beam ductility demands. However, the finite element models used as the basis for the proposals presented by Harries (2001) did not appear to account for the risk of wall compression zone failures.

From the perspective of wall response, coupling ratios larger than 0.5 are risky for systems with rectangular walls. However, an absolute limit on coupling ratio may not be the most efficient way to ensure a safe coupled wall design because of the variability in system geometry and reinforcement detailing. It is possible that the particular geometry or reinforcement of a system (for example, well confined wall boundary elements or wall flanges) leads to improved component ductility and allows for higher coupling ratios. However, given the risks associated with high coupling ratios, it is strongly recommended that care be taken in design to accurately estimate the expected shear force in the coupling beams and to consider the impact the resulting axial forces will have on the wall response. When the expected shear demand in the coupling beams is considered, if the total flexural capacity of the walls is not shown to be compromised (i.e. $WSI \cong 1$), then the selected coupling ratio may be permissible. Sophisticated computer simulations are useful for estimating the component ductility demands and the lateral stiffness of the system to determine whether the coupled wall system achieves the design goals.

6.2.2.4 Effect of Underestimating the Axial Force Acting on Walls

Given the important impact that axial forces have on the performance of walls, and specifically the importance of limiting excessive compression or tension forces acting on individual walls, it is especially concerning that current ACI Building Code (ACI 318-08) procedures may under-estimate the capacity of coupling beams by as much as 75-180% (see Section 6.2.1). If the axial forces due to coupling are underestimated, the estimated axial force demands in the walls will be inaccurate, thereby potentially leading to walls with $P < 0$ or $P > P_{bal}$. This risk is even higher if coupling due to slabs, which is typically neglected, is taken into consideration.

Consider the same hypothetical coupled system with rectangular walls presented in Section 6.2.2.2. Assume that this system is designed so that an axial load due to gravity near $0.15P_o$ is imposed on the walls, and that a safe coupling ratio of 0.45 is selected (as indicated by the plot of WSI in Figure 6.11). If the coupling beams develop a peak capacity that is 50% larger than the "conservative" capacity prediction used in design, then the coupling ratio may reach 0.55, which is potentially unsafe. If the slabs provide additional coupling, the situation is exacerbated.

To prevent such inaccuracies from negatively impacting the strength and ductility of the system, it is critical that: 1) the capacity of the coupling beams be accurately estimated, which may involve calculation of an upper bound capacity that involves more accurate models, consideration of coupling beam axial forces, and neglect of phi-factors, and, 2) the coupling ratio (calculated using realistic coupling beam capacities and considering the effect of slabs and axial forces on the wall capacity) be limited to values shown to result in a $WSI \cong 1.0$ for the system in question, unless careful analysis that considers the risks of net tension forces and large compression force demands on walls show that the particular geometry and reinforcement detailing of the system are adequate to ensure a ductile system response.

6.3 ESTIMATION OF "BACKBONE" CURVE FOR HPFRC COUPLING BEAMS

It has become common practice for engineers to subject non-linear finite element models of building designs to time history analyses to evaluate the performance of the selected structural system under various ground motions. This process is valuable for determining whether the selected structural system meets the design objectives, which likely includes limiting component drift demands and story drifts. The validity of these non-linear time history analyses is highly dependent on the validity of the parameters selected for modeling the behavior of each component of the system. When specimens that are reasonably representative of the building component in question have been evaluated experimentally, these parameters can be estimated based on the test results. However, the cost of large-scale experimental work limits the number of specimens that can be tested, and therefore it can be difficult to find specimens that are sufficiently representative of the components being modeled. A reasonably simple method for approximating the envelope (or "backbone") of the load versus drift response for HPFRC coupling beams is proposed in this section. This model is intended to be helpful for calibrating input parameters for HPFRC coupling beams when sufficiently relevant experimental results are not available.

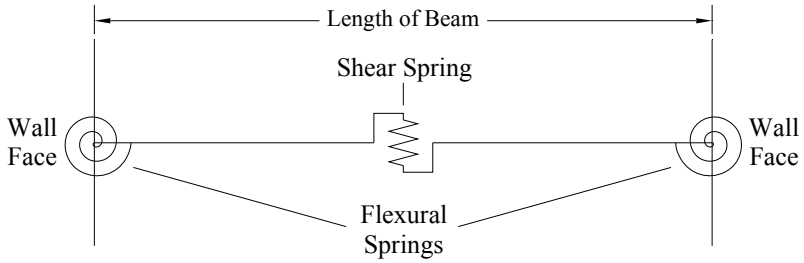

Figure 6.12 – Schematic of spring model for coupling beam

A schematic of the assumed model is shown in Figure 6.12. The contribution of curvature of the coupling beam to drift is estimated by equations derived using the moment area theorems. Rotations at the wall face due to strain penetration into the wall are approximated by rotational springs located at the wall face. Shear deformations are approximated by a linear spring located at midspan. The stiffness of the shear spring is taken as an average calculated for the whole span, and is a function of shear stress and curvature. These springs are defined in more detail in the following sections.

The three points that this model is designed to approximate are shown in Figure 6.13. The first two points represent the shear force and drift of the coupling beam at the first instance of flexural yielding (δ_1, V_1) and at peak capacity (δ_2, V_2). The third point is defined with ordinates of (δ_3, $0.8V_2$), where δ_3 is identified from experimental results as the drift capacity of coupling beams for the given aspect ratio.

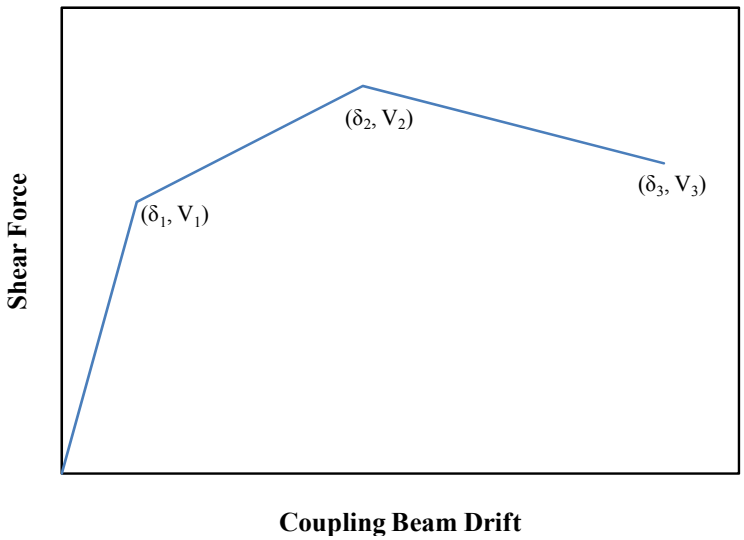

Figure 6.13 – Schematic of coupling beam backbone curve

6.3.1 FLEXURAL MECHANISMS

Precast HPFRC coupling beams designed in accordance with the recommendations of Section 6.1 will develop flexural hinges at both ends of the coupling beam that control the beam capacity. Therefore, the ordinates shown in Figure 6.13 that represent the coupling beam strength at first yield, peak strength, and ultimate drift (V_1, V_2 and V_3) are to be approximated from the results of moment-curvature analyses. It is recommended that moment-curvature analyses be performed for the coupling beam section at the wall face to determine the moment and curvature of the coupling beam at first yield (M_y and ϕ_y) and peak moment (M_{peak} and ϕ_{peak}). It is also recommended that an axial force of zero be assumed for determining M_y and ϕ_y, and that an axial force equal to $0.4V_2$ be assumed for determining M_{peak} and ϕ_{peak}. Eq. 6.3-6.5 can be used to determine V_1, V_2 and V_3, where ℓ_n is the clear span length of the coupling beam.

$$\mathrm{V}_1 = \frac{2M_y}{\ell_n} \tag{6.3}$$

$$\mathrm{V}_2 = \frac{2M_{peak}}{\ell_n} \tag{6.4}$$

$$\mathrm{V}_3 = 0.8\mathrm{V}_2 \tag{6.5}$$

Estimation of the three values shown in Figure 6.13 that represent the drift of the coupling beam is more involved, and will be the subject of the remainder of Section 6.3. The combined contributions of flexural deformations within the span of the coupling beam and rotations at the wall face due to penetration of reinforcement strains into the wall will be considered flexural deformations. These flexural mechanisms were shown to account for approximately 60% of the coupling beam deformations for the specimens tested (Figure 4.31).

Prior to yielding of the longitudinal and diagonal reinforcement, referred to in this section as flexural reinforcement, the entire span of the coupling beam is assumed to have a constant cracked-elastic stiffness (determined at yield) such that the curvature is a linear function of the applied moment. Therefore, at the point of first yielding of the flexural reinforcement, the curvature in the coupling beam is assumed to be equal to the yield

curvature, ϕ_y, at the wall face and vary linearly to zero at midspan, as shown in Figure 6.14. On this basis, the displacement of the coupling beam due to flexural deformations within the span of the coupling beam at first yield (i.e. the amount one wall face displaces relative to the opposite wall face at the first instance of coupling beam flexural reinforcement yielding) can be directly calculated by Eq. 6.6.

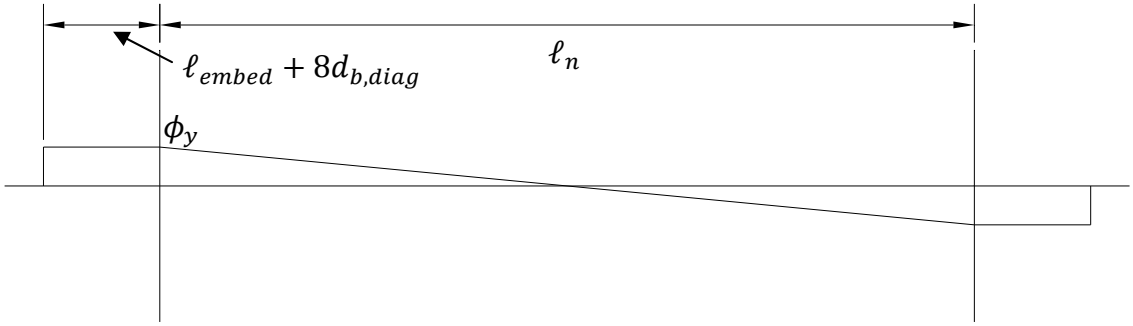

Figure 6.14 – Assumed distribution of curvature at first instance of flexural yielding

$$\Delta_{f1,yield} = \frac{\phi_y \ell_n^2}{6} \tag{6.6}$$

The stresses that develop in the flexural reinforcement of the coupling beam at the wall face must be developed over a certain length, resulting in reinforcement strains penetrating into the wall. Structurally, these strains manifest as rotations concentrated at the wall face. An analysis of the rotations measured during the tests of the three coupling beams included in this study was presented in Chapter 4. This analysis indicated that the rotations at the wall face can be approximated by assuming that the curvature of the beam at the wall face extends the length of the coupling beam embedment (ℓ_{embed}) plus eight times the largest coupling beam bar diameter ($8d_{b,largest\ bar}$) into the wall. Although this analysis was performed when the beam was subjected to the peak shear capacity, this length of strain penetration is assumed to also provide a reasonable estimate of the strain penetration at first yielding. Therefore, the relation shown in Eq. 6.7 can be used to estimate the coupling beam displacement resulting from the rotations at the wall face due to strain penetration at first yield.

$$\Delta_{f2,yield} = \phi_y\left(\ell_{embed} + 8d_{b,largest\ bar}\right)\ell_n \tag{6.7}$$

Therefore, the coupling beam drift at first yield due to flexural mechanisms, $\delta_{f,yield}$, can be estimated by Eq. 6.8, where ℓ_n, ℓ_{embed} and $d_{b,diag}$ are all geometric properties of the beam and ϕ_y is calculated assuming no axial force is acting on the coupling beam.

$$\delta_{f,yield} = \frac{\Delta_{f1,yield} + \Delta_{f2,yield}}{\ell_n} = \frac{\phi_y \ell_n}{6} + \phi_y\left(\ell_{embed} + 8d_{b,largest\ bar}\right) \tag{6.8}$$

For calculating the flexural deformations at peak coupling beam strength, plastic hinges are assumed to develop over a length of $h/2$ into the span of the coupling beam, where h is the height of the beam. It is assumed that the curvature throughout the plastic hinge is constant and equal to the curvature at the peak strength, ϕ_{peak}, as determined by a moment-curvature analysis. It is assumed that the beam curvature abruptly changes from ϕ_{peak} to ϕ_y at a distance of $h/2$ from the wall faces, and then varies linearly to zero at midspan, as shown in Figure 6.15. The moment area theorem was used to derive Eq. 6.9, which can be used to estimate the coupling beam displacement at peak strength resulting from flexural deformations within the span.

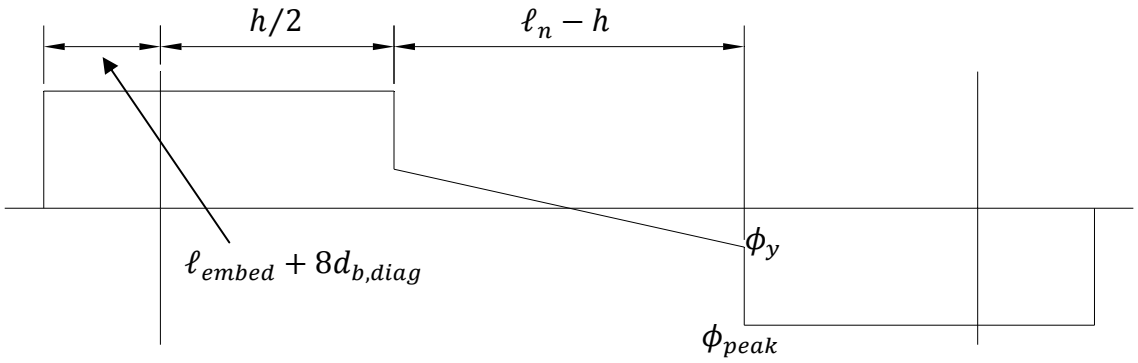

Figure 6.15 – Assumed distribution of curvature at peak shear demand

$$\Delta_{f1,peak} = \frac{\phi_y(\ell_n - h)^2}{6} + \frac{\phi_{peak} h(2\ell_n - h)}{4} \tag{6.9}$$

To estimate the coupling beam displacement due to rotations localizing at the wall face, it is again assumed that the curvature in the beam at the wall face extends into the wall the length of the coupling beam embedment (ℓ_{embed}) plus eight times the largest coupling beam bar diameter ($8d_{b,largest\ bar}$). On this basis, Eq. 6.10 can be used to estimate the coupling beam displacement due to rotations at the wall face.

$$\Delta_{f2,peak} = \phi_{peak}\left(\ell_{embed} + 8d_{b,largest\ bar}\right)\ell_n \tag{6.10}$$

Therefore, the coupling beam drift at peak strength due to flexural mechanisms, $\delta_{f,peak}$, can be estimated by Eq. 6.11.

$$\delta_{f,peak} = \frac{\Delta_{f1,peak} + \Delta_{f2,peak}}{\ell_n} \tag{6.11a}$$

$$\delta_{f,peak} = \frac{\phi_y(\ell_n - h)^2}{6\ell_n} + \frac{\phi_{peak}h(2\ell_n - h)}{4\ell_n} + \phi_{peak}\left(\ell_{embed} + 8d_{b,largest\ bar}\right) \tag{6.11b}$$

6.3.2 Shear Deformations

When shear deformations of the coupling beam specimens were discussed in Chapter 4, sliding shear deformations at the dominant failure crack and at the cold joint between the wall and the precast coupling beam were separated from "true" shear deformations in the HPFRC material. It was shown in Figure 4.31 that the combined contribution of both sliding shear mechanisms to coupling beam drift prior to peak shear stress was small (less than 5%). Because this model has been developed to estimate the drift at the first instance of flexural yielding and at peak strength of the coupling beam, estimation of the sliding shear deformations is not included in the model. The following parameters proposed for the linear shear spring shown in Figure 6.12 neglect the influence of sliding shear.

The capacity of the coupling beam at the first instance of flexural yielding and at peak capacity has been previously determined by flexural analysis. Therefore, a definition of the effective shear stiffness of the coupling beam is needed to relate the

average shear stresses to shear strains, and thus estimate the drift due to shear deformations. To determine an appropriate relationship between shear stress and strain for the beams tested, nine different portions of each specimen, referred to as strips (shown in Figure 4.17), were analyzed. The effective shear stiffness was expected to degrade as shear stresses increased because of the associated development and widening of diagonal cracks. Work by Parra-Montesinos and Chompreda (2007) showed that effective shear stiffness is also a function of curvature, so the influence of curvature was evaluated. The effect of axial force on the effective shear stiffness was also considered.

Based on this analysis, Eq. 6.12 is proposed for estimating the effective shear stiffness of the coupling beam, G_{eff}, as a function of shear stress and curvature. Eq. 6.12 requires the following inputs: f_c', the compressive cylinder strength of the concrete; υ, Poisson's ratio, assumed to be 0.15; ϕ, the curvature of the beam at the location of the shear spring; ϕ_y, the theoretical curvature of the beam at the first instance of flexural yielding; and τ, the average shear stress applied to the coupling beam ($\tau = V/bh$).

$$G_{eff} = \frac{0.6G_c}{\beta\sqrt{\alpha}} \tag{6.12}$$

where:

$$G_c = 57{,}000\sqrt{f_c'}/2(1+\upsilon)$$

$$\alpha \leq \begin{Bmatrix} 1 & \phi/\phi_y \leq 1 \\ \dfrac{\phi}{\phi_y} & else \end{Bmatrix}$$

$$\beta \leq \begin{Bmatrix} 1 & \tau \leq 2\sqrt{f_c'} \\ \dfrac{\tau}{2\sqrt{f_c'}} & else \end{Bmatrix}$$

The rationale behind the development of Eq. 6.12 is as follows:

- The theoretical shear modulus of the HPFRC, G_c, was initially assumed to represent the stiffness of the coupling beam section prior to diagonal cracking. However, analysis of the measured stiffness of the coupling beams, presented in Chapter 4, indicated that a value of $0.6G_c$ is a better estimate of the shear stiffness prior to the development of shear-related cracking. Whether this is

indicative of the effect of shrinkage or flexural cracking on the shear stiffness, or other mechanisms, is unclear. Regardless, $0.6G_c$ is taken as the coupling beam shear stiffness prior to diagonal cracking.

- The denominator of Eq. 6.12 reflects the influence of both shear stress (β) and curvature (α) on the shear stiffness of the coupling beam. Prior to diagonal cracking and flexural yielding, both α and β are equal to 1.0, resulting in $G_{eff} = 0.6G_c$, the stiffness prior to diagonal cracking.
- When shear stresses exceed the stress required to induce diagonal cracking, taken as $2\sqrt{f_c'}$ (coupling beam test results presented in Chapter 4 indicated values between $2.1\sqrt{f_c'}$ and $2.6\sqrt{f_c'}$), the β-factor in the denominator increases. This reflects the decrease in shear stiffness associated with the diagonal cracking induced by shear stress. This model is based on specimens with minimal yielding of transverse reinforcement, so if yielding of transverse reinforcement is expected to play an important role in the behavior of the specimen, modification of Eq. 6.12 is required.
- After the coupling beam curvature exceeds ϕ_y, the α-factor also increases. This reflects the decrease in shear stiffness associated with wider flexural cracks and a shallower compression zone. Regression analyses indicated that using the square-root of α provides relatively good agreement with test data.
- Analysis of results did not indicate a strong correlation between shear stiffness and axial stress, and so this factor was not included in Eq. 6.12. If the shear spring were to consider sliding shear deformations, which become important at larger drifts, axial force would be among the critical parameters.

For estimating the displacement and drift of the coupling beam due to shear deformations at the first instance of flexural yielding ($\Delta_{s,yield}$ and $\delta_{s,yield}$), the shear stiffness is assumed to be constant over the full length of the beam because $\alpha = 1$ and β is constant over ℓ_n. Therefore, the contribution of shear strain to the displacement and drift of the coupling beam at first yielding can be estimated by Eqs. 6.13 and 6.14.

$$\Delta_{s,yield} = \frac{\tau}{G_{eff}} \ell_n = \frac{V_1}{bh} \frac{\beta}{0.6G_c} \ell_n \tag{6.13}$$

$$\delta_{s,yield} = \frac{\tau}{G_{eff}} = \frac{V_1}{bh} \frac{\beta}{0.6G_c} \tag{6.14}$$

To estimate the displacement and drift of the coupling beam due to shear deformations at the peak shear stress ($\Delta_{s,peak}$ and $\delta_{s,peak}$), the shear stiffness is assumed to vary over the length of the beam because, although β is constant over ℓ_n, α varies. Within the plastic hinge length, $\alpha = \phi_{peak}/\phi_y$. In the midspan region, where flexural yielding has not occurred, $\alpha = 1$. Therefore, a weighted average of the effective shear stiffness over the beam length is required to estimate the contribution of shear strain to the coupling beam displacement and drift at peak shear stress, as shown in Eqs. 6.15-16.

$$\Delta_{s,peak} = \frac{V_2}{bh} \frac{\beta}{0.6G_c} (\ell_n - h) + \frac{V_2}{bh} \frac{\beta\sqrt{\phi_{peak}/\phi_y}}{0.6G_c} h \tag{6.15}$$

$$\delta_{s,peak} = \frac{V_2}{bh} \frac{\beta}{0.6G_c} \frac{(\ell_n - h)}{\ell_n} + \frac{V_2}{bh} \frac{\beta\sqrt{\phi_{peak}/\phi_y}}{0.6G_c} \frac{h}{\ell_n} \tag{6.16}$$

6.3.3 Sliding Shear Deformations

In deriving the equation recommended for estimating effective shear stiffness given in Eq. 6.12, sliding shear deformations were ignored. This is justified when estimating the coupling beam drift at the first instance of flexural yielding and at peak coupling beam strength, given how little sliding shear displacements contributed to the drift of coupling beam Specimens CB-2 and CB-3 prior to reaching the peak strength of the beam. However, beyond peak coupling beam strength and after repeated load cycles, sliding shear deformations become an increasingly important contributor to the deformation of the coupling beam, as shown in Figure 4.31. A model to estimate the coupling beam deformations caused by sliding shear would necessarily be appreciably more intricate than either model proposed for rotations or shear deformations described previously. A model for sliding shear would require multiple parameters, likely including axial force, beam curvature, longitudinal and diagonal reinforcement area, amount of

confinement, and certain material parameters including size and strength of aggregate. Proposing such a model on the basis of the three specimens tested would be unreasonable because of their similar reinforcement, geometry, and material composition.

Therefore, it is proposed that the coordinates of the third point shown in Figure 6.13 be approximated as follows. The strength of the coupling beam should be defined by Eq. 6.5 as 80% of the peak capacity. The drift of the coupling beam should be defined based on tests of specimens with aspect ratios and detailing similar to that being considered in design. For HPFRC coupling beams with aspect ratios between 1.5 and 2, designed in accordance with the recommendations of Section 6.1, it is suggested that δ_3 be defined by Eq. 6.17.

$$V_3 = 0.8V_3 \tag{6.5}$$

$$\delta_3 = 0.05 \tag{6.17}$$

6.3.4 Comparison of Model and Test Results

To estimate the tri-linear backbone curve for a given coupling beam (a schematic of this curve is shown in Figure 6.13), moment curvature analyses need to be performed for the beam section at the wall face. The critical results from these analyses are the moment and curvature at first yielding and at peak strength (ϕ_y, M_y, ϕ_{peak}, M_{peak}). From these inputs, Eqs. 6.3-6.5 can be used to estimate the shear force in the coupling beam for the three points defining the backbone curve.

The drift of the coupling beam at the first two points can be estimated by summing the contributions from flexural and shear deformations calculated previously. Eq. 6.18, which is the sum of the drifts obtained from Eqs. 6.8 and 6.14, can be used to estimate the drift of the coupling beam at first yielding.

$$\delta_1 = \frac{\phi_y \ell_n}{6} + \phi_y\left(\ell_{embed} + 8d_{b,largest\ bar}\right) + \frac{V_1}{bh}\frac{\beta}{0.6G_c} \tag{6.18}$$

Similarly, Eq. 6.19, which is the sum of the drifts obtained from Eqs. 6.11 and 6.16, can be used to estimate the drift of the coupling beam at peak shear force.

$$\delta_2 = \frac{\phi_y(\ell_n - h)^2}{6\ell_n} + \frac{\phi_{peak} h(2\ell_n - h)}{4\ell_n} + \phi_{peak}\left(\ell_{embed} + 8d_{b,largest\ bar}\right) + \frac{V_2}{bh}\frac{\beta}{0.6G_c}\frac{(\ell_n - h)}{\ell_n} + \frac{V_2}{bh}\frac{\beta\sqrt{\phi_{peak}/\phi_y}}{0.6G_c}\frac{h}{\ell_n} \quad (6.19)$$

Finally, Eq. 6.17 can be used to define the ultimate drift capacity for the coupling beam.

The resulting backbone curve calculated for each of the three specimens tested is shown in Figure 6.16, along with the test results for comparison. For all three specimens, the first line segment underestimated the initial stiffness of the coupling beam prior to flexural cracking, but provided a relatively accurate estimate of the drift and strength at first yield. In the three specimens tested, the drift at first yielding was recorded to be between 0.35-0.4% drift. The drift calculated by this method for first yielding was approximately 0.35%. Furthermore, through this method it was estimated that 50-60% of the drift at first yield was due to flexure, which is close to the approximately 60% contribution recorded from the tests. Prediction of the second point, intended to represent peak strength, was somewhat less consistent with test results. The estimated peak was not close for Specimen CB-1, but this specimen had inadequate detailing that prevented it from achieving its peak strength, and is not considered representative of beams designed according to Section 6.1. The estimated peak was much closer for Specimen CB-2. In the positive loading direction the estimate was within 5% of the strength and drift recorded from the test. The negative loading direction was not as accurate, but this loading direction developed some sliding at the critical flexural crack prior to attaining peak capacity. Because sliding is not considered by this model, this premature degradation was not captured. Similarly, the predicted displacement and strength at peak capacity was very close for Specimen CB-3 in the negative loading direction, but less close in the positive loading direction where sliding displacements developed prior to attaining the peak capacity. The third point, which represents the drift capacity of the beam, was not close for Specimen CB-1, but was reasonable for Specimens CB-2 and CB-3 in the loading direction least affected by sliding shear displacements.

The proposed model does a reasonably good job estimating both the strength and drift of the coupling beam at the first instance of flexural yielding and at peak strength. The inaccuracies of this model stem mostly from deviations from the assumed axial load of $0.4V_2$, and from sliding shear displacements, which were not considered. Thus, the primary potential improvement requires consideration of sliding shear displacements.

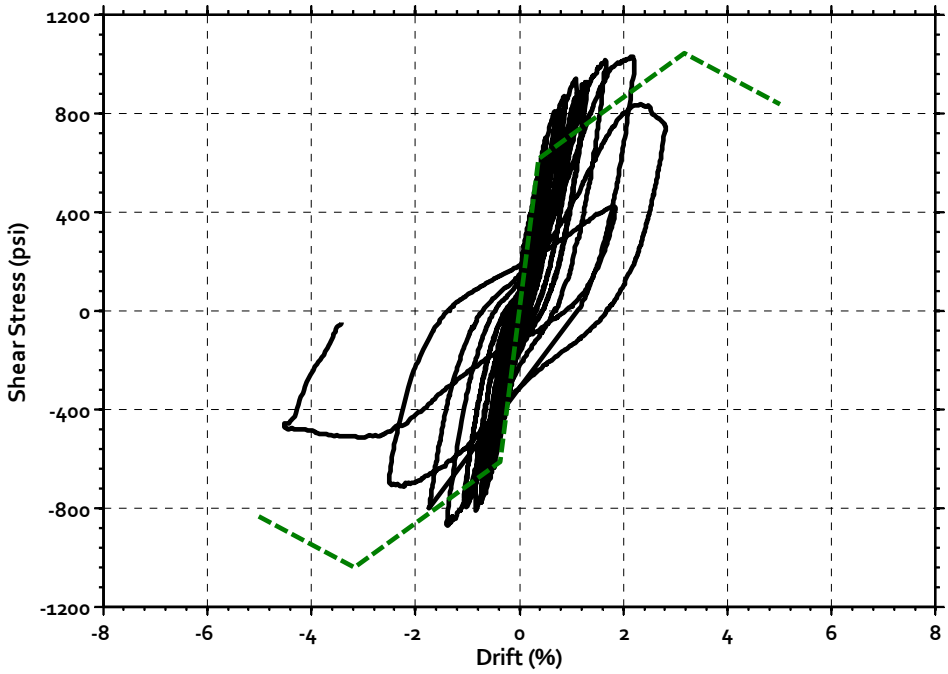

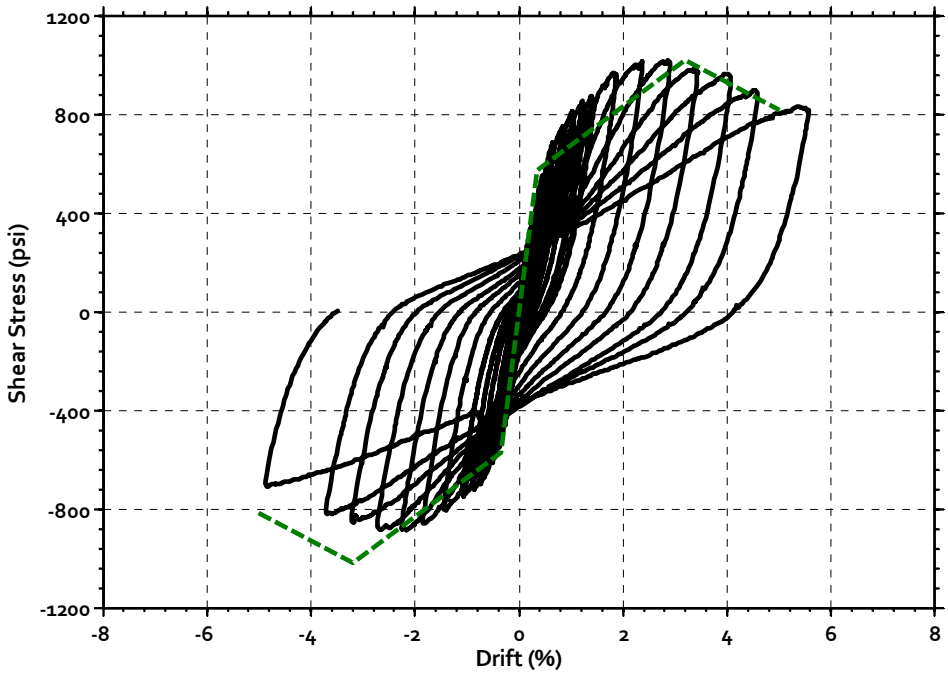

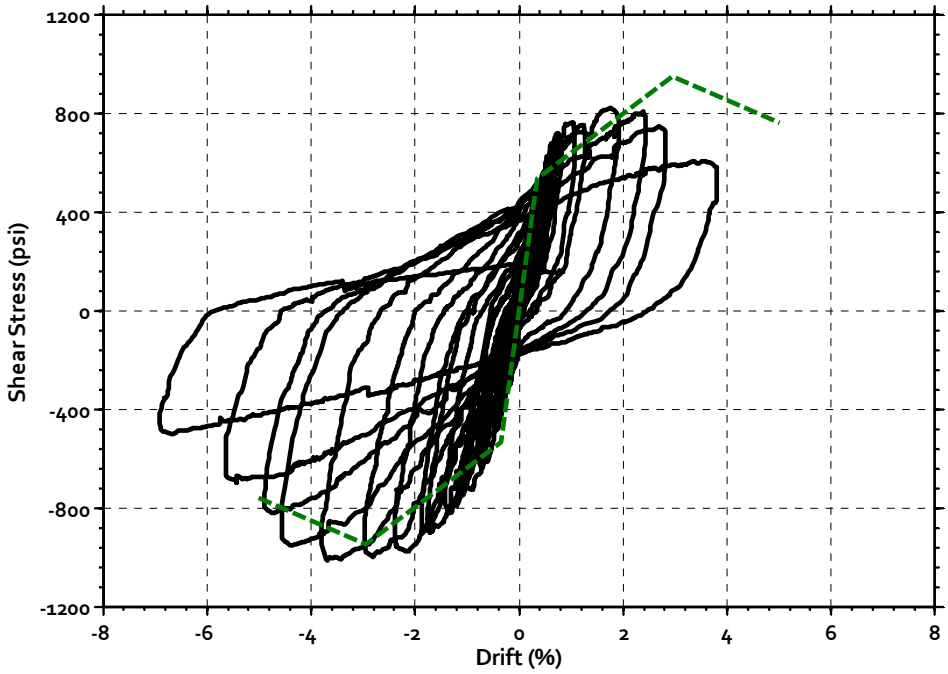

Figure 6.16 – Comparison between calculated tri-linear backbone curve and test results for Specimens CB-1, CB-2 and CB-3 (top to bottom, respectively)

CHAPTER 7:
SUMMARY AND CONCLUSIONS

7.1 BACKGROUND

Concrete structural walls are commonly used as the primary lateral force resisting system for both medium- and high-rise buildings. Architects generally place these walls near the center of the building's floor plan, and often require that the walls have openings for doors and windows. When these openings occur at every story level, the result is the splitting of an otherwise solid wall into two or three walls connected by coupling beams. If these coupling beams are sufficiently strong, stiff, and ductile, much of the stiffness and strength lost by splitting the solid wall can be regained. Coupling of the individual walls mobilizes the axial stiffness and strength of adjacent walls, which leads to additional lateral strength and stiffness for the system. This coupling therefore provides a means to limit structural drifts while reducing the demand for flexural stiffness and strength from the individual walls.

For the coupled system to behave as intended during a seismic event, the coupling beams are required to possess a high shear force capacity and endure large displacement demands. The heavily confined diagonal reinforcement required by the ACI Building Code for short coupling beams subjected to high shear stresses has been shown to provide stable behavior by preventing sliding shear failures and increasing the ductility and energy dissipation capacity of the coupling beams. Unfortunately, the dense reinforcement required is difficult to construct and can often be the controlling factor of the construction schedule for tall buildings. Although several alternatives have been proposed and investigated, none provide the same ductility and strength as diagonally reinforced coupling beams without imposing other construction difficulties. Of these

potential solutions, steel and hybrid steel-concrete coupling beams exhibit the most favorable response to reversed cyclic loading, and have begun to find their way into design practice. However, despite the improved hysteretic behavior achievable with steel coupling beams, providing proper anchorage of the steel section without disrupting reinforcement in the wall remains a significant challenge to engineers and contractors.

Desirable performance of a coupled wall system is also dependent on the base of each wall developing a ductile flexural hinge. These lower stories must accommodate appreciable flexural rotations without exhibiting significant shear distress, buckling of reinforcement, or crushing of concrete. To achieve the required ductility, concrete walls are typically reinforced with both horizontal and vertical shear reinforcement and tightly spaced boundary element confinement reinforcement that can be time consuming to place and interferes with the development of coupling beam reinforcement.

7.2 RESEARCH GOALS

There is a need to develop a more constructible coupling beam that exhibits strength, ductility, and energy dissipation characteristics comparable to diagonally reinforced concrete coupling beams. Through this research, it was sought to extend promising work by Canbolat, Parra-Montesinos and Wight (2005) on precast HPFRC coupling beams with aspect ratios of 1.0 to more slender coupling beams with an aspect ratio 1.75. Specifically, the project goals were to:

1) Evaluate the performance and viability of HPFRC coupling beams with an aspect ratio of 1.75,
2) Develop embedment details for the precast HPFRC section that do not interfere with wall boundary reinforcement, and,
3) Propose a reliable and practical design methodology for precast HPFRC coupling beams.

In addition to relaxing the reinforcement requirements for coupling beams, it is believed that HPFRC can be used to simplify the reinforcement detailing requirements in

the plastic hinge region of coupled structural walls. Therefore, this part of the project was designed to:

1) Investigate whether HPFRC can reduce the amount of shear reinforcement in coupled walls,
2) Study the performance of HPFRC coupled walls with reduced boundary element confinement.

7.3 SUMMARY OF TESTS

Three precast HPFRC coupling beam specimens were tested to evaluate various embedment details and reinforcement layouts. These tests were described in Chapter 3. The specimens were designed to resist high shear stresses that exceeded the upper limit of $10\sqrt{f_c'}, [psi]\left(0.83\sqrt{f_c'}, [MPa]\right)$ permitted by the ACI Building Code (ACI 318-08). Each of the specimens was then subjected to a displacement history that included multiple load reversals that gradually increased the drift demand until failure of the specimen. Analysis of these tests included investigation of the coupling beam strength, stiffness, energy dissipation, and damage tolerance. Whenever feasible, comparisons were made with diagonally reinforced concrete coupling beams with a similar aspect ratio and strength. The results of these tests, as well as data analyses, were presented in Chapter 4.

A second experimental phase was undertaken that consisted of the testing of two large scale (approximately 1/3 scale) coupled wall specimens. These tests were described in Chapter 3. The specimens were pseudo-statically subjected to a loading history that included multiple displacement reversals that gradually increased the drift demand until failure of the specimen. Both specimens consisted of four coupling beams linking two T-shaped structural walls. Slabs were included at the second and fourth levels to facilitate application of lateral displacements. Three of the coupling beams were precast with high-performance fiber-reinforced concrete (HPFRC) and one was precast with regular concrete. The design of the coupling beams was based on the coupling beam component tests discussed in Chapters 3 and 4. The same coupling beam designs were used in the two wall specimens, except that the longitudinal reinforcement of the coupling beams

used in the first wall specimen was terminated near the connection with the wall, whereas all coupling beam reinforcement was fully developed into the walls in the second specimen. The reinforcement of the first two stories of the walls also differed. The walls in the first specimen were designed and detailed to satisfy the requirements of the ACI Building Code (318-08), whereas HPFRC was used in the first two stories of the second specimen. In the HPFRC walls, the boundary element confinement reinforcement was reduced and a higher shear stress was assumed to be resisted by the concrete. Further details on the specimens were provided in Chapter 3. Analysis of these tests included investigation of the system strength, stiffness, and damage tolerance. A detailed analysis of the deformations within the first story of the walls and the coupling beams was conducted. The results of these tests and data analyses were presented in Chapter 5.

7.4 CONCLUSIONS

At the end of Chapters 4 and 5, the conclusions based on the analysis of the coupling beam and coupled wall tests were listed. The most important conclusions are restated in this section.

Based on the conclusions listed in Chapter 4, a simplified flexure based method (SFBM) was proposed for design of HPFRC coupling beams (described in Section 6.1). Use of this method will result in a ductile, damage tolerant coupling beam that is appreciably easier to construct and connect to structural walls without interfering with wall reinforcement. Following this procedure should ensure a flexural failure mode and provide a conservative estimate of the coupling beam capacity for use in designing the walls. A model was also developed for estimating the envelope of the shear force versus drift response of HPFRC coupling beams that accounts for flexural and shear deformations (described in Section 6.3). Extending the model to account for sliding shear displacements is a potential improvement of the model.

Some of the conclusions listed in Chapters 4 and 5 led to a discussion of the causes of axial forces in coupling beams and walls, as well as the risks of neglecting their effects in design. This discussion was presented in Section 6.2. It is emphasized that

additional information is required regarding axial forces in coupling beams before the effects of these forces can be quantified, and if necessary, accounted for in design.

7.4.1 Conclusions From Coupling Beam Tests

- Precasting the HPFRC coupling beam and embedding the concrete section only as deep as the wall cover proved to be an effective design alternative. The development of the diagonal, longitudinal and dowel reinforcement was shown to be adequate to transfer the moment capacity, and associated shear, of the coupling beam into the wall. Shear keys at the beam-to-wall interface slightly reduced sliding, but were found to not be required. This precast method is believed to simplify the construction of coupled-wall systems and limit the use of HPFRC to where it is most effective.
- Axial restraint of coupling beams resulted in axial forces on the order of $0.4V_{max}$. The axial elongation that developed in the coupling beams was shown to be proportional to the maximum flexural rotations imposed on the specimen.
- For design, a flexural section analysis is appropriate for calculating the capacity of plastic hinges at both ends of the coupling beam that ultimately control the beam shear demand. Assuming $f_s = f_y$ and $P = 0k$ resulted in a lower-bound coupling-beam capacity that was achieved at 0.75% drift and sustained until termination of the test. Assuming $f_s = 1.25f_y$ and $P = 0.4V_{max}$ resulted in an upper-bound coupling-beam capacity that was close to the measured peak shear force.
- Diagonal reinforcement provided 20-30% of the resistance to applied shear force, and stirrups and HPFRC effectively resisted the remainder. Assuming that $v_c = 5\sqrt{f_c'}, [psi]\left(0.41\sqrt{f_c'}, [MPa]\right)$ appears to provide a conservative estimate of the contribution of the HPFRC to shear stress capacity under drift reversals.
- HPFRC provides adequate confinement of diagonal reinforcement, so no special confinement is required to provide stability to these bars. Special column-type confinement is, however, required throughout the flexural plastic hinge at each end of the coupling beam to ensure stable behavior.

- Energy dissipated per cycle, when normalized by the energy corresponding to an equivalent elasto-plastic system with the same peak shear force and drift, and with a loading and unloading stiffness equal to the secant stiffness measured in the first cycle to 0.5% drift, was approximately 0.40 at drifts larger than 1%. This level of energy dissipation is comparable to that for well-detailed diagonally reinforced concrete coupling beams with similar aspect ratios.
- A flexural stiffness of $0.2E_cI_g$ provides a better estimate for calculating cracked stiffness for use in non-linear analyses than the $0.3E_cI_g$ value adopted by Supplement 1 of ASCE/SEI 41/06. For "equivalent" linear analyses, assuming an effective flexural stiffness of $0.2E_cI_g$, $0.1E_cI_g$ and $0.05E_cI_g$ to account for cracking and yielding was found appropriate for drift demands associated with immediate occupancy, life safety and collapse prevention, respectively, as defined by ASCE/SEI 41/06.
- The specimens exhibited a shear stiffness of approximately $0.04E_cA_g$ at drifts beyond 1%, which is only ten percent of the $0.4E_cA_g$ proposed by ASCE/SEI 41/06 for modeling coupling beams.

7.4.2 Conclusions From Coupled Wall Tests

7.4.2.1 Walls

- In the first coupled wall test, the walls detailed in accordance with the ACI Building Code (318-08) behaved very well.
- In the second coupled wall test that used HPFRC at the base of the shear walls, assuming HPFRC could resist an average shear stress of $4\sqrt{f_c'}, [psi]\left(0.33\sqrt{f_c'}, [MPa]\right)$ in the design of the walls was shown to lead to adequate resistance to shear.
- HPFRC walls with a relaxed boundary element confinement spacing of $t_w/2$ behaved well when subjected to large drift demands (up to 3.5% drift), with no indication of buckling of wall longitudinal reinforcement throughout the test.

- Dowel bars crossing the cold joint between the HPFRC walls and the foundation successfully prevented localization of damage along this interface. This is further indication that dowel bars are advisable across cold joints in HPFRC structures.

7.4.2.2 Coupling Beams

- HPFRC coupling beams were shown to be significantly more damage tolerant than comparable reinforced concrete coupling beams subjected to similar deformation demands, despite the use of substantially more transverse reinforcement in the reinforced concrete beams.
- When system drifts were large (on the order of 1.0 to 1.5%), the coupling beams were subjected to drift demands of 3.0 to 4.5%. The response of HPFRC coupling beams was shown to be stable at these drift levels. At even larger system drifts, coupling beam drifts continued to increase to beyond 10%, which highlights the significant drift demands coupling beams can be subjected to in response to seismic events.
- It was shown that coupling beam axial forces result from two distinct phenomena: 1) a shift of wall shear force to the stiffer compression wall near the foundation, and 2) resistance by stiff walls to beam elongation caused by the opening and partial re-closing of cracks and the accumulation of plastic deformation in coupling beam reinforcement as drift demands increase.
- In addition to affecting flexural and shear capacity of coupling beams, axial forces were shown to increase the beam shear stiffness. This had the effect of reducing shear deformations, but forced an increase in the curvature ductility demands to accommodate the imposed drift demands. This is an example of the potentially important role of axial forces on the behavior of coupling beams.
- Full development of the longitudinal reinforcement is required to develop the flexural capacity of the beams and to prevent localization of damage at the beam-to-wall interface.

7.4.2.3 Coupled Wall System

- Incorporation of precast coupling beams into the construction sequence of the coupled system was shown to be a straightforward process and a viable alternative to current construction methods. Formwork easily supported the precast beam prior to casting the wall concrete, and wall boundary confinement reinforcement was successfully placed with little interference from beam reinforcement.
- The overturning moment capacity of the system was predicted to within 3% for both loading directions of Specimen CW-1 and for the negative loading direction of Specimen CW-2. This calculation assumed a flexural hinge would simultaneously form at the base of each wall, at the ends of each coupling beam, and in the slabs (which were treated independently from the coupling beams because they were cast adjacent to, but not connected with, the precast coupling beam). This method over-predicted, by approximately 6%, the capacity in the positive loading direction of Specimen CW-2. The compression wall ultimately failed in shear in this loading direction.
- The thin slabs at the second and fourth levels were shown to develop plastic hinges and contribute to the coupling of the walls. Without considering this contribution, the overturning moment capacity of the system would have been under-predicted by between 5 and 9%.
- A Wall Strength Index (WSI) was proposed as a complement to the coupling ratio (CR). The WSI is defined as the sum of the flexural capacity of the walls considering axial forces due to coupling, divided by the sum of the flexural capacity of the walls without the axial forces due to coupling. WSI is a direct measure of the effect axial forces due to coupling have on the flexural strength of walls. For systems with $WSI < 1.0$, additional coupling reduces the flexural capacity of the walls, and thus increasing CR would not be the most efficient way to increase the lateral capacity of the system. Furthermore, $WSI < 1.0$ indicates that the flexural ductility of the walls may be reduced by the axial forces from coupling.

7.5 FUTURE WORK

This project has provided information regarding the performance and design requirements of precast HPFRC coupling beams and HPFRC coupled walls. Aside from further testing of similar specimens, which will help refine the proposed design procedure and provide engineers with additional modeling guidance, further study is warranted to address a number of issues raised by this study. Some studies, including one aimed at investigating the performance of slender HPFRC coupling beams with aspect ratios greater than 2.5, both with and without diagonal reinforcement, have already been initiated to address some of the issues raised. Other issues have yet to be resolved. The following is a list of unresolved issues that the writer believes warrant further study.

- The causes of axial forces in coupling beams need to be quantified to develop a practical model that predicts the magnitude of these forces. Such a model will likely include a measure of the maximum flexural deformations imposed on the beam, the aspect ratio of the beam, and a measure of the stiffness of the walls and slabs. Experimental and analytical study of coupled wall systems is required to quantify the resistance (stiffness) provided by slabs and walls to the tendency of coupling beams to elongate.
- Sliding shear mechanisms still need further investigation. Numerous researchers have studied sliding shear mechanisms, but there is still enough uncertainty regarding the factors that trigger sliding shear deformations that accurate prediction is not possible. Issues that need to be resolved include quantifying the relative influence of axial force, beam curvature, longitudinal and diagonal reinforcement area, amount of confinement, and certain material parameters including size and strength of aggregate. Also, whether it is correct to assume that compression reinforcement contributes to the clamping force across a potential sliding plane, as assumed by the ACI Building Code, is questionable.
- Additional study is required regarding boundary element confinement requirements in HPFRC walls. It is likely that boundary element confinement can be spaced more widely than $t_w/2$; however, the results of the tests described herein are not sufficient to support recommending a wider spacing.

- It would be interesting to investigate the relationship between wall coupling ratio and the spread of inelastic deformations throughout the lower wall stories. Diagonal cracking in the walls of the two coupled wall specimens developed throughout the first two stories of the system, similar to what might be expected if the walls were solidly joined (i.e. $CR = 1.0$), yet flexural deformations localized within the first story of the walls.

REFERENCES

ACI Committee 318 (1999), *Building Code Requirements for Structural Concrete (ACI 318-99)*, American Concrete Institute, Farmington Hills, MI, 391 pp.

ACI Committee 318 (2008), *Building Code Requirements for Structural Concrete (ACI 318-08)*, American Concrete Institute, Farmington Hills, MI, 430 pp.

ACI Committee 374 (2006), *Recommendations for Design of Coupling Beams in Monolithic Reinforced Concrete Structures-Draft,* American Concrete Institute, Farmington Hills, MI, 37 pp.

ACI Committee 544 (1973), "State-of-the-Art Report on Fiber Reinforced Concrete," *Journal of the American Concrete Institute,* 70 (11), 729-744.

ACI Committee 544 (1988a), "Design Considerations for Steel Fiber Reinforced Concrete," *ACI Structural Journal,* 85 (5), 563-580.

ACI Committee 544 (1988b), "Measurement of Properties of Fiber Reinforced Concrete," *ACI Materials Journal,* 85 (6), 583-593.

ACI Committee 544 (2007), *Indirect Method for Obtaining a Model Stress-Strain Curve of Strain Softening FRCs (Draft),* American Concrete Institute, Farmington Hills, 18 pp.

ACI Committee Report (1920), "Concrete Shear Values Proposed to Concrete Institute," *Engineering News-Record,* 84, 465-470.

ACI Publication SP-44 (1974), *Fiber Reinforced Concrete,* American Concrete Institute, Detroit, 554 pp.

Aktan, A. E. and Bertero, V. V. (1984), "Seismic Response of R/C Frame-Wall Structures," *Journal of Structural Engineering,* ASCE, 110 (8), 1803-1821.

Aktan, A. E. and Bertero, V. V. (1985), "RC Structural Walls: Seismic Design for Shear," *Journal of Structural Engineering,* ASCE, 111 (8), 1775-1791.

Alsiwat, J. M. and Saatcioglu, M. (1992), "Reinforcement Anchorage Slip Under Monotonic Loading," *Journal of Structural Engineering,* ASCE, 118 (9), 2421-2438.

Aristizabal-Ochoa, J. D. and Sozen, M. A. (1976), *Behavior of Ten-Story Reinforced Concrete Walls Subjected to Earthquake Motions,* PhD Dissertation, University of Illinois, Urbana-Champaign, IL, 378 pp.

ASCE/SEI 41/06, 2007, *Seismic Rehabilitation of Existing Buildings*, American Society of Civil Engineers, Reston, Virginia.

ASCE/SEI 41/06, 2007, *Seismic Rehabilitation of Existing Buildings – Supplement 1*, American Society of Civil Engineers, Reston, Virginia.

Ashour, S. A., and Wafa, F. F. (1993), "Flexural Behavior of High-Strength Fiber Reinforced Concrete Beams," *ACI Structural Journal,* 90 (3), 279-287.

ASTM Standard C39/C39M, (2003), "Standard Test Method for Compressive Strength of Cylindrical Concrete Specimens," ASTM International, West Conshohocken, PA.

ASTM Standard C1609/C1609M, (2005), "Standard Test Method for Flexural Performance of Fiber-Reinforced Concrete (Using Beam With Third-Point Loading)," ASTM International, West Conshohocken, PA.

ATC (2009), *Quantification of Building seismic Performance Factors,* ATC 63, FEMA P695, prepared by Applied Technology Council for the Federal Emergency Management Agency, Washington, D. C.

Athanasopoulou, A. (2010), *Shear Strength and Drift Capacity of Reinforced Concrete and High-Performance Fiber reinforced Concrete Low-Rise Walls Subjected to Displacement Reversals*, PhD. Dissertation, University of Michigan, Ann Arbor, MI, 302 pp.

Barney, G. B., Shiu, K. N., Rabbat, B. G., and Fiorato, A. E. (1976), *Earthquake Resistant Structural Walls – Tests of Coupling Beams (Progress Report),* Portland Cement Association, Skokie, Illinois, 137 pp.

Barragan, B. E., Gettu, R., and Zerbino, R. (2002), "Tensile Behavior of Steel Fiber Reinforced Concrete – Evaluation of a Test Methodology," *Proceedings, Third International Conference on High Performance Concrete: Performance and Quality of Concrete Structures,* SP-207, American Concrete Institute, Detroit, 91-110.

Bass, R. A., Carrasquillo, R.L., and Jirsa, J. O. (1989), "Shear Transfer Across New and Existing Concrete Interfaces," *ACI Structural Journal,* 86 (4), 383-393.

Batson, G., Jenkins, E., and Spatney, R. (1972), "Steel Fibers as Shear Reinforcement in Beams," *ACI Journal,* 69 (10), 640-644.

Balaguru, P., Narahari, R., and Patel, M. (1992), "Flexural Toughness of Steel Fiber Reinforced Concrete," *ACI Materials Journal,* 89 (6), 541-546.

Bayasi, Z. and Gebman, M. (2002), "Reduction of Lateral Reinforcement in Seismic Beam-Column Connection via Application of Steel Fibers," *ACI Structural Journal,* 99 (6), 772-780.

Beck, H. (1962), "Contribution to the Analysis of Coupled Shear Walls," *Journal of the American Concrete Institute,* 59 (8), 1055-1070.

Bertero, V. V. and Popov, E. P. (1975), "Hysteretic Behavior of Reinforced Concrete Flexural Members With Special Web Reinforcement," *Proceedings of the US National Conference on Earthquake Engineering,* 316-326.

Binney, J. R. (1972), *Diagonally Reinforced Coupling Beams*, MS Thesis, University of Canterbury, Christchurch, New Zealand, 131 pp.

Biskinis, D. E., Roupakias, G. K., and Fardis, M. N. (2004), "Degradation of Shear Strength of Reinforced Concrete Members with Inelastic Cyclic Displacements," *ACI Structural Journal,* 101 (6), 773-783.

Bolander, J. E. (1989), *Towards Realistic FE Models for Reinforced Concrete Shear Wall Dominant Buildings Subjected to Lateral Loading,* Ph.D. Dissertation, University of Michigan, Ann Arbor, MI, 475 pp.

Brown, R. H. and Jirsa, J. O. (1971), "Reinforced Concrete Beams Under Load Reversals," *ACI Journal,* 68 (5), 380-390.

Buchanan, A. H. (1979) "Diagonal Beam Reinforcing for Ductile Frames," *Bulletin of the New Zealand National Society for Earthquake Engineering,* 12 (4), 346-356.

Canbolat, B. A., Parra-Montesinos, G. J., and Wight, J. K. (2005), "Experimental Study on Seismic Behavior of High-Performance Fiber-Reinforced Cement Composite Coupling Beams," *ACI Structural Journal,* 102 (1), 159-166.

Cardenas, A. E., Hanson, J. M., Corley, W. G. and Hognestad, E. (1973), "Design Provisions for Shear Walls," *ACI Journal,* 70 (3), 221-230.

Chao, S.-H. (2005), *Bond Characterization of Reinforcing Bars and Prestressing Strands in High Performance Fiber Reinforced Cementitious Composites Under Monotonic and Cyclic Loading*, PhD. Dissertation, University of Michigan, Ann Arbor, MI, 475 pp.

Chen, W.-F. and Carson, J. L. (1971), "Stress-Strain Properties of Random Wire Reinforced Concrete," *ACI Journal,* 68 (12), 933-936.

Cheng, M.-Y., Parra-Montesinos, G. J., and Shield, C. K. (2008), "Effectiveness of Steel Fibers Versus Shear Stud Reinforcement for Punching Shear Resistance in Slab-Column Connections Subjected to Bi-Axial Lateral Displacements," *Proceedings of the 14th World Conference on Earthquake Engineering,* Beijing, China.

Chitty, L. (1947), "On the Cantilever Composed of a Number of Parallel Beams Interconnected by Cross Bars," *The London, Edinburgh, and Dublin Philosophical Magazine and Journal of Science,* 38, 685-699.

Choi, K.-K., Park, H.-G., and Wight, J. K. (2007), "Shear Strength of Steel Fiber-Reinforced Concrete Beams Without Web Reinforcement," *ACI Structural Journal,* 104 (1), 12-21.

Compione, G. and Mindess, S. (1999), "Compressive Toughness Characterization of Normal and High-Strength Fiber Concrete Reinforced with Steel Spirals," *Structural Applications of Fiber Reinforced Concrete,* SP-182, American Concrete Institute, Farmington Hills, MI, 141-161.

Coull, A. and Choudhury J. R. (1967), "Stresses and Deflections in Coupled Shear Walls," *ACI Journal,* 64 (2), 65-72.

Dazio, A., Buzzini, D., and Trub, M. (2008), "Nonlinear Cyclic Behavior of Hybrid Fiber Concrete Structural walls," *Engineering Structures*, 30, 3141-3150.

Doran, B. (2003), "Elastic-Plastic Analysis of R/C Coupled Shear Walls: The Equivalent Stiffness Ratio of the Tie Elements," *Journal of the Indian Institute of Science,* 83 (3-4), 87-94.

El-Tawil, S., Fortney, P., Harries, K., Shahrooz, B., Kurama, Y., Hassan, M., and Tong, X. (2010). *Recommendations for Seismic Design of Hybrid Coupled Wall Systems*. SEI/American Society of Civil Engineers. 70 pp.

El-Tawil, S. and Kuenzli, C. M. (2002a), "Pushover of Hybrid Coupled Walls. I: Design and Modeling," *Journal of Structural Engineering,* ASCE, 128 (10), 1272-1281.

El-Tawil, S. and Kuenzli, C. M. (2002b), "Pushover of Hybrid Coupled Walls. II: Analysis and Behavior," *Journal of Structural Engineering,* ASCE, 128 (10), 1282-1289.

Elsied, A., Ragab, A., and Emam, H. M. (1990), "Dynamic Behavior of Coupled Shear Wall Through Analytical Models," *Computers and Structures,* 35 (2) 183-187.

Elwood, K. J. and Eberhard, M. O. (2009), "Effective Stiffness of Reinforced Concrete Columns," *ACI Structural Journal,* 106 (4), 476-484.

Ezeldin, A. S. and Balaguru, P. N. (1989), "Bond Behavior of Normal and High-Strength Fiber Reinforced Concrete," *ACI Materials Journal,* 86 (5), 515-524.

Ezeldin, A. S. and Balaguru, P. N. (1992), "Normal- and High-Strength Fiber-Reinforced Concrete Under Compression," *Journal of Materials in Civil Engineering,* ASCE, 4 (4), 415-429.

Fanella, D. A. and Naaman, A. E. (1985), "Stress-Strain Properties of Fiber Reinforced Mortar in Compression," *ACI Journal,* 82 (4), 475-483.

Filiatrault, A., Ladicani, K., and Massicotte, B. (1994), "Seismic Performance of Code-Designed Fiber-Reinforced Concrete Joints," *ACI Structural Journal,* 91 (5), 564-571.

Fischer, G. and Li, V. C. (2002), "Effect of Matrix Ductility on Deformation Behavior of Steel-Reinforced ECC Flexural Members Under Reversed Cyclic Loading Conditions," *ACI Structural Journal,* 99 (6), 781-790.

Fischer, G. and Li, V. C. (2003), "Deformation Behavior of Fiber-Reinforced Polymer Reinforced Engineered Cementitious Composite (ECC) Flexural Members Under Reversed Cyclic Loading Conditions," *ACI Structural Journal,* 100 (1), 25-35.

Fortney, P. J., Rassati, G. A. and Shahrooz, B. M. (2008), "Investigation on Effect of Transverse Reinforcement on Performance of Diagonally Reinforced Coupling Beams," *ACI Structural Journal,* 105 (6), 781-788.

Fortney, P. J. and Shahrooz, B. M. (2009), "Boundary Detailing of Coupled Core Wall System Wall Piers," *Advances in Structural Engineering,* 12 (3), 299-310.

Galano, L. and Vignoli, A. (2000), "Seismic Behavior of Short Coupling Beams with Different Reinforcement Layouts," *ACI Structural Journal,* 97 (6), 876-885.

Godfrey, E. (1920), "Reinforcement for Diagonal Tension in Reinforced Concrete Beams," *Concrete,* 17 (1), 15-20.

Gong, B. and Shahrooz, B. M. (2001a), "Concrete-Steel Composite Coupling Beams. II: Subassembly Testing and Design Verification," *Journal of Structural Engineering,* ASCE, 127 (6), 632-638.

Gong, B. and Shahrooz, B. M. (2001b), "Steel-Concrete Composite Coupling Beams – Behavior and Design," *Engineering Structures,* 23, 1480-1490.

Gopalaratnam, V. S. and Shah, S. (1987), "Failure Mechanisms and Fracture of Fiber Reinforced Concrete," *Fiber Reinforced Concrete – Properties and Applications,* SP-105, American Concrete Institute, Detroit, 1-25.

Halvorsen, G. T. and Kesler, C. E. (1979), "Moment-Curvature Relationships for Concrete Beams with Plain and Deformed Steel Fibers," *ACI Journal,* 76 (6), 697-706.

Harajli, M. H. (2009), "Bond Stress-Slip Model for Steel Bars in Unconfined of Steel, FRC, or FRP Confined Concrete under Cyclic Loading," *Journal of Structural Engineering*, ASCE, 135 (5), 509-518.

Harries, K. A., Fortney, P. J., Shahrooz, B.M. and Brienen, P. J. (2005), "Practical Design of Diagonally Reinforced Concrete Coupling Beams – Critical Review of ACI 318 Requirements," *ACI Structural Journal*, 102 (6), 876-882.

Harries, K. A., Gong, B. and Shahrooz, B. M. (2000), "Behavior and Design of Reinforced Concrete, Steel, and Steel-Concrete Coupling Beams," *Earthquake Spectra,* 16 (4), 775-799.

Harries, K. A., Mitchell, D., Redwood, R. G. and Cook, W. D. (1998), "Nonlinear Seismic Response Predictions of Walls Coupled with Steel and Concrete Beams," *Canadian Journal of Civil Engineering,* 25 (5), 803-818.

Harries, K. A., Moulton, D. and Clemson, R. L. (2004), "Parametric Study of Coupled Wall Behavior – Implications for the Design of Coupling Beams," *Journal of Structural Engineering*, ASCE, 130 (3), 480-488.

Harries, K. A. (2001), "Ductility and Deformability of Coupling Beams in Reinforced Concrete Coupled Walls," *Earthquake Spectra,* 17 (3), 457-478.

Hassan, M. and El-Tawil, S. (2004), "Inelastic Dynamic Behavior of Hybrid Coupled Walls," *Journal of Structural Engineering,* ASCE, 130 (2), 285-296.

Henager, C. H. (1977), "Steel Fibrous, Ductile Concrete Joint for Seismic-Resistant Structures," *Reinforced Concrete Structures in Seismic Zones,* SP-53, American Concrete Institute, Detroit, 371-386.

Higashiyama, H. and Banthia, N. (2008), "Correlating Flexural and Shear Toughness of Lightweight Fiber-Reinforced Concrete," *ACI Materials Journal*, 105 (3), 251-257.

Hisatoku, T. and Matano, H. (1972), "Experimental Study on Physical Characteristics of Coupled Shear Wall," *Takenaka Gijutsu Kenkyu Hokoku (Japanese)*, (8), 1-23.

Hognestad, E. (1952), "Inelastic Behavior in Tests of Eccentrically loaded Short Reinforced Concrete Columns," *ACI Journal,* 49 (10), 117-139.

Hossain, K. M. A. (2003), "Nonlinear Performance of Slabs in Coupled Shear Wall Structures," *Advances in Structural Engineering,* 6 (4), 339-352.

Hung, C.-C. (2010), *Computational and Hybrid Simulation of High Performance Fiber Reinforced Concrete Coupled Wall Systems*, PhD. Dissertation, University of Michigan, Ann Arbor, MI, 191 pp.

International Code Council (2000), *2000 IBC Structural/Seismic design manual, Vol. 3: Building Design Examples for Steel and Concrete,* 340 pp.

Irwin, A. W. and Ord, A. E. C. (1976), "Cyclic Load Tests on Shear wall Coupling Beams," *Proceedings of the Institution of Civil Engineers, Part 1 – Design and Construction,* 61 (2), 331-342.

Jiuru, T., Chaobin, H., Kaijian, Y., and Yongcheng, Y. (1992), "Seismic Behavior and Shear Strength of Framed Joint Using Steel-Fiber Reinforced Concrete," *Journal of the Structural Division,* ASCE, 188 (2), 341-358.

Kabeyasawa, T. and Nakamura, Y. (1998), "Displacement-Based Design of Hybrid Core Wall System," *Structural Engineering World Wide 1998 – Proceedings,* Paper Number T186-1, Elsevier Science Ltd., 7 pp.

Kato, M., Sugaya, K.-I. and Nagatsuka, N. (1996), "Optimum Moment Distribution Between Shear Walls and Boundary Beams of Coupled Shear Wall With Flange Walls," *Eleventh World Conference on Earthquake Engineering – Proceedings,* Paper Number 775, Elsevier Science Ltd., 8 pp.

Kent, D. C. and Park, R. (1971), "Flexural Members with Confined Concrete," *Journal of the Structural Division,* ASCE, 97 (7), 1969-1990.

Khuntia, M., Stojadinovic, B., and Goel, S. C. (1999), "Shear Strength of Normal and High-Strength Fiber Reinforced Concrete Beams Without Stirrups," *ACI Structural Journal*, 96 (2), 282-290.

Kim, K. and Parra-Montesinos, G. J. (2003), "Behavior of HPFRCC Low-Rise Walls Subjected to Displacement Reversals," *High Performance Fiber Reinforced Cement Composites (HPFRCC 4),* Proceedings of the Fourth International RILEM Workshop, A. E. Naaman and H. W. Reinhardt, eds., RILEM Publications, 505-515.

Kuramoto, H., Minami, K., and Wakabayashi, M. (1988), "Deformation Capacity of Diagonally Reinforced Concrete Short Columns Subject to Axial Compressive Stress," *Proceedings of Ninth World Conference on Earthquake Engineering,* IV, 377-382.

Krstulovic-Opara, N., Watson, K. A., and LaFave, J. M. (1994), "Effect of Increased Tensile Strength and Toughness on Reinforcing-Bar Bond Behavior," *Cement and Concrete Composites,* 16, 129-141.

Kwan, A.K.H., and Zhao, Z.-Z. (2002), "Cyclic Behavior of Deep Reinforced Concrete Coupling Beams," *Structures and Buildings*, 152 (3), 283-293.

Lam, W.-Y., Su, R. K.-L. and Pam, H.-J. (2005), "Experimental Study on Embedded Steel Plate Composite Coupling Beams," *Journal of Structural Engineering,* ASCE, 131 (8), 1294-1302.

Lee, J.-H., Yoon, Y.-S., Lee, S.-H., Cook, W. D., and Mitchell, D. (2008), "Enhancing Performance of Slab-Column Connections," *Journal of Structural Engineering,* ASCE, 134 (3), 448-457.

Lequesne, R. D., Setkit, M., Parra-Montesinos, G. J., and Wight, J. K. (2009), "Seismic Detailing and Behavior of Coupling Beams Incorporating High-Performance Fiber Reinforced Concrete," *Antoine E. Naaman Symposium – Four Decades of Progress in Prestressed Concrete, Fiber Reinforced Concrete, and Thin Laminate Composites,* SP-XX, American Concrete Institute, Farmington Hills, MI, 14 pp.

Lequesne, R. D., Setkit, M., Kopczynski, C., Ferzli, J., Cheng, M.-Y., Parra-Montesinos, G. J., and Wight, J. K. (2011), "Implementation of High-Performance Fiber Reinforced Concrete Coupling Beams in High-Rise Core-Wall Structures in the Seattle Area," *American Concrete Institute SP-XXX, In Review,*13 pp.

Li, Z., Li, F., Chang, T.-Y. P., and Mai, Y.-W. (1998), "Uniaxial Tensile Behavior of Concrete Reinforced with Randomly Distributed Short Fibers," *ACI Materials Journal,* 95 (5), 564-574.

Liao, W.-C., Chao, S.-H., Park, S.-Y. and Naaman, A. E. (2006), *Self-Consolidating High Performance Fiber Reinforced Concrete (SCHPFRC) – Preliminary Investigation,* Report No. UMCEE 06-02, 76 pp.

Lu, X. and Chen, Y. (2005), "Modeling of Coupled Shear Walls and Its Experimental Verification," *Journal of Structural Engineering,* ASCE, 131 (1), 75-84.

Luisoni, C. J., Somenson, H. M., and Ungaro, M. A. (1971), "Verificacion Experimental de un Calculo Plastico y otro Elastico de una Pared de Corte," *XIV Jornadas Sudamericanas de Ingenieri a Estructural: y IV Simposio Panamericano de Estructuras Proceedings*, 5, 230-286.

Lybas, J. M. and Sozen, M. A. (1977), *Effect of Beam Strength and Stiffness on Dynamic Behavior of Reinforced Concrete Coupled Walls,* Vol. 1 and 2, PhD Dissertation, University of Illinois, Urbana-Champaign, IL, 569 pp.

Mahin, S. A. and Bertero, V. V. (1976), "Nonlinear Seismic Response of A Coupled Wall System," *Journal of the Structural Division,* ASCE, 102 (9), 1759-1780.

Massicotte, B., Mossor, B., Filiatrault, A., and Tremblay, S. (1999), "Compressive Strength and Ductility of Steel Fiber Reinforced Concrete," *Structural Applications of Fiber Reinforced Concrete,* SP-182, American Concrete Institute, Farmington Hills, MI, 163-180.

Mirza, M. S. (1980), "Study of the Behavior of Coupled Shear Wall Systems," *Reinforced Concrete Structures Subjected to Wind and Earthquake Forces,* SP-63, American Concrete Institute, Detroit, MI, 301-328.

Monfore, G. E. (1968), "A Review of Fiber Reinforcement of Portland Cement Paste, Mortar, and Concrete," *Journal of the PCA Research and Development Laboratories,* 10 (3), 43-49.

Morsch, E. (1909), *Concrete-Steel Construction*, Trans. E. P. Goodrich. New York: The Engineering News Publishing Company, 368 pp.

Morsch, E. (1927), "Zur Frage Der Schubsicherung der Eisenbetonbalken (The Problem of Diagonal Shear Reinforcement of Reinforced-Concrete Beams)," *Der Bauingenieur,* 8 (16), 277-283.

Muttoni, A., Schwartz, J., and Thurlimann, B. (1997), *Design of Concrete Structures with Stress Fields,* Birkhauser Verlag, 151 pp.

Naaman, A. E. (1985), "Fiber Reinforcement for Concrete," *Concrete International,* 7 (3), 21-25.

Naaman, A. E., Otter, D., and Najm, H. (1991), "Elastic Modulus of SIFCON in Tension and Compression," *ACI Materials Journal,* 88 (6), 603-612.

Naaman, A. E. and Reinhardt, H. W. (1996), "Characterization of High Performance Fiber Reinforced Cement Composites – HPFRCC," *High Performance Fiber Reinforced Cement Composites 2 (HPFRCC 2),* Proceedings of the Second International RILEM Workshop, A. E. Naaman and H. W. Reinhardt eds., E&FN Spon, London, 1-24.

Naaman, A. E. (1998), "New Fiber Technology (Cement, Ceramic & Polymeric Composites," *Concrete International*, 20 (7), 57-62.

Naaman, A. E. (2003), "Strain Hardening and Deflection Hardening Fiber Reinforced Cement Composites," *High Performance Fiber Reinforced Cement Composites 4 (HPFRCC 4),* Proceedings of the Fourth International RILEM Workshop, A. E. Naaman and H. W. Reinhardt eds., E&FN Spon, London, 95-113.

Naaman, A. E., Likhitruangsilp, V., and Parra-Montesinos, G. J. (2007), "Punching Shear Response of High-Performance Fiber-Reinforced Cementitious Composite Slabs," *ACI Structural Journal,* 104 (2), 170-179.

Naish, D., Fry, J. A., Klemencic, R. and Wallace, J. (2009), *Reinforced Concrete Link Beams: Alternative Details for Improved Constructability,* Report to Charles Pankow Foundation. UCLA-SGEL, 103 pp.

Narayanan, R. and Darwish, I. Y. S. (1987), "Use of Steel Fibers as Shear Reinforcement," *ACI Structural Journal,* 84 (3), 216-227.

Noghabai, K. (1999), "Effect of Various Types of Fibers on Bond Capacity – Experimental, Analytical, and Numerical Investigations," *Structural Applications of Fiber Reinforced Concrete,* SP-182, American Concrete Institute, Farmington Hills, MI, 109-127.

Oh, B. H. (1992), "Flexural Analysis of Reinforced Concrete Beams Containing Steel Fibers," *Journal of Structural Engineering,* ASCE, 118 (10), 2821-2936.

Oh, B. H., Lee, H. J., Yoo, S. W., and Kim, E. S. (1998), "Flexural and Shear Behavior of Steel Fiber Reinforced Beams for Structural Applications," *Proceedings of Structural Engineering World Wide 1998,* Paper No. T183-5.

Oh, B., Lim, D., Hong, K., Yoo, S., and Chae, S. (1999), "Structural Behavior of Steel Fiber Reinforced Concrete Beams in Shear," *Structural Applications of Fiber Reinforced Concrete,* SP-182, American Concrete Institute, Detroit, 9-28.

Oesterle, R. G., Fiorato, A. E., Johal, A. E., Carpenter, J. E., Russell, H. G. and Corley, W. G., (1976), *Earthquake Resistant Structural Walls-Tests of Isolated Walls*, Report to National Science Foundation, Construction Technology Laboratories, Portland Cement Association, 315 pp.

Park, R. and Paulay, T. (1975), *Reinforced Concrete Structures*, John Wiley & Sons, New York, NY, 746 pp.

Park, W.-S., Yun, H.-D., Chung, J.-Y. and Kim, Y.-C. (2005), "Experimental Studies on Seismic Behavior of Steel Coupling Beams," *Structural Engineering and Mechanics,* 20 (6), 695-712.

Parra-Montesinos, G. J. and Wight, J. K. (2000), "Seismic Response of Exterior RC Column-to-Steel Beam Connections," *Journal of Structural Engineering,* ASCE, 126 (10), 1113-1121.

Parra-Montesinos, G. J. (2005), "High-Performance Fiber-Reinforced Cement Composites: An Alternative for Seismic Design of Structures," *ACI Structural Journal,* 102 (5), 668-675.

Parra-Montesinos, G. J. (2006), "Shear Strength of Beams With Deformed Steel Fibers," *Concrete International,* 28 (11), 57-66.

Parra-Montesinos, G. J., Canbolat B. A. and Jeyaraman, G. R. (2006), "Relaxation of Confinement Reinforcement Requirements in Structural Walls Through the Use of Fiber Reinforced Cement Composites," *8th National Conference of Earthquake Engineering,* San Francisco, CA.

Parra-Montesinos, G. J. and Chompreda, P. (2007), "Deformation Capacity and Shear Strength of Fiber-Reinforced Cement Composite Flexural Members Subjected to Displacement Reversals," *Journal of Structural Engineering,* ASCE, 133 (3), 421-431.

Parra-Montesinos, G.J., Peterfreund, S., and Chao, S.-H. (2005), "Highly Damage Tolerant Beam-Column Joints Through the Use of Strain-Hardening Fiber Reinforced Cement Composites," *ACI Structural Journal*, 102 (3), 487-495.

Parra-Montesinos, G. J., Wight, J. K. and Setkit, M. (2010), "Earthquake-Resistant Coupling Beams without Diagonal Reinforcement," *Concrete International*, 32 (12), 36-40.

Paulay, T. (1969), *The Coupling of Shear Walls,* PhD Dissertation, University of Canterbury, Christchurch, New Zealand, 435 pp.

Paulay, T. (1971), "Coupling Beams of Reinforced Concrete Shear Walls," *Journal of the Structural Division,* ASCE, 97 (ST3), 843-861.

Paulay, T. and Binney, J. R. (1974), "Diagonally Reinforced Coupling Beams of Shear Walls," *Shear in Reinforced Concrete*, SP-42, American Concrete Institute, Detroit, MI, 2, 579-598.

Paulay, T. and Loeber, P. J. (1974), "Shear Transfer by Aggregate Interlock," *Shear in Reinforced Concrete,* SP-42, American Concrete Institute, Detroit, 1-15.

Paulay, T. and Santhakumar, A. R. (1976), "Ductile Behavior of Coupled Shear Walls," *Journal of the Structural Division,* ASCE, 102 (ST1), 93-108.

Paulay, T. and Spurr, D. D. (1977), "Frame-Shear Wall Assemblies Subjected to Simulated Seismic Loading," *Proceedings of the Sixth World Conference on Earthquake Engineering,* New Delhi, India, 1195-1200.

Paulay, T. (2002), "A Displacement-Focused Seismic Design of Mixed Building Systems," *Earthquake Spectra,* 18 (4), 689-718.

Pekau, O. A. and Gocevski, V. (1978), "Behavior of Coupled Non-Linear Shear Walls," *Canadian Journal of Civil Engineering,* 5, 367-373.

Pfrang, E.O., Siess, C.P. and Sozen, M.A. (1964), "Load-Moment-Curvature Characteristics of Reinforced Concrete Cross Sections," *ACI Journal,* 61 (4), 763-778.

Rehm, G. and Eligehausen, R. (1979), "Bond of Ribbed Bars Under High Cycle Repeated Loads," *ACI Journal*, 76 (2), 297-309.

RILEM TC 162-TDF (2000), "RILEM TC 162-TDF: Test and Design Methods for Steel Fiber Reinforced Concrete. Bending Test Recommendations," *Materials and Structures,* 33 (225), 3-5.

Romualdi, J. P. and Mandel, J. A. (1964), "Tensile Strength of Concrete Affected by Uniformly Distributed and Closely Spaced Short Lengths of Wire Reinforcement," *ACI Journal,* 61 (6), 657-670.

Saatcioglu, M., Derecho, A. T., and Corley, W. G. (1983), "Modeling Hysteretic Behavior of Coupled Walls for Dynamic Analysis," *Earthquake Engineering and Structural Dynamics,* 2, 711-726.

Sakai, J. and Mahin, S. A. (2004), *Analytical Investigations of New Methods for Reducing Residual Displacements of Reinforced Concrete Bridge Columns, PEER-2004/02*, Pacific Earthquake Research Center, University of California at Berkeley, California.

Scribner, C. F. and Wight, J. K. (1980), "Strength Decay in R/C Beams Under Load Reversals," *Journal of the Structural Division,* ASCE, 106 (ST4), 861-876.

Shah, S. P. and Rangan, B. V. (1971), "Fiber Reinforced Concrete Properties," *ACI Journal,* 68 (2), 126-135.

Shahrooz, B. M. and Gong, B. (1998), "Steel-Concrete Coupling Beams: A Critical Overview of Design Guidelines," *Structural Engineers World Wide 1998.*

Shahrooz, B. M., Remmetter, M. A. and Qin, F. (1993), "Seismic Design and Performance of Composite Coupled Walls, *Journal of the Structural Division,* ASCE, 119 (11), 3291-3309.

Shiu, K. N., Barney, G. B., Fiorato, A. E., and Corley, W. G. (1978), "Reversing Load Tests of Reinforced Concrete Coupling Beams," *Central American Conference on Earthquake Engineering – Conferencia Centroamericana de Ingenieria Siemica, Proceedings,* 239-249.

Shiu, K. N., Aristizabal-Ochoa, J. D., Barney, G. B., Fiorato, A. E., and Corley, W. G. (1981), *Earthquake Resistant Structural Walls – Coupled Wall Tests,* Portland Cement Association, Skokie, Illinois, 151 pp.

Sonobe, Y., Kanakubo, T, Fujisawa, M., Fukuyama, H., Tanigaki, M., and Okamoto, T. (1995), "Structural Performance of Concrete Beams Reinforced with Diagonal FRP Bars," *Non-Metallic (FRP) Reinforcement for Concrete Structures, Proceedings of FRPRCS-2,*Ghent, Belgium, August 23-25, 344-351.

Soranakom, C. and Mobasher, B. (2007), "Closed-Form Solutions for Flexural Response of Fiber-Reinforced Concrete Beams," *Journal of Engineering Mechanics,* ASCE, 133 (8), 933-941.

Soranakom, C. and Mobasher, B. (2008), "Correlation of Tensile and Flexural Responses of Strain Softening and Strain Hardening Cement Composites," *Cement and Concrete Composites,* 30, 465-477.

Sorensen, H. C. (1974), "Efficiency of Bent-Up Bars As Shear Reinforcement," *Shear in Reinforced Concrete,* SP-42, American Concrete Institute, Detroit, MI, 267-283.

Snyder, M. J., and Lankard, D. R. (1972), "Factors Affecting the Flexural Strength of Steel Fibrous Concrete," *ACI Journal,* 69 (2), 96-100.

Smith, B. S., Girgis, A. M., and Abate, A. (1981), "Analogous Frames for the Analysis of Tall Shear Wall Structures," *Canadian Journal of Civil Engineering,* 8, 179-185.

Subedi, N. K. (1991), "RC-Coupled Shear Wall Structures. I: Analysis of Coupling Beams," *Journal of Structural Engineering,* ASCE, 117 (3), 667-680.

Swamy, R. N. and Bahia, H. M. (1979), "Influence of Fiber Reinforcement on the Dowel Resistance to Shear," *ACI Journal*, 76 (2), 327-355.

Swamy, R. N. and Bahia, H. M. (1985), "The Effectiveness of Steel Fibers as Shear Reinforcement," *Concrete International,* 7 (3), 35-40.

Swamy, R. N. and Al-Ta'an, S. A. (1981), "Deformation and Ultimate Strength in Flexure of Reinforced Concrete Beams Made with Steel Fiber Concrete," *ACI Journal*, 78 (5), 395-405.

Swamy, R. N., Al-Ta'an, S. A., and Ali, S. A. R. (1979), "Steel Fibers for Controlling Cracking and Deflection," *Concrete International,* 1 (8), 41-49.

Takayanagi, T. and Schnobrich, W. C. (1979) "Non-Linear Analysis of Coupled Wall Systems," *Earthquake Engineering and Structural Dynamics,* 7 (1), 1-22.

Tan, K. H., Murugappan, K., and Paramasivam, P. (1993), "Shear Behavior of Steel Fiber Reinforced Concrete Beams," *ACI Structural Journal,* 90 (1), 3-11.

Tassios, T. P., Moretti, M., and Bezas, A. (1996), "On the Behavior and Ductility of Reinforced Concrete Coupling Beams of Shear Walls," *ACI Structural Journal,* 93 (6), 1-10.

Tegos, I. A. and Penelis, G. G. (1988), "Seismic Resistance of Short Columns and Coupling Beams reinforced with Inclined Bars," *ACI Structural Journal,* 85 (1), 82-88.

Teshigawara, M., Kato, M., Sugaya, K. and Matsushima, Y. (1998a), "Energy Absorption Mechanism and the Fluctuation of shear Force in the Coupled shear Walls," *Structural Engineering World Wide 1998 – Proceedings,* Paper Number T-186-5, Elsevier Science Ltd., 8 pp.

Teshigawara, M., Sugaya, K., Kato, M. and Matsushima, Y. (1998b), "Seismic Test on 12-Story Coupled Shear Wall with Flange Walls," *Structural Engineering World Wide 1998 – Proceedings,* Paper Number T-186-4, Elsevier Science Ltd., 7 pp.

Theodorakopoulos, D. and Swamy, R. (1999), "Ultimate Punching Shear Strength-Analysis of Slab-Column Connections With Steel Fibers," *Structural Applications of Fiber Reinforced Concrete,* SP-182, American Concrete Institute, Detroit, 181-214.

Vondran, G. L. (1991), "Applications of Steel Fiber Reinforced Concrete," *Concrete International,* 13 (11), 44-49.

Wallace, J. W. and Moehle, J. P. (1992), "Ductility and Detailing Requirements of Bearing Wall Buildings," *Journal of Structural Engineering,* ASCE, 118 (6), 1625-1644.

Wallace, J. W. (1995), "Seismic Design of RC Structural Walls. Part I: New Code Format," *Journal of Structural Engineering,* ASCE, 121 (1), 75-87.

Wallace, J. W. and Thomsen, J. H. (1995), "Seismic Design of RC Structural Walls. Part II: Applications," *Journal of Structural Engineering,* ASCE, 121 (1), 88-101.

Wallace, J. W. (2007), "Modeling Issues for Tall Reinforced Concrete Core Wall buildings," *The Structural Design of Tall and Special Buildings,* 16, 615-632.

Wang, Y., Li, V. C., and Backer, S. (1990), "Experimental Determination of Tensile Behavior of Fiber Reinforced Concrete," *ACI Materials Journal,* 87 (5), 461-468.

Wight, J. K. and Sozen, M. A. (1975), "Strength Decay of RC Columns Under Shear Reversals," *Journal of the Structural Division,* ASCE, 101 (ST5), 1053-1065.

Yun, H.-D., Kim, S.-W., Jeon, E., Ji, S.-K. and Park, W.-S. (2007), "Seismic Performance of Shear Dominant Coupling Beams Using High-Performance Fiber-Reinforced Cement-Based Composites," *Conference Proceedings, 8th Pacific Conference on Earthquake Engineering,* 9 pp.

Yun, H.-D., Kim, S.-W., Jeon, E., Park, W.-S., and Lee, Y.-T. (2008), "Effects of Fiber-Reinforced Cement Composites' Ductility on the Seismic Performance of Short Coupling Beams," *Magazine of Concrete Research,* 60 (3), 223-233.

Zhang, H., Zhang, R., and Huang, C. (2007), "Experimental Study of Shear Resistance of Steel Fiber Reinforced High-Strength Concrete Coupling Beams," *Tumu Gongcheng Xuebao,* 40 (11), 15-22.

Zhao, Z. Z. and Kwan, A. K. H. (2003), "Nonlinear Behavior of Deep Reinforced Concrete Coupling Beams," *Structural Engineering and Mechanics,* 15 (2), 181-198.